Fall 2010

Noninvasive near infrared spectroscopy on living tissue with multivariate calibration approaches

Chuannan Bai
University of Iowa

NONINVASIVE NEAR INFRARED SPECTROSCOPY ON LIVING TISSUE WITH MULTIVARIATE CALIBRATION APPROACHES

by

Chuannan Bai

An Abstract

Of a thesis submitted in partial fulfillment
of the requirements for the Doctor of
Philosophy degree in Chemistry
in the Graduate College of
The University of Iowa

December 2010

Thesis Supervisor: Professor Mark A. Arnold

ABSTRACT

Near infrared (NIR) spectroscopy is being developed on living tissue models for noninvasively measuring *in vivo* glucose concentrations in individuals with diabetes. Multivariate calibration models have been built and the selectivity of each multivariate signature has been evaluated by several means. The primary objective of the research detailed in this dissertation is to practically apply noninvasive NIR glucose measurements on animal models for both short-term and long-term studies and preview future human subject evaluations.

In the animal study, living tissue spectra were collected through a modified optical interface with hyper- and hypo-glycemia control. Selective measurements of glucose molecules are illustrated by the partial lease squares (PLS) algorithm, net analyte signal (NAS) vector, and hybrid linear analysis (HLA). Each model demonstrates the ability to predict prospective glucose concentrations in the short term.

A restraint platform was developed for the long-term study on conscious animals. Conscious animal spectra were collected on multiple days. The anesthetized animal experiment follows on the final day. Principal component analysis (PCA) of spectra collected on different days demonstrates no significant difference between conscious animal spectra and anesthetized animal spectra. Moreover, an NAS vector analysis from conscious animal spectra has the ability predict glucose concentrations which follow the blood glucose transient during the anesthetized animal experiment. This procedure has great potential to be applied in future NIR glucose monitoring device.

Before the application of this noninvasive NIR technology on people with diabetes, the impact of skin difference must be determined. In this human subject study, human skin color and baseline spectra were collected and analyzed to determine differences among individuals and within groups of people. To compare *in vivo* NIR spectra with different skin characteristics, PCA was performed to obtain principal

component (PC) scores. Poor correlation between PC scores and skin characteristics concludes that noninvasive near-infrared technology is insensitive to different types of skin. In addition, glucose prediction was performed by a NAS analysis. The prediction results demonstrate that it is feasible to build a NAS glucose model for noninvasive NIR glucose predictions in human subjects.

Abstract Approved: _____
Thesis Supervisor

_____
Title and Department

_____
Date

NONINVASIVE NEAR INFRARED SPECTROSCOPY ON LIVING TISSUE WITH MULTIVARIATE CALIBRATION APPROACHES

by

Chuannan Bai

A thesis submitted in partial fulfillment
of the requirements for the Doctor of
Philosophy degree in Chemistry
in the Graduate College of
The University of Iowa

December 2010

Thesis Supervisor: Professor Mark A. Arnold

Graduate College
The University of Iowa
Iowa City, Iowa

CERTIFICATE OF APPROVAL

_____

PH.D. THESIS

_____

This is to certify that the Ph.D. thesis of

Chuannan Bai

has been approved by the Examining Committee
for the thesis requirement for the Doctor of Philosophy
degree in Chemistry at the December 2010 graduation.

Thesis Committee: _____
Mark A. Arnold, Thesis Supervisor

_____
Gary W. Small

_____
Lei Geng

_____
Claudio J. Margulis

_____
Julie L. P. Jessop

To my wife Wei Wang and my loving parents

ACKNOWLEDGMENTS

I would like to thank everyone who has helped and supported me during my graduate study. Their direct and indirect contributions to this dissertation are highly appreciated.

At the very first, I am honored to express my deepest and sincerest gratitude to my research advisor, Dr. Mark A. Arnold, for his continuous support during my Ph.D. study. His patience, motivation, enthusiasm, and immense knowledge have made my research life smooth, productive, and full of good memories. I am also thankful for the excellent example that he provided as successful scientist and chemist.

I am also extremely grateful to Dr Gary W. Small for the invaluable discussions and instructions. Dr. Small is more like my second research advisor and who led me into this chemometrics world. Anytime when I had difficulties in my research, he was always there to help with his intelligence, diligence, and patience.

It is my pleasure to thank my other committee members: Dr. Lei Geng, Dr. Claudio J. Margulis, Dr. Julie L. P. Jessop, and Dr. Daniel M. Quinn for the valuable discussion and suggestions about my research.

Special thanks also go to Dr. Jonathon T. Olesberg and Dr. Lingzhi Liu for the animal study training and generous sharing of many computer codes. Without their initial setup and studies, this work would not been half as complete. Their success in this research has set an excellent example for me.

I would also like to thank Terry L. Graham for her help in the animal study and data collection. It was she who taught me the right way to handle animals. She was more like a translator between the animals and I.

I am indebted to every member in Arnold Research Group to support me. I would like to thank Dong, Lingzhi, Min, David, Sherif, Wenjiao, Valerie, Joo Young, Natasha,

Jue, Ryan, and Bo for a variety of help in my experiments, support during my presentation practice, and discussions in the group meeting.

I wish to thank my parents for providing me a loving environment and supporting me for whatever decision I made.

Last but not least, I would like to thank my wife, Wei Wang, for the support throughout my graduate study and encouragement during my thesis writing.

ABSTRACT

Near infrared (NIR) spectroscopy is being developed on living tissue models for noninvasively measuring *in vivo* glucose concentrations in individuals with diabetes. Multivariate calibration models have been built and the selectivity of each multivariate signature has been evaluated by several means. The primary objective of the research detailed in this dissertation is to practically apply noninvasive NIR glucose measurements on animal models for both short-term and long-term studies and preview future human subject evaluations.

In the animal study, living tissue spectra were collected through a modified optical interface with hyper- and hypo-glycemia control. Selective measurements of glucose molecules are illustrated by the partial lease squares (PLS) algorithm, net analyte signal (NAS) vector, and hybrid linear analysis (HLA). Each model demonstrates the ability to predict prospective glucose concentrations in the short term.

A restraint platform was developed for the long-term study on conscious animals. Conscious animal spectra were collected on multiple days. The anesthetized animal experiment follows on the final day. Principal component analysis (PCA) of spectra collected on different days demonstrates no significant difference between conscious animal spectra and anesthetized animal spectra. Moreover, an NAS vector analysis from conscious animal spectra has the ability predict glucose concentrations which follow the blood glucose transient during the anesthetized animal experiment. This procedure has great potential to be applied in future NIR glucose monitoring device.

Before the application of this noninvasive NIR technology on people with diabetes, the impact of skin difference must be determined. In this human subject study, human skin color and baseline spectra were collected and analyzed to determine differences among individuals and within groups of people. To compare *in vivo* NIR spectra with different skin characteristics, PCA was performed to obtain principal

component (PC) scores. Poor correlation between PC scores and skin characteristics concludes that noninvasive near-infrared technology is insensitive to different types of skin. In addition, glucose prediction was performed by a NAS analysis. The prediction results demonstrate that it is feasible to build a NAS glucose model for noninvasive NIR glucose predictions in human subjects.

TABLE OF CONTENTS

LIST OF TABLES

LIST OF FIGURES

CHAPTER I

INTRODUCTION

Diabetes

Diabetes is a syndrome of disordered metabolism which causes abnormal blood glucose levels. Glucose is one of the primary sources of energy for all kinds of body activities. Glucose concentration in the blood stream is regulated by insulin, a hormone produced in the pancreas. Generally, there are two different types of diabetes: type I which the body cannot produce sufficient amount of insulin and type II where insulin cannot be properly used. In 2008 diabetes has been recognized as the seventh leading cause of death in the United States and the annual societal cost of diabetes was estimated to be 174 billion dollars.[1]

Due to the lack of blood glucose regulation, hyper- and hypo- glycemia are two common manifestations for people with diabetes. Long term complications associated with diabetes includes eye disease, kidney disease, nerve disease and heart disease.[2] Although there is no cure for diabetes currently, study has shown that tight glycimia control can reduce the risk of complications and extend patients' lives by five to eight years.[3-5] In order to maintain regular blood glucose levels, people with type 1 diabetes need insulin delivery by pump or injection during hyperglycemia and glucose intake during hypoglycemia. For people with type 2 diabetes, physical activity, low carbohydrate diet, and certain medications are used to control blood glucose levels. No matter which type of diabetes, frequent blood glucose measurements are recommended for tight glycemic control.

Conventional blood glucose measurements are based on glucose monitors that employ test strips. This method involves a finger prick, capillary blood collection, and portable meter reading. This type of sensor is based on an enzymatic reaction of either glucose oxidase or glucose dehydrogenase with the glucose molecules. The

corresponding electrochemical signal is detected from the production of H_2O_2.[6] The produced current is selective for glucose due to the application of a glucose specific enzyme. Since this type of glucose device is portable, easy to use, and highly sensitive and selective for glucose, it has been widely applied for self blood glucose monitoring (SBGM). However, this enzyme electrochemical based monitor has three major disadvantages: first, the required blood collection is painful and creates a risk of infection; second, one time use enzyme based test strips are costly which limits the frequency of testing for hypo- and hyper- glycemia; and third, discrete measurements do not reflect fluctuations in the blood glucose concentrations.[7] Therefore, great efforts have been made in the last two decades for the development of the next generation glucose monitoring device which is designed to overcome these limitations.

Continuous Glucose Monitoring

Continuous glucose monitoring (CGM) is believed to better track glucose fluctuations and measure the rate of glucose variations.[8] It also can be combined with an insulin pump to better regulate glycemia. Most CGM systems are based on an implantable glucose biosensors.[9] The active surface of these implantable biosensors is positioned in the subcutaneous tissue and provides a continuous measure of the concentration of glucose in the interstitial fluid (ISF).[10] These ISF glucose levels are correlated to blood glucose levels through an *in situ* calibration that is based on a test-strip measurement. The principal complication of these implantable systems is the biologic response to the implant which significantly alters the sensor's response. In the best case, sensor readings can be calibrated periodically to compensate for these *in vivo* changes. However, in the worst case, the biologic response completely isolates the sensing unit, thereby rendering the sensor useless. Several implantable biosensors are available commercially, but their use is restricted due to accuracy concerns, particularly at low concentrations. Although implantable biosensors face some challenges, this

technology provides valuable continuous glucose concentration information and can track rates and direction of concentration changes.

In recent years, significant progress has been made in the commercialization of CGM. The first commercial CGM device, CGMS® developed by MiniMed (Northridge, CA) was approved by the Food and Drug Administration (FDA) in 1999. Afterwards, the MiniMed systems Guardian®, Guardian RT®, and Paradigm REAL-Time® were available in 2004, 2005, and 2006, respectively. DexCom, Inc. (San Diego, CA) developed its STS® glucose monitor in 2006. Newer models, SEVEN® and SEVEN PLUS® were approved in 2007 and 2009, respectively. In addition, Abbott Diabetes Care (Alameda, CA) offers the FreeStyle Navigator® glucose monitor which was approved in 2008. All of these CGM systems use a glucose selective enzyme that are inserted into subcutaneous tissue. Other than FreeStyle Navigator®, they all rely on the electrochemical detecting of H_2O_2. The FreeStyle Navigator® uses Wired Enzym™ technology where an osmium-based mediator molecule is detected instead of H_2O_2.

A different type of CGM device, the GlucoWatch Biographer® which is based on extraction of transdermal interstitial fluid by reverse iontophoresis, was developed by Cygnus, Inc. (Redwood City, CA) and was approved by the FDA in 2001. Unfortunately, this product was discontinued in 2007.

Further improvements in the CGM systems will result in longer lifetimes, better performance, and increased comfort for the user.

Noninvasive Glucose Monitoring

Although so much work has been done on the replacement of conventional glucose sensing technology,[11] the first actual noninvasive glucose monitoring device is not yet available. A reliable noninvasive glucose sensor will not only release the patients with diabetes from the tedious, painful, and frequent glucose tests, but will also decrease the economic issues for those patients, their families and even the whole society.

Furthermore, a successful noninvasive monitor could deliver more accurate glucose information to the insulin pump system, thereby improving tighter glycemic control and reducing the risk of death and onset of major health complications.

The first challenge for a noninvasive glucose sensor is measuring glucose concentration accurately and precisely in the most demanding concentration range (2-5 mM) required for the effective clinical treatment.[12] The conventional test strip glucose sensors have relative accuracies of 6-10% which must be matched by any future noninvasive sensing technology.[13] The second issue is selectivity. Most of the current test strip glucose sensors are based on enzymatic reactions of glucose with either glucose oxidase (GOx) or glucose dehydrogenase (GDH) which are highly selective. However, the selectivity of noninvasive techniques must be evaluated and established.

Noninvasive sensing technology can be categorized as being either an indirect or direct measurement.[14] Indirect measurements are based on the effect of glucose on the physical, chemical, or physiological state of the probed tissue. Direct measurements are based on directly probing an intrinsic property of the glucose molecule.

The scattering of electromagnetic radiation as it propagates through tissue is a common example of an indirect glucose measurement. The scattering coefficient of living tissue depends on the refractive index of the ISF, which is affected by the concentration of glucose. As a result, a strong correlation exists between glucose concentration and the magnitude of scattering as light propagates through the tissue. It is fairly straightforward to record such a correlation and many of the early reports for noninvasive glucose sensing were likely based on this phenomenon.[15, 16]

Optical coherence tomography (OCT) is a related measurement that also correlates *in vivo* glucose concentrations to the scattering properties of tissue.[17-20] A unique feature of OCT is the ability to measure scattering at specific depths into the tissue matrix. Such measurements consist of a low coherent light source, interferometer with a moving mirror arm and a sample arm, and a detector for recording the

interferogram. The interferogram corresponds to the interference pattern between back scattered light from the sample and light reflected from the reference mirror. By moving the reference mirror, the OCT measurement can scan tissue to a depth of approximately 1mm, thereby reaching the dermis layer of skin tissue. Strong correlations between OCT values and blood glucose concentration have been reported, presumably on the basis of refractive index changes in the ISF.

Although strong correlations are reported between blood glucose concentration and optical scattering of skin tissue, this approach suffers from poor selectivity. Glucose is not the only osmolyte that affects the refractive index of the ISF and, as such, many different conditions, both chemical and physical, can adversely affect the signal. Indeed, selectivity is a major issue for all indirect approaches, including measurements based on correlations between blood glucose concentrations and optical scattering, thermal conductivity, and electrical impedance.

In addition, other properties, such as temperature-modulated localized reflectance ultrasound reflectance, and impedance, have also been proposed.[11, 21-23] However, establishing a correlation between blood glucose concentrations and the indirect property of interest is necessary for a valid noninvasive measurement technique. Alone, however, such correlations are insufficient and incapable of developing into a robust and reliable clinical measurement for a wide population of people with diabetes. Before indirect approaches can advance, a detailed understanding of the basis of interferences must be established under both typical and atypical clinical conditions.

Direct noninvasive glucose measurements are based on an intrinsic property of the glucose molecule. Analytical information is mostly obtained from the bonding within the molecule. Common measurement modes include absorption spectroscopy at either mid-infrared or near-infrared wavelengths, and Raman scattering spectroscopy. Such measurements involve passing a selected band of electromagnetic radiation into the tissue of interest and collecting a spectrum of the radiation that exits the body. This spectrum

is analyzed to obtain the concentration of glucose in the tissue.

For both near-infrared and mid-infrared spectroscopic methods, absorption of the incident radiation is monitored. Different measurement geometries are reported for such measurements, including transmission, diffuse reflectance, transflectance, and photoacoustic optical configurations. Concentrations are related to absorbance values at wavelengths associated with the glucose vibration spectrum. The corresponding near-infrared absorption features correspond to combination and overtone transitions, whereas the fundamental absorption bands are probed in the mid-infrared spectra.

For Raman scattering spectroscopy, the excitation radiation is launched into the tissue of interest and the Raman spectrum is recorded as this excitation radiation propagates through the tissue matrix.[24-28] Analytical information is obtained from an analysis of the resulting Raman spectrum where concentrations are related to the magnitude of emission bands associated with the Raman spectrum of glucose.

Selectivity is the major issue for both absorption and Raman spectroscopic approaches, owing to the chemical and physical complexity of living tissue. No magic wavelength, or set of wavelengths, exists where glucose exclusively absorbs or emits radiation that can be used for a selective glucose measurement. Indeed, the spectroscopic information for glucose originates from C-H and O-H bonds which are ubiquitous within biological matrixes. As a result, noninvasive spectroscopic measurements are composed of the superposition of absorption bands and scattering emission bands associated with all chemical components within the tissue matrix, such as proteins, amino acids, organic acids, urea, lipids, etc.

An example of the degree of spectral overlap is presented in Figure I-1. This figure shows the superimposed absorption spectra for a set of common biological molecules. In this case, the spectral range corresponds to the combination region of the near infrared spectrum, which spans 5000-4000 cm^{-1} in wavenumbers or 2.0-2.5 μm in

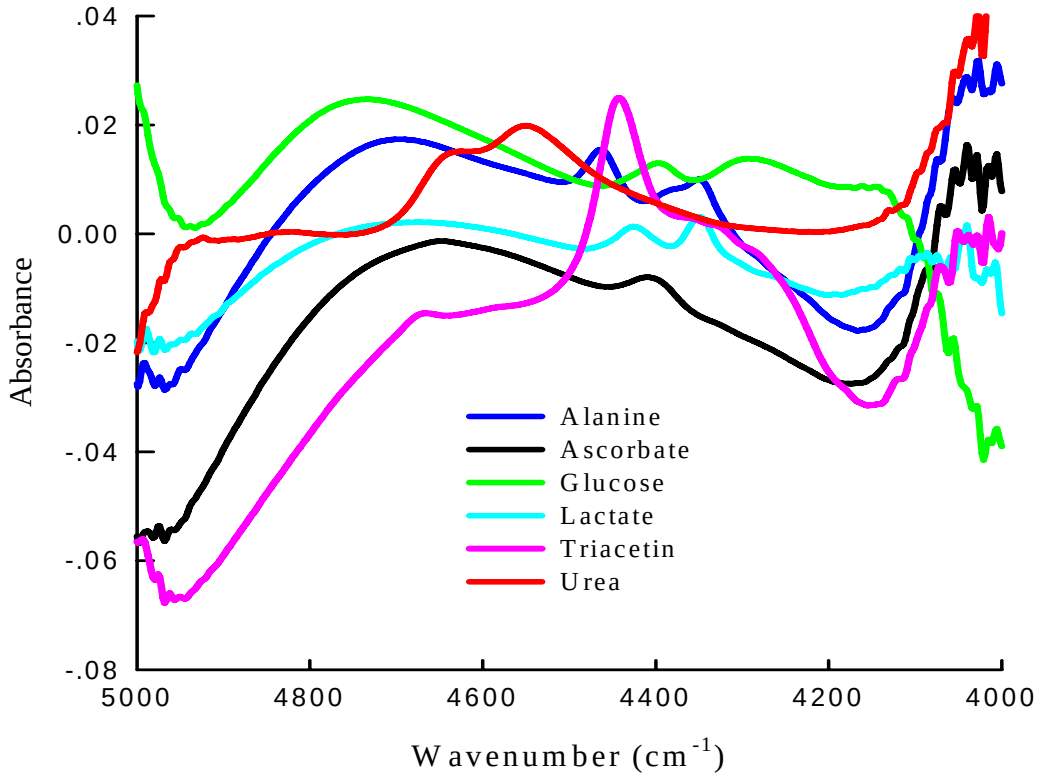

Figure I-1 Example of near-infrared spectra for selected biological molecules. Superimposed absorption spectra are shown for glucose, lactate, alanine, ascorbate, triacetin and urea over the combination spectral range.

wavelength. Absorption bands in this spectral range correspond to the combination of stretching and bending vibrations associated with C-H, N-H, and O-H bonds. This spectral range falls between two large water absorption bands centered at 5200 and 3600 cm^{-1} and corresponds to a window through aqueous media. A strong degree of spectral overlap is evident for the combination absorption bands associated with these molecules. Nevertheless, each spectrum is unique and this uniqueness is the chemical basis for selectivity in such measurements.[29]

Spectra from both mid-infrared absorption and Raman scattering measurements correspond to fundamental vibrational transitions, and are typically more distinctive and less overlapping in comparison to near-infrared absorption spectra.[27] As a result, mid-infrared and Raman spectroscopic methods offer greater chemical selectivity compared to near-infrared spectroscopy. Conversely, mid-infrared spectra are limited by the strong absorption properties of water which limits penetration depths of mid-infrared radiation to tens-of-microns into the skin matrix. As a result, mid-infrared spectra correspond to the epidermis layer where glucose levels are limited and correlations with blood glucose are ineffective. Raman spectroscopy, on the other hand, can propagate deep into skin tissue, but Raman spectra of living skin are complicated by background fluorescence signals and poor instrumental signal-to-noise ratios (SNRs).

Besides interferences from chemical substances, the physical condition of the tissue also can dramatically alter the collected spectrum and, hence, measurement accuracy. Temperature of the tissue is an example of a physical parameter that affects the infrared spectrum of water, which greatly impacts the noninvasive spectrum of tissue given the high concentration of water in such samples. Similarly, signals from Raman scattering spectroscopy are strongly affected by any parameter that alters the scattering properties of the tissue matrix, such as temperature, hydration, osmolyte concentration, etc.

Several fluorescence based methods of analysis are proposed for noninvasive

glucose measurements. As discussed below, both reagentless and reagent-based methods are under investigation.

Reagentless measurements correspond mainly to the auto-fluorescence of skin which is related to the formation of advanced glycation end-products (AGE's).[30] The formation of AGE's in skin results from chronic hyper-glycemia according to a set of well known non-enzymatic reactions between protein and carbohydrates (glucose).[31] Such fluorescence-based AGE measurements cannot respond to the rapid fluctuations in real-time blood glucose concentrations, however, they might be useful as the basis for a diabetes screening procedure that can identify people with diabetes.[32]

Reagent-based noninvasive systems involve the measurement of glucose in tear fluid. The concept is to place an object, such as a contact lens, in the tear fluid and monitor glucose through a reagent-enhanced analytical measurement. The reagents are embedded within the polymer structure of the contact lens. A change in either the color[33-35] or fluorescence intensity[36-39] of the membrane (lens) is measured and related to blood glucose concentrations through a calibration curve.

In one case, the sensing mechanism centers on an array of colloidal particles embedded in a hydrogel matrix.[33-35] The colloidal array establishes a refraction grating that disperses white light and is viewed as a rainbow of color. Glucose binds to the array particles through chemical interactions and alters the distance between the particles in the array, thereby changing the diffraction pattern. A change in color is observed which can be related to the concentration of glucose.

Two types of glucose recognition chemistry are used for these types of measurements. The first involves complexation between glucose and derivatives of boronic acid which are immobilized within the membrane. Molecular orientation of the boronic acid group provides strong and reversible binding to diol-containing species, such as glucose. The second approach involves competitive binding between glucose and fluorescently labeled dextran for a fixed number of concanavolin A (Con A) binding

sites. The Con A is also labeled with a complementary fluorophore to provide a fluorescence resonance energy transfer (FRET) measurement. In the absence of glucose, the Con A binding sites are filled with labeled dextran and FRET is maximized. The bound dextran is displaced by glucose, thereby lowering the extent of FRET and altering the measured fluorescence signal.

A major issue for these methods based on tear fluid glucose concentrations is the relationship between the concentration of glucose in the tear fluid and that in blood.[40] These concentrations must be strongly correlated to provide a useful clinical device and researchers continue to explore the robustness of this correlation. A challenging aspect is the low concentration of glucose in tear fluid. Typically the concentrations of glucose in tear fluid are in the low micro-molar concentration range, which demands high sensitivity for reliable measurements.

Near Infrared (NIR) Spectroscopy

Fundamentals of Near Infrared (NIR) Spectroscopy

The NIR region of the electromagnetic spectrum extends from 12800 to 4000 cm^{-1} (0.78 to 2.5 μm). This region contains chemicals' absorption information associated with the combinations and overtones of C-H, O-H, and N-H fundamental vibrations.[41, 42] The absorption is described by the Beer-Lambert law:

$$A = -\log(\frac{I}{I_0}) = \varepsilon \cdot c \cdot l \qquad \text{Equation I-1}$$

where A is the absorbance, I and I_0 are the intensities of the incident and transmitted light, respectively, ε is the molar absorptivity with the unit of $(mol/L)^{-1}\ mm^{-1}$, c is the concentration in mol/L, and l is the optical path length in mm.

Compared to fundamental vibrations in the mid-IR region (4000~200 cm^{-1}) which is also called the ‘fingerprint’ region, NIR absorbance peaks are one to three orders of

magnitude weaker. Therefore, reasonably long path length at mm level is required. This makes it possible to measure raw materials directly without sample preparation. In contrast, much higher absorbance in the mid-IR region is commonly used for the qualitative identification of chemical compounds. Meanwhile, absorption peaks in NIR region are broad and heavily overlapped. For the purpose of quantitative analysis, multivariate calibration methods are widely used to extract chemical information from such overlapping spectral features.

Considerable research has been done on NIR spectroscopy of biomolecules because of its potential applications in the agricultural,[43, 44] food,[45-50] petroleum,[51-53] and pharmaceutical[54-58] industries. Compared to conventional methods and other spectroscopy techniques, NIR spectroscopy has several major advantages: first, the low energy of NIR radiation is nondestructive, which makes NIR spectroscopy applicable for both online and inline monitoring; second, NIR spectroscopy is associated with the combinations and overtones of C-H, O-H, and N-H fundamental vibrations,[41, 42] which means most biomolecules have features in the NIR region, therefore, NIR spectroscopy can be used for a variety of analytes; third, fast spectra acquisition times combined with complex data analysis makes NIR spectroscopy well suited for real time sensing; and finally, reasonable path length requirements from the Beer-Lambert law makes it possible to analyze a variety of samples with minimal pretreatment. However, peak broadening and overlapping spectral signatures make NIR challenging for quantitative analysis in complex mixtures. Various multivariate calibration methods have been applied to interpret spectra of complex samples and isolate target analyte information. A brief review of multivariate methods is provided in a subsequent section.

Fourier Transform Infrared (FTIR) Spectrometer

An FTIR spectrometer consists of a light source, Michelson interferometer, sample compartment, detector, and associated electronics. The Michelson interferometer

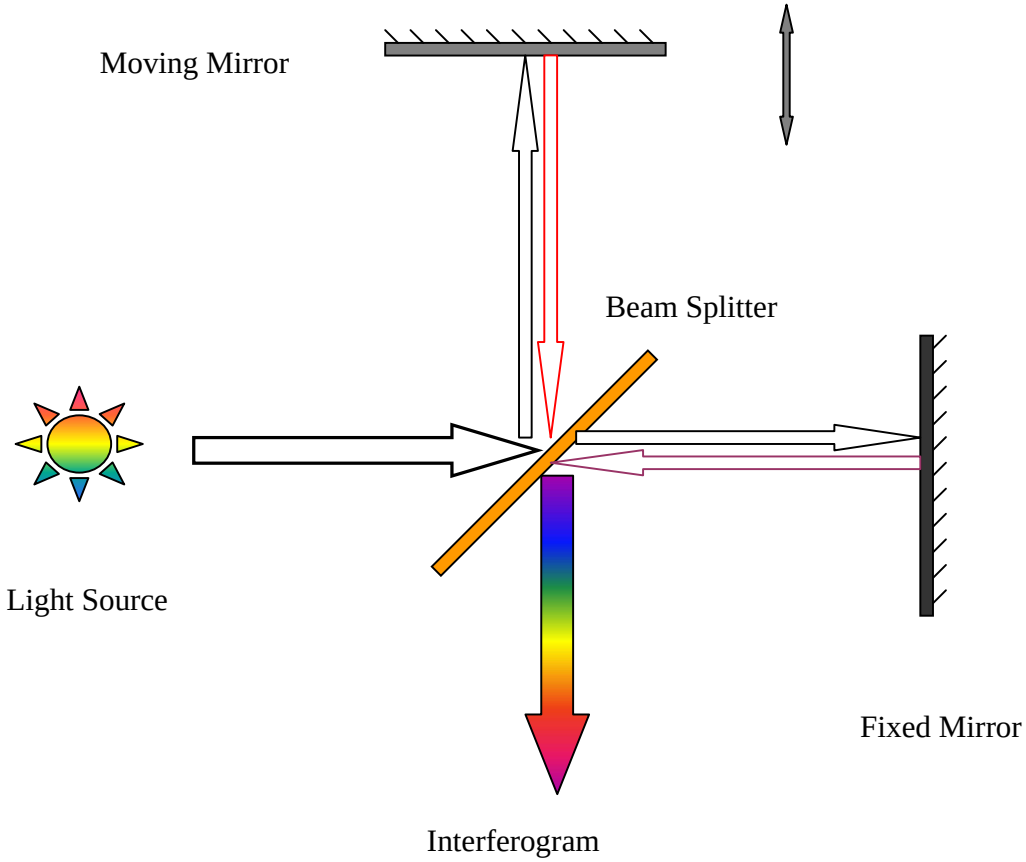

Figure I-2. Schematic diagram of a Michelson interferometer

FTIR spectrometer was by Michelson in the late 19th century and is the heart of the FTIR spectrometer. [59, 60] The schematic diagram of Michelson interferometer is shown in Figure I-2. The interferometer consists of a beam splitter, a fixed mirror, and a moving mirror with precise translation control. The beam splitter partially reflects and partially transmits the incident light. The reflected and transmitted light rejoins after being reflected by the fixed and moving mirror, respectively. There is an optical path length difference between the reflected and transmitted light, which is caused by the position of the moving mirror. Therefore, the recombined beam produces an interferogram pattern. After propagating through the sample and reaching the detector, the corresponding time domain signal is converted to the single-beam spectrum by applying the Fast Fourier Transform (FFT) algorithm.

The FTIR spectrometer has the multiplexing advantage or Fellgett's advantage over the conventional dispersive spectrometer.[42, 61] This means the simultaneous collection of all frequencies allows shorter acquisition time and more scans for spectra averaging, which can increase the efficiency and enhance the signal to noise ratio (*S/N*). In contrast, the conventional dispersive spectrometer must scan each frequency/wavelength one by one, which results in longer spectral collection time and lack of efficiency. Another advantage is the throughput advantage and it is also known as the Jacquinot advantage.[42, 61] Due to the lack of slits the signal level at the detector is much greater than for a scanning spectrometer, thereby increasing the magnitude of the signal and enhancing the S/N. Resolution of FTIR spectrometer depends on the distance the moving mirror travels. In contrast, the slit on conventional spectrometer controls the spectral resolution by limiting the solid angle which reduces the signal and lowers the S/N. A HeNe laser is used as internal wavelength reference which provides excellent frequency precision and wavelength repeatability of less than 0.01 cm^{-1}. In traditional dispersive spectrometers, the frequency precision relies on the mechanics of monochrometer, which may induce more error. For FT instrument, high frequency

precision and wavelength repeatability induce less uncertainty during spectral averaging, thus increasing the *S/N*. However, for all FT instruments, the moving elements become an obstacle when considering a portable or miniaturized design that can operate in non-laboratory environemtns.

Multivariate Calibration

Although NIR spectroscopy has so many advantages, it is not straightforward for quantitative application, because absorbance features in the NIR region are relatively low in magnitude, and peaks are broad and heavily overlapping. Therefore, multivariate techniques are generally required to separate target analyte information for the complex matrix components. In general, multivariate analysis uses information derived from multiple wavenumbers or wavelengths instead of single one. Calibration is based on the relationship between the spectral variances at particular wavenumbers or wavelengths and changes in the target analyte concentrations. This relationship can be established by two different approaches: projection analysis and correlation analysis. Several algorithms used in this dissertation, including principal component analysis (PCA), partial least squares (PLS) analysis, net analyte signal (NAS) analysis, and hybrid linear analysis (HLA) are described below.

Principal Component Analysis (PCA)

Principal component analysis (PCA) is a mathematical procedure to decompose the spectral matrix into several uncorrelated principal components (PCs).[62-65] This decomposition is expressed as follows:

$$\boldsymbol{X} = \boldsymbol{T}\boldsymbol{P}^{\boldsymbol{T}} + \boldsymbol{E} \qquad \text{Equation I-2}$$

where $\boldsymbol{X}$ is the whole spectral matrix, which is composed of n spectra and each spectrum contains p absorbance values collected at p wavenumbers or wavelengths. $\boldsymbol{T}$

is the score matrix and $\boldsymbol{P}$ is the loading vectors, and $\boldsymbol{E}$ is the noise that cannot be explained by these loadings. The $\boldsymbol{P}$ matrix contains spectral loadings which are orthogonal to each other. The loadings are sorted by the contribution to the spectra variances. The first loading represents the most significant spectral variance, while the last one represents the least. The number of PCs, which is also called latent variables or number of factors, depends on the complexity of the original spectra matrix. More PCs lead to higher chance of overfitting. In general, noisy features in the loading spectrum is an indicator that that factor contains no chemical information –only noise.

There are two different approaches to decompose the original spectral matrix: the singular value decomposition (SVD) algorithm[64, 66] and the nonlinear iterative partial least squares (NIPALS) algorithm[65].

In the singular value decomposition (SVD) algorithm, the decomposition of the spectral matrix $\boldsymbol{X}$ $(n \times p)$ is described in Equation I-3:

$$\boldsymbol{X} = \boldsymbol{U}\ \boldsymbol{\Sigma}\ \boldsymbol{V} \qquad \text{Equation I-3}$$

where $\boldsymbol{U}$ is a $n \times n$ orthogonal matrix containing eigenvectors of $\boldsymbol{XX^T}$ in each column, $\boldsymbol{\Sigma}$ is a $n \times p$ diagonal matrix , and $\boldsymbol{V}$ is a $p \times p$ orthogonal matrix containing eigenvectors of $\boldsymbol{X^T X}$ in each column. Diagonal elements in the $\boldsymbol{\Sigma}$ matrix are called singular values of the matrix, which are equal to the square root of the eigenvalues of $\boldsymbol{XX^T}$. In the case where k latent variables are selected, *i.e.*, number of factors = k, the k spectral loadings are the first k columns of the $\boldsymbol{V}$ matrix ($\boldsymbol{V_k}$: $p \times k$). The corresponding score matrix $\boldsymbol{T_k}$ $(n \times k)$ is:

$$\boldsymbol{T_k} = \boldsymbol{U_k \Sigma_k} \qquad \text{Equation I-4}$$

where $\boldsymbol{U}_k$ $(n \times k)$ is the matrix of the first k columns in the $\boldsymbol{U}$ matrix and $\boldsymbol{\Sigma}_k$ is the $k \times k$ diagonal matrix from the first k elements in the $\boldsymbol{\Sigma}$ matrix. This singular value decomposition (SVD) algorithm is also used in the calculation of the net analyte signal (NAS), which is discussed below.

Nonlinear iterative partial least squares (NIPALS) algorithm is an iteration based algorithm.[65, 67, 68] The procedure is as follows:

1. Initial score estimation: one randomly selected observation from the spectral matrix $\boldsymbol{X}$ $(n \times p)$ is treated as the initial score $\boldsymbol{t}_k$ for the *k*th latent variable. In practice, a spectrum with the maximum standard deviation is preferred;

2. Projection of the matrix $\boldsymbol{X}$ onto $\boldsymbol{t}_k$ to obtain the corresponding loading $\boldsymbol{p}_k$ by the following equation:

$$\boldsymbol{p}_k = \frac{\boldsymbol{X}^T \boldsymbol{t}_k}{\boldsymbol{t}_k^T \boldsymbol{t}_k} \qquad \text{Equation I-5}$$

3. Normalizing loading $\boldsymbol{p}_k$ to length = 1:

$$\boldsymbol{p}_k = \frac{\boldsymbol{p}_k}{\boldsymbol{p}_k^T \boldsymbol{p}_k} \qquad \text{Equation I-6}$$

4. Projection of the matrix $\boldsymbol{X}$ onto $\boldsymbol{p}_k$ to obtain the new score $\boldsymbol{t}_{k-new}$:

$$\boldsymbol{t}_{k-new} = \frac{\boldsymbol{X}\boldsymbol{p}_k}{\boldsymbol{p}_k^T \boldsymbol{p}_k} \qquad \text{Equation I-7}$$

5. Calculation of the convergence between the $\boldsymbol{t}_{k-new}$ in Step 4 and initial $\boldsymbol{t}_k$ in Step 1. If the difference is larger than a predefined threshold, replace $\boldsymbol{t}_k$ with $\boldsymbol{t}_{k-new}$ and then go back to Step 2. Otherwise, remove the *k*th PCA component from the matrix $\boldsymbol{X}$:

$$\boldsymbol{X} = \boldsymbol{X} - \boldsymbol{t}_k \boldsymbol{p}_k \qquad \text{Equation I-8}$$

6. Starting the next latent variable with Step 1.

In this NIPALS algorithm, there are three predefined parameters: number of latent variables, threshold of score convergence, and maximum number of iterations. The latent variables depend on the complexity of the spectral matrix. More latent variables are preferred for a more complex matrix. The threshold of score convergence determines the accuracy of the score estimation. The maximum number of iterations affects the computation speed.

Decomposition of the $\boldsymbol{XX^T}$ matrix is involved in the SVD algorithm. When the $\boldsymbol{X}$ matrix is large, the calculation is extremely slow. The NIPALS algorithm on the other hand deals with the latent variables one by one, thus it runs faster and it is preferred when dealing with large data matrices. In this dissertation, the PCA with NIPALS algorithm is only applied in Chapter IV to cope with the large human subject data set. The SVD algorithm is applied in the computation of the NAS as described below.

PCA is a powerful tool to explore the spectral components. The spectral loadings obtained from a PCA provide information about the components that contribute most to spectral variances. Peaks in the loading spectra can help locate the chemical components in the matrix, while broad features such as slope and curve can indicate certain physical and environmental variances like scattering and temperature. As more and more latent variables are used, the loading spectrum becomes more complicated. At a certain number of factors, the noise becomes dominant in the loadings, which indicates overfitting due to too many factors. The maximum number of factors with non-noise loadings indicates no more chemical information is available, which, ideally, is related to the number of major components in the sample matrix. The PC scores indicate the magnitude of each PC loading vector. The distribution of PC scores can to identify the spectral outliers. In addition, sequential changes of scores reflect temporal variations within the sample

The loadings and scores obtained in the PCA can be correlated with the reference concentrations of the observations by Principal Component Regression

(PCR). Since PCR is not used in this dissertation, this topic is not covered. Details of this algorithm can be found elsewhere.[56-62]

Partial Least-Square (PLS) Regression

Partial least-square (PLS) regression is a correlation based technique. The PLS model tracks the correlation between variances in spectral features and variances in analyte concentrations.[69, 70] It is one of the most popular regression methods used to analyze NIR spectral data. Based on number of components in the samples, two methods are available: PLS1 and PLS2. In PLS1, each model only deals with one analyte, which means the reference matrix contains only one column. In PLS2, models are established for multiple components simultaneously.[71] With the fast development of computer performance, computation speed is not a big concern, thus, PLS1 is preferred to obtain individual models for each analyte in most cases. The algorithm for PLS1 is discussed in detail in the following section.

First of all, the normalized first loading weight set $\boldsymbol{w}_1$ is calculated as the following equation:

$$\boldsymbol{w}_1 = \frac{\boldsymbol{X}^T \boldsymbol{y}}{\left\| \boldsymbol{X}^T \boldsymbol{y} \right\|} \qquad \text{Equation I-9}$$

where $\boldsymbol{X}$ is the $n \times p$ spectral matrix, $\boldsymbol{y}$ is the $n \times 1$ vector of analyte concentrations. Then, the first score $\boldsymbol{t}_1$ is estimated by:

$$\boldsymbol{t}_1 = \boldsymbol{X}\boldsymbol{w}_1 \qquad \text{Equation I-10}$$

The corresponding spectral loading $\boldsymbol{p}_1$ is calculated as:

$$\boldsymbol{p}_1 = \frac{\boldsymbol{X}\boldsymbol{t}_1}{\boldsymbol{t}_1^T \boldsymbol{t}_1}$$ Equation I-11

Then, the new score $\boldsymbol{t}_{1-new}$ is obtained by:

$$\boldsymbol{t}_{1-new} = \frac{\boldsymbol{X}\boldsymbol{p}_1}{\boldsymbol{p}_1^T \boldsymbol{p}_1}$$ Equation I-12

The convergence between the $\boldsymbol{t}_{1-new}$ and the initial estimated $\boldsymbol{t}_1$ is calculated. If the difference is larger than the predefined threshold, replace $\boldsymbol{t}_1$ with $\boldsymbol{t}_{1-new}$ and repeat the above procedure until the score $\boldsymbol{t}_1$ is convergent. The next step is to calculate the concentration loading $\boldsymbol{q}_1$ by the following equation:

$$\boldsymbol{q}_1 = \frac{\boldsymbol{t}_1^T \boldsymbol{y}}{\boldsymbol{t}_1^T \boldsymbol{t}_1}$$ Equation I-13

Before the calculation in the next latent variable, both the spectra $\boldsymbol{X}$ and reference $\boldsymbol{y}$ should be deflated by the following two equations:

$$\boldsymbol{X} = \boldsymbol{X} - \boldsymbol{t}_1 \boldsymbol{p}_1$$ Equation I-14

$$\boldsymbol{y} = \boldsymbol{y} - \boldsymbol{t}_1 \boldsymbol{q}_1$$ Equation I-15

The calculation of the k th latent variable is the same as in previous steps starting from equation I-9. After all the k desired latent variables are calculated, the calibration vector $\boldsymbol{b}$ ($p \times 1$), or the regression coefficient vector, is obtained:

$$\boldsymbol{b} = \boldsymbol{W}(\boldsymbol{P}^T \boldsymbol{W})^{-1} \boldsymbol{q}$$ Equation I-16

where $\boldsymbol{W}$ is a $p \times k$ matrix which contains k weighting factors ($\boldsymbol{w_1}$ to $\boldsymbol{w_k}$), $\boldsymbol{P}$ is a $p \times k$ matrix which contains k spectral loadings ($\boldsymbol{p_1}$ to $\boldsymbol{p_k}$), and $\boldsymbol{q}$ is the concentration loading vector ($k \times 1$) which contains $\boldsymbol{q_1}$ to $\boldsymbol{q_k}$. The concentration predictions can be done by:

$$\hat{c} = \boldsymbol{Xb} \qquad \text{Equation I-17}$$

Evaluation of Partial Least-Squares (PLS) Regression

The partial least-square (PLS) regression method is based on the correlation between the spectral variance and concentration variance. With different latent variables, the performance of the predictions varies significantly. With fewer factors used, the regression model is likely underestimated, while more latent variables may lead to overmodelling where noise patterns are counted in the regression.[72] Generally, the optimal number of latent variables is related to the dimensionality of the sample matrix which includes not only chemical components but also physical and environmental changes, such as temperature and flow rate fluctuations. To find the optimal latent variables, two popular routines are widely applied. The first one is to separate the whole data set into calibration and prediction sub-sets. Most of the time, the calibration data set is further divided into training and monitoring sub-sets. The training data set is used to create a PLS regression model, the monitoring data set is used to determine the optimal latent variables, and the prediction data set is used to evaluate the performance of the relative PLS model. To quantitatively evaluate the model, the standard error of calibration or monitoring (SEC or SEM) or standard error of prediction (SEP) are used and the formulas for each are described in Equations I-18 to 20[29, 73, 74]:

$$\text{SEC} = \sqrt{\frac{\sum (c_c - \hat{c}_c)^2}{n_c - k - 1}} \qquad \text{Equation I-18}$$

$$\text{SEM} = \sqrt{\frac{\sum (c_m - \hat{c}_m)^2}{n_m}} \qquad \text{Equation I-19}$$

$$\text{SEP} = \sqrt{\frac{\sum (c_p - \hat{c}_p)^2}{n_p}} \qquad \text{Equation I-20}$$

where c_c, c_m, and c_p are reference concentrations of calibration and prediction sets, respectively, $\hat{c}_c$, $\hat{c}_m$, and $\hat{c}_p$ are the concentration predictions of calibration and prediction sets, respectively, n_c, n_m, and n_p are the numbers of spectra in calibration, monitoring, and prediction sets, respectively, and k is the number of latent variables used in the PLS regression. In Equation I-18, the degree of freedom is $n_c - k - 1$ because one degree of freedom is usually used for mean centering of the original data matrix and k degrees of freedom are consumed for k latent variables. For the prediction data set, the degree of freedom is the number of independent observations which is the number of spectra.

The second method is called the leave-several-samples-out cross validation. A portion of the entire data set is separated for monitoring purposes. The remaining data set is used to build calibration model. This procedure is repeated m times until each spectrum has been removed once for prediction. The cross validation standard error of prediction (CVSEP) is calculated by the following equation[29, 73, 74]:

$$\text{CVSEP} = \frac{1}{m}\sum^{m}\sqrt{\frac{\sum (c_p - \hat{c}_p)^2}{n_p}} \qquad \text{Equation I-21}$$

In both of these methods, SEC, SEM, SEP, and CVSEP are computed at different number of factors. Usually, the number of latent variables that gives the minimum SEC, SEM, SEP, or CVSEP are selected as optimal. However, to avoid overmodelling, SEC, SEM, SEP, or CVSEP with fewer number of factors are compared with the minimum by using the F-test. If no significant difference is found, less latent variables are preferred.

Spectral range is also an important parameter to be optimized. By eliminating spectral regions where the target analyte has no absorption features, the PLS regression performance can be improved significantly. The spectral range optimization is done by a grid search of different spectral window sizes and positions. This spectral range optimization is usually combined with the search for the optimum number of latent variables. The spectra windows with various window sizes and positions are scanned through the entire spectral region. The spectral window with the minimum prediction error and a reasonable number of factors is selected. This spectral range is also double-checked with the analyte absorption regions. They should be consistent for a selective PLS model.[27, 75-77]

Since the PLS regression is a correlation-based algorithm, it is possible to correlate the target analyte with other components or noise in the sample matrix. Thus the selectivity of the PLS regression must be evaluated. Pure component selectivity analysis (PCSA) was developed for this purpose.[27, 75, 78-82] Samples with various levels of the target analyte and interferences are prepared separately, spectra of these two types of samples are input into the previously established PLS model. For a selective PLS model, the correct analyte concentration is obtained from an analyte spectrum and zero is obtained from a sample contains only interference. This method has been used in different applications.[27, 75, 81, 82] Unfortunately, PCSA is not applicable for the noninvasive sensing on living tissue, because it is impossible to obtain the sample matrix with interferences only. To access the selectivity for glucose in the *in vivo* living tissue study, the net analyte signal (NAS) and hybrid linear analysis (HLA) algorithms are available and details for these two algorithms are covered in the following sections.

Net Analyte Signal (NAS)

Net analyte signal (NAS) is the portion of the spectrum of the pure target analyte that is orthogonal to the background spectra which contain all the spectral components

except the analyte. This concept was firstly proposed by Lorber in 1986.[83] Figure I-3 illustrates the NAS concept through vector projection. To realize this procedure, a pure target analyte spectrum and back ground spectra which contain all sorts of variances except the target analyte should be collected. The NAS of the interested component i can be obtained by the following equation:

$$\boldsymbol{NAS}_i = (\boldsymbol{I} - \boldsymbol{A}_{-i}\boldsymbol{A}_{-i}^{+})\boldsymbol{a}_i \qquad \text{Equation I-22}$$

where $\boldsymbol{a}_i$ is the pure component spectrum of the component of interested i, $\boldsymbol{A}_{-i}$ is the background matrix containing all sources of variances except the component i, $\boldsymbol{A}_{-i}^{+}$ is the pseudo inverse of $\boldsymbol{A}_{-i}$, and $\boldsymbol{I}$ is the identity matrix with the same dimension as $\boldsymbol{A}_{-i}\boldsymbol{A}_{-i}^{+}$.The original background spectra are in a much high dimension of space and these spectra also contain noise. Projection of the pure analyte absorbance vector onto each of these dimensions is always time consuming and the sensitivity of the final NAS is extremely low. To reduce the time and to enhance the NAS performance, a PCA or PLS process is applied on the background spectra for dimension reduction.[83, 84] Certain numbers of principal components (PCs) or loadings are selected to represent the background. The pure analyte spectrum is projected onto the first PC and the remaining orthogonal portion is then projected onto the second PC. The projection onto the kth PC can be described as:

$$\boldsymbol{a}_i^{*} = \boldsymbol{a}_i - \frac{\boldsymbol{a}_i \cdot \boldsymbol{v}_k}{\boldsymbol{v}_k^{T} \cdot \boldsymbol{v}_k}\boldsymbol{v}_k \qquad \text{Equation I-23}$$

where $\boldsymbol{a}_i^{*}$ is the remaining orthogonal portion after projection, and $\boldsymbol{v}_k$ is the kth PC loading from the PCA analysis. The same procedure is repeated until the optimal number of latent variables is found. The procedure to explore the optimal number of factors is the same as that in the PLS method and exactly the same SEC, SEM, and SEP terms are used

to evaluate the performance of the NAS model.

The length of the NAS vector is determined by the path length and concentration of the analyte used to collect the pure analyte spectrum $\boldsymbol{a}_i$. For quantitative purpose, the NAS vector must be normalized by the following equation:

$$\boldsymbol{NAS}_i = \frac{\boldsymbol{a}_i^*}{\left\|\boldsymbol{a}_i^*\right\|} \qquad \text{Equation I-24}$$

where $\left\| \right\|$ denotes the magnitude or the norm of the $\boldsymbol{a}_i^*$ vector. The concentration prediction of the component i can be obtained by Equation I-25:

$$\hat{c}_i = NAS_i \boldsymbol{X} \qquad \text{Equation I-25}$$

Since the NAS is derived from intrinsic molecular information, it provides more information about the chemistry compared to the statistical correlation used in the PLS algorithm. Moreover, NAS demonstrates the spectral contributions with the existence of the background matrix, thus the NAS is a good calibration vector for quantitative analysis. The NAS can be applied not only for quantification, but can also eb used to compare spectral features with other multivariate models on the basis of chemistry. Due to the uniqueness of the NAS, it also provides valuable information about selectivity, sensitivity, and limit of detection (LOD).

Sensitivity

Sensitivity in analytical chemistry is defined as the slope of the calibration curve and is a measure of the magnitude of signal change for a given change in concentration.[85] It measures the smallest concentration difference that the calibration model can differentiate. In the NAS algorithm, the sensitivity of a NAS calibration model is estimated from Equation I-26[83, 84]:

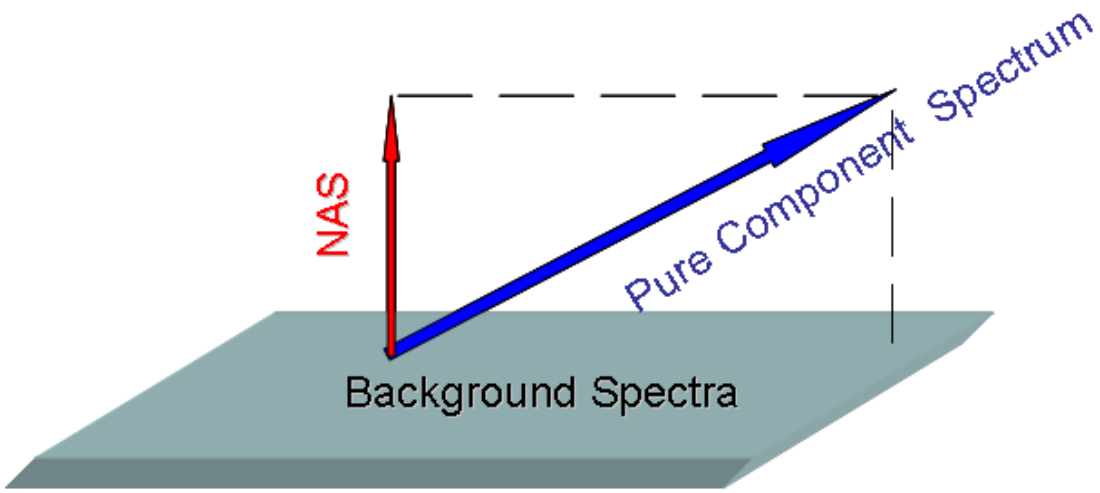

Figure I-3. An illustration of NAS projection in a 3 dimensional space.

$$\text{Sensitivity} = \frac{\left\| \boldsymbol{NAS}_i \right\|}{c_i} \qquad \text{Equation I-26}$$

Selectivity

Selectivity of a method is defined as the ability to quantify a particular analyte in a mixture or matrix without interferences from other components within the matrix. Selectivity of a NAS calibration model is defined as the angle between the NAS calibration vector NAS_i and the pure analyte vector $\boldsymbol{a}_i$,[83, 84] which can be expressed as:

$$\text{Selectivity} = \frac{\left\| \boldsymbol{NAS}_i \right\|}{\left\| \boldsymbol{a}_i \right\|} \qquad \text{Equation I-27}$$

In an ideal case in which no interference exists in the sample matrix, the analyte vector is perpendicular to the background, therefore, the corresponding NAS is the pure analyte vector itself and the selectivity is equal to 1. In the worst scenario, the analyte vector is parallel to the background matrix, thus, the angle between the NAS and analyte vectors is 0. In other cases, the selectivity is between 0 and 1 and a larger number corresponds to higher selectivity for the analyte.

NAS-Based Signal-to-Noise Ratio (S/N_{NAS})

The signal-to-noise ratio (S/N) is a useful term to evaluate the performance of an instrumental analysis. In this particular NAS-based signal-to-noise ratio (S/N_{NAS}), the signal is defined as the magnitude of the NAS vector, and the noise is from two major sources: chemical and instrumental. In this NAS method, projection of the background spectra onto the NAS vector leads to negative or positive residuals. The standard deviation of magnitudes of these residuals defines the NAS-based noise. Thus, the NAS-based signal-to-noise ratio (S/N_{NAS}) can be expressed as:[83, 84]

$$S/N_{NAS} = \frac{\|\boldsymbol{NAS}\|}{\varepsilon_{NAS}}$$ Equation I-28

where ε_{NAS} is the NAS-based noise.

Limit of Detection (LOD)

The limit of detection (LOD) is defined as the smallest amount of concentration that one analytical method can reliably detect in a given type of sample matrix.[86] In the NAS algorithm, LOD is defined as:[83, 84]

$$LOD = \frac{c_0}{\frac{\|\boldsymbol{NAS}\|}{3\varepsilon_{NAS}} - 1}$$ Equation I-29

where c_0 is the concentration of the analyte used in the pure component spectrum. In most cases, the signal-to-noise ratio (S/N_{NAS}) term is much larger than 1, thus, the LOD expression is inconsistent with the regular International Union of Pure and Applied Chemistry (IUPAC) definition of LOD.

Hybrid Linear Analysis (HLA)

Hybrid linear analysis (HLA) is an alternative way to obtain the NAS. The HLA method was first proposed by Berger et al.[87] It was then widely applied in multivariate analysis and compared with the PLS algorithm.[88-91] Instead of establishing an experimental background, it calculates the background spectra from the calibration data set. In the HLA algorithm, the concentrations of calibration samples are measured by a reference method. To obtain the background matrix which contains no analyte information, the spectral contribution of the target analyte is subtracted from the original calibration data set by the following equation:

$$A_{0i} = A_i - \varepsilon b c_i \qquad \text{Equation I-30}$$

where A_{0i} is one of the calculated background spectra, A_i is one of the original spectra, ε is the absorptivity of the analyte molecule, *b* is the optical path length, and c_i is the measured analyte concentration. With this calculation, spectral variance associated with the analyte is mathematically removed from the spectral matrix. After the background is calculate, the HLA algorithm is exactly the same as the NAS algorithm. The HLA methods keeps all the advantages of the NAS method while not requiring a physical background. This is especially beneficial for *in vivo* analyses where a zero background is difficult to obtain.

Scope of the Dissertation

In this dissertation, major achievements were made from the following three aspects: first, hardware improvement including the modification of the existing FTIR spectrometer, optical interface design for living tissues, and multiple pumping system for the animal models; second, establishment of multiple animal models with various transients of target analytes including glucose, lactate, and urea, as well as chemometric modeling and evaluation; and third, preliminary human subject data and analysis.

In Chapter II, the hardware that used for collecting NIR noninvasive spectra of living tissue is described. The hardware includes a customized FTIR spectrometer with enhanced light source and detector, optical interface for living tissue, and pumping systems for the animal models. In addition, multiple animal models are established with various transients of glucose, including both hyper- and hypo- glycemia. Finally, chemometric models are established with different algorithms, including PLS, NAS, and HLA. Models are presented for different animal experiments and model performance and selectivity are evaluated.

Chapter III focuses on validating the glucose chemometric models with external prediction data sets. In this study, the ability to predict glucose concentrations from prospective spectra is evaluated. This study identifies the short-term and long-term performances of these glucose models, and determines the factors that interfere with glucose concentration predictions. Four different approaches are investigated to establish external validation data sets. The first three approaches are based on the three animal models introduced in Chapter II. The forth model is based on a new multiple-day animal model. With different approaches, glucose models with the ability to predict from prospective spectra are obtained.

A preliminary human subject baseline study is presented in Chapter IV. Different skin colors, ages, genders, and ethnic groups are considered. Spectral comparison results concluded that no significant differences are found among different groups of participants, which means the NIR noninvasive method is applicable to a variety of populations. Issues with current instrumentation are also discussed, such as the optical throughput and the optics-skin interface.

In Chapter V, another two important biomolecules, lactate and urea, are examined with the similar instrumentation as in Chapters II to IV. This chapter illustrates NIR noninvasive calibration methods are possible for these other metabolites.

CHAPTER II

IN VIVO NEAR-INFRARED SPECTROSCOPY STUDY OF RAT SKIN TISSUE WITH VARYING BLOOD GLUCOSE LEVELS

Introduction

Diabetes is a disease of metabolism disorder, which the body cannot produce enough insulin or properly use insulin. The World Health Organization (WHO) projects a worldwide diabetes population of 336 million by 2030.[92] Unfortunately, there is no effective cure right now. However, studies have shown that tight glycemic control (*i.e.*, control of hyper- and hypo- glycemia) can reduce the onset of complications and extend patients' lifetime. Thus, frequent glucose measurements are beneficial for diabetes. The current glucose reading device is based on an electrochemistry enzymatic reaction and the required capillary blood sample is collected by a finger prick. This conventional method is not continuous, costly and poses a risk of infection. For the last several decades, great effort has been placed on the development of the next generation of glucose monitoring devices. Among these new techniques, near infrared (NIR) spectroscopy is one of the most promising approaches because it is potentically noninvasive, continuous, and economic.

Near infrared (NIR) spectroscopy for noninvasive glucose monitoring involves passing a band of NIR radiation through a certain body compartment and extracting glucose concentration information from the corresponding NIR spectrum. The penetration depth makes NIR spectroscopy applicable to skin tissue. In this study, a spectral range of 5000 – 4000 cm^{-1} in wavenumbers or 2.0–2.5 μm in wavelength is used, because this spectral range falls between two large water absorption bands centered at 5200 and 3600 cm^{-1} and corresponds to a window through aqueous media.[7, 29, 73] In our study, a commercial FTIR spectrometer equipped with an external light source, external

detector, and customized sapphire-rod interface is used to collect all *in vivo* spectra of living skin.

Molecular glucose displaces absorption peaks at 4300 and 4400cm^{-1} due to the combination of C-H bending and C-H stretching modes, as well as at 4750 cm^{-1} which is caused by the combination of O-H stretching and C-H bending modes.[93] The unique glucose molecular absorption features in this NIR region make it possible to predict glucose selectively. Since the spectral variance caused by glucose concentration change is extremely low (in the μAU level) compared with the overall skin absorbance (in the AU level), multivariate calibration techniques are always used to correlate spectral variations with glucose concentrations. Partial least-squares (PLS) regression is one of the most popular methods, which is commonly used to build glucose models. However, PLS is a statistical based correlation method that is prone to chance correlations with interferences and noise. In addition, no spectral information from glucose molecules is necessarily involved in the calibration. Therefore, the selectivity of PLS models must be evaluated. Previous studies in our laboratory have demonstrate that PLS models from *in vivo* animal spectra can be selective for glucose, but a variety of evaluations are necessary, such as comparing the similarity between PLS calibration vectors and glucose net analyte signal (NAS) vectors. The glucose NAS approach has two unique features: first, it is derived from a pure glucose absorption spectrum which impacts glucose selectivity; and second, the glucose NAS is the orthogonal part of the glucose absorption spectrum after being projected onto the background which contains all sources of spectral from the matrix. Due to these two characteristics, the glucose NAS can be used for the quantitative determination of glucose concentrations in complex matrix, such as living skin tissue.[76, 77] In this study, we extensively investigate the selectivity for glucose and apply the resulting glucose calibration models to measure under both hyper- and hypo- glycemic conditions. The glucose NAS vector generally requires adequate number of glucose baseline spectra. However, in the real case, even when the animal is fasted overnight, there are still

glucose fluctuations which can degrade the effectiveness of the NAS model. Hybrid L-linear analysis (HLA) is conducted in this study to assess the effectiveness if this alternative method.

Previous studies in our lab have successfully identified a selective glucose signature from noninvaisve NIR spectra of living animal models.[76, 77, 94] The research in this dissertation focuses on the blood glucose range from 1 to 17 mM, which covers the normal blood glucose range[95] as well as hyper- and hypo- glycemia. In this study, three animal models were established with multiple glucose transients (both hyper- and hypo-glycemia). Glucose transients were achieved by a three-pump hyper- and hypo- glycemic control system. PLS, NAS, and HLA algorithms were applied. Performance of these chemometric models was evaluated and the selectivity for glucose was also investigated. In comparison, the findings in the previous studies[76, 77, 94, 96] correspond to a single transient at a glucose concentration level that is abnormally high – even for a subject with Type I diabetes. Our objective here is to demonstrate the NAS concept for selective glucose measurements for multiple transients at more clinically relevant concentrations. The findings reported below verify a functional selectivity for glucose and illustrate our ability to monitor concentration transients over both hyper- and hypo-glycemia levels.

Experimental Section

Reagents

Pentobarbital sodium injection solution from Ovation Pharmaceuticals (Deerfield, IL) was used to anesthetize rats. 50% dextrose from IVX Animal Health Inc. (St. Joseph, MO) was used directly as glucose injection solution. 0.9% sodium chloride injection solution (saline) was purchased from Baxter Healthcare (Deerfield, IL) and was used as a solvent for insulin and heparinized saline. A 0.5 unit insulin injection solution was prepared by diluting 100 units/ml Novoline® regular human insulin injection solution (Novo Nordisk Inc. Princeton, NJ). It was prepared by mixing 0.075 ml Novolin® in

14.925 ml saline. The heparinized saline was prepared by mixing 1 ml of 1000 USP units heparin sodium that was purchased from American Pharmaceutical Partners, Inc. (Schaumburg, IL) in 49 ml of saline. A 2% lidocaine HCl solution (Abbott Laboratory, Chicago, IL) was used topically during surgery for infiltration and nerve block. All reagents were obtained from the University of Iowa Hospitals and Clinics (UIHC) pharmacy. All procedures were approved by the University of Iowa Animal Care and Use Committee (ACURF # 0507182).

Surgical Procedure

Adult male Sprague-Dawley rats (retired breeders, weighting ~ 400 g) were used as the animal model in this work. A skin fold on the back of neck was selected as the object based on previous results in our laboratory illustrating similarity of NIR absorbance features and magnitude between rat neck and skin fold on the back of a human hand.[76, 77, 94] Figure II-1 shows this similarity between human and animal skin tissue spectra. Other than that, rat tissue has stronger absorption peaks around 4300 cm^{-1} than that of human skin, and the overall absorbance magnitudes are different due to skin thicknesses and variation of scattering properties. Rats were fasted overnight prior to the *in vivo* study to minimize the initial blood glucose fluctuations. Animals were anesthetized with pentobarbital sodium injection solution at the dosage of 50 mg/kg before the canulation surgery. Anesthesia was also maintained during the experiment with pentobarbital at a dosage of 25 mg/kg/hour. After the anesthetization, hair on the upper back and femoral area was removed. During the surgery, two catheters were canulated into a femoral vein and artery. The venous catheter was used for the infusion of glucose, insulin, saline and anesthetic. The arterial catheter was used for frequent blood sampling during the experiment. After the surgery, the animal was transferred to the spectroscopy station, and the body temperature was maintained at 38.3 °C by a closed-loop temperature controller R/S 68900 (Barnant Company, Port Huron, MI).

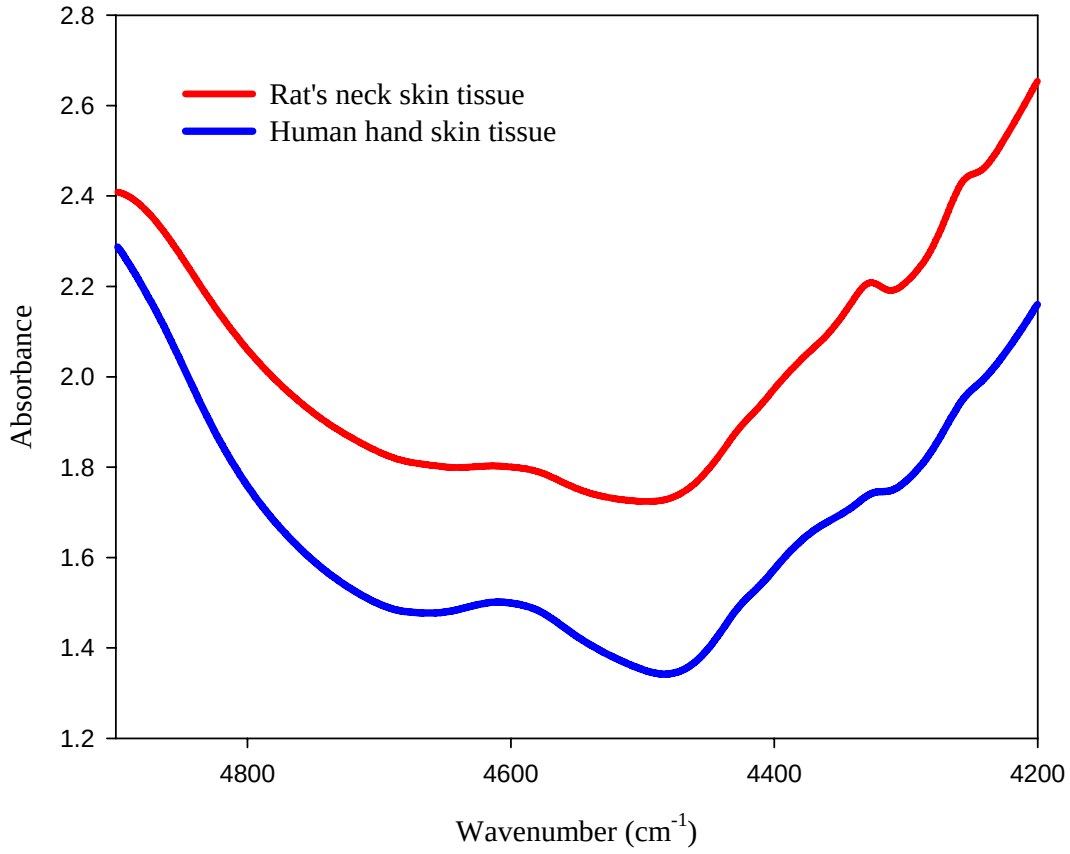

Figure II-1. NIR skin tissue spectra of human and rat.

Supplemental oxygen was provided at the rate of 1.5 L/hour. A MouseOX® pulse oximeter probe (STARR Life Sciences, Oakmont PA) was hooked up to rat's leg to monitor its pulse rate and distension, oxygen saturation, as well as breathe rate and distention.

Instrumentation

Skin tissue spectra were collected on a Nicolet 670 FTIR spectrometer (Nicolet Analytical Instruments, Wisconsin, MI). Figure II-2 demonstrates the instrumental setup. A 50-W tungsten-halogen light bulb (Gilway, Technical Lamp, Peabody, MA) with an integrated, gold-coated reflector was used as the light source. An E3633A 200-watt DC power supply (Agilent Technology, Van Nuys, CA) was used to maintain the light bulb at 12.00 V and 4.10 A. A custom sapphire-rod interface was used to bring the light from the spectrometer to the skin tissue and then to couple the transmitted light to an external detector. This interface contains two pieces of 3-mm-diameter sapphire rods, one for guiding the interferogram to the skin tissue and the other one for coupling to the detector. Collected light was detected by a two-stage thermoelectrically cooled extended-wavelength InGaAs detector with a diameter of 1 mm and a 2.6-μm cutoff (Judson Technologies, Montgomeryville, PA). The current signal was amplified to a voltage signal by a low-noise transimpedance amplifier (Femto Messtechink GmbH, Berlin, Germany). Figures II-3(b) and (d) shows the image of the whole instrumentation and the detail of the interface, respectively. Optical filters in the optical path restrict the spectral range of 5000 to 4000 cm^{-1}. Spectra were collected at a resolution of 8 cm^{-1} with 128 co-added scans. Each spectrum required slightly more than 60 seconds for collection. The interferograms were Fourier transformed to single-beam spectra with triangular apodization, standard Mertz phase correction, and 1-level of zero filling. After the canulation surgery was finshed, the rat was connected to the hyper- and hypo-glycemic control system and skin tissue was placed in the optical interface as shown in Figures II-3

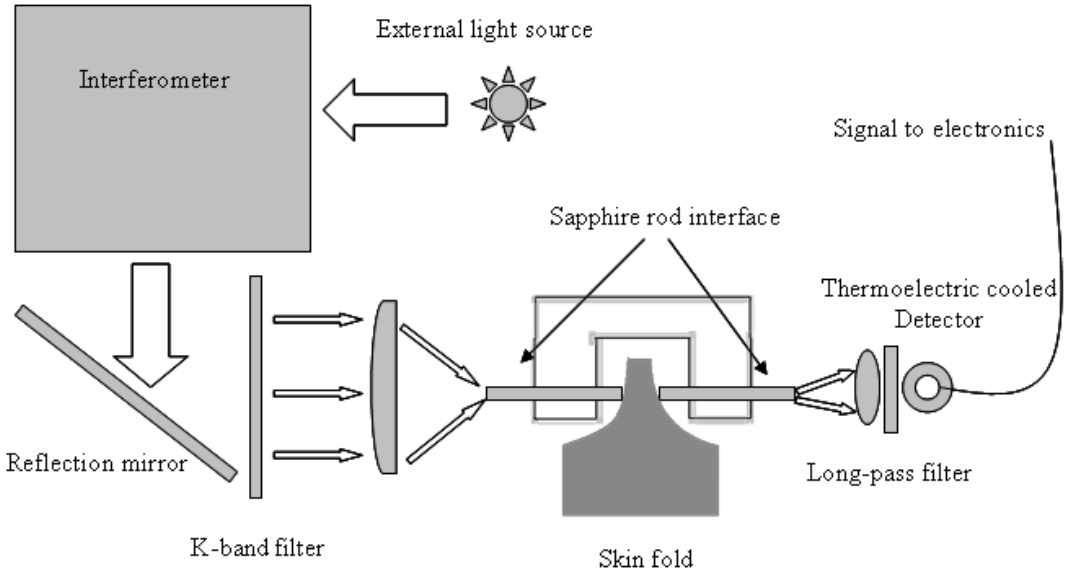

Figure II-2. Schematic layout of animal experimental instrumentation.

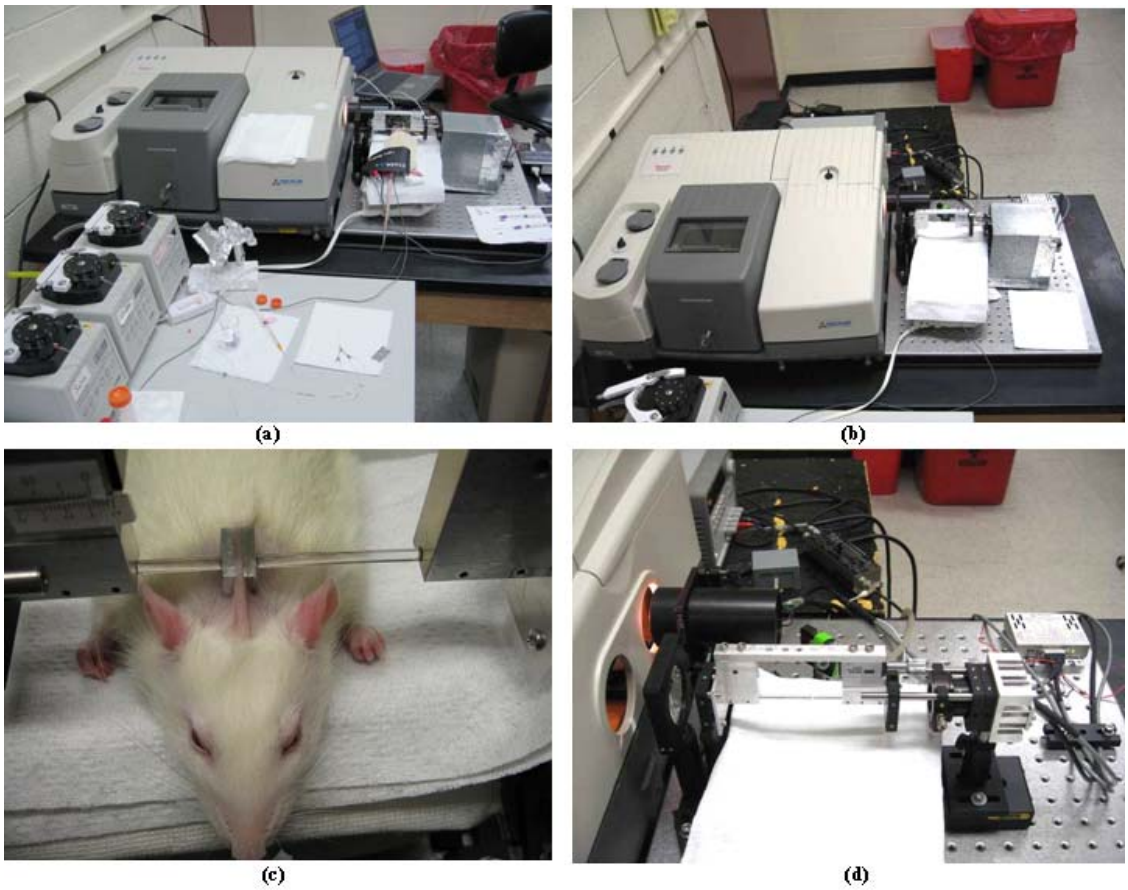

Figure II-3. Experimental setup of a typical animal experiment showing (a) overview of the instrumentation and hyper- and hypo- glycemic control pump system; (b) customized FT-NIR spectrometer with external light source, sapphire-rod interface, and external detector; (c) an anesthetized rat being clamped during a typical animal study; and (d) close-up view of the external light source, sapphire-rod interface, and external detector..

(a) and (c), respectively. Two pieces of metal blocks with central holes were glued onto the skin tissue to help fix the tissue sample in position and consequently minimize the impact of unconscious movement on spectral quality. Initially, spectra were collected without glucose or insulin perfusion and only saline was perfused to prevent dehydration. Since the animal had fasted overnight, the blood glucose reference values were similar over the initial time period. After sufficient baseline spectra were collected, either the glucose or insulin pump was started. The infusion rate was adjusted according to the rat's body mass and the blood glucose value. Glucose and insulin were infused alternatively to achieve hyper- and hypo- glycemia. With this procedure, one, two, and three cycles of hyper- and hypo- glycemia were obtained on three individual rats. At the end, blood glucose levels were allowed to return to the baseline levels without any infusion of glucose or insulin. This baseline condition was maintained until sufficient spectra were collected. The corresponding blood glucose profiles for rats 1, 2, and 3 are shown in Figure II-4.

Hyper- and Hypo- Glycemic Control and Glucose Profile

During spectral collection, single or multiple glucose transients were obtained infusing glucose/insulin solutions alternatively through the venous catheter by two dynamax peristaltic pumps (Rainin Instrument Co., Wpburn, MA). A third pump was also used to infuse saline to compensate for body dehydration. Meanwhile, blood samples were taken from the arterial catheter every 5-10 minutes for reference blood glucose measurements. Blood glucose measurements were taken as the averaging of two Freestyle® glucose monitors (Abbott Laboratory, Chicago, IL) readings.

Data Processing

MATLAB R2007a (the MathWorks, Natick, MA) was used for all the data analysis. Multivariate calibration models were established and evaluated by PLS, NAS, and HLA based algorithms with absorbance spectra.

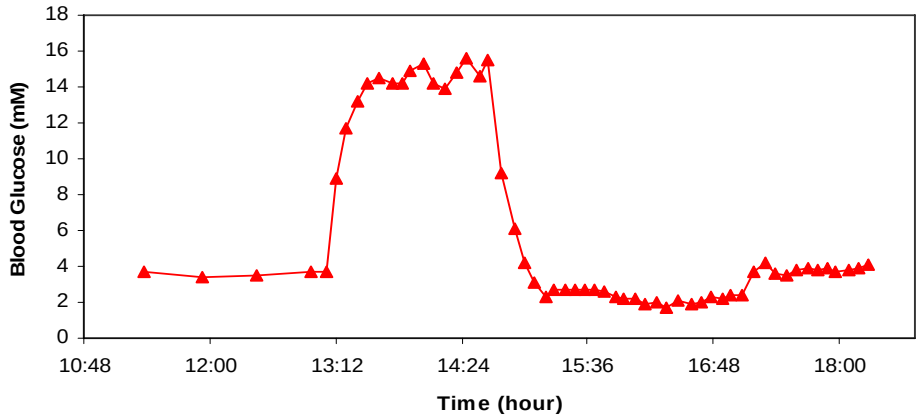

(a)

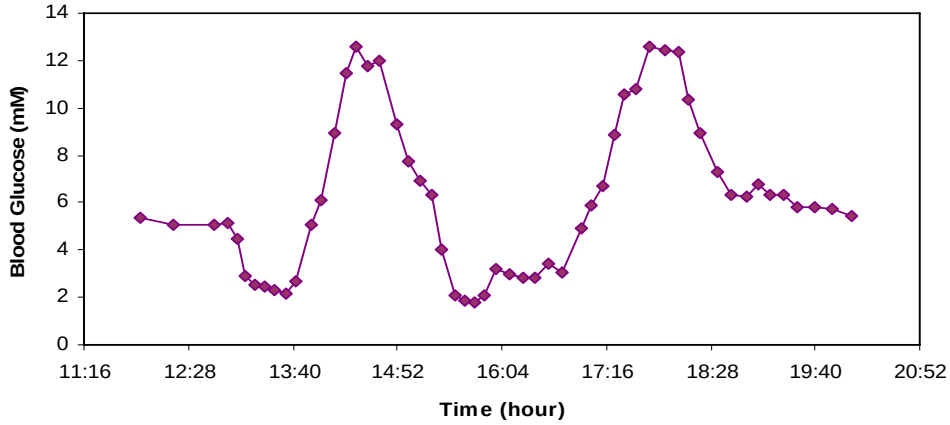

(b)

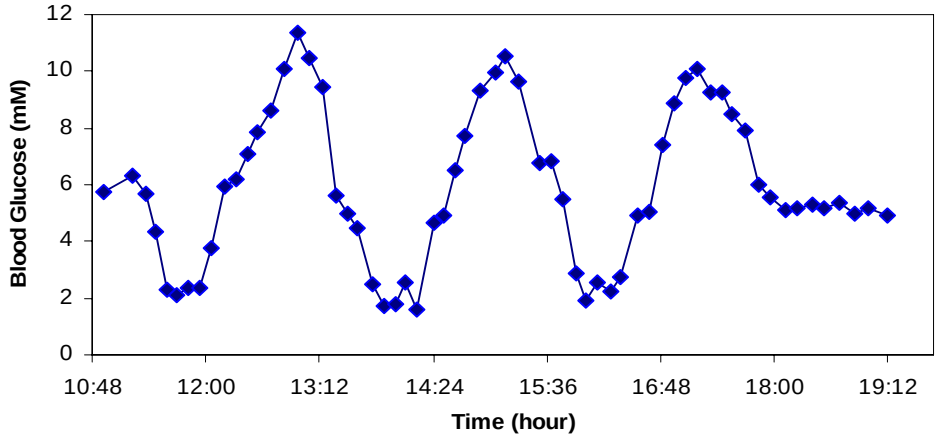

(c)

Figure II-4. Glucose profiles of (a) rat 1, (b) rat 2, and (c) rat 3. Dots indicate the blood glucose reference readings.

Results and Discussion

Noise Level Estimation

Since the glucose absorption features are extremely low (in the tens of μAU level), to effectively quantify glucose absorbance, it requires low noise levels from the instrumentation. To estimate this noise, spectra were collected on a 1 mm thick sample of water sandwiched by two pieces of a Teflon attenuator, which produced a signal level eqivalent to living skin tissue. Root-mean-square (RMS) noise on 100% lines after a second-order polynomial fit over the 4400-4500 cm^{-1} spectral range was ~ 10 μAU, which is lower than the glucose absorbance.

Absorbance Spectra

Raw spectra were collected as single-beam spectra. 1 mm of air spectra were collected before and after each animal experiment. The average of air single-beam spectra was used as the reference to calculate all skin absorption spectra. Rat skin absorption spectra were calculated by taking the negative logarithm of each skin single-beam spectrum to the averaged air single-beam spectrum. From the skin absorption spectrum as shown in Figure II-1, we can see that water is the most significant contributor to the overall spectral feature. The peak at 4600 cm^{-1} is due to proteins (collagen and keratin), and peaks at 4250 and 4350 cm^{-1} are due to fat absorbances.

Four pure component spectra of pure water, collagen, keratin, and fat were collected individually. These spectra can be used to model skin spectra as discussed in the next section. The water spectrum was collected from deionized water in a 1 mm cuvette. The collagen spectrum was collected from an aqueous solution of type I collagen in a 1 mm path length cell. The spectrum of a section of human finger nail was collected as a spectrum of keratin protein. A fat sample was prepared from blended and liquefied beef fat. The prepared fat sample was sandwiched between two sapphire windows. Thickness of the fat was controlled by a Teflon spacer between these windows.

Calculation of absorption spectra from these pure components is the same as that for the skin absorption spectra. A single-beam spectrum of each component was referenced to a single-beam spectrum of 1 mm air.

Skin Components and Aqueous Optical Path Length Estimations

Skin absorption spectra are significantly affected by different skin thicknesses, pressure from the interface, and even slight movement in the sensing location. In addition, changes in skin hydration and dehydration during the measurement can cause fluctuations in the aqueous optical path length, which creates uncertainties in glucose concentration predictions. To compensate for changes in these variables and enhance glucose prediction accuracy, a simple linear regression procedure can be performed in terms of the four known pure components: water, collagen, keratin, and fat, to estimate skin components and aqueous optical path length. In addition to these four chemical components, a constant term is included to compensate for scattering effects, as well as a slope term to account for the combination of scattering and temperature fluctuations.

This skin component estimation regression is described by the following equation:

$$A_{skin} = c_1 A_{water} + c_2 A_{collagen} + c_3 A_{keratin} + c_4 A_{fat} + c_5 A_{constant} + c_6 A_{slope} \qquad \text{Equation II-1}$$

where A_{skin} is one of the overall skin absorption spectra, A_{water}, $A_{collagen}$, $A_{keratin}$, and A_{fat} represent pure component absorption of water, collagen, keratin, and fat, respectively, c_i represents the corresponding regression coefficient and $A_{constant}$ and A_{slope} have shapes of a horizontal line and a slope, respectively. Figures II-6 (a), (b), and (c) show how the regression coefficients of each component vary across time on rats 1, 2, and 3. Scattering is the dominant light attenuator which accounts for approximately half of the overall skin absorption. Since each pure component spectrum has been normalized to a thickness of 1 mm, the regression coefficients represent the physical thicknesses of these pure chemical

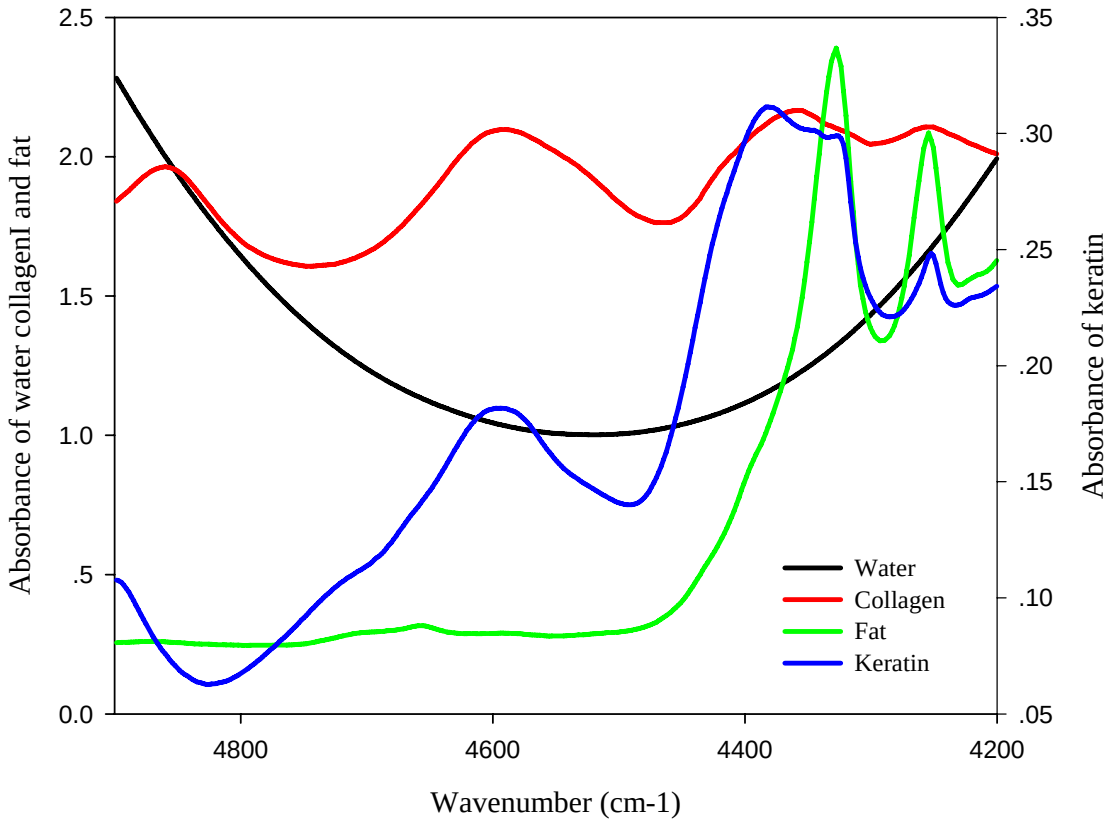

Figure II-5. Spectra of pure components used in the skin components regression.

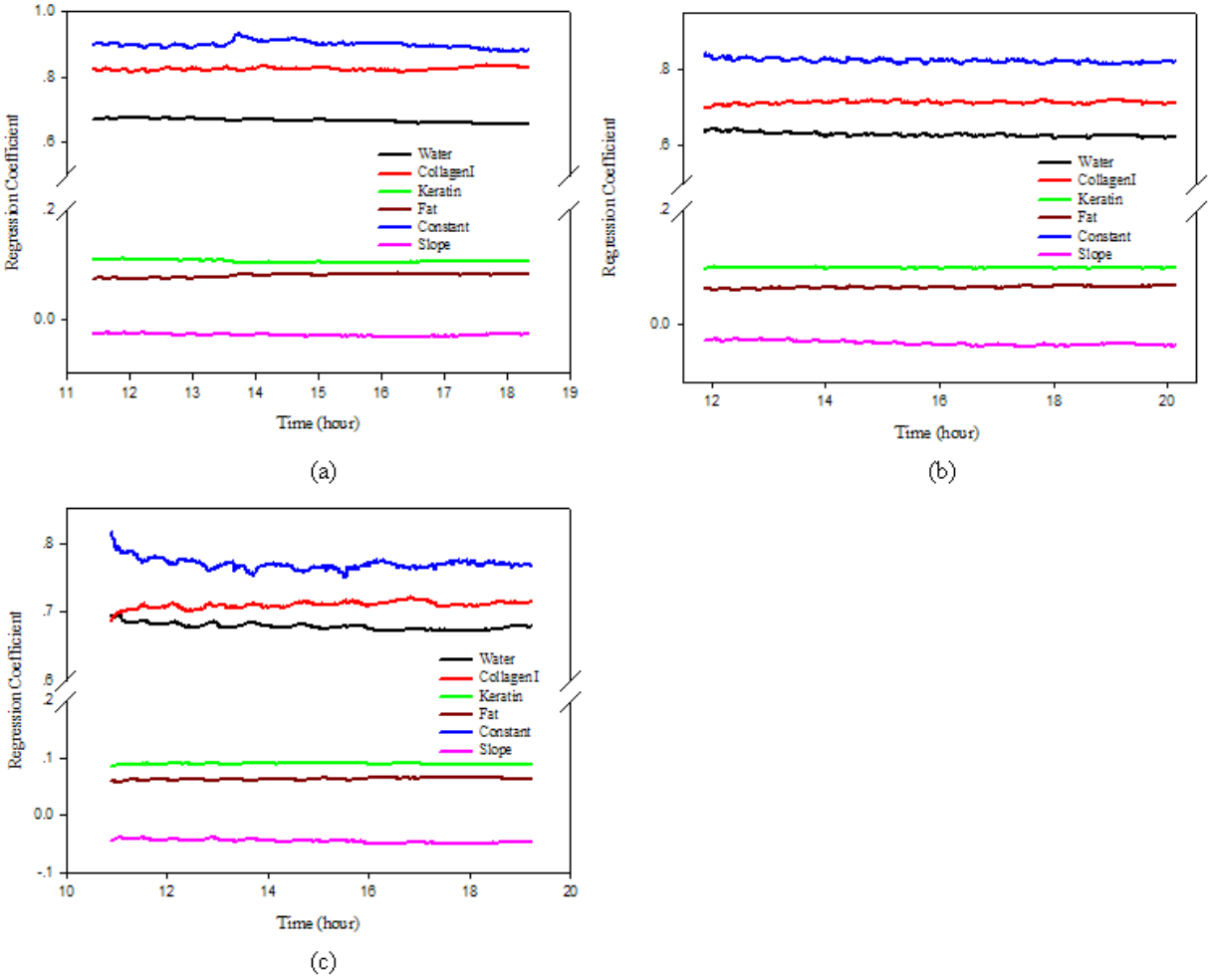

Figure II-6. Regressed skin tissue components as a function of time for each individual rat. Regression coefficients of water, collagen, keratin, and fat are proportional to the thicknesses of the corresponding component.

components. The regression coefficient of water represents the overall aqueous path length, which is approximately 0.7 mm. Since water is the dominant chemical in the tissue, aqueous path lengths can be estimated reliably by this approach. The second most abundant absorber is protein. Two major types of protein exist in the skin tissue, collagen and keratin. Collagen is primarily rich in the dermal layer and keratin is the key component in epidermal layer. The estimated collagen layer thickness is around 0.7 to 0.9 mm, which varies from rat to rat. Since collagen is one type of elastic protein, the thickness can be affected by the pressure applied to the skin tissue. The estimated keratin layer thickness is around 0.2 mm. Keratin is one type of rigid protein and it can maintain the structure under different conditions. Thus, the fluctuation of the keratin coefficient during the experiment is minimal compared with the other less rigid components. The regression coefficient for fat is less than 0.1. Both fat and keratin have strong absorptions in the region of 4400 – 4200 cm^{-1}, which strongly overlap with glucose peaks. To minimize interferences from keratin and fat, the skin tissue on the back of the neck was selected after scanning different body compartments, because keratin and fat contents are relatively low. The small regression coefficients of keratin and fat (< 0.1) are consistent with these low levels. Sum of the four chemical layers is over 1.5 mm which is larger than the physical thickness of the skin tissue in the optical interface. This is reasonable because the transmitted light penetrates the highly scattering skin tissue through a random path which is longer than the direct path of skin thickness. The regression coefficient of each component has different magnitudes of fluctuations. Possible reasons could be the interface pressure applied to the skin tissue, slight tissue components variations, environmental variations, such as temperature and humidity, unconscious body movements, etc.

Since water absorption is strong and water layer thickness is not constant with time, absorption of water molecules contributes greatly to spectral variations. To compensate for the impact of water fluctuations, the estimated aqueous path lengths from

the regression coefficients are used as internal standard. This is accomplished by scaling the target analyte concentrations times the estimated aqueous path lengths. For example, in a glucose study, the glucose concentration times the corresponding estimated aqueous path is used as the independent variable instead of the concentration itself. Thus, the model output is also in terms of the glucose concentration × aqueous path length product. This product is proportional to the number of glucose molecules in the optical path. For an unknown sample, the measured product can be converted to concentration by using the measured ware coefficient for that sample.

Partial Least-Squares (PLS) Analysis

For all of the following chemometric methods, a fixed spectral range of 4900 – 4200 cm^{-1} was used. Spectral range optimization studies have shown that wider spectral range can provide more consistent calibration and prediction results among different animal models and chemometric methods. In addition, featureless scattering has interferences across the entire spectral range. By using a full spectral range, scattering impact can be better modeled. Therefore, this fixed spectral range, 4900 – 4200 cm^{-1}, is applied to this entire study, and two spectral tails were not used due to the low S/N in those regions. To assign one glucose concentration to each individual spectrum, linear interpretation was applied between two blood glucose measurements. To compensate for the difference between glucose levels in the arterial blood and in the subcutaneous interstitial fluid, 12, 12 and 5 minutes delays were used to adjust the glucose concentrations in the transient profiles for rats 1, 2 and 3, respectively. Such delay adjustments merely enhances the performances of the chemometric models, and does not reflect any physiological difference between blood glucose and glucose concentrations in the skin matrix. These numbers of delay time were determined by good calibration and prediction performance of all calibration models. Since spectral collection rate (~ 1 per minute) and blood glucose reference times (every 5 to 10 minutes) are not the same,

glucose concentration was assigned to each individual spectrum by linear interpretation between two blood glucose reference measurements. In the PLS analysis, spectra were randomly separated into calibration (~ 85%) and prediction (~ 15%) data sets. The PLS calibration and prediction results are shown in Figure II-7. For all of theses three animal models, the predicted glucose concentrations for both calibration and prediction data sets follow the induced glucose transient profiles. The concentration correlation plots show good correlations between predicted values and reference values. The corresponding R^2 values were summarized in Table II-1. Performance of these PLS models was evaluated by the standard error of calibration (SEC) and standard error of prediction (SEP). The corresponding values were summarized in Table II-1. In this table, we can see that PLS glucose models were well established with SEC and SEP values less that 1 mM in each case. Based on SEC and SEP values, these three PLS models provide good glucose prediction ability, which indicates that the PLS algorithm may have potential application for glucose sensing. These results taken alone, however, do not prove the capability to predict glucose concentrations selectively by the PLS algorithm. Because the PLS method is statistically based, models can be based on chance correlation with non-anlyte variances. There is no requirement that glucose-specific spectral information is incorporated into the final calibration model. For this reason, the selectivity of the PLS model must be evaluated further to assess the chemical basis of the analytical measurement. Such an evaluation was done by using net analyte signal (NAS) algorithm and hybrid linear analysis (HLA) for comparison.

Net Analyte Signal (NAS) Analysis

In this study, the net analyte signal is defined as the part of the pure glucose spectrum that is orthogonal to the variances within the baseline skin matrix, as defined by Lorber.[83, 84] Before calculating NAS, the spectra of baseline must be defined for skin matrix. For the *in vitro* experiment, baseline spectra can be collected from samples void

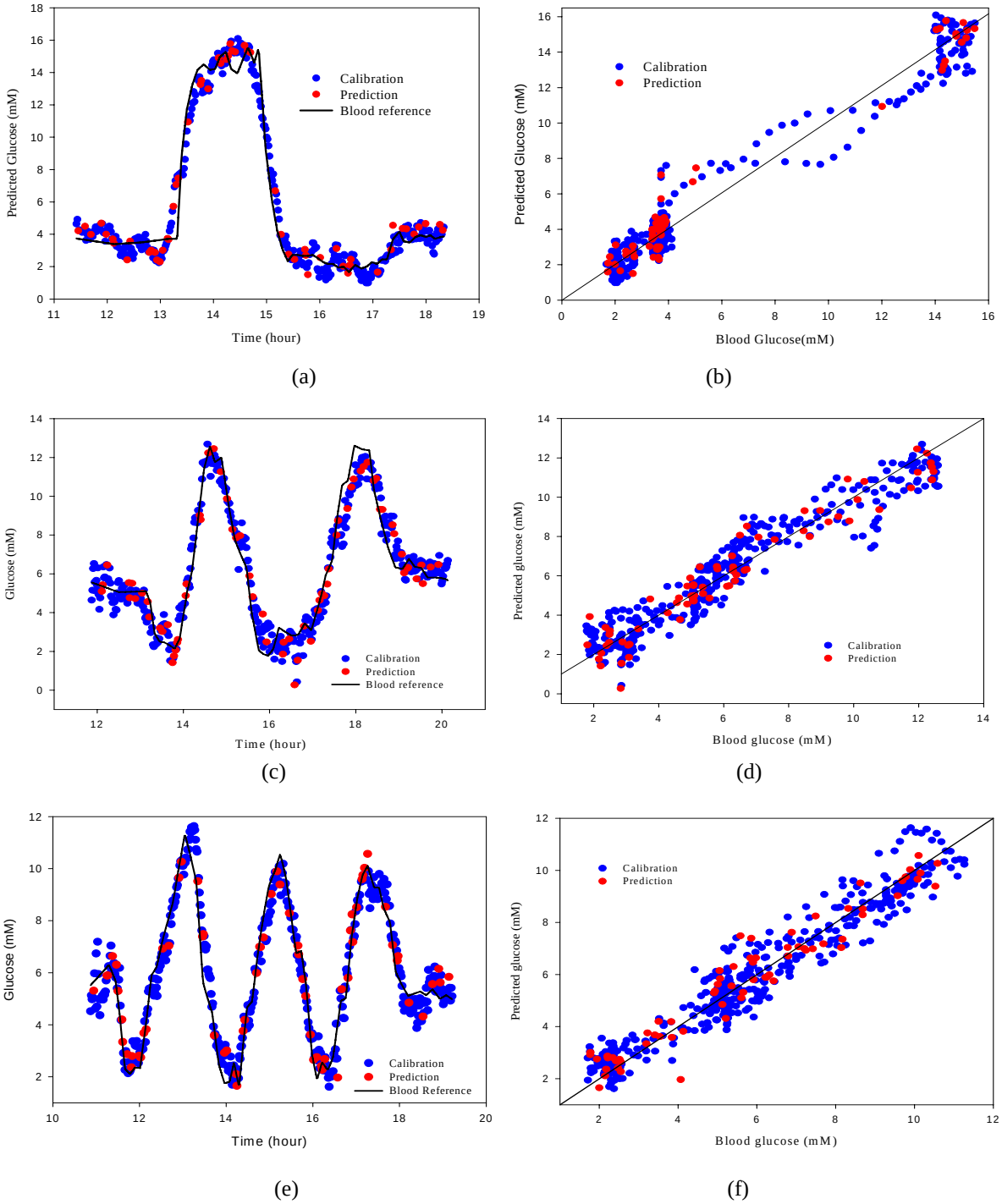

Figure II-7. PLS results of (a) and (b) rat 1, (c) and (d) rat 2, and (e) and (f) rat 3 where plots on the left show how the predicted glucose values follow reference values, and plots on the right illustrate concentration correlations with the line showing the ideal case where the slope is equal to one.

Table II-1. PLS calibration and prediction results

PLS model	Rat 1	Rat 2	Rat 3
Total spectra collected	382	459	452
Spectra in calibration	325	390	384
Spectra in prediction	57	69	68
Glucose profile delay adjusted (minutes)	12	12	5
SEC (mM)	0.9	0.9	0.7
SEP (mM)	0.9	0.8	0.7
R^2 (calibration)	0.9611	0.9209	0.9282
R^2 (prediction)	0.9647	0.9311	0.9350
Latent variables	8	9	9

of the analyte of interest. This method is not possible for *in vivo* experiments of animal skin matrix where samples zero glucose concentration are not available. Therefore, spectra with minimal glucose fluctuation at the beginning and end of the transient were selected as baseline spectra. A pure glucose spectrum was projected onto the mean subtracted baseline spectra by the following equation:

$$\boldsymbol{g}_{\perp} = \boldsymbol{(I - AA^{+})g} \qquad \text{Equation II-2}$$

where $\boldsymbol{g}_{\perp}$ is NAS of glucose, $\boldsymbol{I}$ is the identity matrix, $\boldsymbol{A}$ is the mean subtracted baseline spectrum matrix, $\boldsymbol{A}^{+}$ is the Moore-Penrose pseudoinverse of $\boldsymbol{A}$, and $\boldsymbol{g}$ is the pure glucose spectrum. This glucose NAS has two features: first, it represents glucose features since it is derived from the pure glucose spectrum; second, it is orthogonal to all sources of spectral variances represented in the baseline spectra, including instrumental, environmental, and chemical variances, therefore, it can be used in the quantitative prediction of glucose concentrations. For the purpose of quantitative analysis, this NAS should be properly scaled as:

$$\boldsymbol{\beta} = \frac{\boldsymbol{g}_{\perp}}{\left|\boldsymbol{g}_{\perp}\right|^{2}} \qquad \text{Equation II-3}$$

where $\boldsymbol{\beta}$ is the scaled calibration vector and $\boldsymbol{g}_{\perp}$ is the NAS. The predicted glucose concentration can be calculated as:

$$\hat{c} = \frac{\boldsymbol{\beta(a - \bar{b})}}{l} + \bar{c}_{B} \qquad \text{Equation II-4}$$

where $\boldsymbol{a}$ is the sample spectrum to be quantified, $\bar{\boldsymbol{b}}$ is the mean baseline spectrum, l is the regressed aqueous path length, and $\bar{c}_{B}$ is the mean concentration of glucose in the baseline spectra. In this NAS model, skin spectra before and after the glucose transients

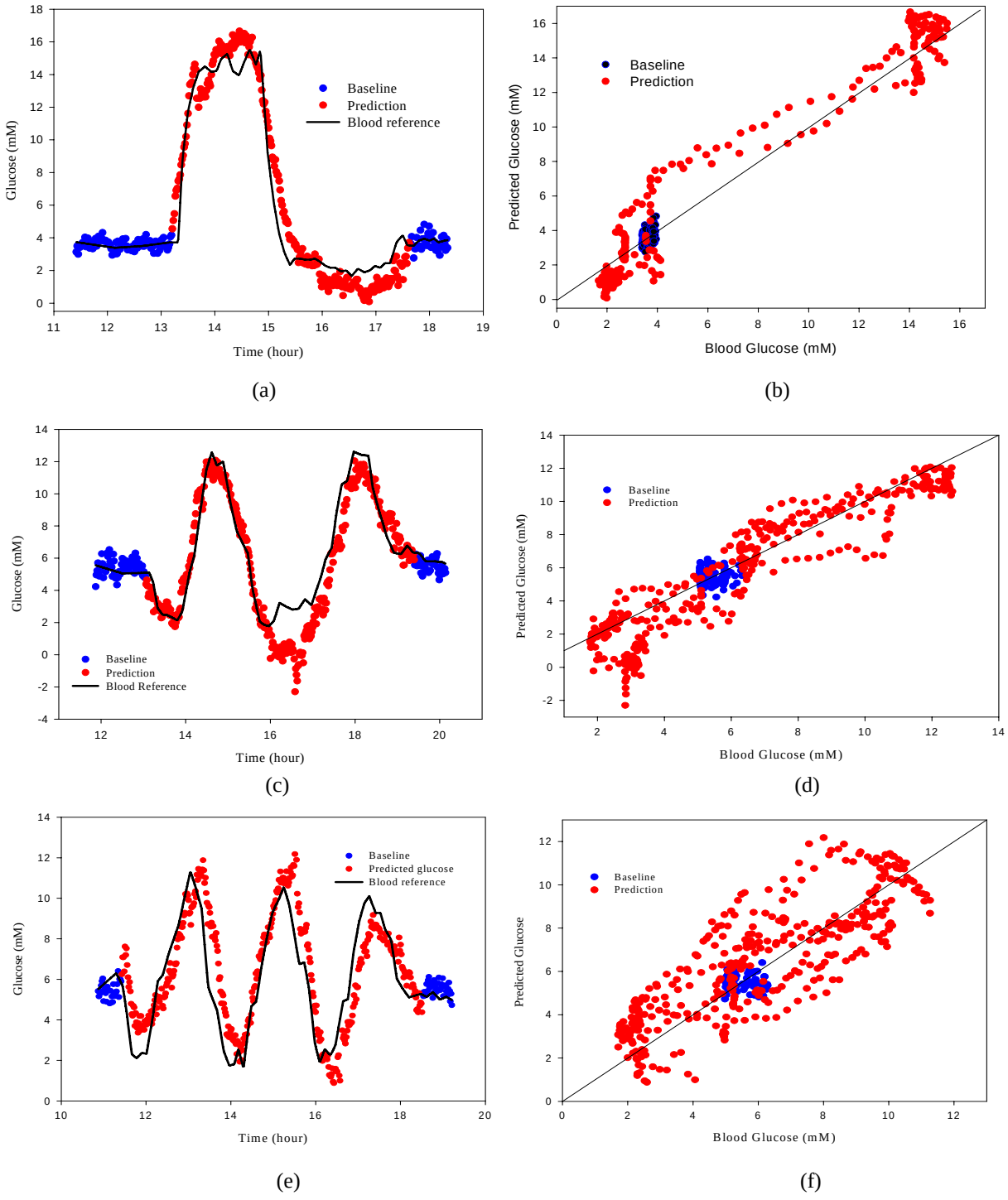

Figure II-8. NAS results of (a) and (b) rat 1, (c) and (d) rat 2, and (e) and (f) rat 3 where plots on the left show how the predicted glucose values follow reference values, and plots on the right illustrate concentration correlations with the line showing the ideal case where the slope is equal to one.

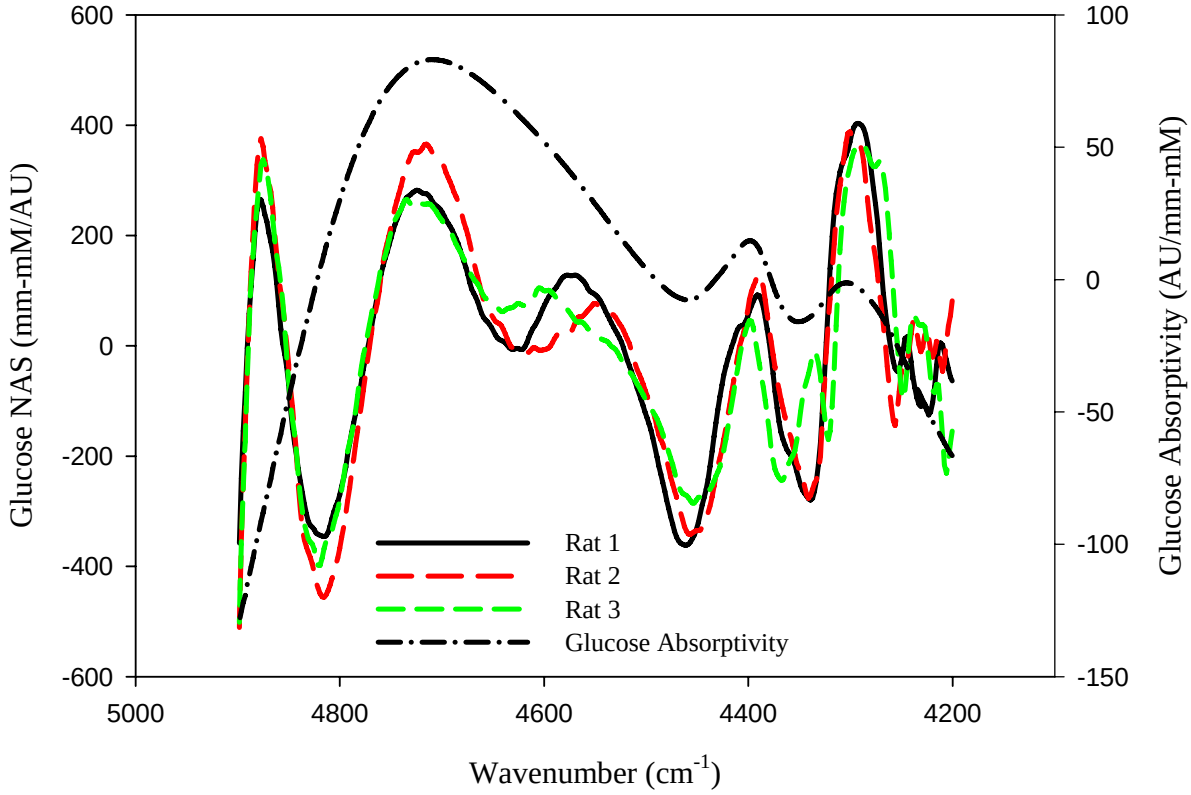

Figure II-9. Glucose NAS calibration vectors for rats 1, 2, and 3 compared to pure glucose absorptivity.

Table II-2. NAS calibration and prediction results.

NAS model	Rat 1	Rat 2	Rat 3
Total spectra collected	382	459	452
Spectra in baseline	138	107	69
Spectra in prediction	244	352	383
Glucose profile delay adjusted (minutes)	12	12	5
SEC (mM)	0.4	0.6	0.6
SEP (mM)	1.4	1.5	1.6
R^2 (prediction)	0.9486	0.8744	0.6972
Latent variables	11	10	8

with minimal concentration variance were selected as the background. The spectral range and glucose profiles time adjustments are the same as those indicated for the previous PLS analysis. The performance of the NAS models for these three rats is shown in Figure II-8 and Table II-2. Predicted glucose concentrations follow the reference profiles with good correlations between predicted and reference values based on high R^2 values. The SECs of baseline periods are ~ 0.5 mM which are less than those of the PLS models, while the SEPs are ~ 1.5 mM which are larger than those of the PLS models. Different from the PLS models, the NAS models are solely based on projection analysis with no correlation analysis involved. Therefore, NAS models are much less prone to chance of correlation and likely derived from glucose-specific spectral information. At 4700, 4400, and 4300 cm^{-1}, the glucose NAS vectors have strong positive peaks which overlap with features in the pure glucose absorptivity spectrum. Since these NASs are derived from pure glucose absorption spectrum, and major overlapped peaks can be found in Figure II-9 by comparing glucose NAS vectors with the pure glucose absorptivity spectrum, we can conclude that the NAS calibration models are selective for glucose and the glucose NAS represent glucose features in the skin matrix.

Hybrid Linear Analysis (HLA)

The NAS algorithm discussed above has demands noninvasive spectra with zero or constant glucose concentrations to define the baseline matrix, which is not easy to be obtained for living tissue. Hybrid linear analysis (HLA) is an alternative approach for estimating NAS where the concentration of glucose can be varied within the tissue matrix. HLA was developed widely applied in 1998, [87, 90, 91] specifically to enhance noninvasive glucose measurements. Instead of obtaining baseline spectra from fasting rats with constant glycemia, each spectrum in the baseline matrix a_b is calculated as follows:

$$\boldsymbol{a}_b = \boldsymbol{a} - clg \qquad \text{Equation II-5}$$

where $\boldsymbol{a}$ is one *in vivo* skin spectrum without any glycemic control, and *c* is the reference glucose concentration. Spectral contribution from glucose molecules is subtracted, and the remaining spectrum is considered to be a baseline spectrum that can be used for the calculation of glucose NAS. The calculation of glucose NAS by the HLA algorithm is the same as the NAS algorithm (see Equation II-2). The predicted glucose concentration from HLA can be calculated as:

$$\hat{c}_{HLA} = \frac{\boldsymbol{\beta}_{HLA}\boldsymbol{a}}{l} \qquad \text{Equation II-6}$$

where $\boldsymbol{\beta}_{HLA}$ is the properly scaled glucose NAS obtained by the HLA method.

The spectral range and glucose profiles time adjustments are the same as those used in the previous PLS and NAS procedures. To be comparable with the PLS results, the same random calibration and prediction data sets were selected for the HLA calculation. Figure II-10 shows the HLA calibration and prediction results for these three animal models. Predicted glucose concentrations follow the reference profiles and there are good correlations between the predicted and reference values. With 8 to 9 latent variables, the HLA models have SEC values around 1.0 mM and SEP values around 1.0 mM for all of these three animal models. Because of the similarity between mechanisms of NAS and HLA, the HLA calibration vectors are also derived from glucose-specific spectral features. Comparison between the HLA calibration vectors and pure glucose absorptivity can be viewed in Figure II-11. Similar to the glucose NAS vector, the HLA calibration vectors have strong positive peaks at 4700, 4400, and 4300 cm^{-1}, where glucose molecules have absorbance features. Therefore, HLA calibration vectors provide an alternative approach to predict glucose selectivity.

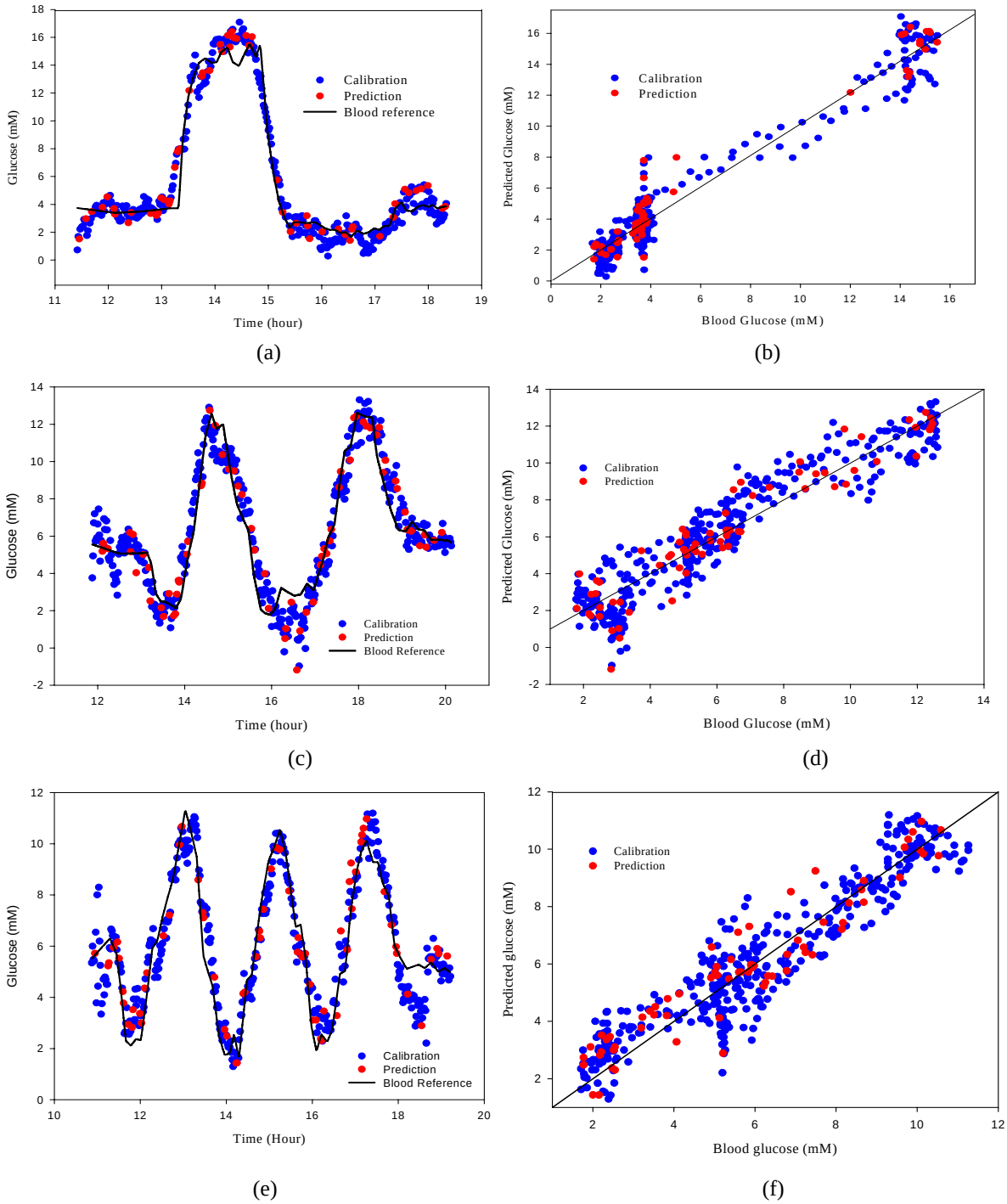

Figure II-10. HLA results of of (a) and (b) rat 1, (c) and (d) rat 2, and (e) and (f) rat 3 where plots on the left show how the predicted glucose values follow reference values, and plots on the right illustrate concentration correlations with the line showing the ideal case where the slope is equal to one.

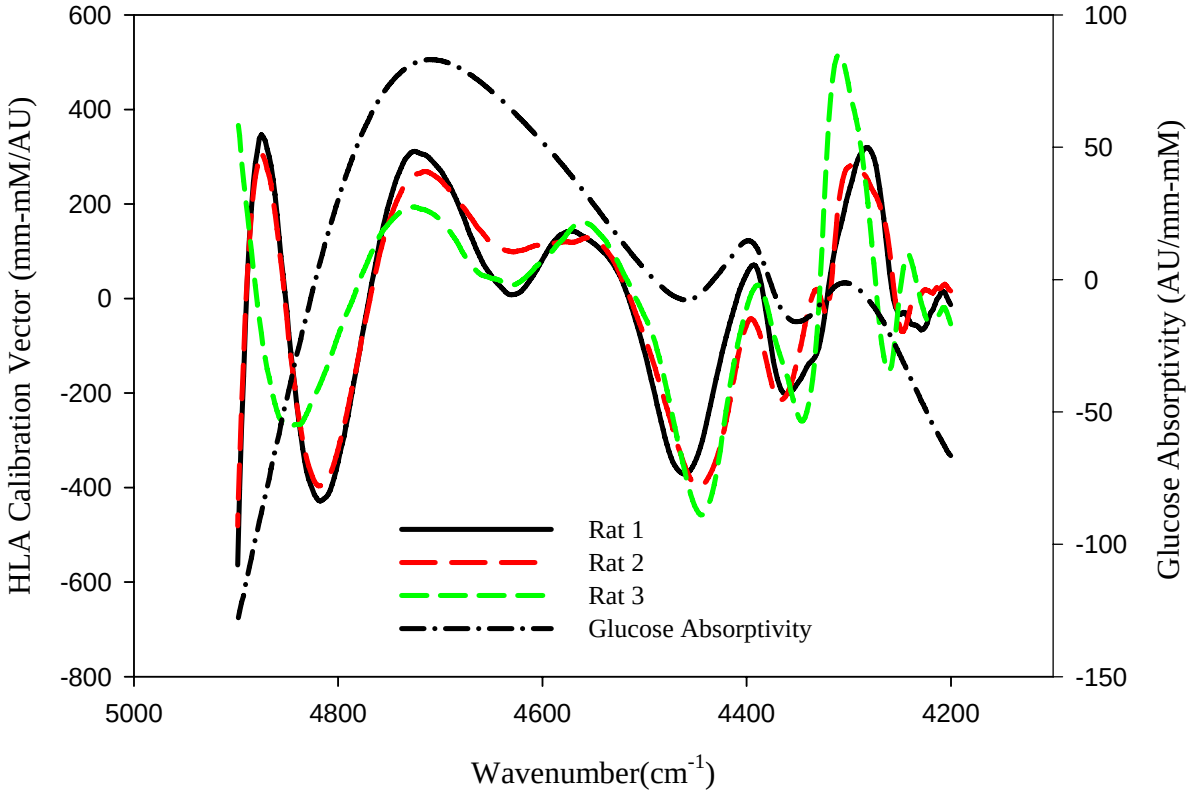

Figure II-11. HLA calibration vectors of rats 1, 2, and 3 compared to pure glucose absorptivity.

Table II-3. HLA calibration and prediction results.

HLA model	Rat 1	Rat 2	Rat 3
Total spectra collected	382	459	452
Spectra in calibration	325	390	384
Spectra in prediction	57	69	68
Glucose profile delay adjusted (minutes)	12	12	5
SEC (mM)	1.0	1.1	1.0
SEP (mM)	1.1	1.1	0.8
R^2 (calibration)	0.9545	0.8829	0.8687
R^2 (prediction)	0.9577	0.8928	0.8481
Latent variables	8	9	9

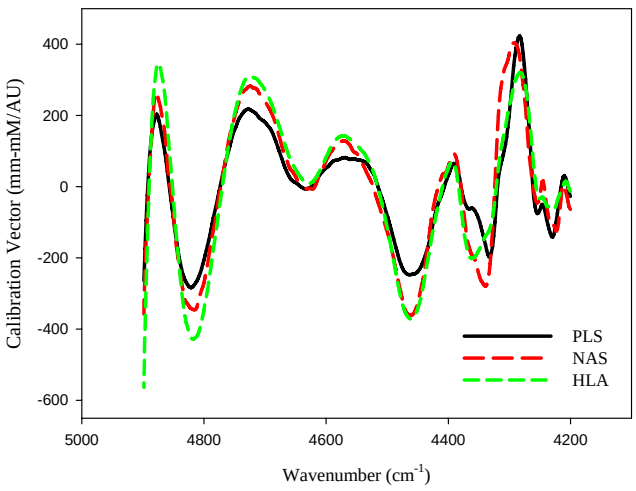

(a)

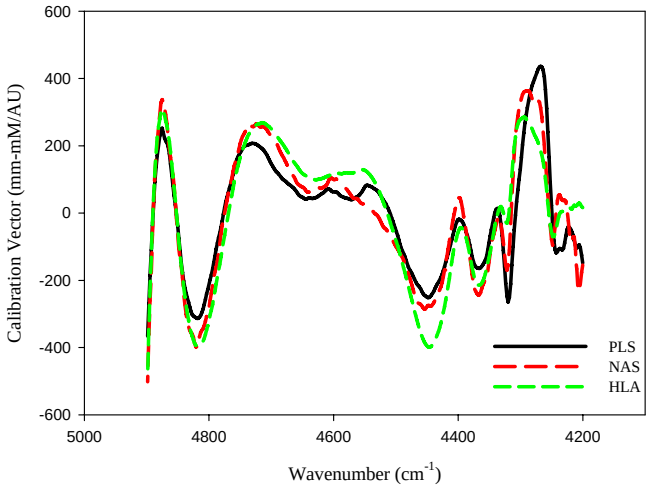

(b)

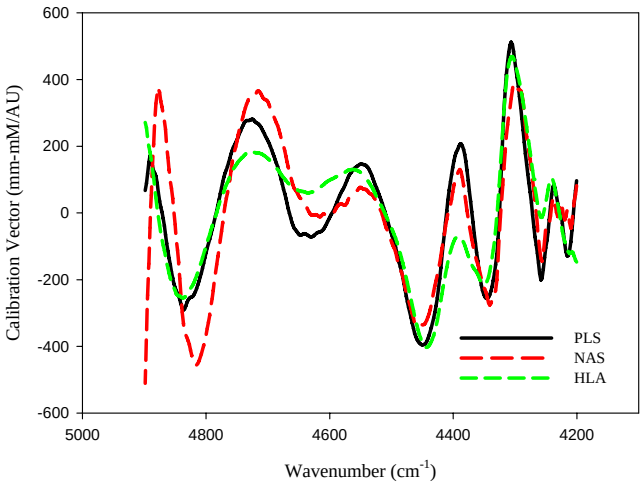

(c)

Figure II-12. Glucose calibration vectors comparison from PLS, NAS and HLA showing results are from of rat (a) rat 1, (b) rat 2, and (c) rat 3.

Comparison of Calibration Vectors

As mentioned previously, PLS models are prone to chance correlations base on the statistical nature of the analysis. To test if the PLS models for glucose are selective, the PLS calibration vectors can be compared with the calibration vectors obtained from the NAS and HLA methods. Figure II-12 presents all three calibration vectors and significant similarity in these vector shapes is evidence for all three animal models. Through this comparison, we can conclude that the PLS models are indeed selective for glucose and the principal features are derived from glucose-specific information embedded with the NIR spectrum.

Selection of the Optimal Latent Variables

In multivariate calibration models, using more latent variables tend to have better performance. Yet the use of too many latent variables can cause overfitting which includes unnecessary correlations with spectral variations related to noise, drift, and environmental factors. Therefore, identifying the optimum number of latent variables is necessary to avoid overfitting. A variety of approaches have been proposed to explore the selection of the number of latent variables. [65, 70] The most commonly used method includes a the *F*-test. Initially, several calibration models are established with latent variables from 1 to a certain number (depends on the complexity of the matrix, in this animal study, 15 is the maximum). The corresponding SEC and SEP values are obtained, and the minimum number of latent variables for which the SEP value is not significantly higher than the minimum SEP value (*F*-test) is selected. However, in this *in vivo* study on complex living tissue, the conventional *F*-test method is not the best method to detect the optimal number of factors due to two main reasons. First, the *F*-test tends to be less sensitive as the degrees of freedom increases. In this study, the degrees of freedom correspond to the number of spectra in the prediction data set which is greater than 50 for all three animal models. Second, glucose variation is buried among all sorts of spectral

variations due to physiological changes of the tissue, thus, it is difficult to judge which factor captures glucose and which captures noises or other non-analyte variations. In this study, empirical judgment was used to find the lowest SEC and SEP values of which the calibration vector maintained its shape without noisy features. To the practical experience, loadings with more than 12 latent variables generally have significant noise and therefore, avoided. Even different animal models have different magnitudes of each skin component, and the overall complexity of skin matrices decides the maximum number of factors that should be applied. Based on scrutiny of features within the calibration vectors and by applying no more than 12 latent variables, we believe chance of overfittng is minimized.

Conclusions

In this chapter, an animal study platform with the capabilities of alternating blood glucose levels and collecting noninvasive NIR skin spectra is established. Three animal models with one, two, and three glucose transients cycles were obtained. The proposed experimental system can be applied for other clinical analytes, besides glucose. Two more studies on lactate and urea will be covered in Chapter V. PLS, NAS, and HLA algorithms are applied, and three different glucose models based on these three algorithms are established for each of the three rat models. These models are evaluated in terms of SEC and SEP. Relatively low values of SEC and SEP (no more than 1.6 mM) illustrate good glucose prediction ability for all of these chemometric models. Errors of multivariate calibration models rely on the error of the reference method, which in this case is the error of two glucose meters. This error is up to 0.8 mM according to vender's specification. Therefore, the actual error from the NIR calibration models may be even less that the reported. In addition, the selectivity for glucose was evaluated by comparing glucose calibration vectors derived from the NAS and HLA methods with pure glucose absorptivity spectrum. Similarities with position of the major peaks demonstrate these chemometric models are selective for glucose.

CHAPTER III

GLUCOSE MODELS WITH ABILITITY TO PREDICT PROSPECTIVELY

Introduction

In the previous chapter, glucose models with good glucose prediction performance from three animal experiments and three chemometric algorithms are described, which indicates that these algorithms have great potential in the noninvasive glucose sensing application. For PLS and HLA models in the previous chapter, the prediction data sets which are used to evaluate the performance of those models are approximately 15% of randomly selected spectra from the entire experiment periods. The baseline periods with constant glucose levels are required for the NAS models. However, in the application of noninvasive glucose sensing, fewer spectra are preferred to build the calibration model, and evaluation of external validation data sets can establish the robustness of the model over certain periods of time.[72] Therefore, we need to build glucose models with the ability to predict accurate glucose concentrations from spectra collected prospectively. In this chapter, different approaches are described to establish glucose models applied to the prospective spectral data.

Four different calibration procedures are presented in this chapter. With data collected on multiple animal models with multiple glucose transient cycles, the first three approaches focus on the three animal models detailed in the previous chapter. The fourth calibration model uses data collected from a different animal model.

The first approach applies the existing chemometric model obtained from one rat onto the other two rats, which means all the spectra from one animal model are used for calibration and spectra from the other two rats are used for external validation. During the comparison of calibration vectors in Chapter II, similarities are also found among different animal models, which is primarily due to the similarities of the skin matrices. In addition, these three rats are the same breed being ordered from the same company. In

this approach, chemometric models (PLS, NAS, and HLA) are obtained from each of individual animal model and applied to the other two rats. Unfortunately, this approach does not work and large prediction errors are obtained. However, strong correlations between prediction and reference values suggest these calibration models are still sensitive to glucose transients but large offsets are observed in the predicted values. The poor external prediction performances are mostly caused by differences in the skin matrices. Even though these rats are genetically closed to each other, variances in the skin components make it impossible to simply transfer these concentration models from one animal to another.

The second approach focuses on creating validation data set from within each individual animal model. Instead of random separation of calibration and prediction data sets, as we did in the previous chapter, data set separation in this approach is done based on time. For the whole data from one animal model, the first half is used for calibration and the second half is used for prediction. Since the second half of the data is collected after the calibration data set, it can be treated as the external prediction data set. Therefore, chemometric models based on the first half of the experiment can be evaluated by the second half. In this approach, spectra in both calibration and external prediction data sets are all from the same animal model, and they are collected on the same day and on exactly the same piece of skin tissue. Therefore, the overall skin variations are minimal. In these three animal models, glucose transients with one, two, and three cycles of hyper- and hypo- glycemia are achieved. During the glucose transients, glucose concentrations are not the only variable, as the concentrations of other bio-molecules also can change during the data collection period. By including different numbers of hyper- and hypo- glycemic cycles in the calibration data set, the impact of these interferences can be evaluated.

The third approach is based on simulated spectra. In the previous chapter, a six-component-estimation procedure was applied to the raw absorbance spectra. In this

procedure, four major chemical components (water, collagen, keratin, and fat) and two physical components (scattering and temperature) are used to quantify the overall spectral variations. Since these six components can represent major skin spectral variations effectively, in this simulation approach, major variations in the simulated spectra are based on these six components. Due to the uniqueness of each individual animal model, a variety of subtle changes in the *in vivo* spectra cannot be simulated by these six components mentioned. Since each animal model is unique and there are many chemicals in the skin matrix, it is impossible to build a universal glucose model with the capability of predicting multiple animal models. In addition, exploring the concentrations of these chemicals in the skin matrix one by one would be extremely difficult because of their low concentrations, lack of effective detecting methodology, and large amount of variety. In this approach, instead of identifying all unknown components, spectral variances due to the unknowns are included in the simulation process.

A detailed simulation procedure is described in the experimental section of this chapter. In this simulation, three types of variance are included in the simulated spectra. The first one is from *in vivo* skin spectra, which contains unique information of the individual animal models. The second is from six known pure components, from which randomly scaled and mixed generate simulated spectra and then added to the *in vivo* spectra. The third one uses glucose spectral features which are added to the already simulated spectra with randomized glucose levels. PLS calibration models are established based on these simulated spectra, and evaluated by all the *in vivo* spectra. This approach simulation has the advantage of including both the major variances of the six major skin components and subtle skin variations from *in vivo* spectra.

A new animal model is used in the fourth approach. A conscious animal study procedure is developed to collected *in vivo* baseline spectra on one animal for multiple days. The whole procedure consists of two parts: rat restraint and blood sampling. Details of this procedure are presented in the experimental section. After five days of collecting

spectra from one conscious animal, the same surgical procedure as described in the previous chapter is performed on the same animal, and a glucose transient study is conducted to achieve two cycles of hyper- and hypo- glycemia. With all the animal data, baseline spectra with constant glucose levels can be used as a NAS or HLA calibration data set and the spectra with glucose transient on the last day can be applied for the external validation. The PLS algorithm cannot be used with this fourth animal model because of minimal glucose variation in the calibration data set. Glucose calibration vectors are calculated based on different combinations of baseline data sets. The whole data set with glucose transients was used as external prediction.

Experimental Section

Conscious Study

All the experimentation including spectral collection and blood reference is exactly the same as described in Chapter II. For the restraint of conscious animals, one adult male Sprague-Dawley rat (retired breeders, weighting ~ 400 g) was studied as the animal model. The rat without any surgical procedure was used for multiple days. A disposable rodent restrainer (Braintree Scientific ING., Braintree, MA) was used to restrain the conscious rat during the data collection. The rat was socialized prior to the experiment and trained to stay calm in the restrainer. The blood reference measurements were obtained by collecting venous blood from the tail every 30 minutes, and 5 total readings are obtained during the each baseline period. Blood was obtained by snipping the very end of the tail for the first reading and peeling off the scab thereafter. Since frequent blood sampling from the vein on the tail will cause the collapse of the blood vessels, 5 limited blood glucose readings are obtained very 30 minutes. The rat was fasted overnight before each baseline period so blood glucose fluctuations were not significant and glucose reference measurements at 30 minutes time intervals were adequate. Each baseline period lasted approximately 2 hours. By the end of the baseline

period, the rat was released back to the cage with food and water supplied.

Results and Discussion

Approach One: Models with Inter-Animal Validation

In this approach, all three animal models are obtained from previous chapter (rats 1, 2, and 3). The calculation of calibration vectors is the same as described in Chapter II. The same terms of SEC and SEP are used to evaluate the performance of the calibration models.

For the PLS algorithm, three PLS models with an optimal number of latent variables are established from animal model 1, 2, and 3, respectively. In each individual PLS model, all of the spectra collected on one animal are used as the calibration data set, and all spectral collected from other two animal models were treated as the prediction data sets. The corresponding results are summarized in Table III-1. Small SEC values indicate good correlations between glucose concentrations and *in vivo* NIR skin spectra are built in each individual animal model as described in the previous chapter. However, large SEP values indicate poor glucose prediction ability with the external prediction data. Moreover, plots of SEP vs. latent variables shown in Figure III-1 do not demonstrate a descending trend, which means variances in the calibration cannot explain spectral variances in the prediction data sets. Therefore, the results suggest that it is not feasible to apply PLS models on multiple animal models. Even though in previous chapter, similarities are found among the shapes of the calibration vectors derived from different animals, the unique subtle features in those calibration vectors make significant contributions to the predicted concentrations.

For the NAS method, each glucose NAS calibration vector reported in Chapter II was directly applied to the other two animal models. The corresponding results are summarized in Table III-2. Similar to the PLS results, SEP values are too high to maintain any glucose predicting ability. These large SEP values illustrate the glucose

NAS models cannot predict glucose concentrations on a different animal model.

To obtain HLA models, the whole data set of each animal model was treated as the calibration data set. Three HLA models with optimal latent variables are obtained and each HLA vector was applied to the other two animal models. The corresponding HLA results are summarized in Table III-3. Despite low SEC values (~ 1 mM), high SEP values are obtained across animals which suggest that these models are incapable of predicting accurate concentrations across external animals.

PLS, NAS, and HLA methods are incapable of accurate glucose concentration predictions across different animals. When comparing the glucose predictions and blood glucose profiles in Figure III-2, the transients in the predictions are consistent with those in the blood glucose profiles, which means the calibration model obtained from another animal model is still sensitive to glucose concentrations. The main reason of the large SEP values is that the external prediction data sets are from different animal models of which the skin samples are significantly different. Thus, in the following approaches, no more calibration transfer among different animal models was tried.

Approach Two: Separation of Calibration and Prediction Data Sets Based on Time

In the practical application for glucose sensing, a robust model is expected to be built at first with certain amounts of *in vivo* data, and then the model should predict glucose concentrations from prospective spectra. To simulate this scenario, in this approach, we separated animal spectra into calibration and prediction data sets based on time. We still focused on the three animal models established before. In each individual animal model, data collected before a set time are selected as the calibration data set, and the data collected after this time point are used as an external prediction data set. With these two data sets, the short-term performance of the calibrations models can be evaluated by the external prediction. In this case, only PLS and HLA models are

Table III-1 PLS calibration and prediction results of approach one.

Model 1 from Rat 1			
Latent Variables	SEC	SEP (Rat 2)	SEP (Rat3)
8	0.9	15.4	29.3
Model 2 from Rat 2			
Latent Variables	SEC	SEP (Rat 1)	SEP (Rat 3)
8	0.9	11.9	5.2
Model 3 from Rat 3			
Latent Variables	SEC	SEP (Rat 1)	SEP (Rat 2)
9	0.7	17.3	7.5

Note: SEC and SEP values have a unit of mM

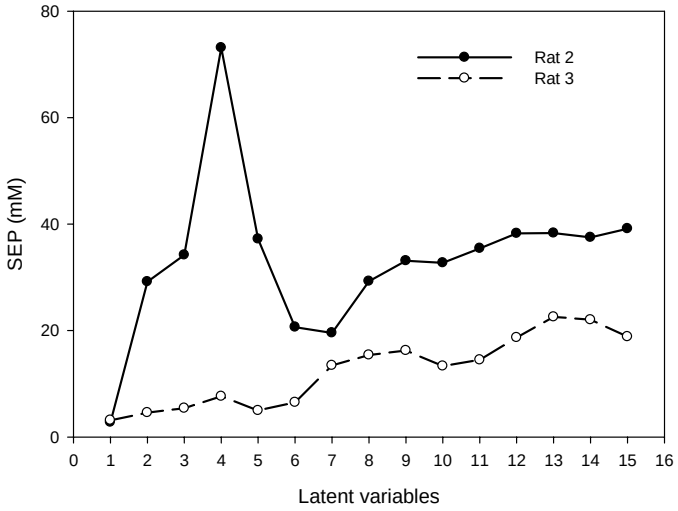

(a)

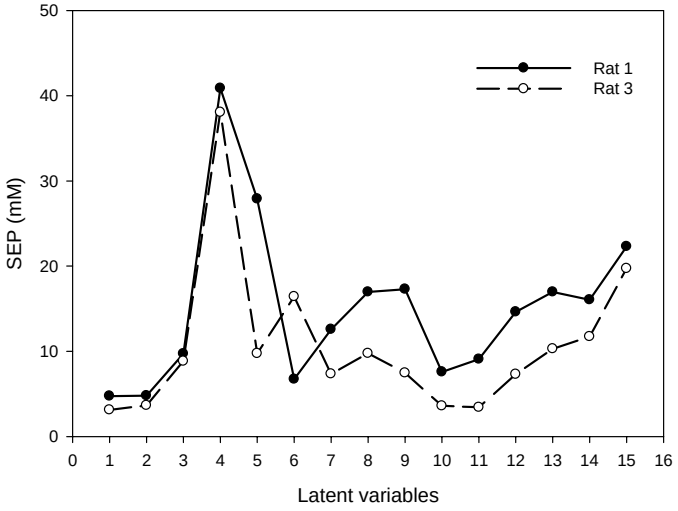

(b)

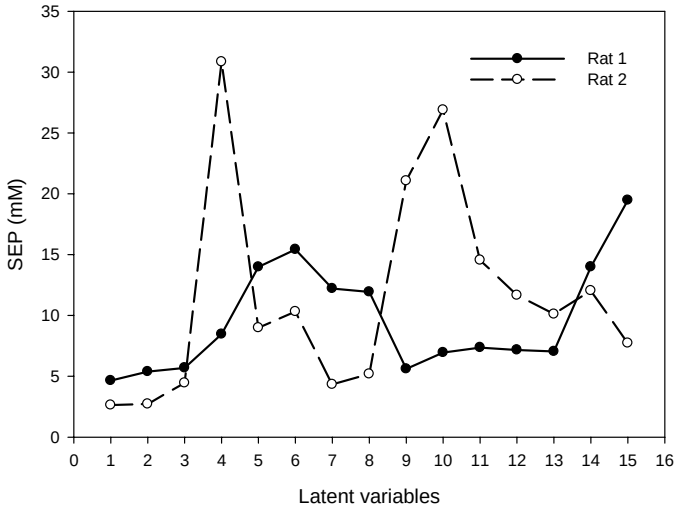

(c)

Figure III-1. SEP values of PLS calibration models versus latent variables for three individual animal models where (a), (b), and (c) are for calibration datasets from rat 1, 2, and 3, respectively.

Table III-2. Glucose NAS results of approach one.

NAS model 1 from rat 1 as calibration set		
Latent Variables	SEP (Rat 2)	SEP (Rat 3)
11	3.3	10.2
NAS model 2 from Rat 2 as calibration set		
Latent Variables	SEP (Rat 1)	SEP (Rat 3)
10	3.0	15.8
NAS model 3 from Rat 3 as calibration set		
Latent Variables	SEP (Rat 1)	SEP (Rat 2)
8	59.3	24.9

Note: SEP values have a unit of mM

Table III-3. Glucose HLA results of approach one.

HLA model 1 from rat 1as calibration set			
Latent Variables	SEC	SEP (Rat 2)	SEP (Rat 3)
8	1.1	18.0	34.9
HLA model 2 from Rat 2 as calibration set			
Latent Variables	SEC	SEP (Rat 1)	SEP (Rat 3)
8	1.2	14.0	16.2
HLA model 3 from Rat 3 as calibration set			
Latent Variables	SEC	SEP (Rat 1)	SEP (Rat 2)
8	0.9	5.6	5.5

Note: SEC and SEP values have units of mM

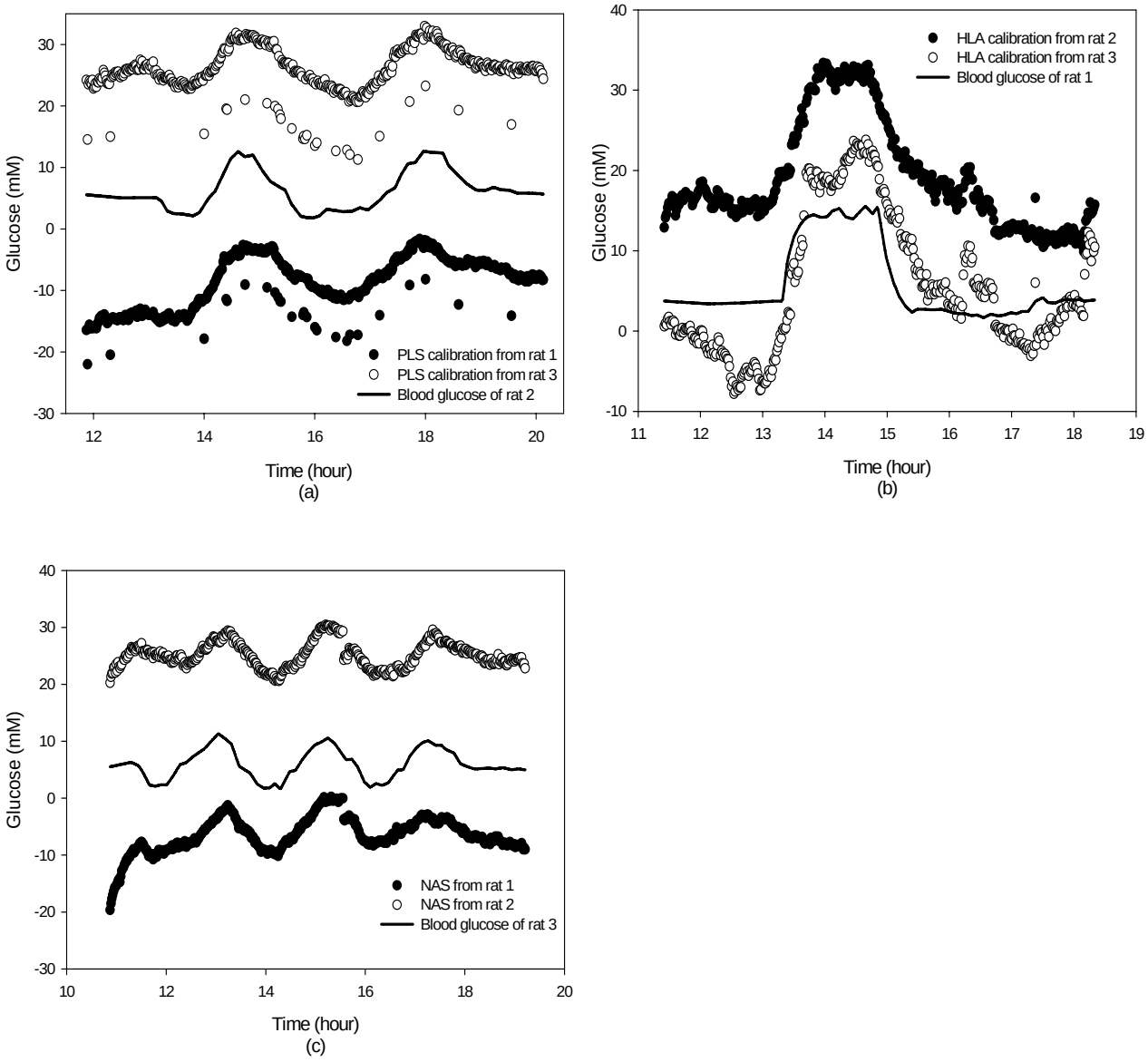

Figure III-2. Prediction results from aaproach one.

established, while the NAS algorithm was not applicable because glucose concentrations in the calibration data set are not constant. The method used to obtain PLS and HLA models are the same as described in Chapter II, and the same terms of SEC and SEP are used to evaluate the corresponding models. Figures III-3 and 4 show the PLS and HLA results from the three animal models, respectively. The corresponding SEC and SEP values are summarized in Tables III-4 and 5. For all of the three animal models, SEC values from both PLS and HLA algorithms stay below 1.0 mM. SEP values vary among the animal models. Animal model 1 has the largest SEP values from both PLS and HLA models, SEP values of both models from animal 2 are lower, and the animal model 3 has the lowest SEP values for both of the algorithms.

In animal model 1, the performances of both PLS and HLA models are poor compared with those presented in Chapter II. Since there is only one glucose transient cycle in this animal model, the concentration range in the calibration only contains the baseline glucose period and hyperglycemic concentrations, which does not cover the lower end of the glucose concentrations in the prediction data set. Thus, insufficient concentration range is one reason leading to high SEP values. In addition, in this *in vivo* experiment, the background in the skin matrix is not constant. With all sorts of fluctuations in the skin tissue, it is possible that the skin tissue variations in the calibration and prediction data sets are not well matched. The subtle skin variation differences could result in the poor performance of these models i. In the second animal model, a full cycle of hyper- and hypo- glycemic was included in the calibration data set, which covers a glucose concentration range of 1 to 13 mM. The glucose concentrations in the prediction data set do not exceed this glucose. Therefore, broad concentration coverage in the calibration data set is one of the major factors for better performance in the predicted values for model 2. In addition, the calibration data set contains more skin variation associated with the glucose transient, which means that the spectra in the calibration data set are more representative of the spectra in the prediction data set. This

could be another reason of better prediction performance for the second animal model. The third animal model has three hypo- and hyper- glycemia cycles, two of which were included in the calibration data set. Similar to the second animal model, the glucose concentration range in the calibration data set covers the prediction values. SEP values from the prediction data set are the lowest for this animal model which is further evidence that larger glucose concentration ranges and more glucose variations can lead to better calibration models with better glucose prediction ability.

In addition to the evaluation of SEC and SEP values, glucose calibration vectors of PLS and HLA algorithms are also compared. Figures III-5 (a) and (b) show this comparison of PLS and HLA calibration vectors from animal models 2 and 3, respectively. The result of animal model 1 is not shown here. Due to the poor glucose prediction results, it is meaningless to compare the calibration vectors from animal model 1. Comparisons of PLS and HLA calibration vectors from animal models 2 and 3 demonstrate major peak overlapping between these two types of calibration vectors. As discussed in Chapter II, this similarity illustrates the selectivity for glucose of the PLS models. Therefore, in this approach, selective glucose calibration models with the capability of predicting concentrations prospectively are established with animal models 2 and 3.

Approach Three: Simulation Spectra

From the previous two approaches, we learned that to obtain a good glucose calibration model, there should be adequate glucose concentration ranges, variations in the calibration data set, and the differences between calibration and prediction data sets should be minimized. In this approach, a simulation procedure was applied on a portion of *in vivo* spectra of each animal model. Because part of *in vivo* spectra is maintained in the simulated spectra, the simulation data set retains unique skin features of the specific animal model. In addition, by adding glucose features artificially, glucose concentration

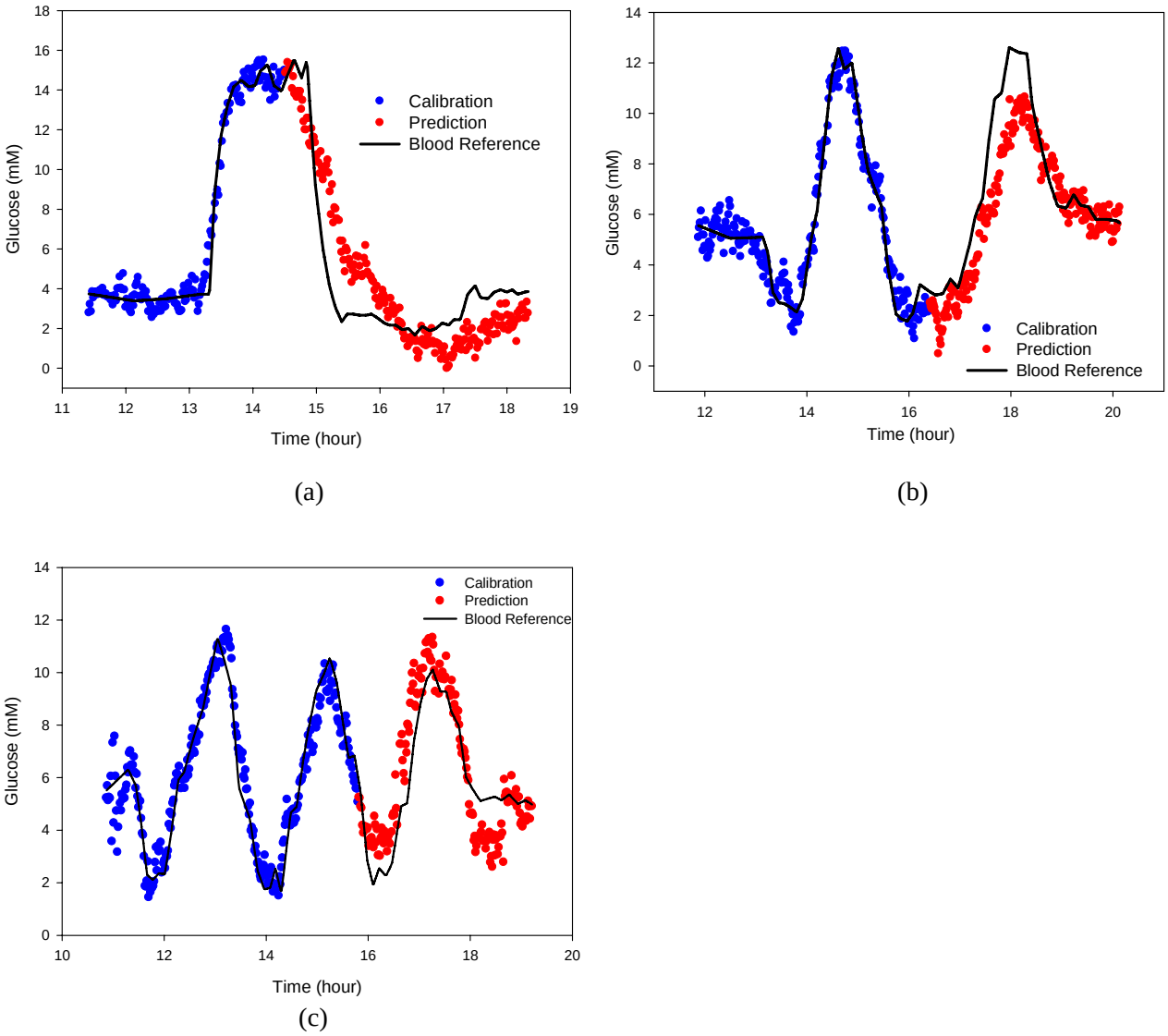

Figure III-3. PLS calibration and prediction results of (a) rat 1, (b) rat 2, and (c) rat 3.

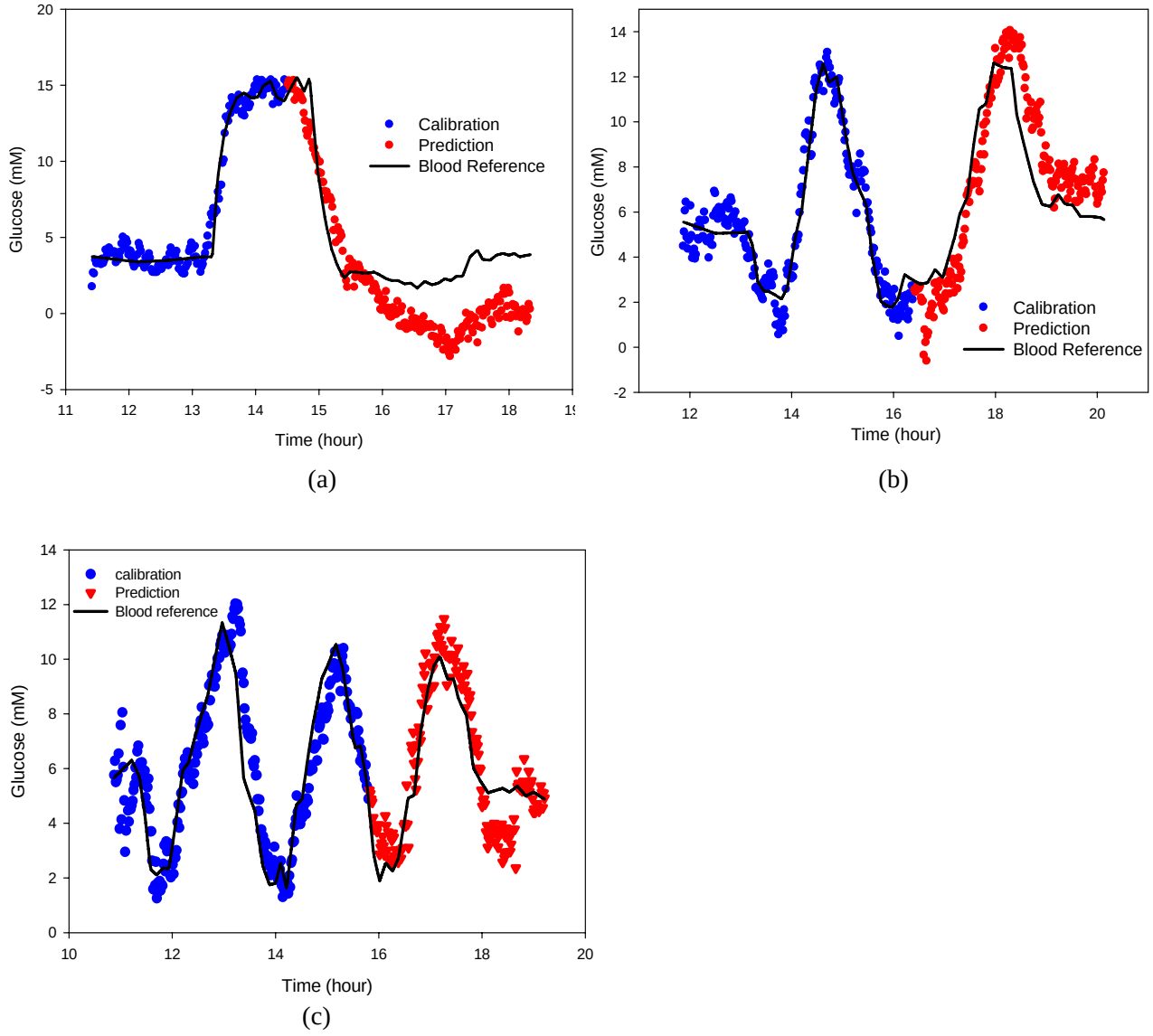

Figure III-4. HLA calibration and prediction results of (a) rat 1, (b) rat 2, and (c) rat 3.

Table III-4. PLS calibration and prediction results from approach II.

PLS model	Rat 1	Rat 2	Rat 3
Total spectra collected	382	459	452
Spectra in calibration	212	252	272
Spectra in prediction	170	207	180
Glucose profile delay ajusted (minutes)	5	12	12
SEC (mM)	0.7	0.7	0.8
SEP (mM)	2.1	1.7	1.3
Latent variables	9	9	8

Table III-5. HLA calibration and prediction results from approach II.

HLA model	Rat 1	Rat 2	Rat 3
Total spectra collected	382	459	452
Spectra in calibration	212	252	272
Spectra in prediction	170	207	180
Glucose profile delay ajusted (minutes)	5	12	12
SEC (mM)	0.8	0.8	0.9
SEP (mM)	2.8	1.8	1.1
Latent variables	9	11	8

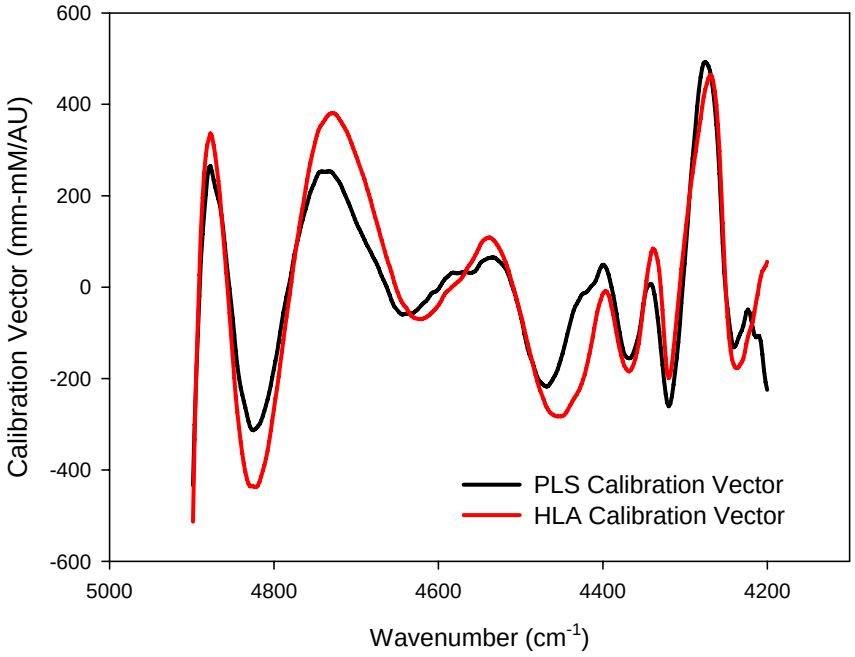

(a)

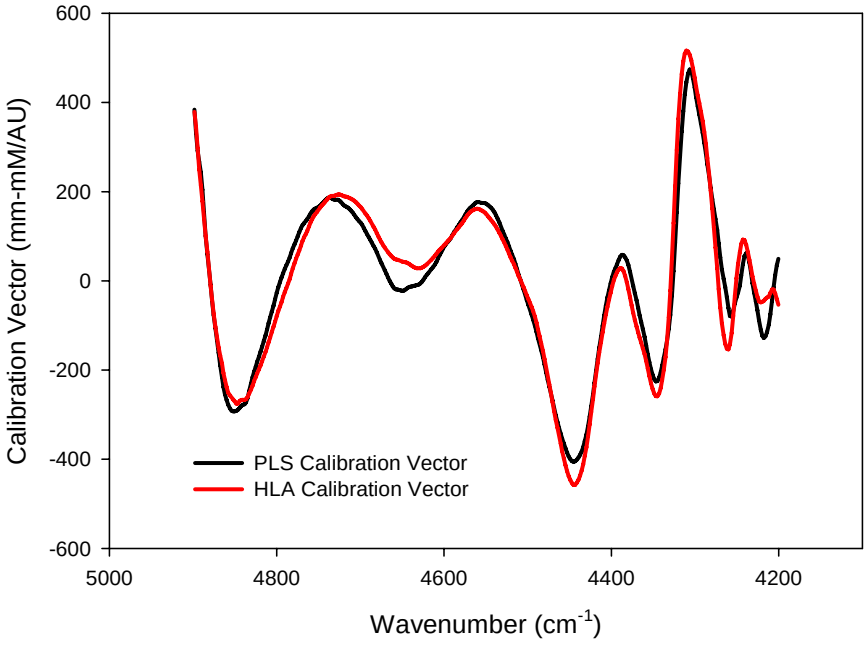

(b)

Figure III-5. Comparison of PLS and HLA calibration vectors from (a) rat 1, (b) rat 2, and (c) rat 3.

levels and ranges can be controlled as desired. In each animal model, the PLS model was built based on the simulated spectra, and then applied on the actual *in* vivo noninvasive spectral data. The same terms of SEC and SEP are used to evaluate the glucose prediction performance.

Two approaches were used to simulate the *in vivo* spectra: first, adding artificial known variances (6 pure components); second, selecting a certain number of *in vivo* spectra to include various unknown variances from the skin matrix. A typical simulation procedure is described as follows: Initially, a certain number of spectra collected from the very beginning of each animal experiment was selected as the basis for the simulated spectra. This portion of the *in vivo* spectra contains unique features for each individual animal and also includes the magnitude of variations from skin tissue caused by endogenous bio-molecules. The magnitude of each of pure component spectra defined in Chapter II (water, fat, collagen, keratin, constant, and slope) are randomized to 128 levels and 128 mixture spectra are produced by mixing these randomly rescaled pure components. The purpose of this step is to simulate variations in the skin spectra during the *in vivo* experiment, and the magnitudes of these simulated variations were comparable with the changes of the pure components coefficients from the skin components estimated in Chapter II. The resulting mixed spectra were added to one *in vivo* spectrum to generate 128 simulated *in vivo* spectra. The same process was applied to a set of selected *in vivo* spectra. Concentrations scaled glucose spectra with random concentrations were added, and the final glucose concentration set as the sum of the background glucose level in that skin spectrum coupled with the added glucose concentration from the simulated spectra. The glucose concentration ranges in the simulated spectra were matched to those obtained in the corresponding animal models. No extra noise was added in the simulation process. A simulated spectrum can be described as:

$$S_{simulation}=S_{in\ vivo}+c_1A_{water}+c_2A_{collagen}+c_3A_{keratin}+c_4A_{fat}+c_5A_{constant}+c_6A_{slope}+c_7A_{glucose}$$

Equation III-1

where $S_{in\ vivo}$ is one of the skin absorption spectrum, A_{water}, $A_{collagen}$, $A_{keratin}$, A_{fat}, and $A_{glucose}$ represent pure component absorption spectrum of water, collagen, keratin, fat, and glucose, respectively. $A_{constant}$ and A_{slope} have shapes of a horizontal line and a slope, respectively, to simulate variances from scattering and temperature fluctuations, and c_i represents the corresponding coefficient of each added component. The magnitude of these randomized coefficients is limited to the maximum of the skin components regression coefficient changes so that the variances due to these components match those determined in the *in vivo* spectra. After obtaining all the simulated spectra with random glucose variations, a PLS model was built based on the simulated data set and the calculated glucose concentrations. Since the artificial glucose features are randomly added, the glucose concentrations in the simulated data set are also random, which avoid the chance of time correlation in PLS calibration vectors. The whole *in vivo* spectral data set was used for prediction. SEP values are used to evaluate the performance of the glucose PLS models. SEC values are not so meaningful in this case, because the SEC values only reflect how the PLS models predict glucose from the simulated spectra. Thus, more effort was placed on SEP values with different latent variables and different number of *in vivo* spectra for the simulation data set.

In this simulation procedure, the number of selected *in vivo* spectra must be determined. Considering the efficiency in the future application of glucose sensing, a minimum number of *in vivo* data is preferred. However, in this particular study, complex subtle features from the skin matrix also play an important role. More *in vivo* spectra will provide more spectral variance and make the simulated spectra more relevant. Thus, a wide range of number of spectra was studied to find out how many *in vivo* spectra are needed. In each animal model, a different number of *in vivo* spectra was used to establish

the simulation data sets based on which PLS model was used. SEP values with different latent variables from 1 to 15 are also tested after applying the calibration vectors onto the whole *in vivo* data set. Figures III-6, 7, and 8 show the corresponding results for animal models 1, 2, and 3, respectively. In an ideal case where the simulated data set can represent the entire *in vivo* data set, the SEP values should get smaller as more latent variables are used. However, in this simulation study, in all three animal models, when there are inadequate *in vivo* spectra included in the simulation data sets, SEP values increase and decrease with more latent variables. The high SEP values indicate that the calibration vector from the simulation cannot predict glucose well indicating these simulated spectra do not represent the *in vivo* spectra. This phenomenon suggests that during the spectral collection period new spectral features show up. To counteract this problem, more *in vivo* spectra are added to the simulation. As shown in Figures III-6, 7 and 8, as more *in vivo* spectra are included, the SEP vs. latent variables curves are smoother and decreasing SEP values are observed. As more *in vivo* information is incorporated, the simulated spectra capture more *in vivo* features, which makes the simulation data set similar to the real *in vivo* data set. Therefore, more *in vivo* spectra are preferred for simulation in the three animal models.

After exploring the effects of the numbers of *in vivo* spectra 100, 190, and 140 *in vivo* spectra were selected for animal models 1, 2, and 3, respectively. These numbers are selected only for the demonstration of PLS prediction performances from this simulation approach, and they are not necessarily optimized. It is meaningless to do a detailed optimization of the number of *in vivo* spectra because each animal model is unique and the optimized number of spectra for one may not be applicable for others. Also, the optimization based on SEP values may be biased on the prediction data set, while the original purpose is to develop calibration models that are capable of predicting prospective spectra. Table III-6 summarized the PLS results of this simulation approach with 100, 190, and 140 *in vivo* spectra selected for animal models 1, 2, and 3,

respectively. PLS models with SEP values below 1.8 mM are obtained with 7 to 9 latent variables. Figure III-9 shows comparison of predicted glucose concentrations with the blood reference values. Predicted glucose concentrations follow the reference profiles and there are good correlations between predicted values and reference values based on the R^2 values presented in Table III-6.

Since glucose levels in the simulation are artificially randomized, the risk of false correlation during the calculation of PLS calibration vectors was minimized. Nevertheless, these PLS calibration vectors can still be compared with the corresponding glucose NAS presented in Chapter II. This comparison is shown in Figure III-10. Major shape similarity illustrates these PLS calibration vectors are selective for glucose. Because many *in vivo* spectra are required in order to obtain a PLS model with the ability to predict glucose concentrations from the prospective spectra, 2~3 hours is needed to collect enough spectra for these simulations. In comparison, 4 hours of data collection are necessary for the previous approach. Based on this comparison, the simulation approach is slightly more efficient. In addition, these results from the simulation study have lower SEP values and fewer numbers of factors than the HLA results using the same *in vivo* data set for calibration, which means the simulation process provide more representative variances from the major skin components than a short term *in vivo* spectra. The major reason that it requires so much *in vivo* information is the lack sufficient information related to variations in the skin spectral features. Therefore, this simulation approach would benefit from a firm understanding of all significant tissue components in the skin matrix.

Approach Four: One Animal Model from Multiple Days

In this approach, a new animal model is proposed where spectra are collected from one animal over several days. Experiments are described with one adult male Sprague-Dawley rat (retired breeders, weighting ~ 400 g). Five baseline periods are

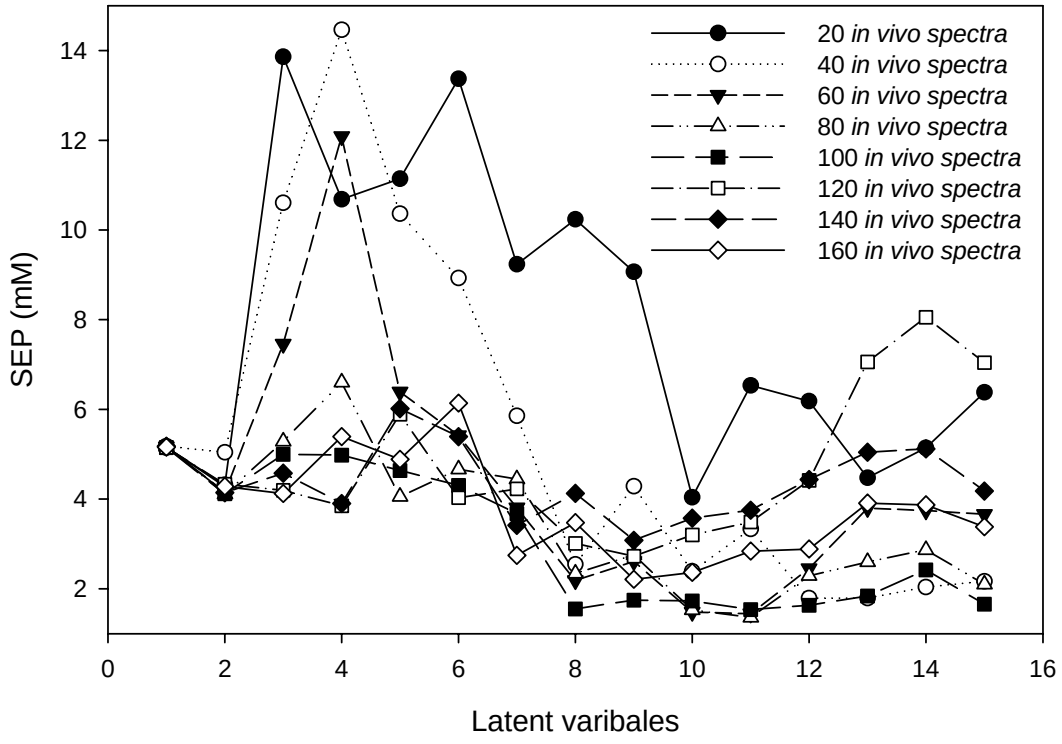

Figure III-6. SEP values of PLS models established by simulation versus latent variables for the first animal model where results show ten simulation trials with 10 to 100 in vivo spectra.

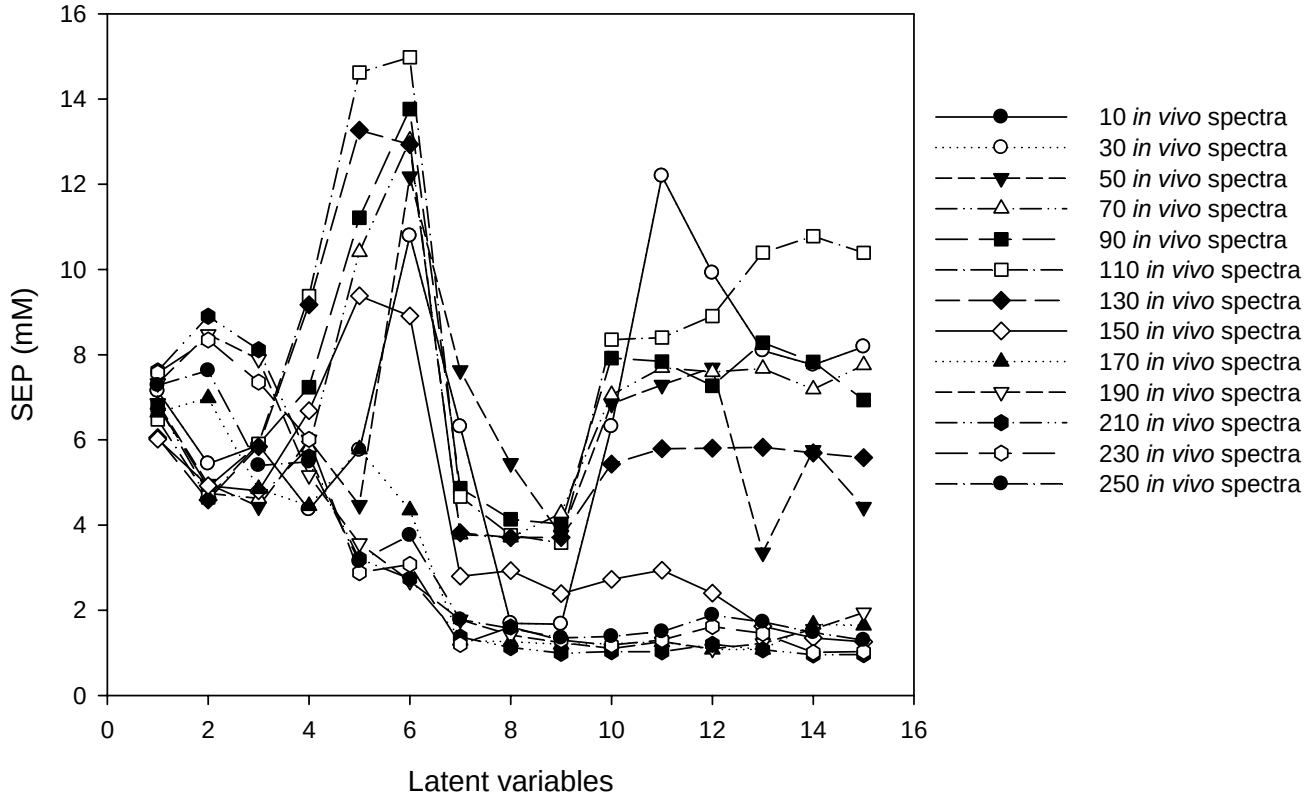

Figure III-7. SEP values of PLS models established by simulation versus latent variables for the second animal model where The results show thirteen simulation trials with 10 to 250 in vivo spectra.

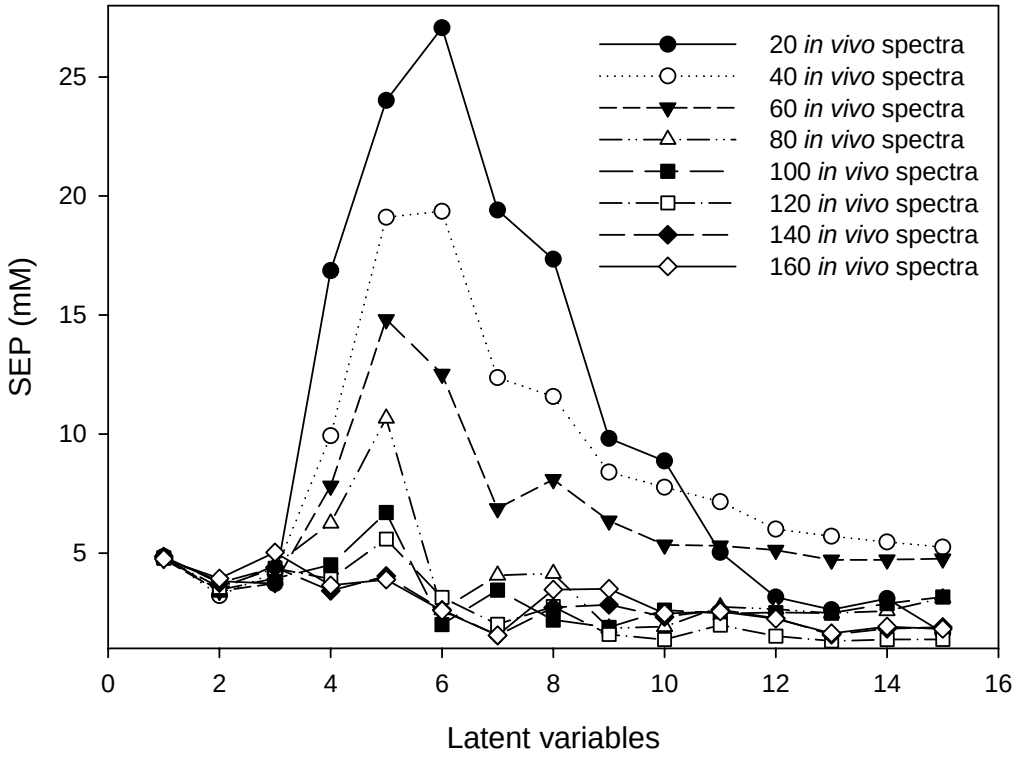

Figure III-8. SEP values of PLS models established by simulation versus latent variables for the third animal model where results show ten simulation trials with 20 to 160 in vivo spectra.

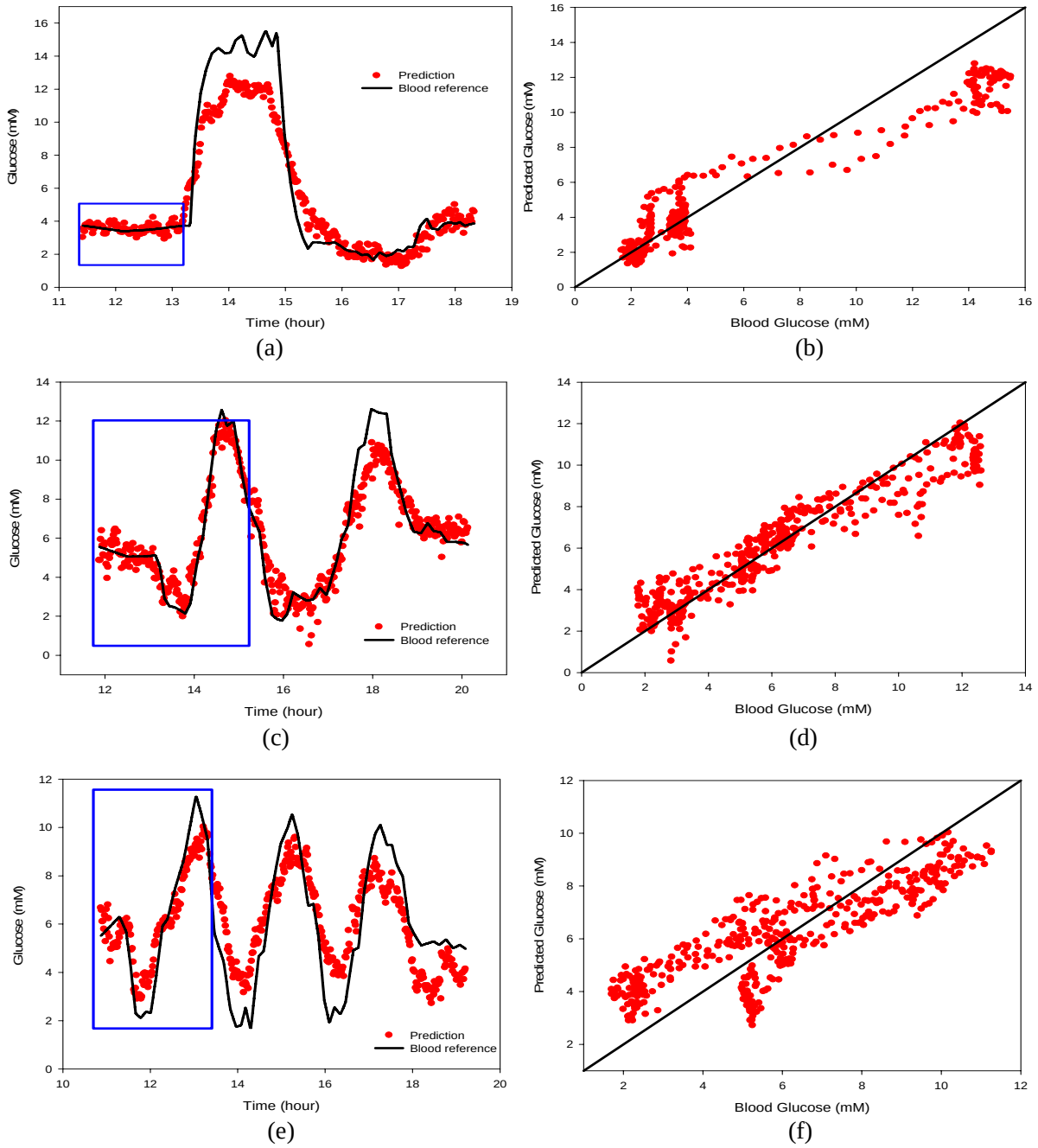

Figure III-9. PLS prediction results from the simulation approach for (a) and (b) rat 1, (c) and (d) rat 2, and (e) and (f) rat 3 where plots on the left show how the predicted glucose values follow references, and plots on the right illustrate concentration correlations and blue squares indicate the portion of selected *in vivo* spectra used for the simulation process.

Table III-6. Summary of PLS prediction results based on simulation approach.

PLS model	Rat 1	Rat 2	Rat 3
Total spectra collected	382	459	452
Spectra in the simulation	100	190	140
Glucose profile delay ajusted (minutes)	5	12	12
SEP (mM)	1.6	1.0	1.4
R^2	0.9438	0.9035	0.7094
Latent variables	8	9	7

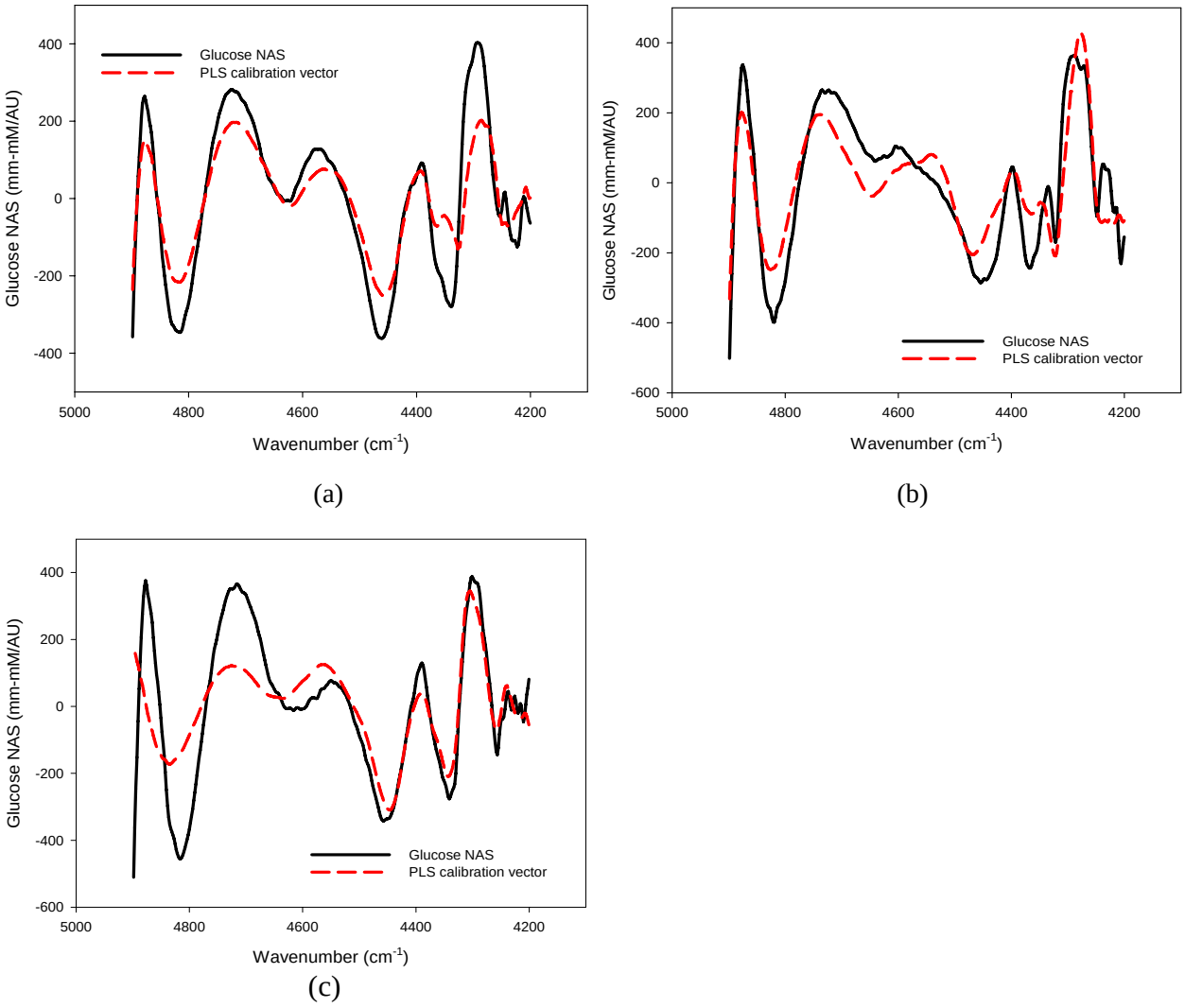

Figure III-10. Comparison of PLS calibration vectors obtained from the simulation approach with glucose NAS from Chapter II showing plots (a), (b), and (c) for animal models 1, 2, and 3, respectively.

collected over five consecutive days with animal conscious before the final surgical study. Details of the data collection of the conscious animal are described in the above experimental section, and the surgical procedures are the same as previously described in Chapter II.

The rat's body weight was measured before each study of data collection. The steadily increasing body weigh indicates that the rat was in a healthy condition, thus the quality of the collected spectra was not affected. Constant baseline glucose concentrations were obtained by fasting the animal overnight before collecting the two hours of baseline spectra. The corresponding glucose concentrations of each day are shown in Figure III-11 (a). Blood glucose fluctuations were only ~ 1 mM during these baseline periods. During the final glucose variation day, cycles of hyper- and hypo glycemia are achieved with the hyper- and hypo- glycemic control system described in Chapter II. This glucose concentration profile is shown in Figure III-11 (b). In the subsequent data analysis, no glucose concentration delay was used. Calibration models were established on the basis of baseline spectra and these models were tested with spectra associated with the glucose transients. Because baseline data sets have minimal glucose fluctuation, only NAS and HLA algorithms are applicable. The mathematical calculations to obtain NAS and HLA calibration vectors are the same as described in Chapter II.

The initial approach is to build glucose NAS calibration vectors from spectra from individual baseline periods and predict glucose levels during the final transient period. None of these glucose NAS calibration models demonstrate the ability to predict glucose during the transient period. This poor performance could be caused by tissue heterogeneity, which has been studied by exploring tissue samples with the NIR microscopy.[97] The skin tissue through which spectra are collected is not exactly the same in experiments on different days. The heterogeneous distribution of skin components results in significant difference in spectral background, which heavily affects the glucose

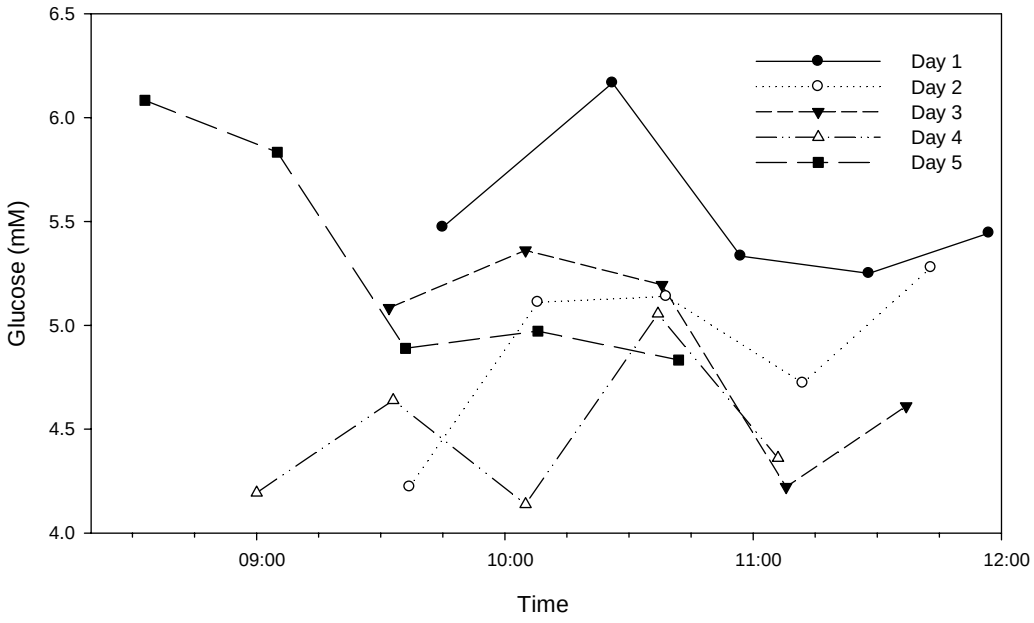

(a)

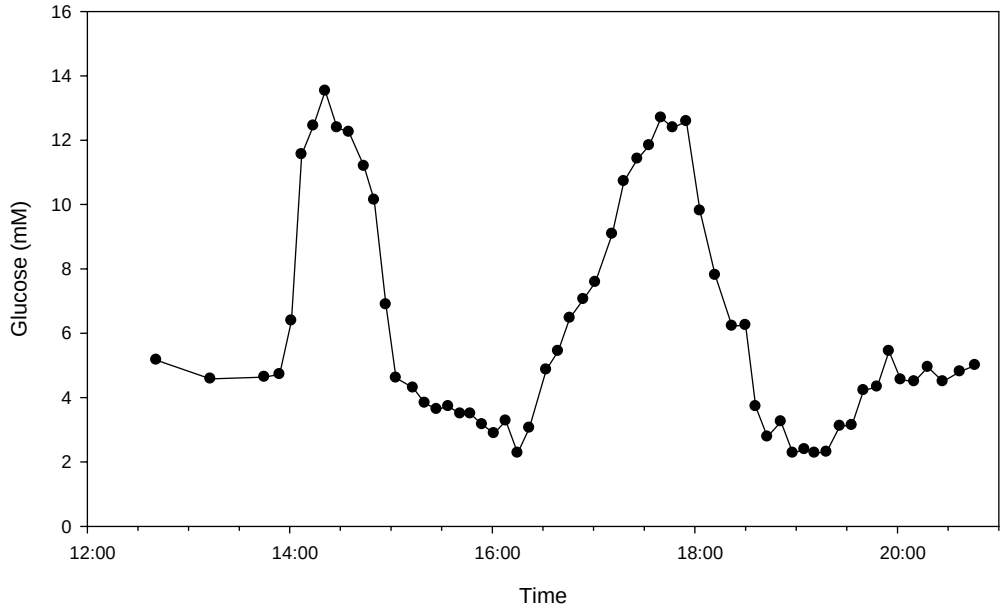

(b)

Figure III-11. Glucose concentration profiles of the 4th rat model where (a) shows glucose concentrations during conscious studies, (b) is from glucose transient study after surgery, and markers indicate the blood glucose reference readings.

prediction performance.

Alternatively, the pre-transient baseline period spectra can be combined withbaseline spectra collected on the day of transient. This means the baseline data set was updated with certain baseline spectra collected on the same day as the transient. The remaining 361 spectra in the glucose transient study are used for prediction. Five glucose NAS vectors and five HLA calibration vectors are obtained from these five combined baseline data sets. These vectors are then applied to the prediction data set to obtain predicted glucose concentrations. Figures III-12 and 14 show the glucose correlations in the prediction data set from NAS and HLA calibrations, respectively. Table III-7 summaries the corresponding latent variables, as well as SEC and SEP values for both NAS and HLA studies. In these results, SEP values vary from 1.2 to 3.0 mM with 8 to 11 latent variables. Combined baseline data sets 2 and 4 have lower SEP values (below 1.7 mM) for both NAS and HLA methods. Different magnitudes of correlations between blood glucose references and predicted concentrations are found in Figures III-12 (b) and 14 (b). Again, predictions from baseline data sets 2 and 4 have better correlation with blood glucose values. Glucose NAS and HLA calibrations vectors are compared to pure glucose absorptivity spectrum in Figures III-13 and 15, respectively. Since both glucose NAS and HLA calibration vectors are derived from the pure glucose spectrum, these models display features that correspond to glucose peaks at 4700, 4400, and 4300 cm^{-1}.

In this trial, it is feasible to select different combinations of different baseline days for constructing the calibration model. Glucose NAS and HLA calibration vectors from these baseline data sets demonstrate the capability of predicting glucose concentrations of prospective spectra.

Alternatively, the different baseline spectral sets can be combined. NAS and HLA calibrations models can be build with these combined baseline data sets. After searching all possible combinations, six baseline combinations with SEP values lower than 3 mM are obtained. The corresponding results are summarized in Table III-8 for models with

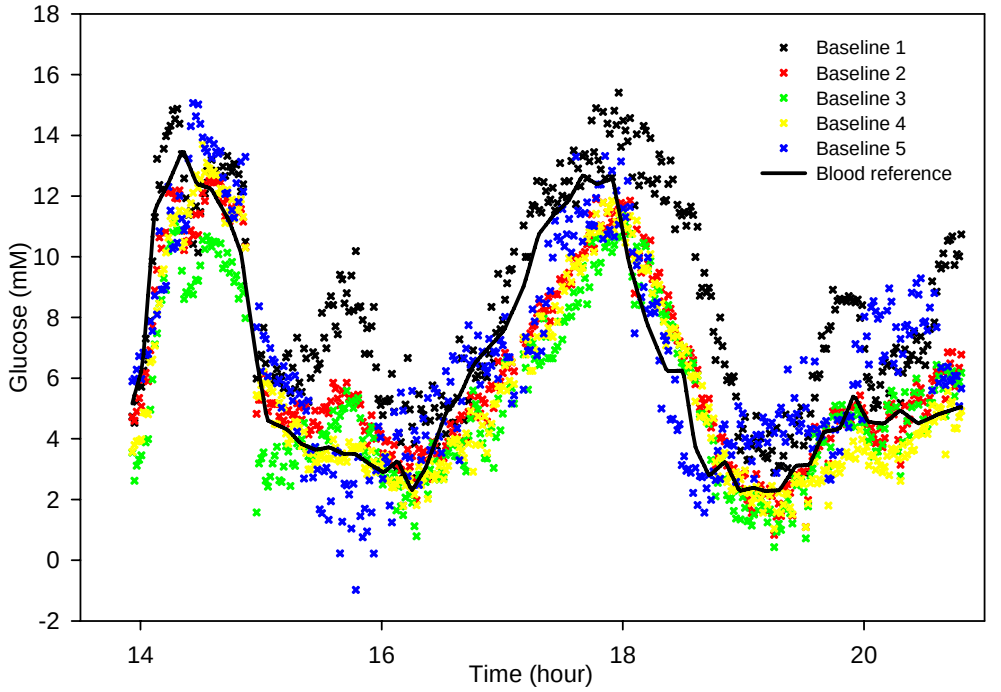

(a)

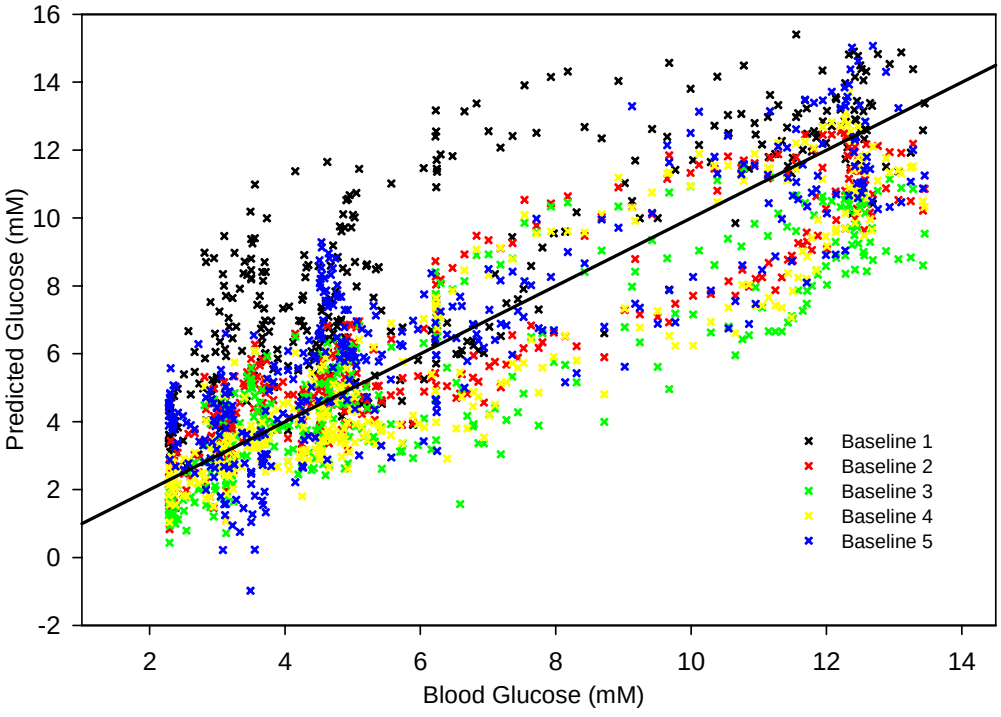

(b)

Figure III-12. NAS prediction results from baseline data sets 1 to 5 showing predicted glucose concentrations compared with blood reference values.

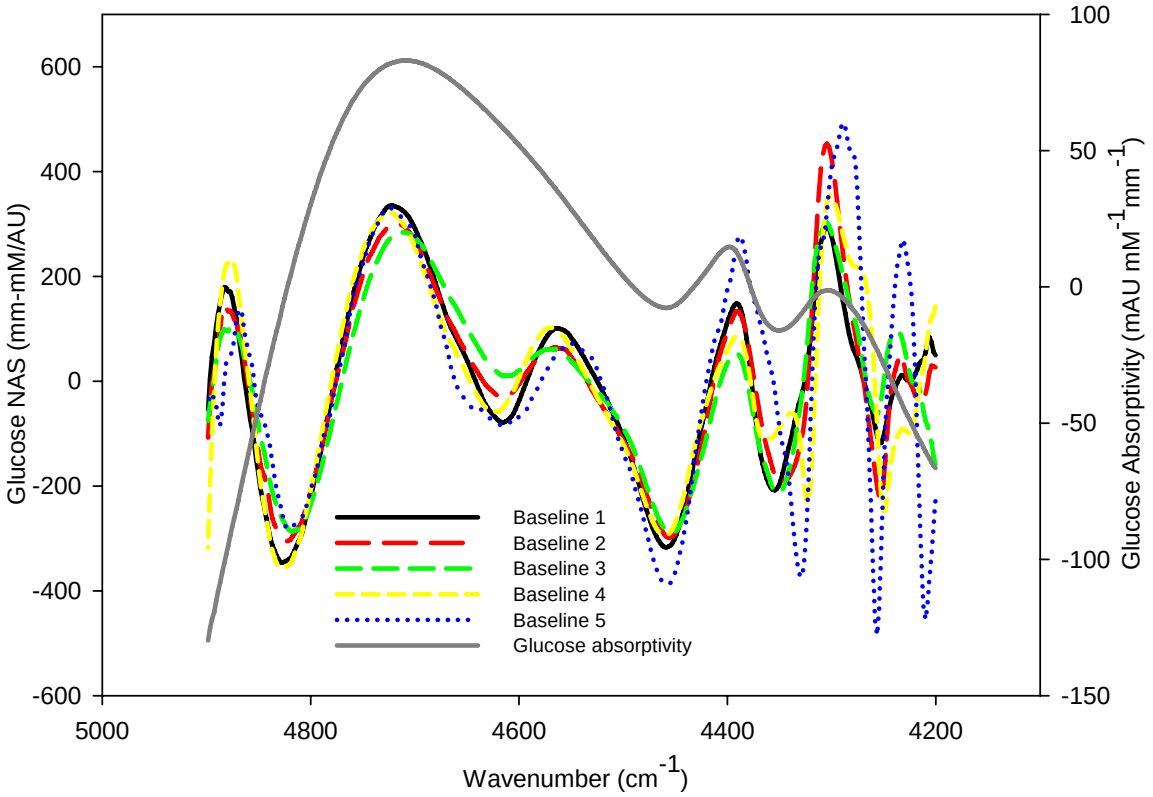

Figure III-13. Glucose NAS vectors obtained from baseline data sets 1 to 5 compared with pure glucose absorptivity spectrum.

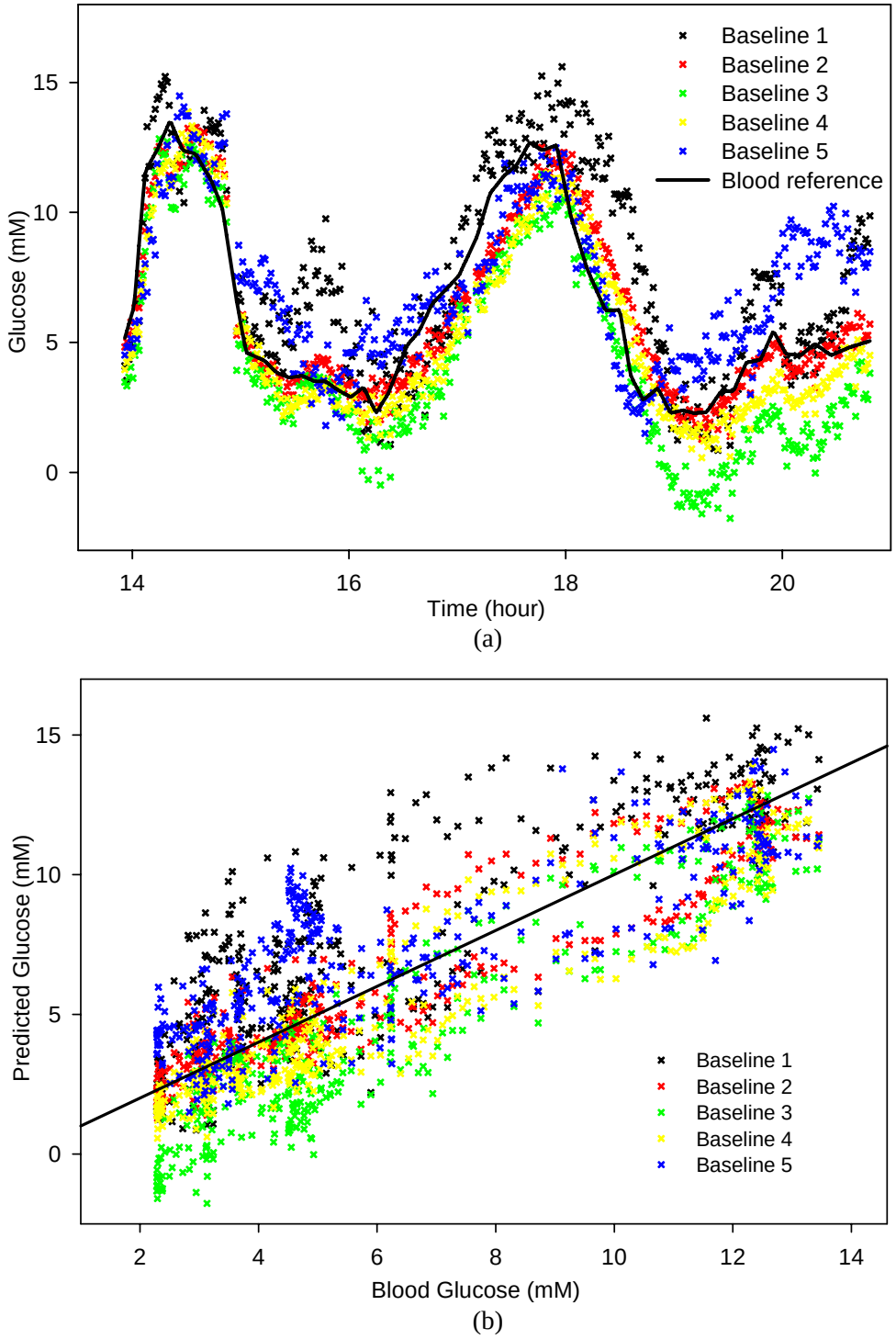

Figure III-14. HLA prediction results from baseline data sets 1 to 5 showing predicted glucose concentrations compared with blood references values.

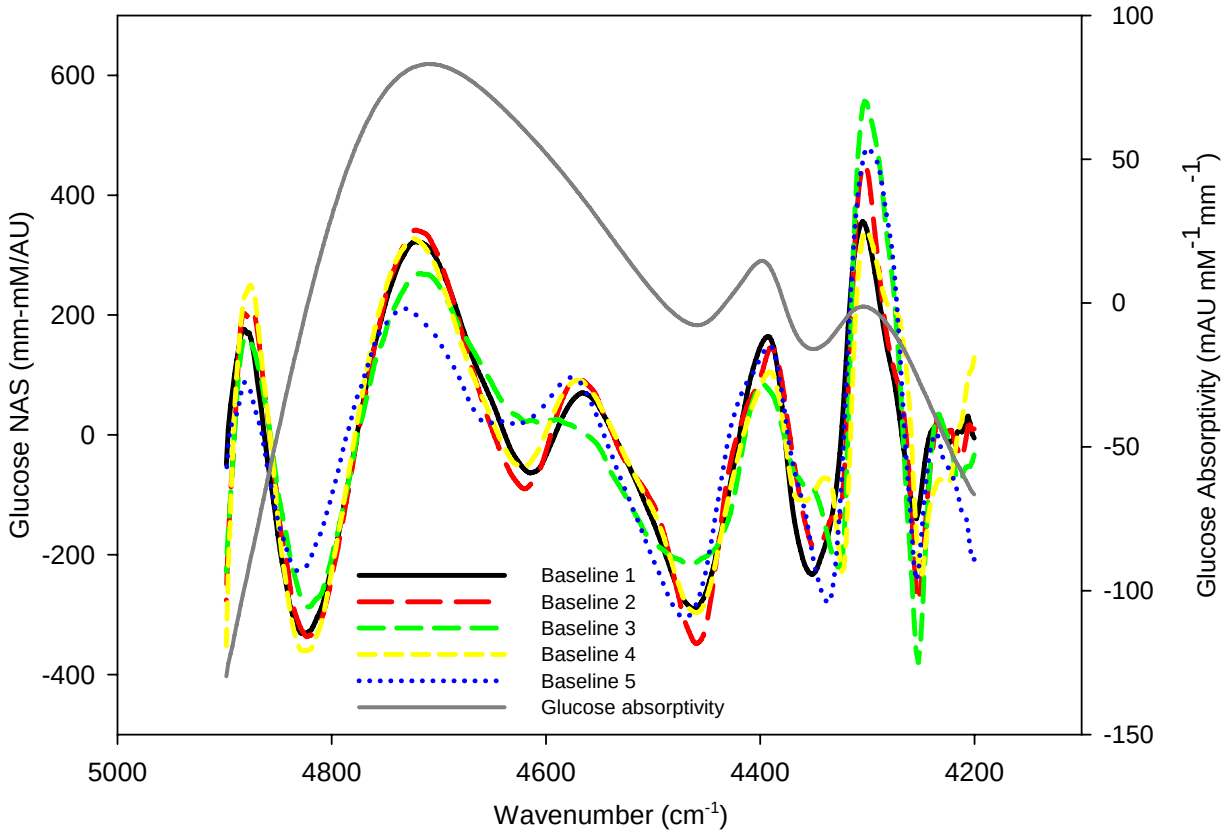

Figure III-15. HLA calibration vectors obtained from baseline data sets 1 to 5 compared with pure glucose absorptivity spectrum.

Table III-7. Summary of the first trial of NAS and HLA results of the 4th animal model.

Combined baseline data set	1	2	3	4	5
Spectra from conscious study	114	114	114	114	114
Spectra from surgical study	67	67	67	67	67
Total in calibration	181	181	181	181	181
Spectra in prediction	361	361	361	361	361
NAS results					
Latent variables	8	9	9	9	9
SEC (mM)	1.5	0.9	0.9	0.7	1.3
SEP (mM)	3.0	1.4	2.0	1.5	1.8
HLA results					
Latent variables	9	9	11	9	8
SEC (mM)	1.5	1.1	0.9	0.5	1.2
SEP (mM)	2.5	1.2	2.3	1.6	2.2

optimal latent variables. Figures III-16 and 17 show the correlations between predicted glucose levels and blood reference values for the NAS and HLA methods, respectively. Glucose NAS and HLA calibration vectors are also compared with the pure glucose absorptivity spectrum in Figure III-18. Figure III-18 illustrates that all these vectors have positive peaks at 4700, 4400, and 4300 cm^{-1} which coinside with known glucose absorption features. These results demonstrate that the predicted glucose concentrations follow the glucose transients with adequate correlations. With 8 to 12 factors, the SEP values from results of baseline combinations 1 to 6 are between 2 and 3 mM. These SEP values are high because no time delay is considered between the blood glucose and glucose in the skin tissue.

The glucose predicting performance in this trial is not as good as the previous model. A major factor that must be considered is the fact that the calibration data sets obtained from the combinations did not include the spectra taken before the glucose transient spectra. Three sources of skin spectral differences must be considered, including the rat kept growing during the entire process, and the body mass increased which might have impact on the fluctuations of skin components. Also, skin tissue was not pinched on the exact same spot each day, therefore the heterogeneous distribution of skin components could have an adverse impact. Third, there could be spectral differences associated with the animal exposed to the anesthesia agent on the day of the transient. To study the influence of the anesthesia agent on the skin tissue spectra, spectra were collected from a separate animal over several days with and without exposure to the anesthesia agent. Spectral analysis results from this experiment are covered in Chapter VI. In addition to skin spectral differences, there also might be certain glucose induced variances in the glucose transient spectra which are not included in the glucose baseline spectra. In the Chapter VI, a survival surgical procedure is proposed in order to establish animal models with glucose transients over multiple days, so that the glucose induced differences can be included in the calibration models.

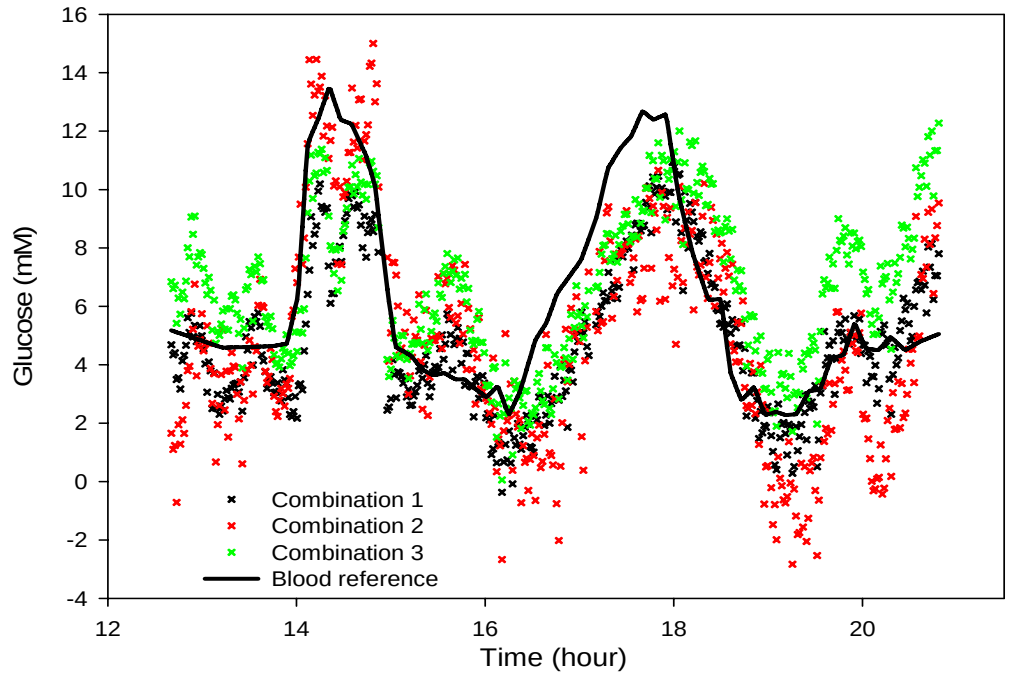

(a)

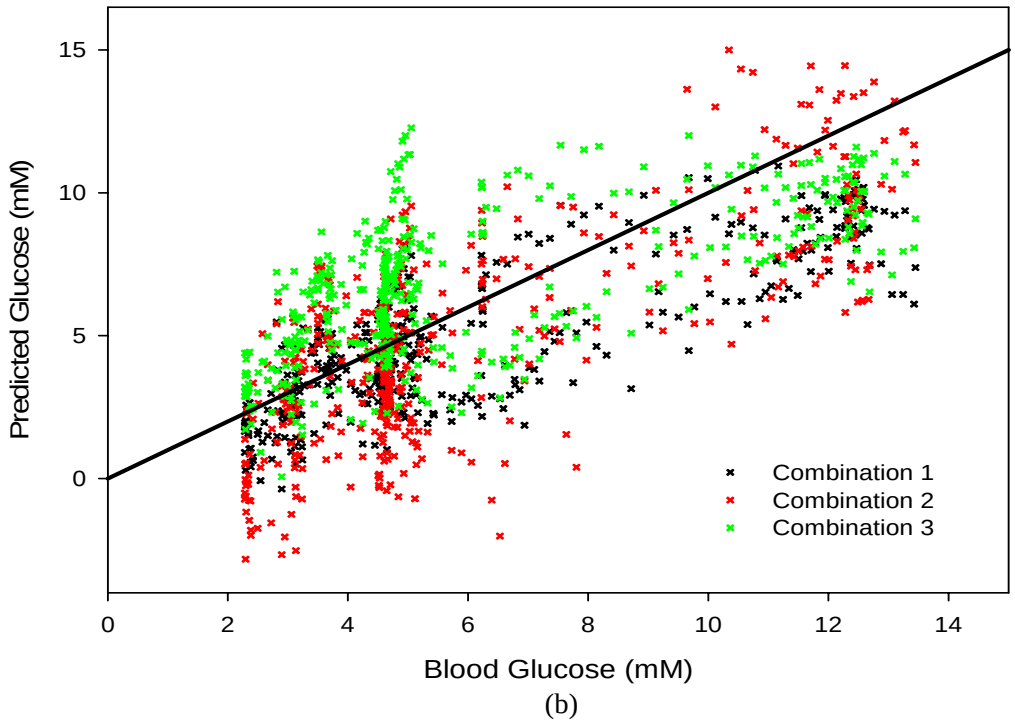

(b)

Figure III-16. NAS prediction results from the combinations 1, 2, and 3 of baseline data sets showing predicted glucose concentrations compared with blood reference values.

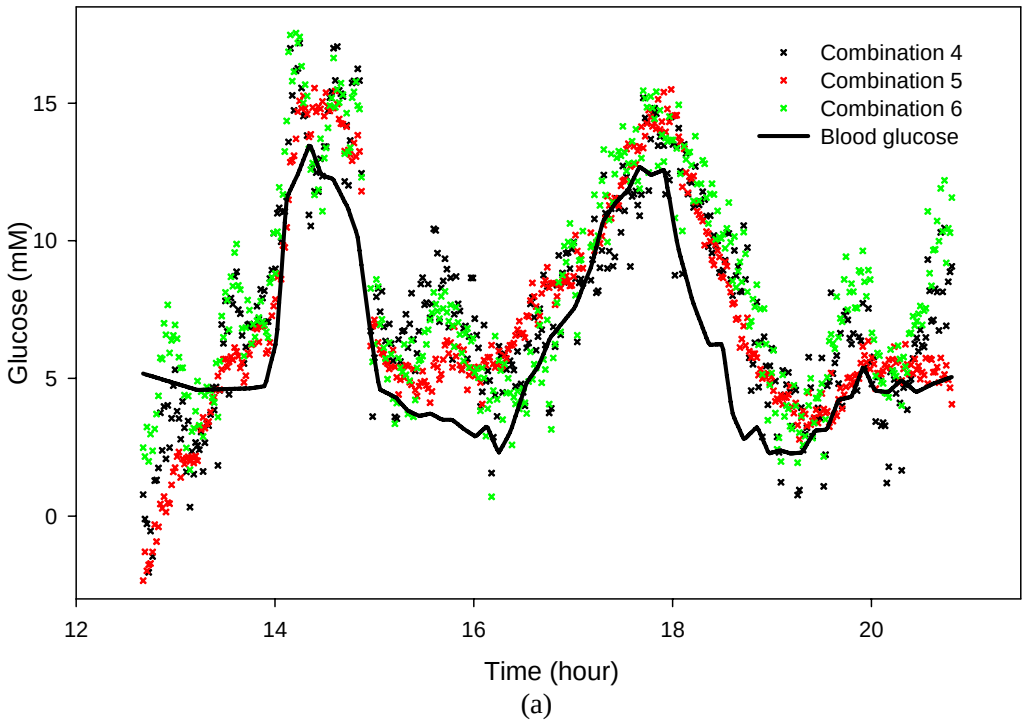

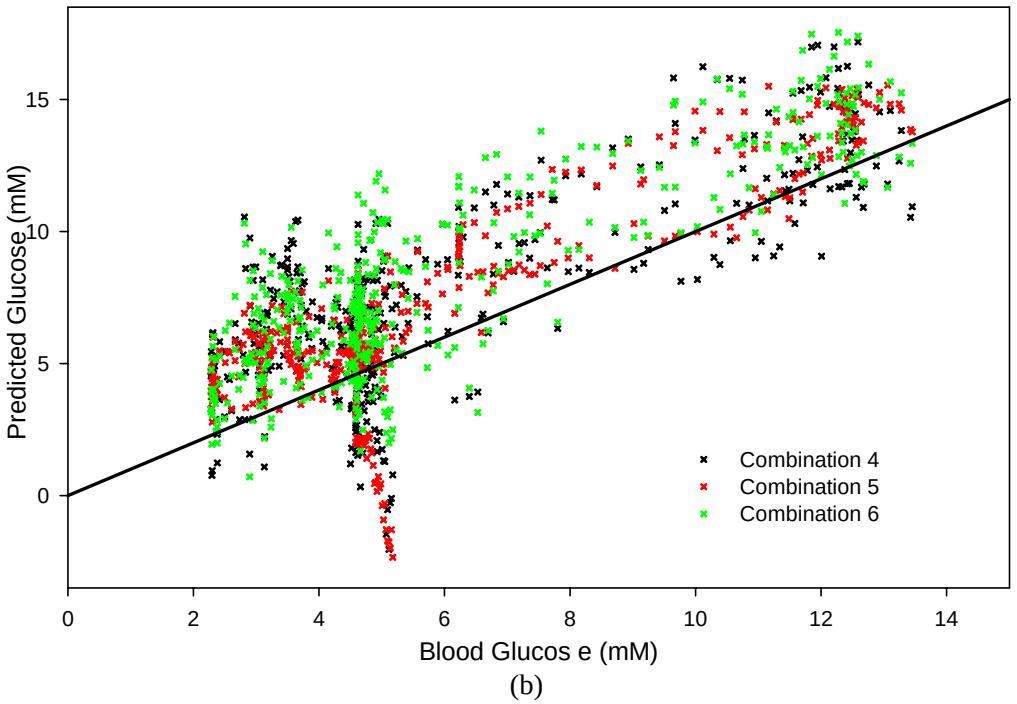

Figure III-17. HLA prediction results from the combinations 4, 5, and 6 of baseline datasets. Predicted glucose concentrations are compared with blood references.

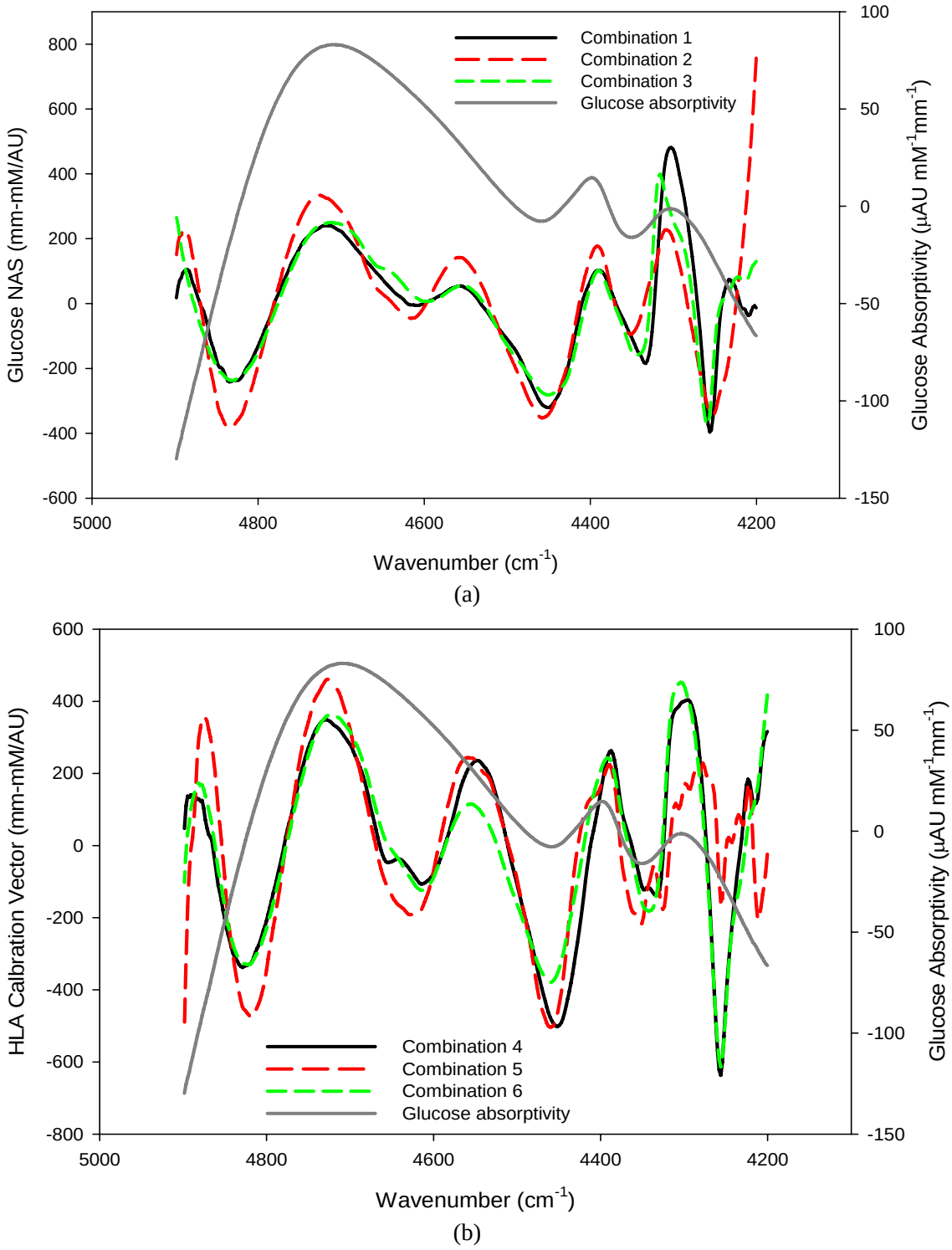

Figure III-18. Glucose (a) NAS and (b) HLA calibration vectors obtained from the combinations 1 to 6 of baseline data sets compared with pure glucose absorptivity spectrum.

Table III-8. Summary of NAS results of the 4th animal model from the second trial.

Combination 1				
Baseline of day 2 and 3				
# of spectra		Latent variables	SEC (mM)	SEP (mM)
Calibration	Prediction			
228	428	8	1.0	2.2
Combination 2				
Baseline of day 1, 2, 3, and 4				
# of spectra		Latent variables	SEC (mM)	SEP (mM)
Calibration	Prediction			
456	428	8	3.4	2.7
Combination 3				
Baseline of day1, 2, 3, and 5				
# of spectra		Latent variables	SEC (mM)	SEP (mM)
Calibration	Prediction			
456	428	8	2.3	2.6

Table III-9. Summary of HLA results of the 4th animal model from the second trial.

Combination 4				
Baseline of day 1 and 5				
# of spectra		Latent variables	SEC (mM)	SEP (mM)
Calibration	Prediction			
228	428	9	2.7	2.9
Combination 5				
Baseline of day 4 and 5				
# of spectra		Latent variables	SEC (mM)	SEP (mM)
Calibration	Prediction			
228	428	12	0.9	2.3
Combination 6				
Baseline of day 1, 2, 3, 4, and 5				
# of spectra		Latent variables	SEC (mM)	SEP (mM)
Calibration	Prediction			
570	428	8	3.4	2.9

The significance of this trial is not only SEP values for good model performance, but also glucose prediction models for multiple days. In this trial on animal model 4, glucose models are established based on glucose baseline spectra for multiple days, and the established glucose models are capable of predicting glucose concentrations during transients on a different day. This is the first time that we are able to predict glucose concentrations from models established on two or more previous data sets. In the future work, more effort should focus on animal models with multiple day spectra. A survivable surgical procedure is described in Chapter VI for this purpose.

Conclusions

In this chapter, calibration models are established with the ability to predict glucose concentrations from prospective spectra. Four different approaches are evaluated. The first approach builds calibration models on one animal model and applies this calibration model to spectra collected from different animals. This approach is not successful and none of these models could predict glucose levels accurately. This failure is primarily caused by variances from rat to rat. The second approach involved separating calibration and prediction data sets in one animal model by time. The results show that with more than half of the whole spectra being used for calibration, both PLS and HLA calibration vectors demonstrate the ability to predict glucose concentrations prospectively. A simulation procedure is also evaluated where the first 100 to 190 *in vivo* spectra are used to create a set of calibration spectra for developing PLS calibration models. A final method is proposed where multiple glucose baseline data sets are available for NAS and HLA calibration purpose. The NAS and HLA models established based on certain combinations of these baseline spectra also can predict glucose concentrations from the external prediction data set with glucose transients.

All of these approaches conclude that in order to build a robust glucose calibration model, adequate amount of variances from skin matrix must be included.

Adequate variance can be achieved by understanding the skin matrix and skin components that affect the *in vivo* NIR spectra. Building large calibration data set to incorporate more spectral variance associated with the skin matrix is critical for prospective calibration model predictions.

CHAPTER IV

ANALYSIS OF NONINVASIVE NEAR-INFRARED HUMAN BASELINE SPECTRA

Introduction

The overall objective of this research program is to develop near-infrared (NIR) sensing technology for the noninvasive measurement of glucose in people with diabetes. Success will improve the quality of life for more than 17 million Americans, and nearly 300 million people worldwide, with diabetes. The proposed technology will enhance tight glycemic control, thereby delaying the onset of the long-term complications associated with diabetes.

The concept of the proposed noninvasive sensing technology is to pass a selected band of harmless NIR light through a section of living tissue and then extract the glucose concentration from the resulting spectral information. Nothing is placed inside the body, and there is no need to draw a sample for analysis. Hence, issues of biocompatibility and sample handling are irrelevant. The challenge is to extract the desired analytical information solely from the spectroscopic data. Chapter II and III present results of work that provide an understanding of the fundamental analytical issues associated with measuring glucose selectively from NIR spectra collected noninvasively from an animal model. A prototype instrument is described that is capable of detecting glucose noninvasively in this animal model. Through careful systematic investigations, successful noninvasive glucose sensing is demonstrated and the critical measurement parameters are identified and defined. The next step is to begin the characterization of this instrument for use with human subjects. The first step toward this characterization is to collect spectra from a number of volunteers and compare the corresponding spectral responses. Results indicate the similarities and differences between noninvasive human spectra collected from different individuals. In this study, human skin color and baseline spectra were

collected and analyzed to determine differences among individuals and within groups of people.

The previous study in the research lab has investigated various sensing sites on the human body.[98] In this human baseline study, the skin fold on the back of the left hand was selected as the measurement site because this site provides NIR spectra with no fat absorption bands and sufficient quantity of interstitial fluid for sound glucose measurements.[96, 99]

Rats used in the previous animal experiments are from the same breeder and the same vender. Thus the skin color did not vary so much. However, for the application of this noninvasive NIR technique on a large population of human subjects, skin color variations will be significant. Hence, the impact of skin color on the NIR spectra should be studied before any direct application of NIR technique on human subjects. In this chapter, the influence of skin color variances on the NIR spectra is investigated by comparing principle component (PC) scores of the spectra with skin color values.

In this preliminary human subject study, volunteers are adult males and females from 18 to 65 years old, include people with and without diabetes, as well as from different ethnic groups. The focus of this project is to assess the impact of gender, age, diabetes, and ethnicity on the quality of noninvasive NIR spectra. The experiment is designed to minimize variations in the concentrations of glucose and other sources of variances. Hence, all the human subjects fasted for ten hours before the study so that glucose fluctuations and other types of metabolic variances were minimal.

Principal component analysis (PCA) was used to characterize the noninvasive skin spectra. PC scores of the spectra were compared with skin color parameters for the investigation of skin color effects on the quality of the NIR spectra. NAS and HLA calibration methods were used to build glucose calibration models, but PLS regression was not used because of insufficient variations in glucose concentration levels.

Experimental Section

Instrumentation

Noninvasive NIR human skin spectra were collected with a Nicolet 6700 FT-IR spectrometer (Thermo Fisher Scientific Inc. Waltham, MA). Similar to the instrumentation used for the animal experiments, a 50-W tungsten-halogen light bulb (Gilway, Technical Lamp, Peabody, MA) with an integrated, gold-coated reflector was used as the light source, an E3633A 200-watt DC power supply (Agilent Technology, Van Nuys, CA) was used to maintain the light bulb at 12.00 V and 4.10 A, and a custom sapphire-rod interface was used to bring the light from the spectrometer to the skin tissue and to collect the transmitted light for detection.. A four-stage thermoelectrically cooled extended-wavelength InGaAs detector with a diameter of 2 mm and a 2.6-μm cutoff (Judson Technologies, Montgomeryville, PA) was used as the detector. Compared to the animal instrumentation, a detector with larger surface area was used in this human subject instrumentation, which can collect more light and thus enhance the *S/N*. Figures IV-1 (a) and (b) show a photograph of the whole instrumentation and a detailed view of the interface, respectively. Optical filters in the optical path limit the spectral range of 5000 to 4000 cm^{-1}. Spectra were collected at a resolution of 8 cm^{-1} with 16 co-added scans. Each spectrum required 8.5 seconds for collection. The interferograms were Fourier transformed to single-beam spectra with triangular apodization, standard Mertz phase correction, and1-level zero of filling.

Blood glucose was measured from capillary blood with a Freestyle® glucose monitor (Abbott Laboratory, Chicago, IL). Skin color was measured with a CR-400 Chroma Meter (Konica Minolta Sensing, Inc., Osaka, Japan) on the same skin region used to collect the noninvasive spectra. Figures IV-2 (a) and (b) show a typical skin color measurement. The measurement probe was positioned on the skin and was allowed to stabilize for 15 seconds before the measurement was made. The skin color was quantified

(a)

(b)

Figure IV-1. Instrumentation and interface used for NIR human subject baseline study.

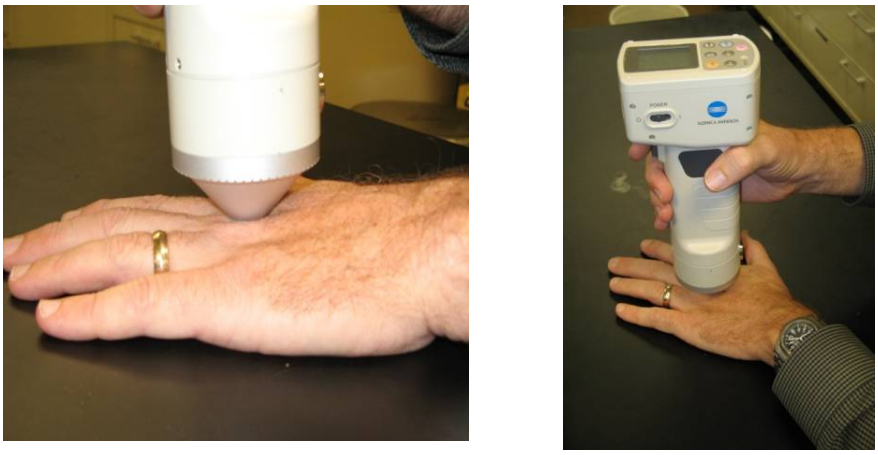

(a) (b)

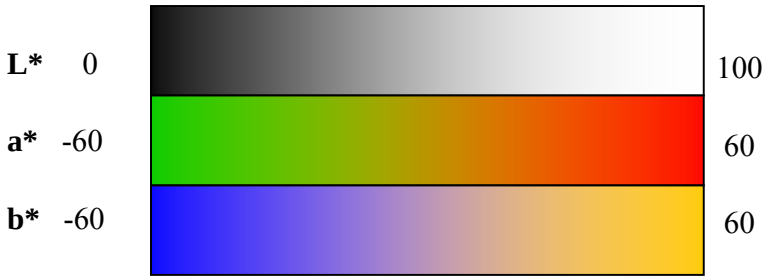

(c)

Figure IV-2. Skin color measurements with the CR-400 Chroma Meter presented in (a) and (b), and demonstration of CIE 1976 (L*, a*, and b*) color space in (c).

by the CIE 1976 (L*, a*, and b*) color space (also called CIELAB).[100] In this color space, L* represents brightness where L* = 0 indicates pure black and L* = 100 yields white, a* indicates red and green colors where a positive value means red and a negative value means green, and b* represents blue and yellow colors where positive is yellow and negative is blue. A demonstration of this CIELAB color space is shown in Figure IV-2 (c). Values of L*, a*, and b* values were recorded for each reading and the average andstandard deviation were recorded for 10 repetitive values for each measurement.

Experimental Procedure

In this study, volunteers were adult males and females from 18 to 65 years old including people with and without diabetes, as well as from different ethnic groups. These volunteers fasted overnight with food restriction for 10 hours. Before spectra were collected, the person's weight and blood pressure were recorded along with information such as age, sex, and racial category. In the second step, the first skin color measurement was obtained on the back of the hand where the interface would be placed. A capillary blood glucose measurement was obtained followed by placing the first glucose reading, the interface on a fold of skin on the back of the hand while the participant sat comfortably at a position beside the spectrometer. Spectra were collected repeatedly and continuously without movement for a period of 90 minutes. During this 90-minute spectra acquisition period, 633 noninvasive skin NIR single beam spectra were collected. Skin thickness between the sapphire rods was measured by an embedded caliper on the interface. Air reference spectra were also collected before and after each set of skin spectra. Three additional glucose readings were recorded: one after 30 minutes, one after 60 minutes, and one at the completion of the 90 minute period. After the spectral collection was completed, a second skin color measurement was performed on the same spot where the skin had been pinched by the interface. In total, forty-eight subjects participated in this study, however, only forty-seven data sets were analyzed, because the

data of one participant was recorded improperly. The human subject study was approved by the University of Iowa Institutional Review Board in compliance with federal human subjects regulations.

Human Subject Group Distribution

Data from 47 participants from 18 to 65 years old were used in the analysis. 22 of the subjects were males and 25 were females. There were 25 subjects without diabetes and 22 with either type I or type II diabetes. A detailed breakdown of each age category is summarized in Table IV-1. Off all 47 subjects, one is Hispanic and the rest are non-Hispanic. There are forty Caucasians, three African Americans, and three Asians.

Results and Discussion

Noise Level Estimation

Spectra of a 1 mm water cuvette sandwiched by two pieces of Teflon attenuator were used to estimate the noise level of the instrument. This setup produced signal levels equivalent to that of a typical sample of skin tissue. Root-mean-square (RMS) noise on 100% lines after a second-order polynomial fit in the range of 4400-4500 cm^{-1} was around 8 μAU. In comparison to the instrumentation used for the animal studies, the spectrometer used in the human study is a newer model and external detector has twice the diameter, but the number of co-added scans was only 1/8 of that used for the animal study. The difference of numbers of co-added scans contributes a factor of square root of 1/8 in the noise level, however, the larger detector area limited RMS noise levels by a factor of four. Thus, theoretical RMS noise of the instrument for the human subjects should be 0.8 of the animal model spectral. This is consistent with what we found in this study. Slightly higher RMS noise in practice could be due to a higher mirror velocity used in the human subject experiment setup. The detector with larger surface area in this instrumentation allowed us to collect spectra with low RMS noise levels and with less

Table IV-1. Human subject group distribution.

	Male			Female		
Age	With diabetes	Without diabetes	Sum	With diabetes	Without diabetes	Sum
18-25	2	3	5	3	5	8
26-35	0	4	4	0	3	3
36-45	3	2	5	2	2	4
46-55	1	3	4	6	2	8
56-65	3	1	4	2	0	2
Total	9	13	22	13	12	25

number of co-added scans. This means less time is required for each spectrum acquisition and more spectra can be collected in a limited time period.

Absorbance Spectra

The average air single-beam spectra were used as the reference to calculate the skin absorption spectra. Human skin absorption spectra were calculated by taking the negative logarithm of each skin single-beam spectrum ratioed to the averaged air single-beam spectrum. Spectra were truncated to a region of 49004200 cm^{-1} for all analyses. Figure IV-3 shows the averaged skin spectra of each human subject. From the skin absorption spectrum as shown in Figure IV-3, we can see that all the spectra from these 47 subjects have similar spectral shapes. Water is the most significant contributor to the overall spectral feature, the peak at 4600 cm^{-1} is due to proteins, mainly collagen and keratin, and the peaks at 4250 and 4350 cm^{-1} are due to fat absorbances. Significant baseline variations are also evident in this plot which is primarily due to different magnitudes of scattering among subjects. The relative peak heights also very slightly, and this is caused by variations in the skin component. Skin components estimation in the next section reveals more details of these variations.

Skin Component Estimations

Skin components were estimated based on a linear regression described in Chapter II. The regression uses a series of six pure components spectra including water, fat, collagen, and keratin plus a horizontal line and a slope term to fit the skin absorbance spectra. The corresponding coefficients represent the relative magnitude of each component.

Figure IV-4 summarizes these coefficients and the corresponding standard deviations. The standard deviation describes how each regression coefficient fluctuated during the data collection for each participant. It can be seen from Figure IV-4 (a) that water and collagen have the largest regression coefficients, which indicates that water

and collagen are the dominant components in the skin tissue. For several subjects, the corresponding standard deviations of water and collagen are significantly high. These large variations could be caused by skin response to the external pressure imposed by the interface, because water is movable and collagen is compressible. The regression coefficients of keratin fluctuate between 0.2 and 0.4. Because keratin is a kind of hard protein, it does not change that much under the external pressure and the corresponding standard deviations are also low. Fat has the lowest coefficients that are close to zero, which means there is little fat in this particular spot. This is one of the reasons this particular skin site was selected for noninvasive glucose sensing. Strong absorptions at 4250 and 4350 cm^{-1} from fat can be significant interferences of glucose absorptions in this region. Therefore, the skin on the back of the hand was chosen as the sensing target to minimize interference from fat.

The coefficients for the constant term vary among individuals, which means the magnitude of scattering also varies between subjects. Moreover, the standard deviations of this coefficient are also quite large, which means considerable change in the magnitude of scattering changed a lot during the 90 minutes of each individual experiment. The scattering was affected by the pressure from the interface and some subtle hand movements. Although each participant was told to minimize hand movements, some movement was unavoidable. The frequency of this kind of movement is also different from person to person. Some with fewer movements had smaller standard deviations, while those who had more movement had larger standard deviations.

Coefficients for the slope term also vary from person to person, which means different individuals have different degree of temperature variation. The standard deviation of this term remains low throughout, which means this type of temperature variation during the 90 minutes spectral collection was small.

This skin components estimation gives us the first impression of origins of optical variations both within individuals and from person to person.

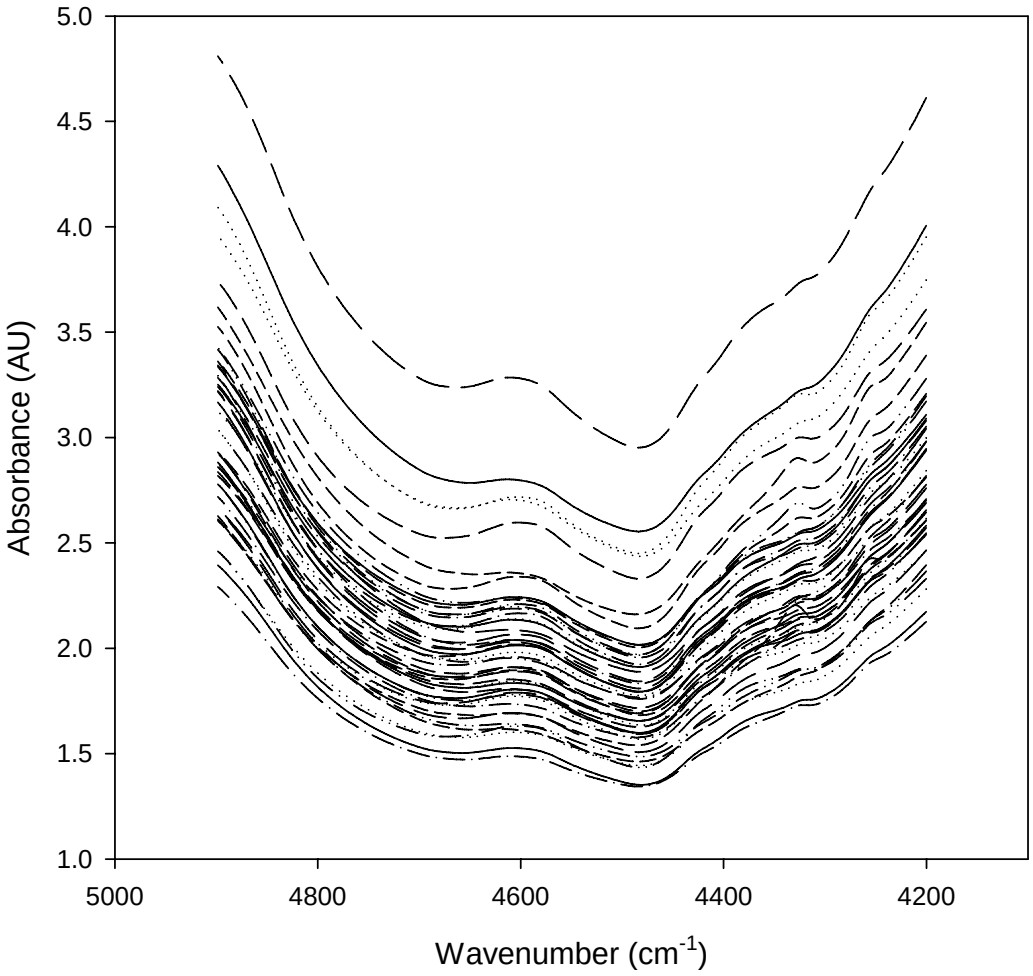

Figure IV-3. NIR skin absorbance spectra of 47 human subjects.

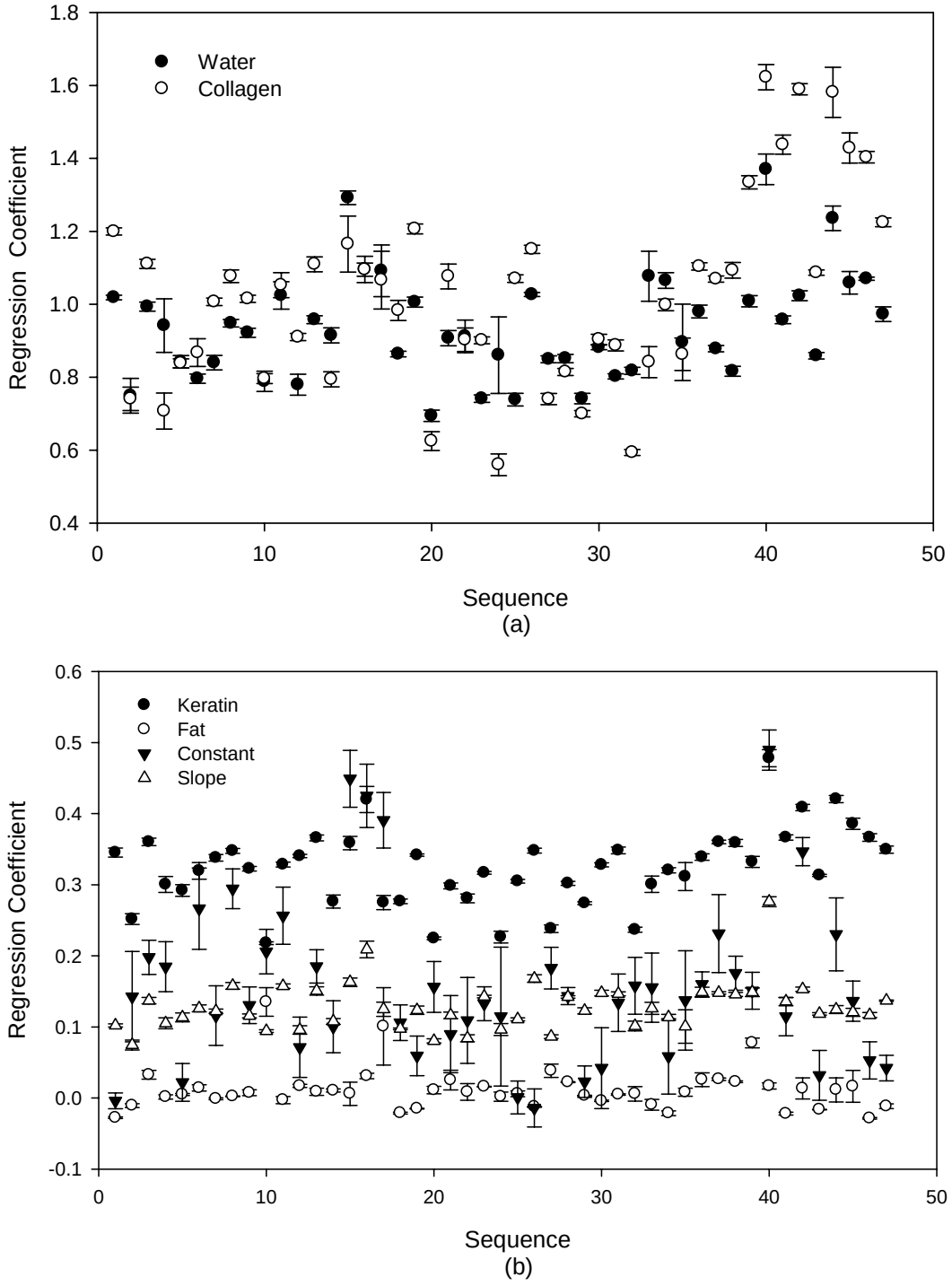

Figure IV-4. Regression coefficients of skin components estimated from spectra of 47 participants.

Skin Color Representation

Skin color was recorded as L*, a*, and b* values. Figure IV-5 summarizes the L*, a*, and b* values and their corresponding standard errors before and after the 90 minutes skin clamp measurements. L* varies from 32 to 72, the range of a* is from 7 to 26, and b* is from 7 to 20. Skin color differences are primarily caused by skin variations from people to people. To study how the skin color changes after being pinched for 90 minutes, the skin color difference was calculated as ΔL*, Δa*, and Δb*. These values and corresponding standard deviations are presented in Figure IV-6. For most of the subjects, the L* value decreased and a* value increased after being clamped for 90 minutes, which means the skin turned darker and redder after the experiment. b* changed in either direction randomly. These skin color values were further compared with NIR skin spectra to investigate how the skin color variations affect the quality of the NIR spectra.

Principal Component Analysis (PCA) of Skin Spectra

All the spectra collected on these 47 subjects were combined as one data set and principal component analysis (PCA) was performed. Because the spectral matrix is large with almost 30,000 spectra, insufficient memory is available for SVD compution of the PC factors so the NIPALS method was used. Thus, the whole spectral data set was decomposed into 15 principal components. This decomposition can be described by the following equation:

$$\boldsymbol{X} = \boldsymbol{T}\boldsymbol{P}^{\boldsymbol{T}} + \boldsymbol{E} \qquad \text{Equation IV-1}$$

where **X** is the whole data matrix, ***T*** is the score matrix, **P** is the loading vectors, and ***E*** is the noise that can not be explained by these loadings. These 15 loading vectors are shown in Figure IV-7. As more principal components (PCs) are added, the loading vectors become more complex. The absence of noise in these factors is significant and suggests

that multivarite models with up to 15 latent variables are possible without overfitting. Only up to 12 latent variables are used in the NAS and HLA calibrations presented below.

PC scores were plotted with two adjacent PCs on the x and y axes in Figures IV-8, 9, 10, 11, 12, 13, and 14. Scores are grouped by female with diabetes, female without diabetes, male with diabetes, and male without diabetes. For all of these comparisons up to 15 PCs, scores from different groups of participants heavily overlap with each other, which means the spectra from groups above are not distinguishable. This indicates that genders and diabetes do not cause any significant spectral difference.

Another PCA analysis was performed on each individual subject with the SVD algorithm used to quantify the skin spectral noise level of each individual. After removing each PC from the spectral matrix, the RMS noise of residual spectra can be calculated. As more PCs are determined, the RMS noise tends to decrease. Once all the PCs related to chemical components are subtracted, the residual matrix only contains spectral noise. Thus, the corresponding RMS noise represents the noise level of the measured skin tissue spectra. To compare the RMS noise levels among individuals, the RMS noise of residuals with 10 PCs removed was calculated. These residual RMS levels vary from 10 to 200 μAU. One of the major contributors is skin thickness, which affects the attenuated light and radiant power at the detector element. The participants' skin thickness between the sapphire rods varies from 1.2 to 2.0 mm. Plot of skin thickness vs. PCA residual RMS noise is shown in Figure IV-15. In this plot, we can see that thinner skin had lower PCA residual RMS noise. For skin thicknesses no more than 1.8 mm, the PCA residual RMS noises are well maintained below 60 μAU. As the skin thickness increases to 2.0 mm, these RMS noise levels dramatically increase to 200 μAU. Since the glucose absorptivity is extremely low, the instrument is required to maintain the noise level lower than the glucose absorptivity to be capable of sensing glucose. This instrument works well for those skin thicknesses below 1.8 mm. Even though the RMS

noise could be as high as 60 μAU, it can be lowered further by spectral averaging since the spectra were collected with a high time resolution. However, for the thickness over 1.8 mm, extremely high noise levels would definitely decrease the glucose prediction performance.

Moreover the high noise is also caused by low optical throughput of skin tissue samples. Skin tissue consists of different layer with different refractive indexes. Light is dramatically attenuated at the interfaces due to the refractive index mismatch when the light transmits through skin tissue, which is one of the limitations of the current instrumentation. Three approaches can be made to overcome this limitation in the future work. The first is enhancing the optical throughput of the instrument by looking for light sources with more irradiance density, interfaces with effective optical coupling, and detectors with larger surface area and lower noise. The second is to explore skin pretreatment methods and that can reduce the refractive index mismatch, therefore reducing the loss of light. The skin reclamping and sliding can be another contributor to the overall RMS noise. From the previous study in our lab,[97] skin heterogeneity will result in the corresponding NIR spectra change which increases the noise level of the spectra. The main reason for reclamping is that the prototype interface does no hold the skin tissue in position constantly. Sweating makes this case even worse. Therefore, the next generation of the skin interface will be able to firmly hold the skin without causing uncomfortableness.

Impact of Skin Color on NIR Spectra

Skin color varies in the visible range of the spectrum, while the noninvasive spectra are collected in the NIR region. Theoretically, the visible color variance should not affect the spectra in the NIR region. In order to study how the skin color affects NIR skin spectra, L*, a*, and b* values obtained from skin color measurement were compared with PC scores from PCA analysis. To make the best correlations, the first skin spectrum

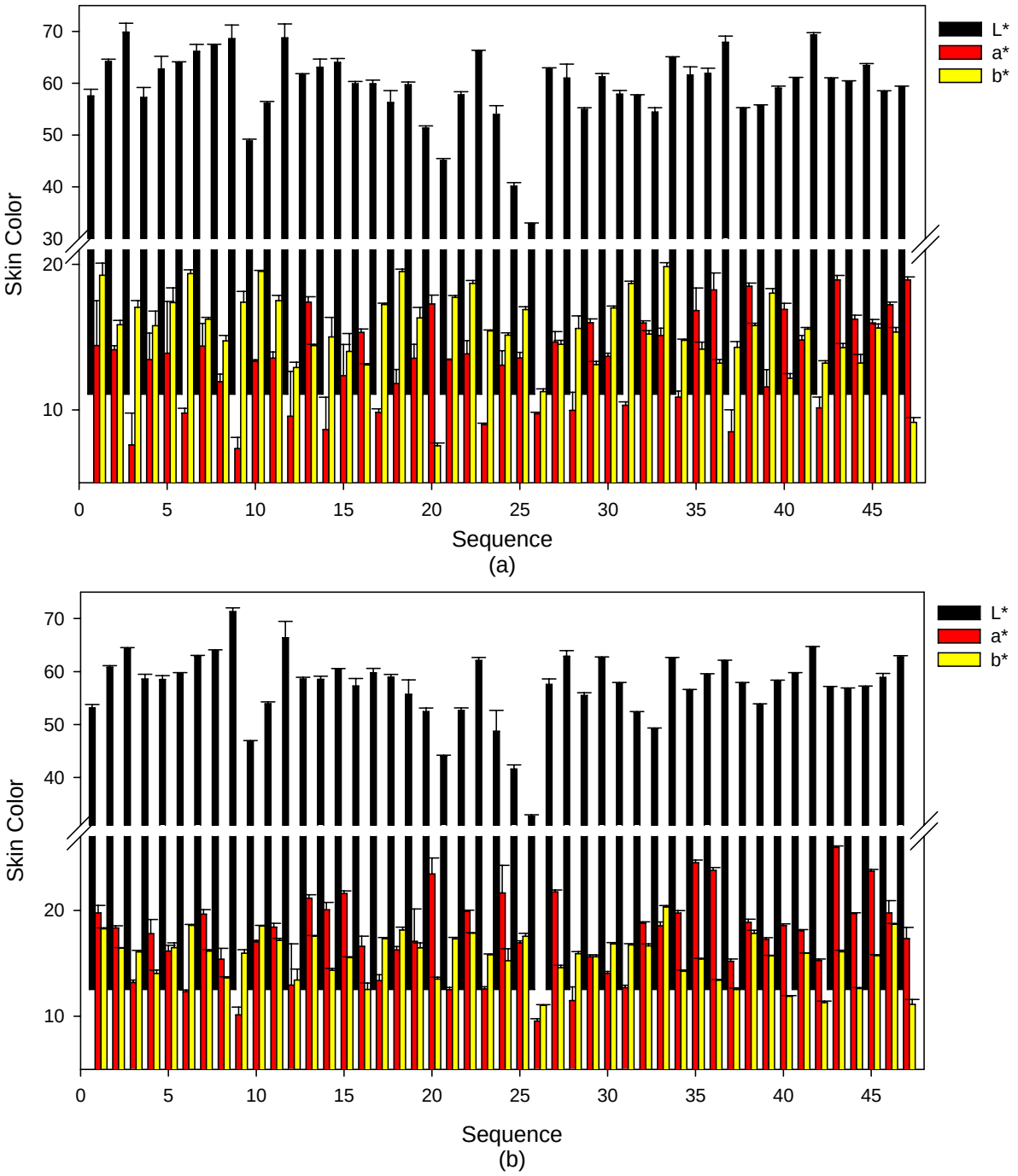

Figure IV-5. Skin color representation in CIELAB color space (a) before and (b) after skin spectra collection for 90 minutes.

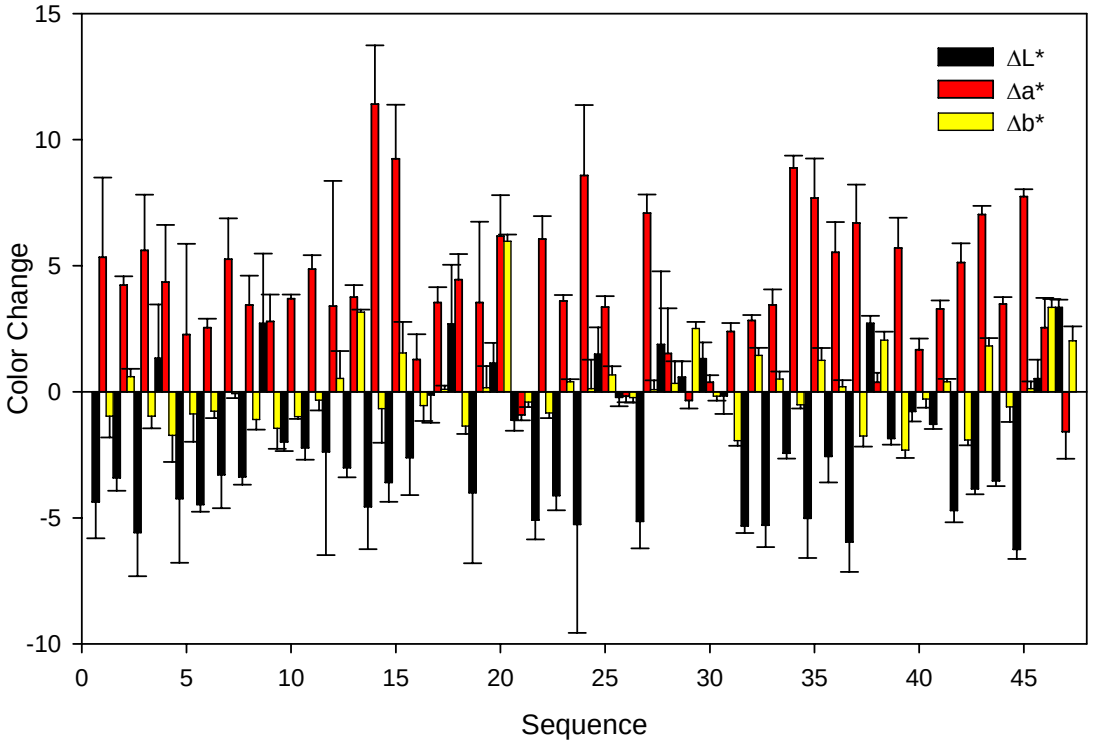

Figure IV-6. Skin color change of each individual before and after the 90 minutes skin spectra collection.

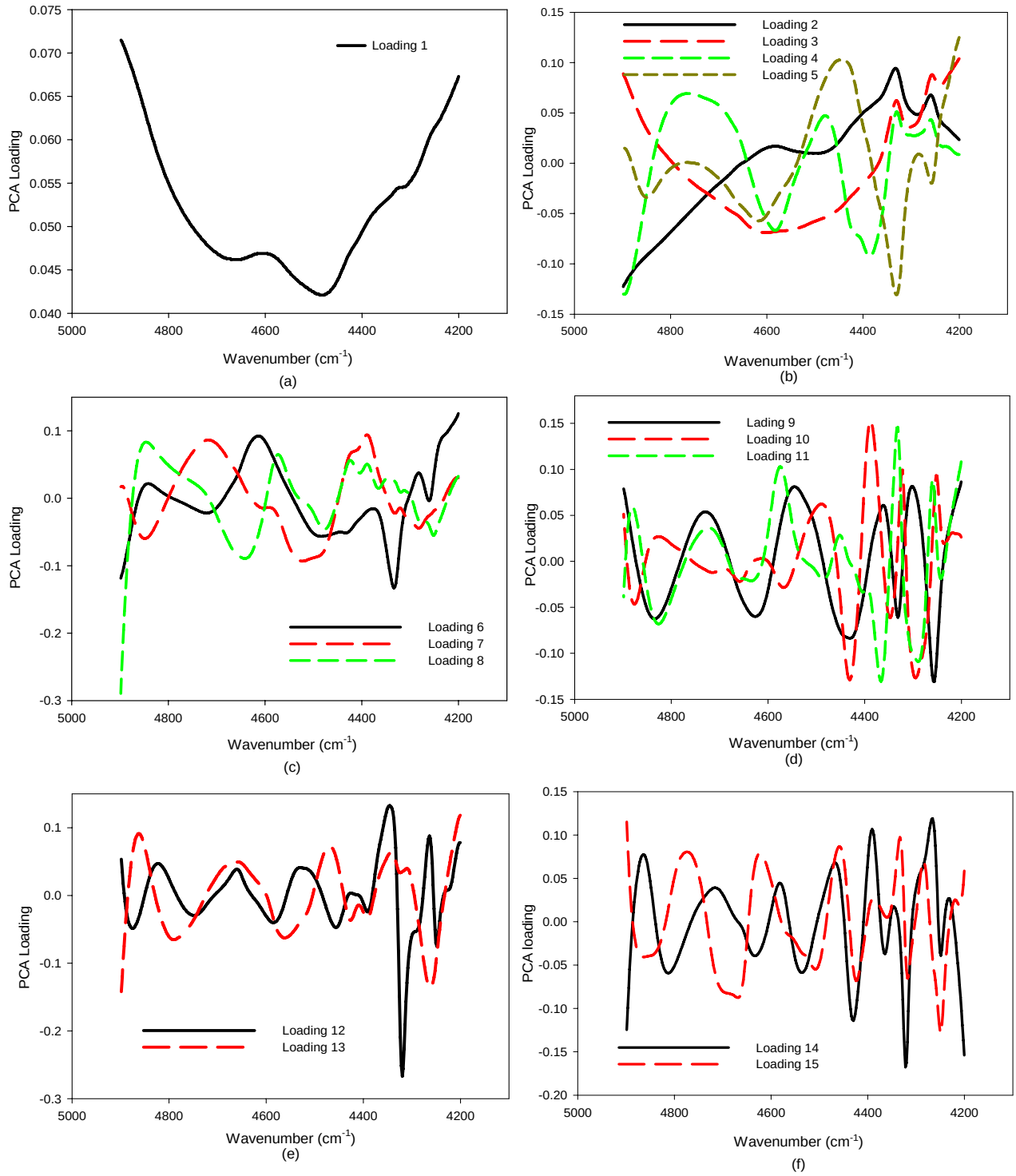

Figure IV-7. PCA loadings of all the NIR skin spectra from 47 human subjects with 1 to 15 latent variables.

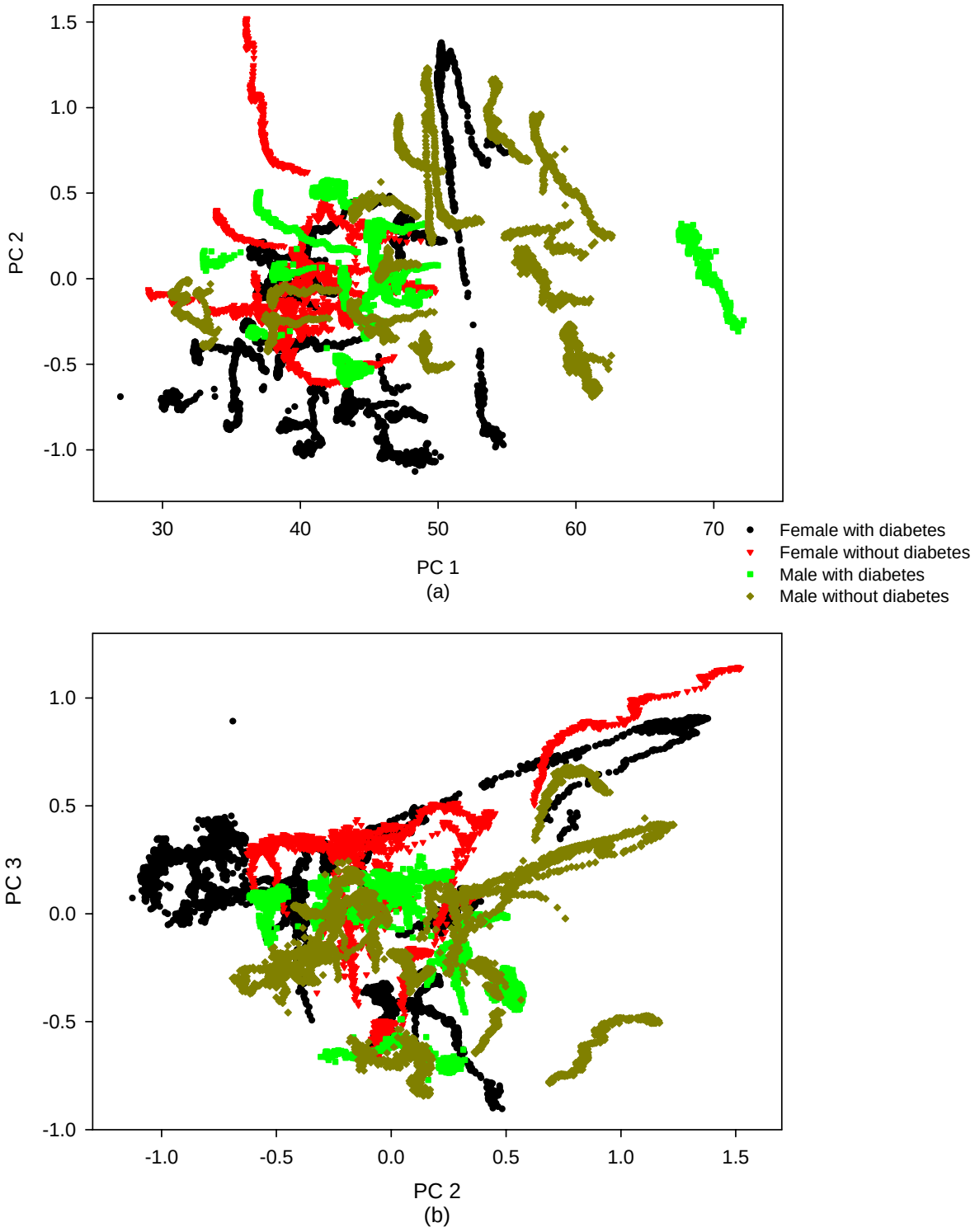

Figure IV-8. Principal component plots showing (a) PC 1 vs. PC 2 and (b) PC 2 vs. PC 3.

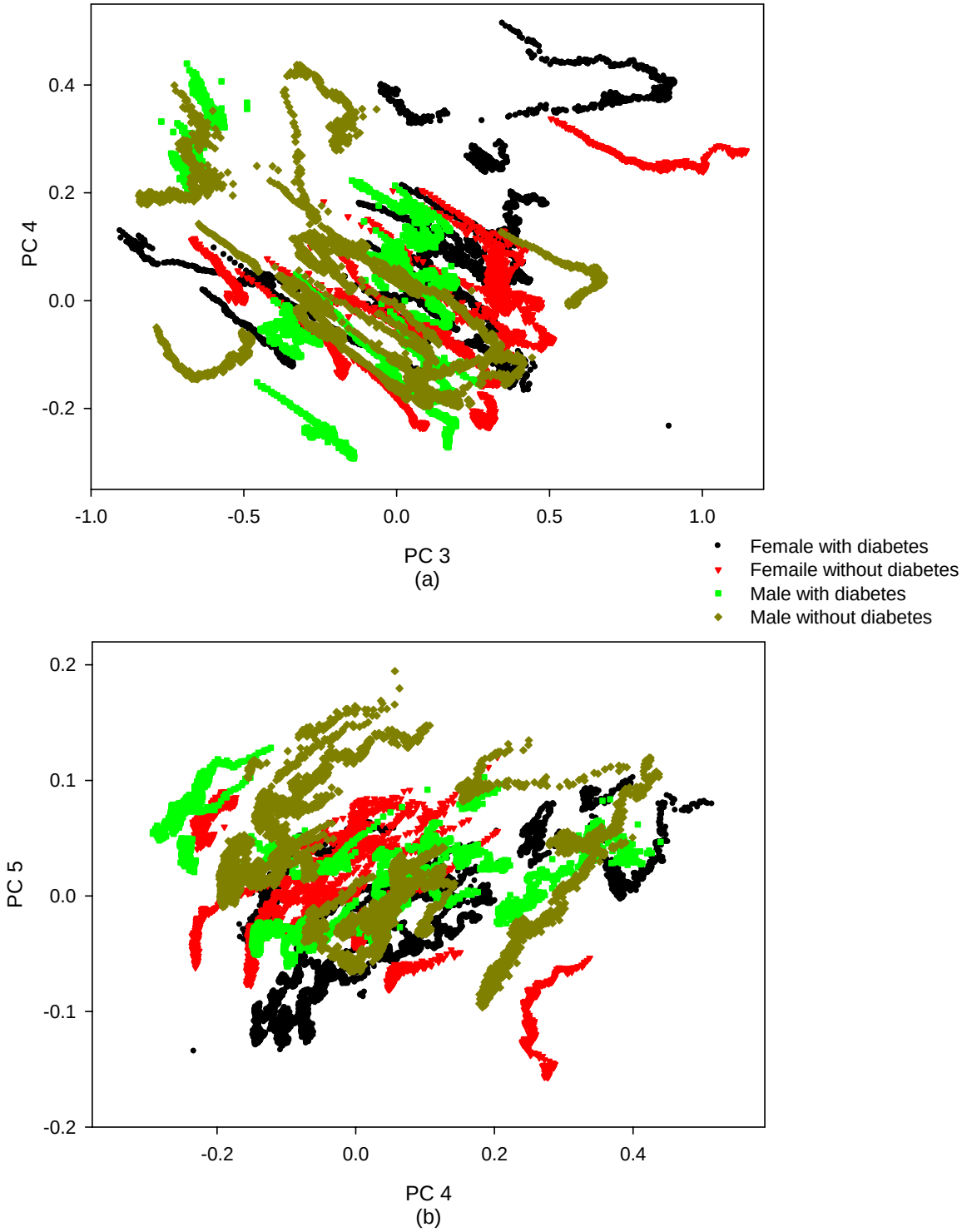

Figure IV-9. Principal component plots showing (a) PC 3 vs. PC 4 and (b) PC 4 vs. PC 5.

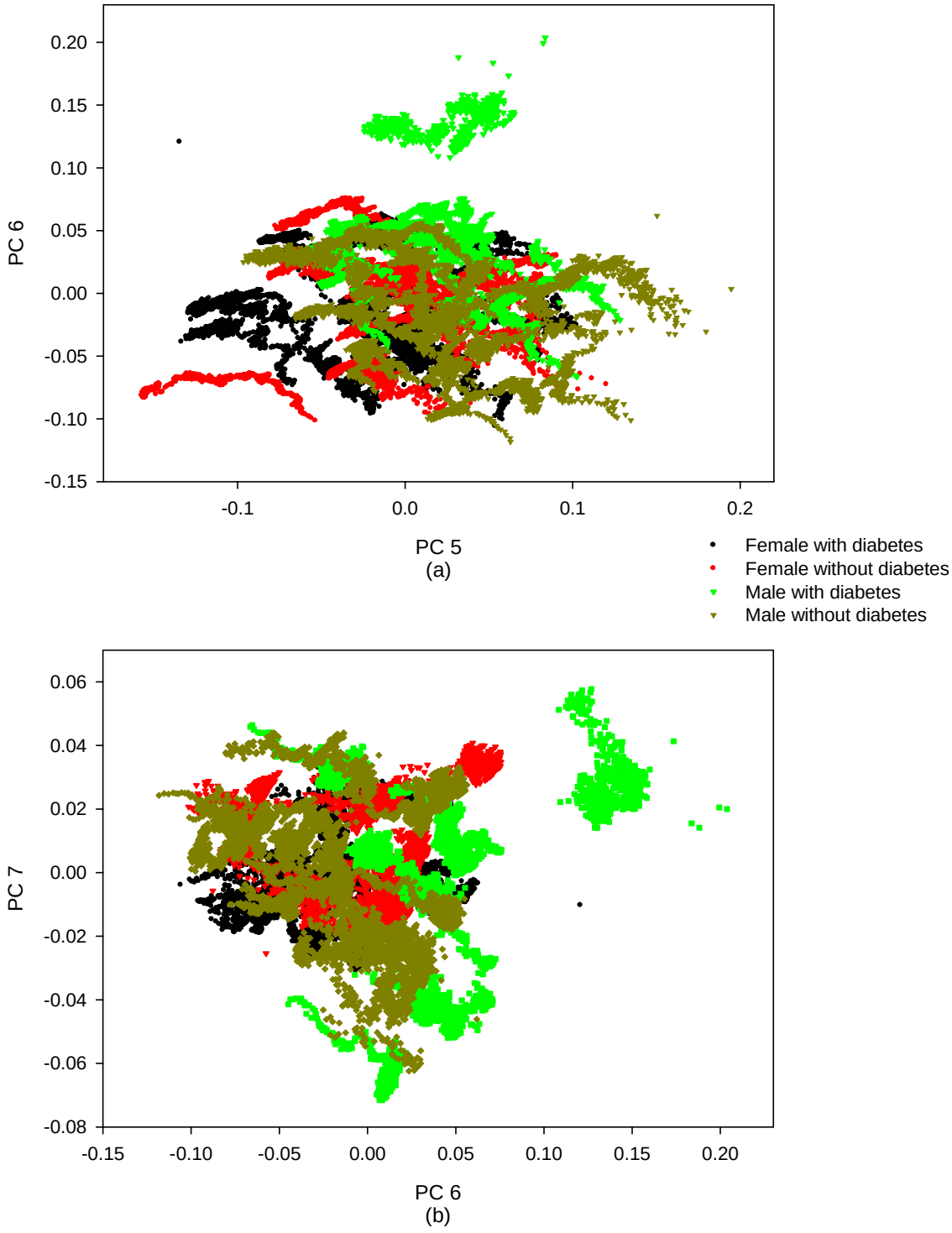

Figure IV-10. Principal component plots showing (a) PC 5 vs. PC 6 and (b) PC 6 vs. PC 7.

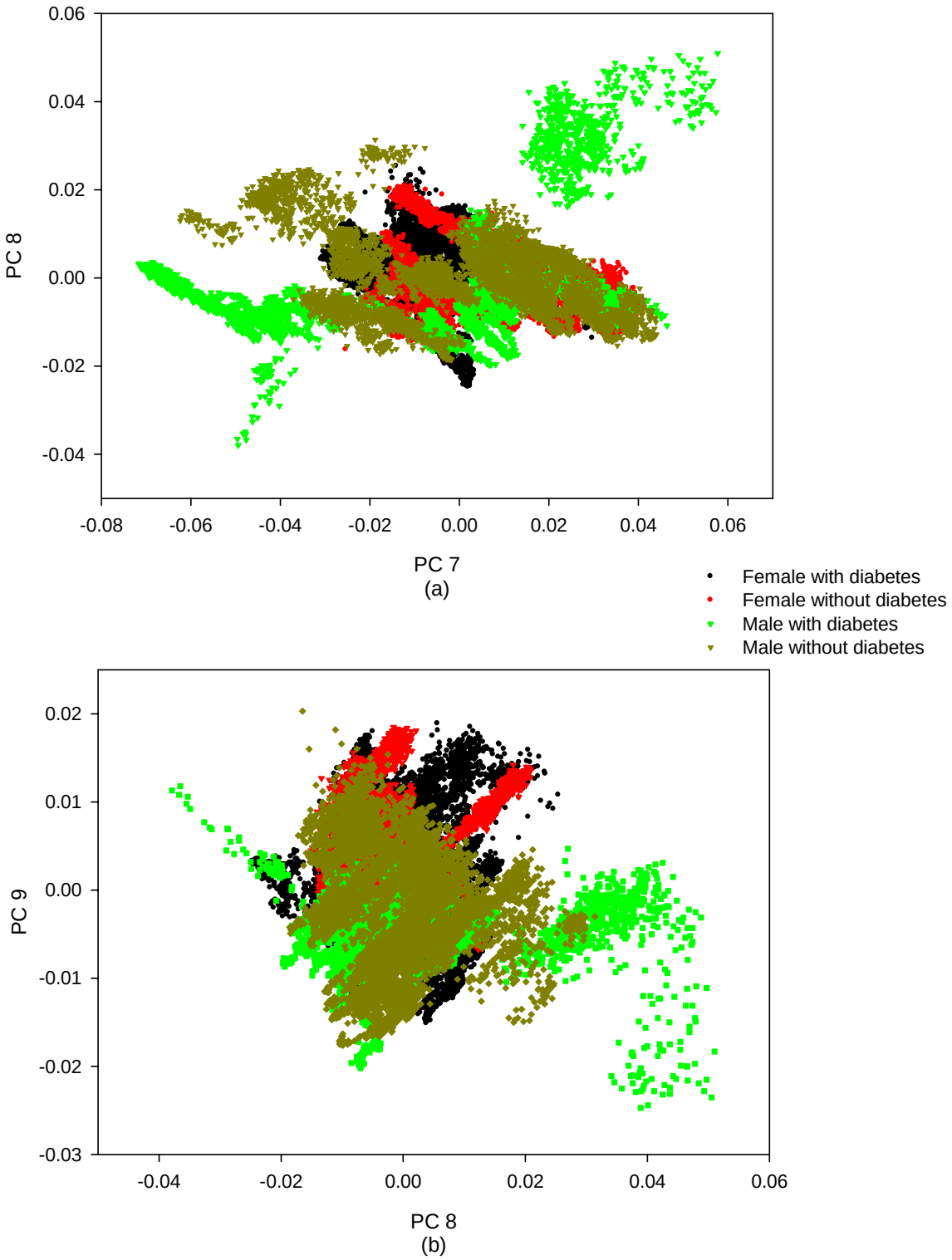

Figure IV-11. Principal component plots showing (a) PC 7 vs. PC 8 and (b) PC 8 vs. PC 9.

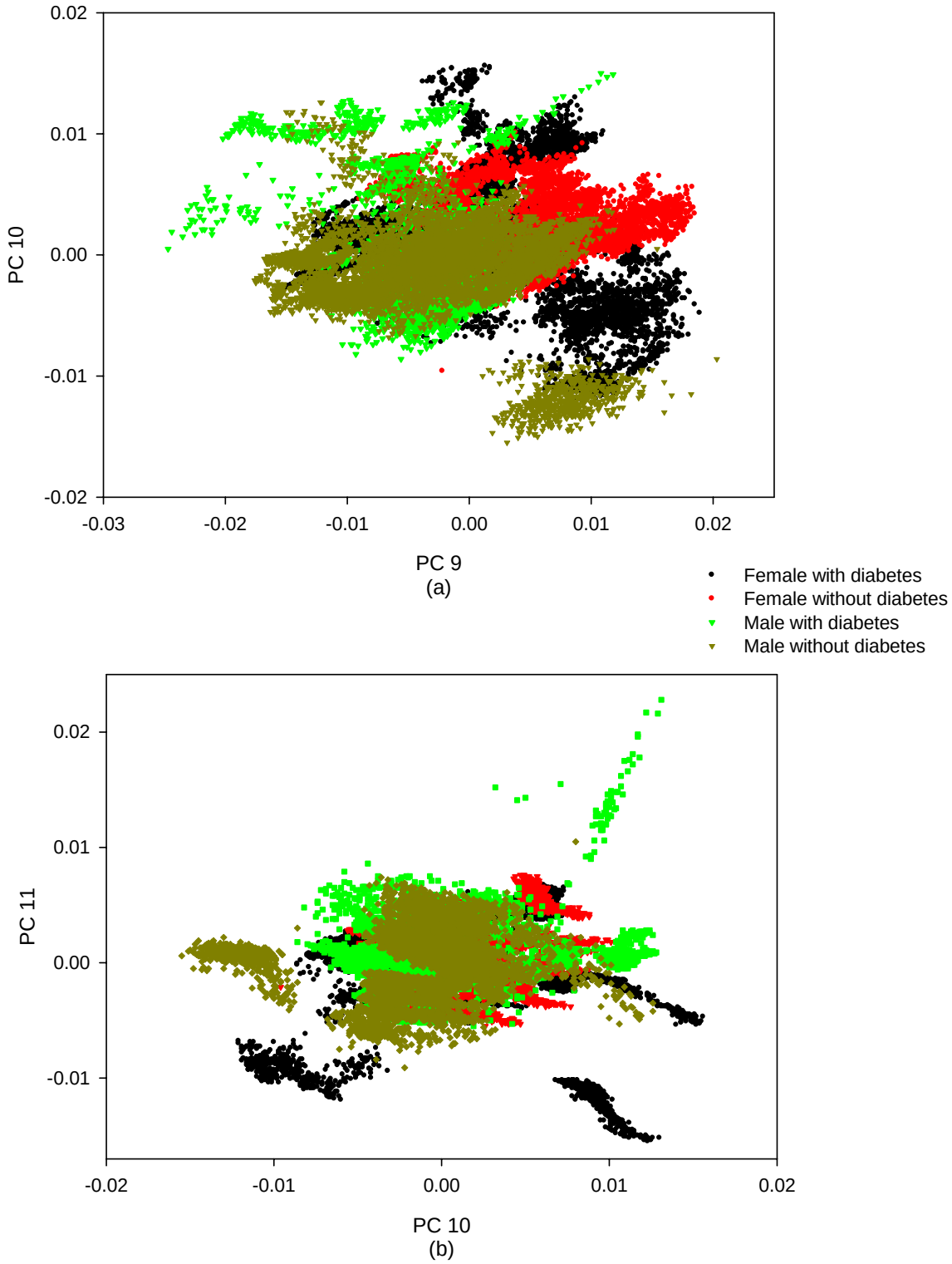

Figure IV-12. Principal component plots showing (a) PC 9 vs. PC 10 and (b) PC 10 vs. PC 11.

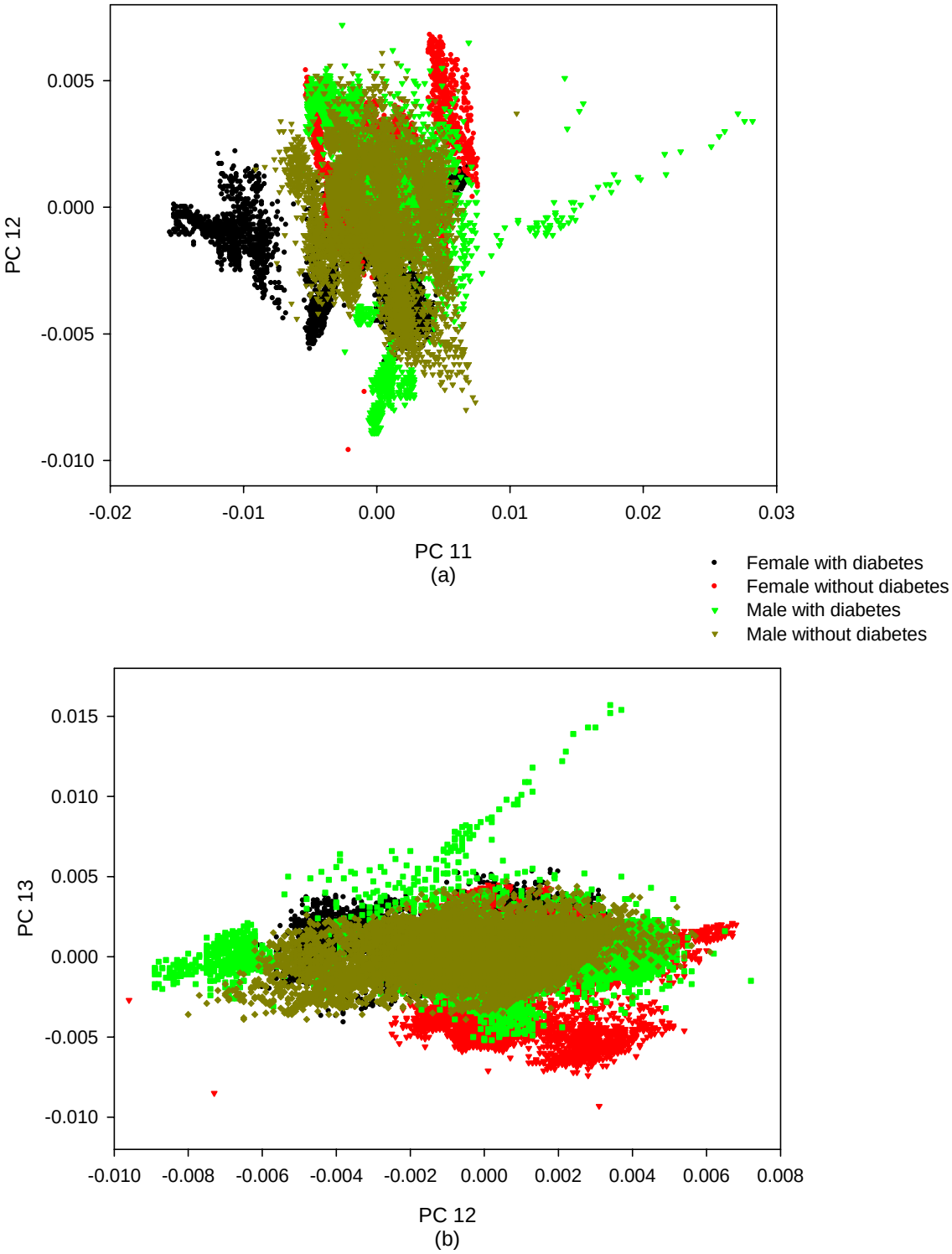

Figure IV-13. Principal component plots showing (a) PC 11 vs. PC 12 and (b) PC 12 vs. PC 13.

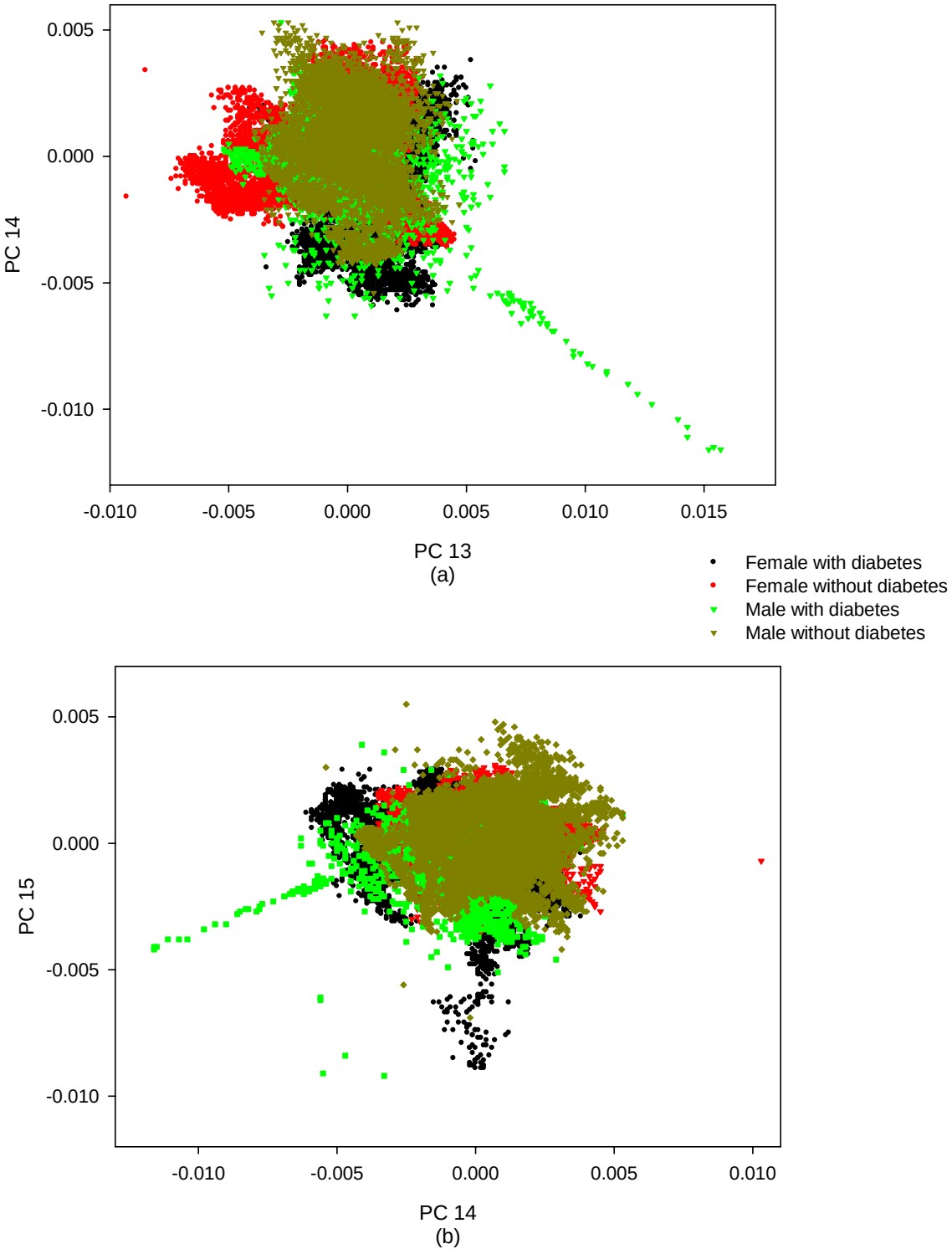

Figure IV-14. Principal component plots showing (a) PC 13 vs. PC 14 and (b) PC 14 vs. PC 15.

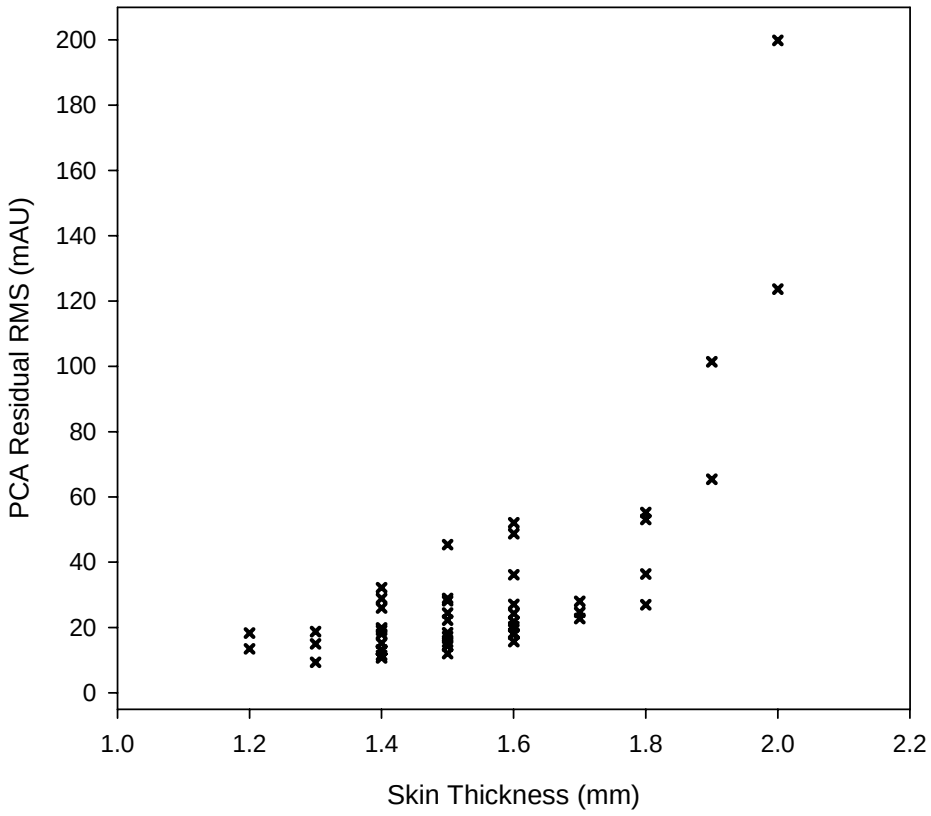

Figure IV-15. Plot of skin thickness vs. PCA residual RMS noise.

was correlated with the skin color values measured before the 90 minutes spectral collection, and the last skin spectrum was plotted versus the L*, a*, and b* values from the second skin color measurement. PC scores from previous PCA analysis were used to represent spectra. The results were shown in Figures IV-16, 17, 18, 19, 20, and 21. Randomly distributed dots in these plots demonstrate that there is not a significant correlation between NIR spectra and skin color. First order polynomial fits were applied to these plots and the corresponding R^2 values were summarized in Table IV-2. The highest R^2 value among these correlations is only 0.19, which means no significant correlation was found between spectra and skin color. These results illustrate that the NIR skin spectra were not affected by the skin color variations. Thus, we can conclude from this skin color study that this noninvasive glucose sensing based on NIR spectroscopy, specifically 5000-4000 cm^{-1}, has potential to be applied on a variety of people with different skin colors.

Glucose Concentration Profiles

During the 90 minute experiment, 4 blood glucose readings were recorded. The participants were required to fast overnight prior to the study, so that glucose fluctuations were minimal. The averaged glucose concentrations of each individual and standard deviations were summarized in Figure IV-22 (a) and (b) for subjects with and without diabetes, respectively. People without diabetes had lower blood glucose concentrations within the range of 4 to 7 mM, while glucose levels of the diabetes group varied from 5 to 21 mM. In addition, the corresponding standard deviations of diabetes group are larger than those of the non-diabetes group. From these two plots, we can see that, with food restriction for over ten hours, most of people without diabetes could maintain nearly constant blood glucose levels, and these glucose levels did not vary much between subjects. For people with diabetes, the blood glucose levels were much higher than the normal range, and there were more fluctuations during the 90 minute data collection

period.

Glucose HLA and NAS Models

PLS could not be used to analyze these human subject data because glucose variations are minimal. For this reason, NAS and HLA method were evaluated. To make the best use of all the spectra collected, the entire data set of each subject was used for calibration purpose. Tables IV-3 and 4 summarize the SEC values of each individual by both HLA and NAS calibrations with the optimal number of latent variables, respectively, and the maximum glucose changes calculated from the four blood reference measurements. Seven to twelve latent variables are used to establish these calibration models. The SEC values vary from 0.5 to 2.7 mM. Figures IV- 23 (a) and (b) show the corresponding glucose NAS and HLA calibration vectors, respectively. The dark blue lines presented in each plot indicate the pure glucose absorptivity spectrum. These vectors have similar shapes both among individual data sets and between the two different algorithms. However, there are still subtle differences among individuals, which originate from different skin absorbance backgrounds. For all of these vectors, major peaks are observed at 4700, 4400, and 4300 cm^{-1} which match glucose absorption features. These peaks indicate that all of the glucose models based on NAS and HLA are selective for glucose. No significant noise was found in these vectors, which indicates little chance of overfitting.

SEC values from NAS and HLA models are compared in Figure IV-24. The slope indicates where these SEC values from NAS and HLA are identical. A good correlation was found between these SEC values, which means the results from these two methods are similar. The NAS method is based on the assumption that the baseline glucose concentration is constant. However, as shown in Tables IV-3 and 4, the maximum glucose change varies from 0.2 to 12.7 mM. Certain data sets with high glucose fluctuations may have negative impact on glucose prediction. While in theory, the HLA

algorithm is not affected by this type of glucose fluctuations. To explore whether HLA is superior to NAS for the data sets with large glucose variance, human subjects baseline data sets were divided into four groups: 1) glucose change is less than 0.5 mM; 2) glucose change is between 0.5 and 1.0 mM; 3) glucose change is between 1.0 and 2.0 mM; 4) glucose change is over 2.0 mM. The corresponding HLA results vs. NAS results are shown in Figure IV-24. From this plot we can see that most SEC values of the first group stay below 1.0 mM. This indicates that minimal glucose baseline variance can lead to better performance of these multivariate models.

However, the HLA results in the other three groups with larger glucose variance do not demonstrate significant improvement. This result indicates that glucose variance is not the dominant spectral variance so that only subtraction of glucose features from the data set cannot effectively enhance the glucose prediction ability. The noise level is one possibility. Therefore, the SEC values from both NAS and HLA calibration models were further compared with PCA residual RMS levels obtained in the previous section. The correlations were shown in Figure IV-25. In this plot, we can see that data sets with high PCA residual RMS noise (over 100 μAU) also have high SEC values. This means the noise level is a major factor impacting glucose prediction. From Figure IV-25 we concluded that the RMS noise heavily affects model performance and the RMS noise level depends on thickness of the skin sample. For several samples with RMS noise levels below 100 μAU, certain data sets still have high SEC values, which means RMS noise is not the only factor affecting the glucose prediction ability. Due to the heterogeneity of the skin tissue, any small movement or clamp repositioning would have significant impact on skin components exposed to the NIR radiation.[97] This would further affect the NIR collected spectra and glucose calibration models.

In all of these 47 data sets, certain glucose models built by the NAS and HLA methods have good glucose prediction ability with SEC values lower than 1.0 mM, while SEC values in other data sets are too high. It could be due to several reasons: low *S/N* due

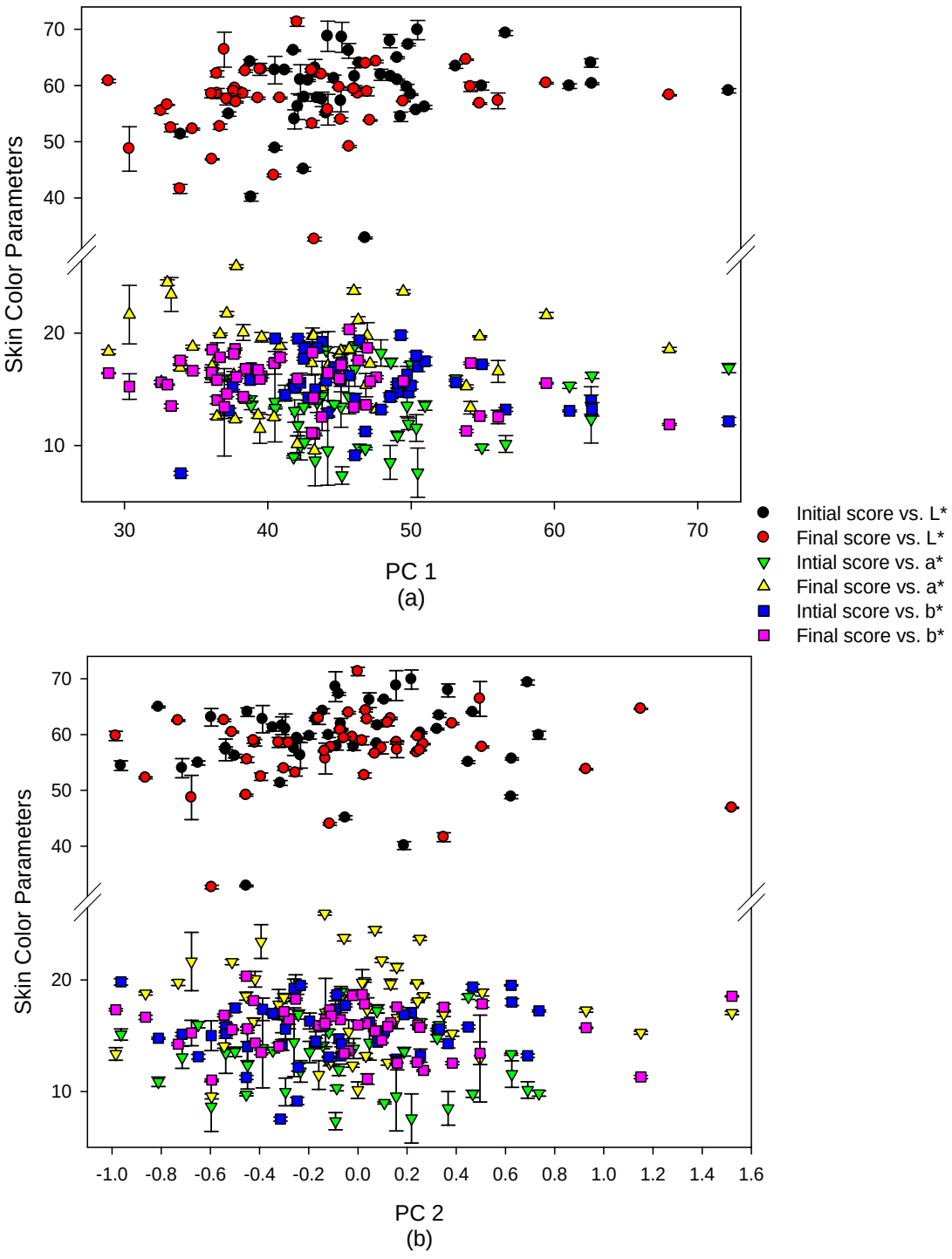

Figure IV-16. Plots of (a) PC 1 and (b) PC 2 vs. skin color parameters (L*, a* and b*).

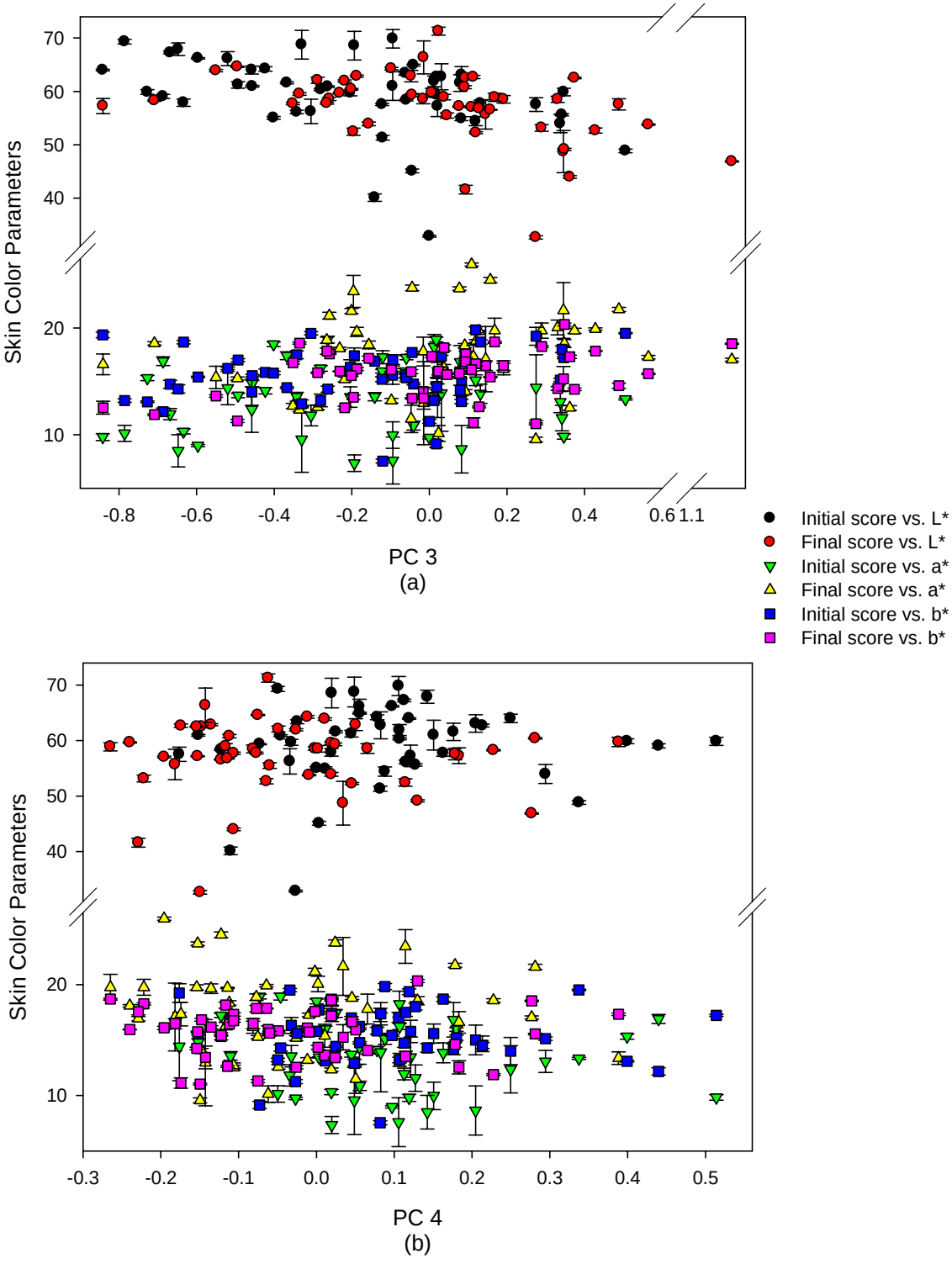

Figure IV-17. Plots of (a) PC 3 and (b) PC 4 vs. skin color parameters (L*, a* and b*).

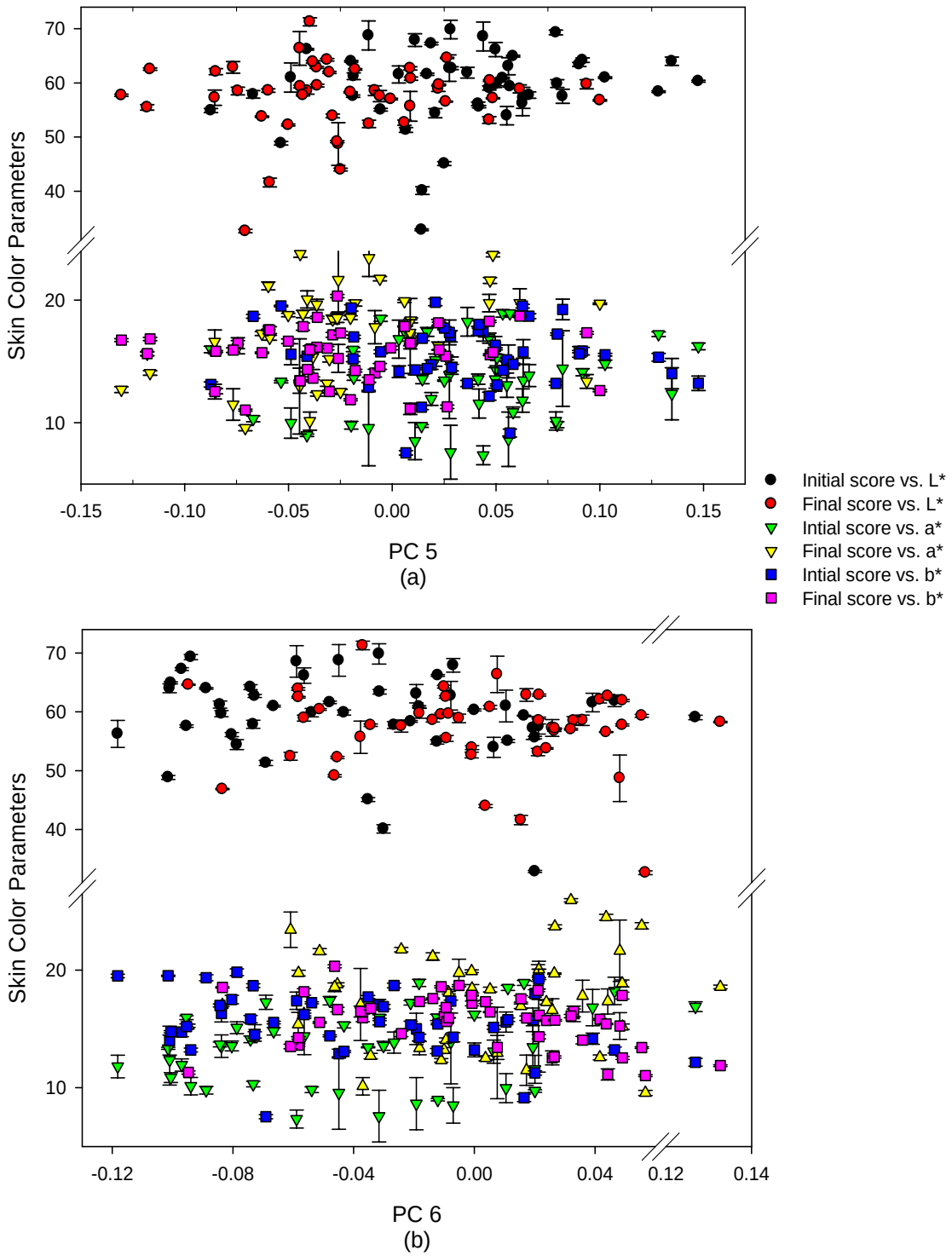

Figure IV-18. Plots of (a) PC 5 and (b) PC 6 vs. skin color parameters (L*, a* and b*).

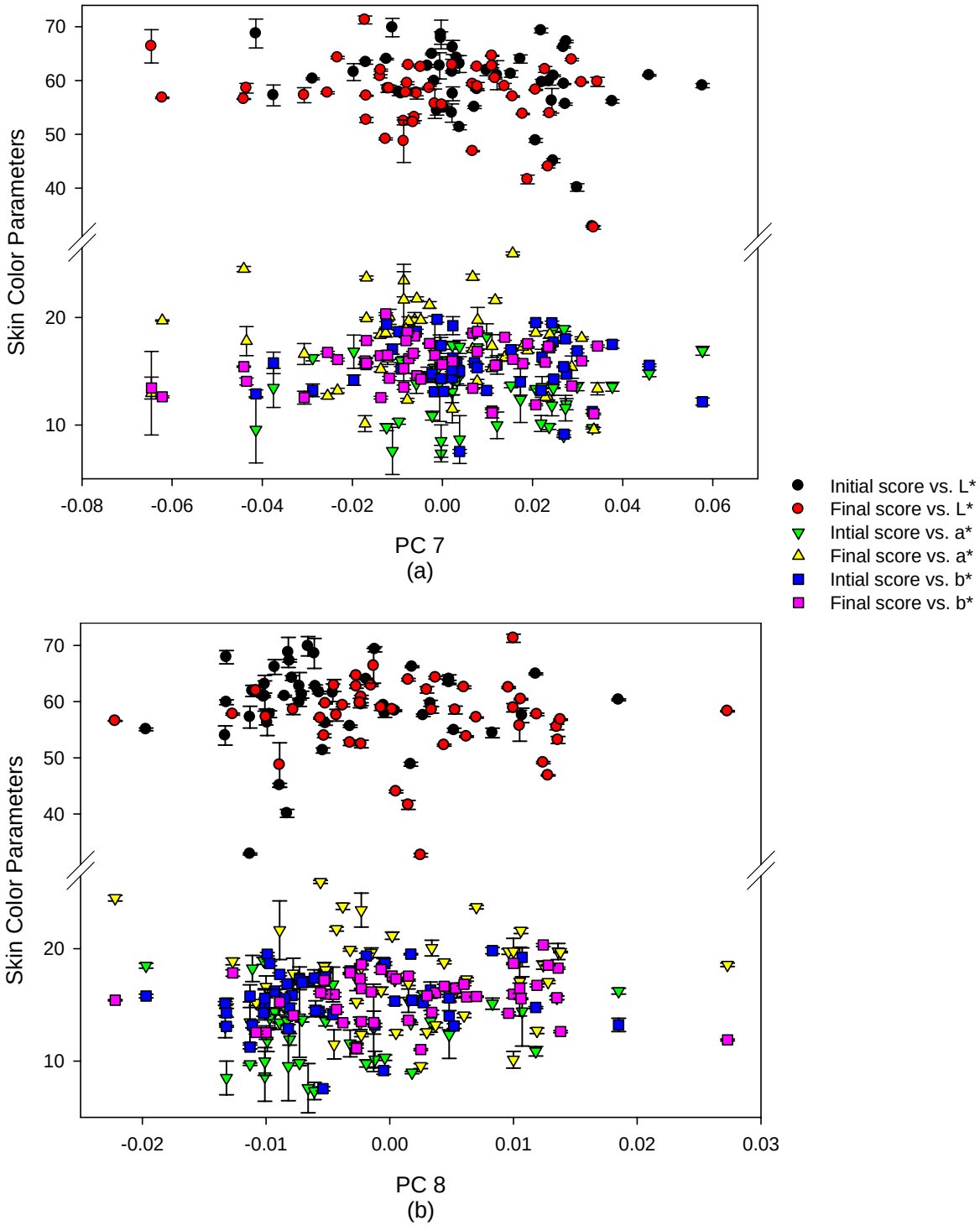

Figure IV-19. Plots of (a) PC 7 and (b) PC 8 vs. skin color parameters (L*, a* and b*).

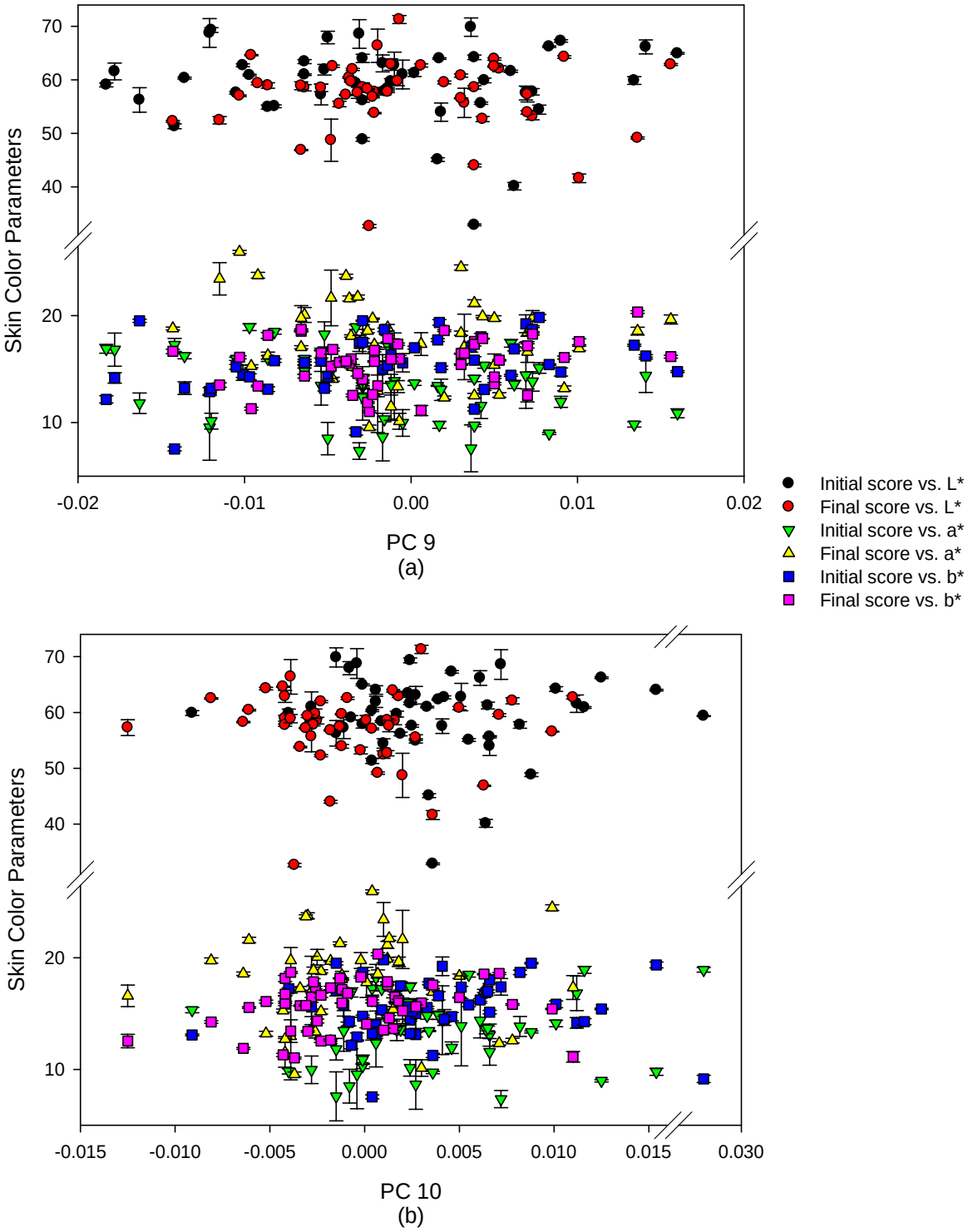

Figure IV-20. Plots of (a) PC 9 and (b) PC 10 vs. skin color parameters (L*, a* and b*).

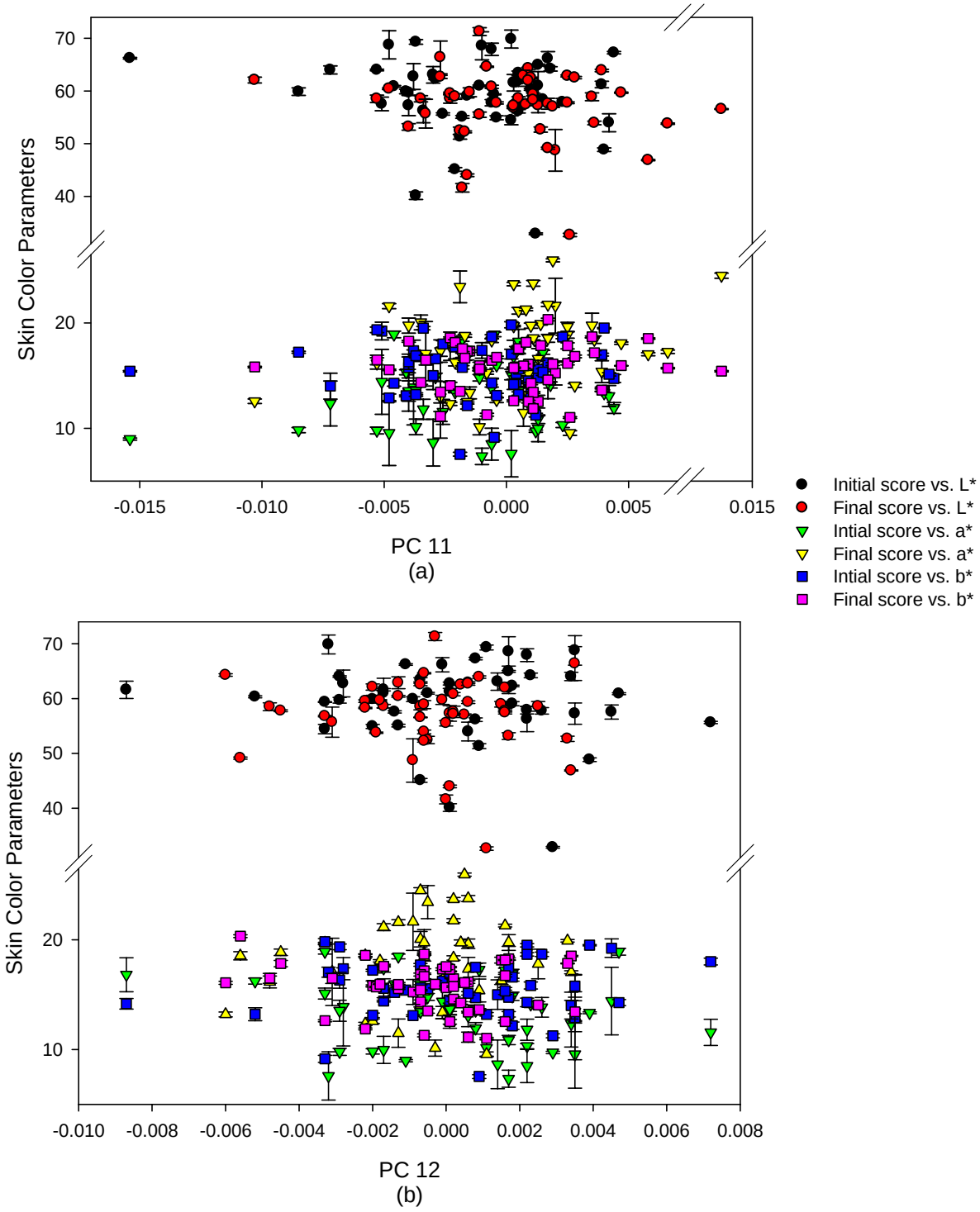

Figure IV-21. Plots of (a) PC 11 and (b) PC 12 vs. skin color parameters (L*, a* and b*).

Table IV-2. Correlations between PCs (1 to 12) and skin color parameters (L*, a* and b*) by R^2 values.

PC	L*		a*		b*	
	Initial	Final	Initial	Final	Initial	Final
1	0.06146	0.03397	0.00036	0.00009	0.02281	0.09617
2	0.02762	0.00837	0.02020	0.00049	0.02115	0.01150
3	0.16180	0.18509	0.01295	0.02183	0.02563	0.11409
4	0.01011	0.00003	0.01894	0.00002	0.00097	0.00168
5	0.02840	0.02233	0.02779	0.14794	0.00676	0.03503
6	0.02647	0.01304	0.07142	0.11937	0.095673	0.09259
7	0.09763	0.06458	0.00350	0.02030	0.001422	0.01031
8	0.03042	0.03195	0.03027	0.02480	0.09165	0.01251
9	0.01034	0.00093	0.01023	0.03206	0.13938	0.06544
10	0.00038	0.00247	0.03681	0.00345	0.00051	0.03773
11	0.01756	0.02296	0.04547	0.07583	0.00059	0.00067
12	0.01282	0.00577	0.03515	0.00078	0.01083	0.02340

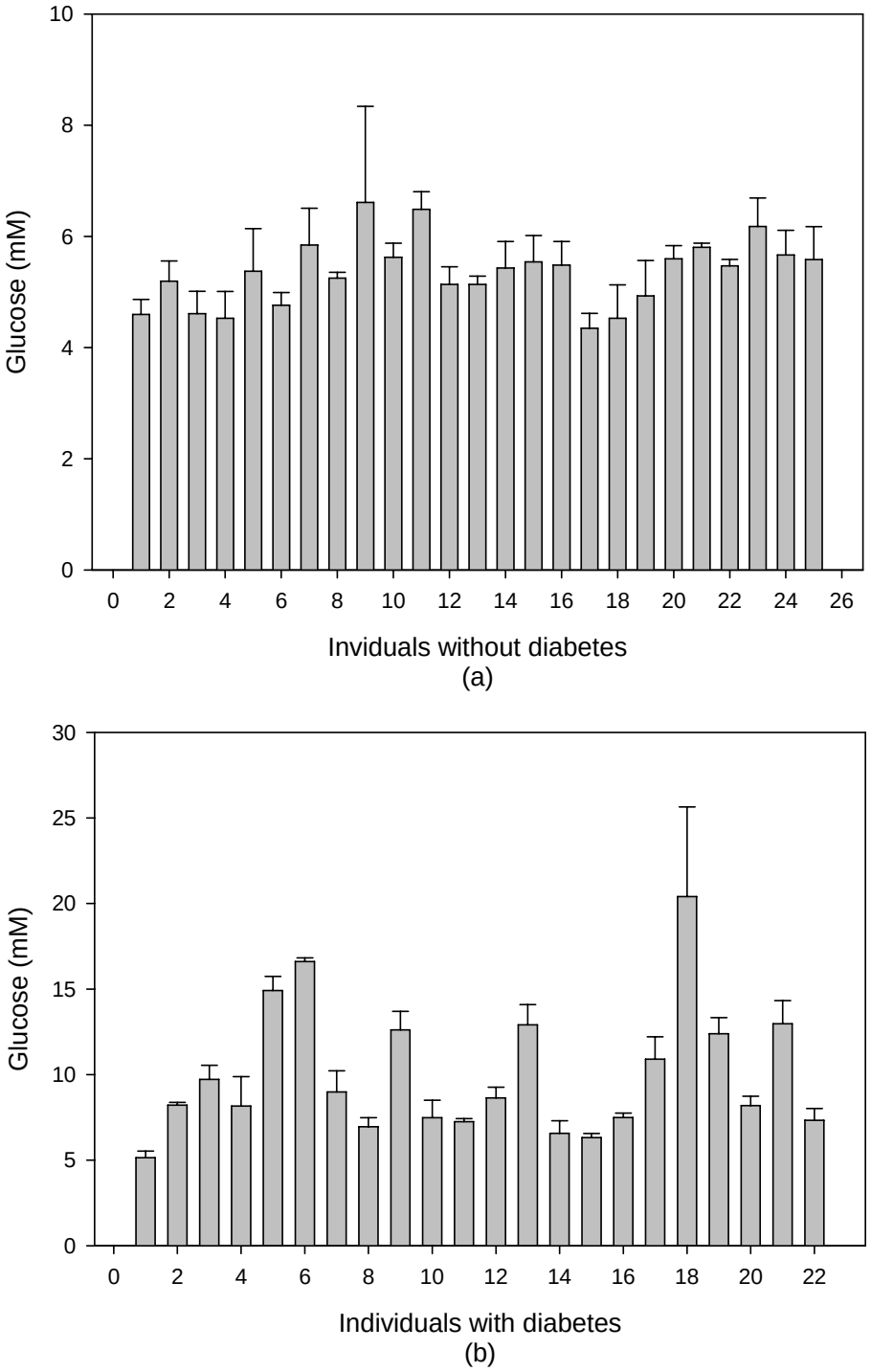

Figure IV-22. Averaged glucose levels and standard deviations of individuals (a) with diabetes and (b) without diabetes.

Table IV-3. NAS and HLA calibration results of subjects without diabetes.

NAS		HLA		Max Blood Glucose Change (mM)
Latent variables	SEC (mM)	Latent variables	SEC (mM)	
9	0.6	9	0.6	0.6
10	1.2	11	1.0	0.8
10	0.9	10	0.8	0.9
10	0.6	10	0.7	1.1
9	0.4	9	0.7	1.7
8	0.9	8	0.9	0.5
11	1.1	10	1.0	1.6
11	0.7	11	0.6	0.2
10	1.3	10	1.5	4.1
9	2.4	11	2.1	0.6
9	1.9	9	1.7	0.7
10	0.5	10	0.6	0.7
10	0.8	10	0.7	0.3
9	1.2	9	1.1	1.2
9	1.5	12	1.1	1.1
12	1.2	12	1.1	0.9
10	0.5	8	0.7	0.6
8	0.7	8	0.7	1.3
9	0.5	9	0.6	1.5
10	1.4	11	2.6	0.6
12	2.6	12	2.7	0.2
10	0.6	10	0.6	0.3
8	2.0	8	1.8	1.1
10	1.6	10	1.5	1.1
8	0.5	7	1.1	1.2

Table IV-4. NAS and HLA calibration results of subjects with diabetes.

NAS		HLA		Max Blood Glucose Change (mM)
Latent variables	SEC (mM)	Latent variables	SEC (mM)	
10	0.8	10	0.7	0.8
12	0.6	11	1.1	0.3
11	0.5	10	0.8	1.9
9	1.4	11	1.6	3.9
10	0.7	9	1.1	1.9
10	1.5	10	1.8	0.5
11	0.4	11	0.8	2.7
10	1.2	12	1.2	1.2
11	0.5	10	0.9	2.6
11	0.8	10	1.0	2.3
10	0.5	10	0.5	0.4
11	0.6	10	0.8	1.2
12	0.7	8	1.2	2.8
12	1.1	11	1.5	1.5
9	0.8	9	0.9	0.4
12	1.7	12	1.9	0.6
8	1.3	8	1.2	2.9
12	0.6	11	0.8	12.7
9	1.2	8	1.2	2.3
10	0.8	10	0.7	1.3
8	0.9	8	0.9	3.2
10	0.8	8	0.9	1.5

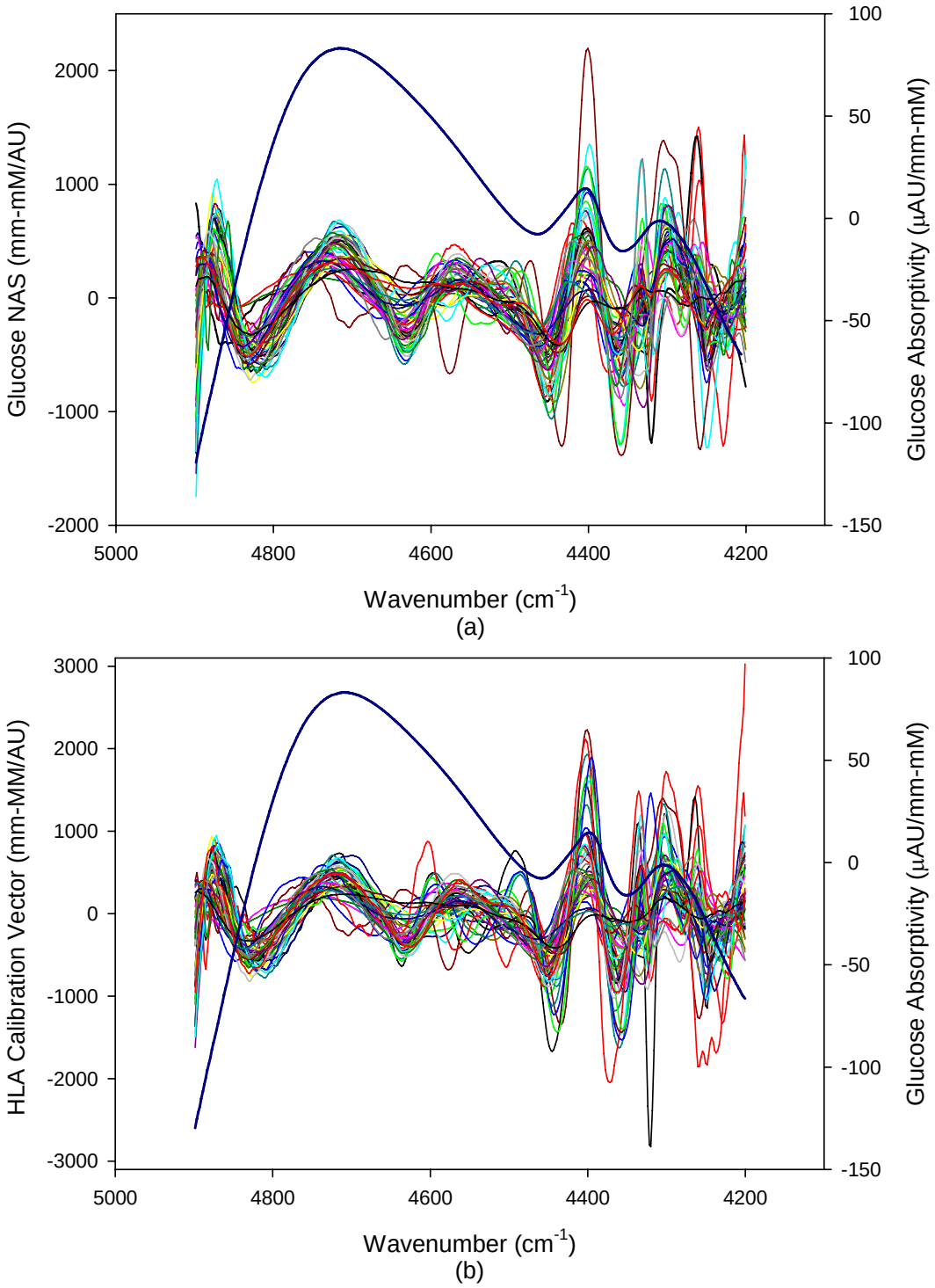

Figure IV-23. Glucose (a) NAS and (b) HLA calibration vectors obtained from 47 human baseline datasets compared with pure glucose absorptivity spectrum (dark blue line).

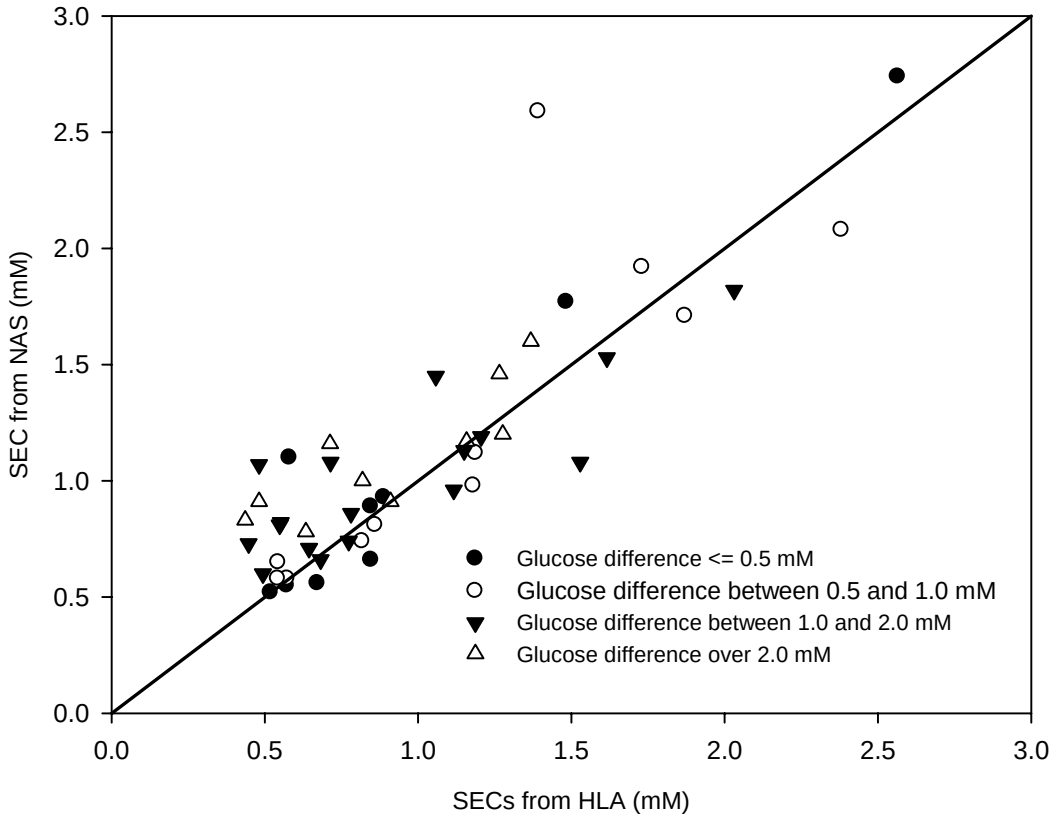

Figure IV-24. Comparison of SEC values from HLA and NAS calibrations.

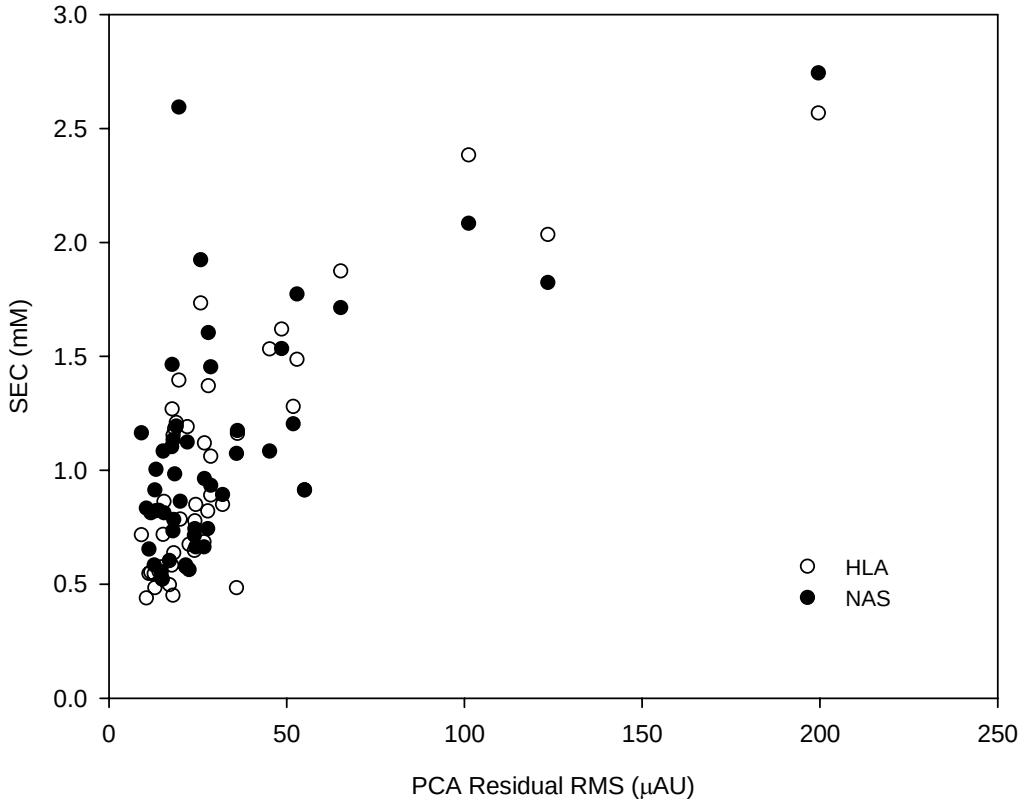

Figure IV-25. Correlation between PCA residual RMS noise and SEC values of NAS and HLA calibration models.

to thick skin, random movements, reclamping after slipping and so on. Future studies must focused on *S/N* enhancement by increasing light power density and detector area, as well as more advanced interface to effectively stabilize the skin tissue. With higher optical throughput, the instrument will be able to accommodate a larger range of skin tissue thicknesses while maintaining low RMS noise levels. A more sophisticated skin tissue interface is also needed not only to restrain the skin tissue without movement, but also to monitor and regulate skin temperature, humidity, and pressure. The current version of the sapphire rod interface can only read the skin thickness which may not correlate well with the aqueous path length. In addition, the clamp must maintain a tight on the skin tissue position in a comfortable manner. In the future design of the optical interface, the clamp must be coupled to the surface of skin tissue in a more efficient and comfortable way to enhance the optical throughput and make patients more comfortable. Moreover, sensors, transducers, and control modules which are capable of monitoring and regulating skin temperature, humidity, and pressure will also be considered for better spectral quality. A preliminary temperature control unit was designed and coupled to the current optical interfaces and is discussed in more detail in Chapter VI.

Conclusions

The ability to measure glucose noninvasively in human subjects is a long term goal of our research group. A unique spectral signature has been identified from near-infrared (NIR) spectra collected across living animal tissue. Before the application of this noninvasive NIR technology on people with diabetes, the impact of skin difference was investigated. Significant skin color changes before and after the spectral collections were discovered. For a majority of the participants, the skin tissue being studied turned darker and redder after the 90 minutes clamp study. However, no significant correlation was found between the NIR skin spectra and skin color parameters (L*, a*, and b*). This result is experimental evidence that the skin color variance in the visible range of the

spectrum has no impact on the NIR spectra of skin tissue. Therefore, the noninvasive NIR spectroscopy can be applied to people with different skin colors for the purpose of glucose sensing.

Spectra from males, females, and people with and without diabetes were also compared by PCA analysis. Adjacent PCs were plotted up to 15 PCs which represent up to 99.999% of the recorded spectral variances. The overlapped PC scores distributions demonstrate that there was not a significant spectroscopic difference among these groups. This result further supports that NIR spectroscopy can benefit different populations of people for noninvasive glucose sensing, regardless of gender, age or diabetes.

Glucose prediction was performed by both NAS and HLA calibration methods. The prediction results demonstrate that it is feasible to build NAS and HLA glucose models for noninvasive NIR glucose prediction. Similar predictions and calibration vectors were obtained from these two different algorithms. Models based on both the NAS and HLA methods are selective for glucose since calibration vectors from both methods have major peak positions that coinside with pure glucose absorptivity spectrum features. There are still certain data sets with poor glucose prediction performance, which correspond to high RMS noise and low *S/N*. Other possibilities could be the limitations of the instrumentation and the skin clamp interface. Thus, more effort is needed to enhance the instrumental performance and develop a more robust interface for noninvasive glucose sensing.

CHAPTER V

IN VIVO NEAR-INFRARED SPECTROSCOPY OF RAT SKIN TISSUE WITH VARYING BLOOD LACTATE AND UREA LEVELS

Introduction

Near-infrared (NIR) spectroscopy, especially Fourier transform infrared (FT-IR) spectroscopy, has been extensively studied for optical sensing due to the advantages of high spectral resolution, excellent reproducibility and good signal-to-noise ratios.[101, 102] Clinical applications center on glucose sensing for diabetes.[76, 77] Besides glucose, other biomolecules such as lactate and urea are of clinical significance. Efforts to measure lactate and urea noninvasively are described in this chapter

Lactate is a reduction product of pyruvate formed by the action of lactate dehydrogenase (LDH) at the end of glycolysis (see Equation V-1). During intensive physical activity, lactate accumulates as a "waste" product and degrades athletic performance.[103] Lactate is also a key clinical marker in the intensive care.[104, 105] Unfortuantely, existing lactate monitoring devices are intermittent and invasive which reduces their impact for clinical care.[105] Therefore, it is desirable to develop an *in vivo*, noninvasive, and continuous lactate sensor to monitor clinical concentrations of lactate in human subjects.

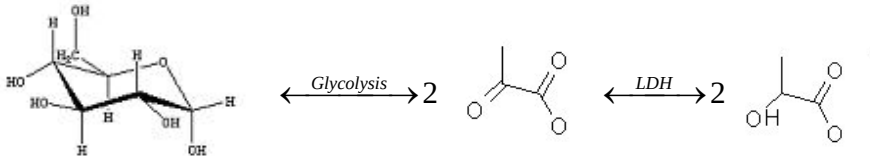

D-glucose Pyruvate Lactate

Equation V-1

A lactate clamp procedure was designed with an animal model, and NIR spectra were collected on the neck skin of the rat as lactate concentrations were varied in the blood. Similar to our glucose study, a lactate PLS calibration model was established to

correlate changes in the concentration of lactate with noninvasive NIR skin spectra. To evaluate the selectivity of this PLS model, the net analyte signal (NAS) calibration was then processed based on arterial blood lactate readings to investigate whether lactate absorption features can be extracted from the *in vivo* rat's skin spectra. An alternative hybrid linear analysis (HLA) algorithm was also applied to extract the lactate calibration vector that is orthogonal to the calculated background. The calibration vectors from these three models were compared later.

Urea is a clinically important molecule. It is a waste product that is normally excreted in the urine for healthy people. For people with renal dysfunction, however, this accumulation can cause uremia and dialysis is necessary to remove excess toxins. Blood urea concentrations are commonly used as an indicator of blood toxicity before and during the hemodialysis process. A need exists to monitor the dialysis treatment by following the removal of urea in order to maximize the efficiency of the dialysis process. Several approaches have been proposed for urea monitoring based on the enzymatic reaction with immobilized urease, which catalytically converts urea to ammonium and bicarbonate ions. These approaches require active enzyme as the consumable reagent, which increases the total cost of the treatment and adds maintenance procedures. NIR spectroscopy provides an alternative approach for urea sensing.[80, 106, 107] As described above, a similar experimental procedure has been carried out to evaluate the potential of monitoring urea noninvasively for hemodialysis optimization.

To explore if the absorption features of glucose, lactate, and urea are distinctive in the combination region of the NIR spectrum (5000-4000 cm^{-1}), absorptivities of these three molecules are compared in Figure V-1. Glucose demonstrates absorption features of C-H stretching and C-H bending combination at 4300 and 4400 cm^{-1}, and O-H stretching and C-H bending combinations at 4750 cm^{-1}.[106] The C-H stretching and C-H bending combinations for lactate shifts to 4350 and 4425 cm^{-1}, and the corresponding peak of O-H stretching and C-H bending combination is much smaller in magnitude compared to

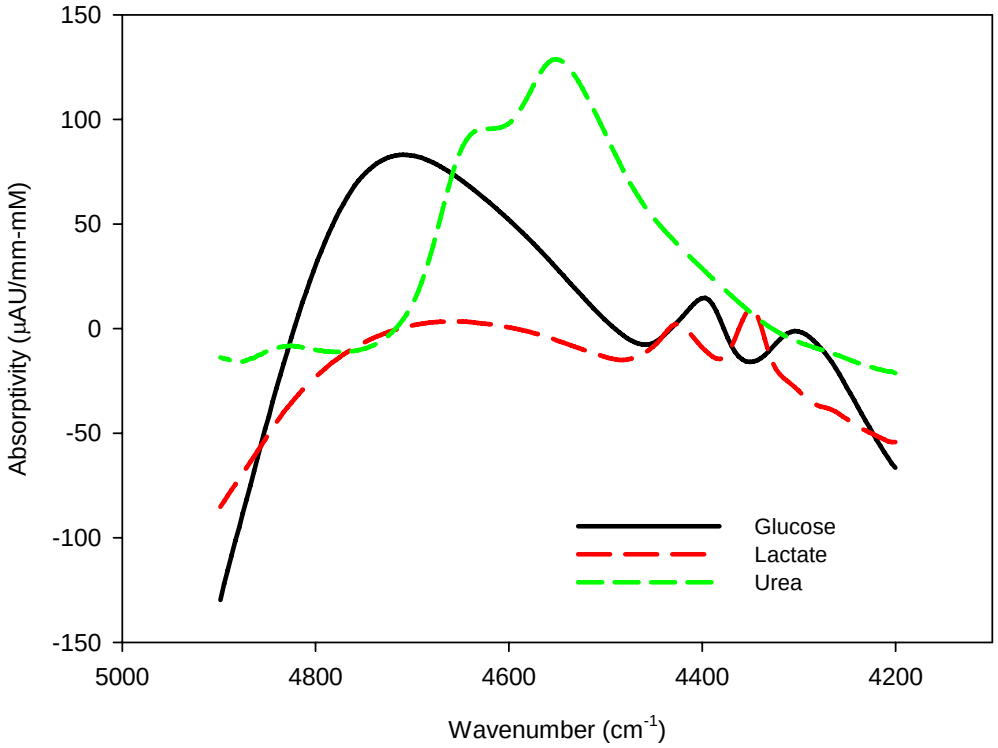

Figure V-1. Comparison of glucose, lactate, and urea absorptivities in the combination region.

glucose due to a fewer number of O-H bonds per molecule (1 versus 6). Urea shows totally different features in this NIR combination region. Peaks at 4650 and 4550 cm^{-1} correspond to the combination of the symmetric (~3350 cm^{-1}) and asymmetric (3450 cm^{-1}) N-H stretching modes coupled with the N-H bending vibration (~1640-1600 cm^{-1}).[106] From this comparison, we can see that the degree of spectral overlap is higher between glucose and lactate, while urea has more distinctive features due to the lack of C-H and O-H bonds.

Experimental Section

Instrumentation

The same Nicolet 670 spectrometer (Nicolet Analytical Instruments, Wisconsin, MI) described in Chapter II and III was used in these experiments. Light source, detector, and pre-amplifier are the same. Two dynamax peristaltic pumps (Rainin Instrument Co., Wpburn, MA) were used to infuse solutions of lactate or urea and a saline solution. The experimental setup in a typical lactate or urea study is shown is Figure V-2 (a) and (b). The only difference from the instrumentation in Chapter II and III is the skin interface. An optical fiber with an internal diameter (id) of 1.8 mm (FiberGuide Industries Inc. Stirling, NJ) was used instead of sapphire rods. Each version of the optical interface has its own advantages and disadvantages. For the sapphire rods used in the glucose work, the rod material itself has no absorbance features throughout the NIR spectrum, thus it is an ideal material for NIR sensing. However, the interface made of sapphire rods lacks flexibility. For the ultimate goal of noninvasive sensing on human subjects, a small and flexible probe is desired. The silica based optical fiber is better suited for this purpose, nevertheless, this type of fiber contains a O-H absorption band which interferes with the target analytes, such as glucose, lactate and urea. This would further lower the magnitude of single beam spectra and decrease the S/N. A detailed picture of this type of interface is shown in Figures V-2 (c) and (d). Spectra were collected at 16 cm^{-1} (8 nm) spectral

resolution with 128 co-added interferograms which were Fourier transformed to single-beam spectra with triangular apodization, 1-level zero filling, and standard Mertz phase correction. It took about 60 seconds to collect each spectrum.

Animal preparation and surgical procedures are the same as those used in the previously described glucose experiments. Rats were fasted overnight to obtain constant lactate or urea baseline concentrations. Animal temperature was maintained at 37.8 °C using a closed-loop temperature controller R/S 68900-11 (Barnant Company, Port Huron, MI) interfaced with a heating pad. A pulse-oximetry probe from SurgiVet Pawprint, Inc. (Waukesha, WI) was applied to monitor the pulse rate and blood oxygen saturation during the procedure.

Lactate Profile

A lactate clamp was performed on an adult male Sprague-Dawley rat (retired breeders, weighting ~ 400 g). The lactate clamp procedure was carried out by pumping 4 mol/L sodium lactate solution into the vein of the rat at 2ml/hr. Saline was also infused to compensate for body dehydration during the course of the experiment. Blood samples were collected from an arterial cannula with 15- 30 minute intervals. The YSI 2300 STAT Plus glucose and lactate analyzer (YSI Incorporated Life Sciences, Yellow Springs, Ohio) was used to measure the lactate levels in the blood samples. The corresponding lactate profile is shown in Figure V-3 (a). Because a larger volume of blood is required for each lactate measurement compared to previous glucose measurement, the time interval between each lactate reference measurement is longer compared to that of the glucose experiments.

Urea Profile

A urea clamp was performed in the same manner as described above for lactate in terms of animal preparation, instrumentation, and experimental procedure. After the canulation surgery, noninvasive NIR spectra were collected continuously during the urea

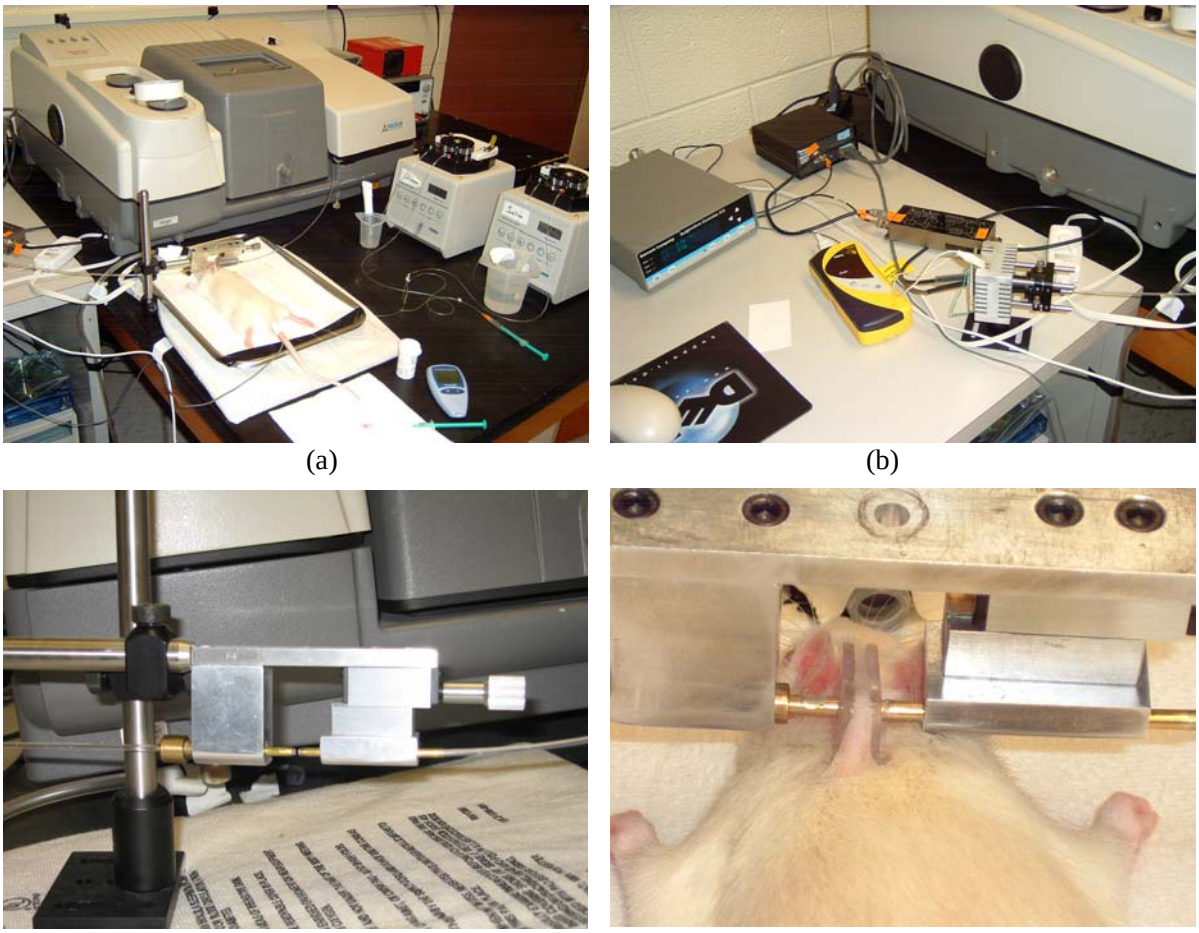

(a) (b)

(c) (d)

Figure V-2. Experimental setup of animal lactate and urea experimentshowing (a) an overview of the instrumentation and lactate and urea clamp control pump system; (b) the customized external InGaAs detector with the preamplifier; (c) the close-up view of the optical fiber interface for holding the skin tissue; and (d) an anesthetized rat being clamped during a typical animal study.

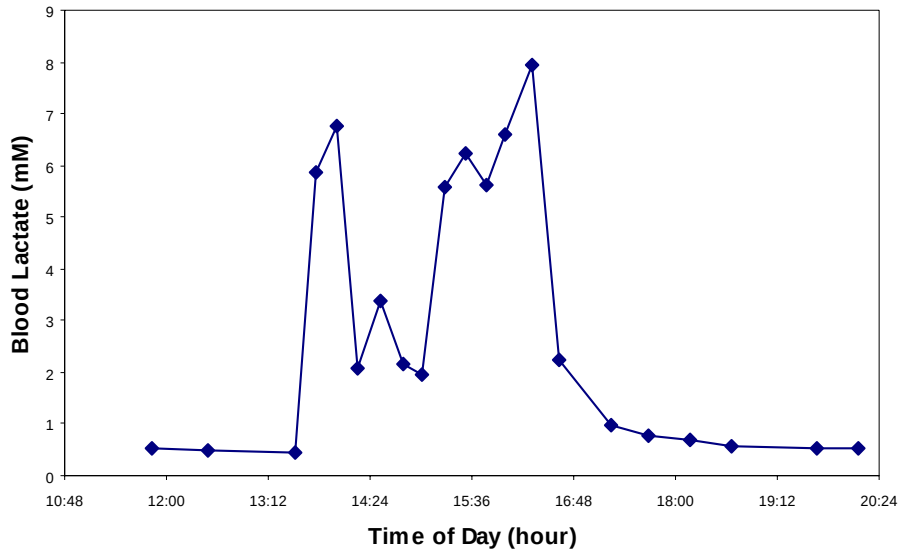

(a)

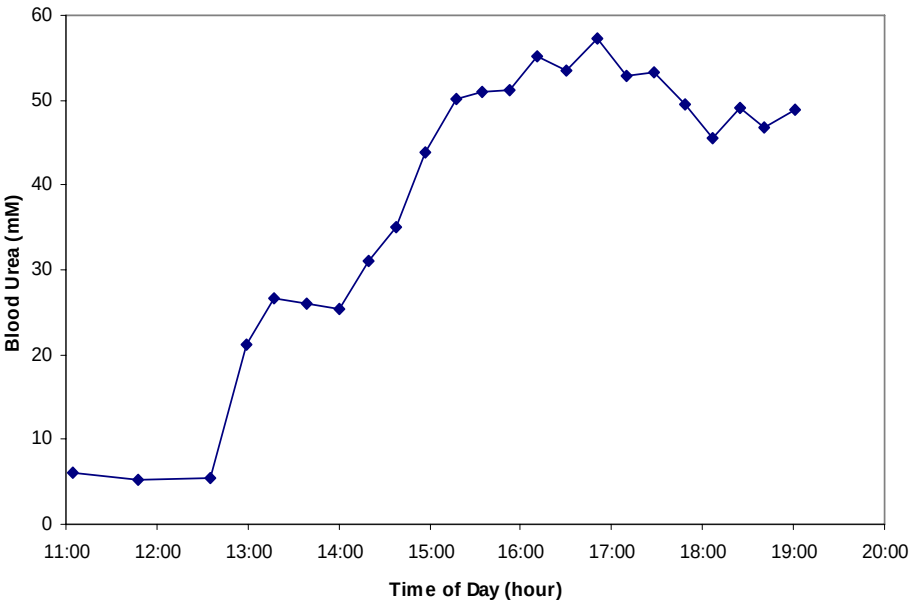

(b)

Figure V-3. Animal model conentration profiles for (a) lactate and (b) urea where points indicate reference values.

baseline and transient periods. During the spectral collection, 0.9% saline was infused at 2 ml/h to compensate for dehydration. A 4 M urea solution prepared in PBS saline (urea purchased from Sigma-Aldrich) was infused into the venous catheter as needed. Arterial blood samples were collected every 15 to 30 minutes to provide reference urea concentrations. Again longer time intervals are needed to minimize blood depletion. Arterial urea concentrations were obtained by using a Stat Fax 3300 chemistry analyzer (Global Medical Instrumentation, Inc. Rarnsey, MN). The corresponding urea profile is shown in Figure V-3 (b).

Results and Discussion

For both lactate and urea, the collected *in vivo* single beam spectra were referenced to 1 mm air spectra collected before and after the clamp procedure to calculate the skin absorbance spectra. The six-component estimation procedure described in Chapter II was used to analyze the skin absorbance spectra. The estimated regression coefficients for water were used as the aqueous path length in building all calibration models. No lag time was adjusted on the lactate or urea reference concentrations, because no significant delay in the predicted concentrations is observed.

Since water absorbance is high, any lactate or urea associated with water fluctuations can result in correlations between spectra and water fluctuation in the calibration model. To minimize the chance of this correlation, the product of lactate or urea concentration times the corresponding estimated aqueous path length mentioned above was calculated. The PLS, HLA, and NAS models were built between the absorbance spectra and this product term. The predicted values of this term from different calibration models were divided by the same estimated aqueous path length to obtain the predicted lactate or urea concentrations. The standard error of calibration (SEC) and standard error of prediction (SEP) values were calculated to evaluate the performances of the different models. Details of the procedure are presented in Chapter II.

For lactate, the blood lactate concentration was maintained at 0.47 and 0.55 mM for the first and second baselines, respectively. Blood lactate concentrations reached 8 mM during the clamp period. 553 skin spectra were collected during the entire experiment. For PLS and HLA models, 470 randomly selected spectra were used as the calibration data set, and the remaining 83 spectra were used for prediction. In the NAS procedure, 268 spectra from two baseline periods (before and after the lactate clamp) were used as background to calculate the lactate NAS calibration vector, and the 285 spectra during the lactate transient were used for prediction. The mean of the baseline spectra was subtracted from the whole spectral matrix. The collected pure lactate spectrum was projected onto this mean subtracted baseline. The orthogonal portion was taken as the NAS for lactate and the normalized lactate NAS was used as the lactate calibration vector. The calculation process is the same as that used for the glucose NAS model described in Chapter II.

The calibration and prediction results of PLS, HLA, and NAS are shown in Figures V-4 (a), (b), and (c), respectively. In all three models, the predicted lactate values follow the lactate reference transient. The corresponding results are summarized in Table V-1. Spectral range was optimized to be 4810-4200 cm^{-1}. With 10 to12 latent variables, these three lactate models result in SEC values around 1.0 to 1.5 mM and the SEP values are around 1.0 to 2.2 mM. Although the SEC and SEP values are relatively small, and the prediction trends follow the lactate transient, the fluctuation of predicted lactate concentrations are too high, which results in poor precision in these models. This fluctuation could be caused by instability of the instrumentation, which tracked too much environmental variances.

Figure V-5 provides the comparison of the calibration vectors for the three calibration methods. Pure lactate absorptivity spectrum is superimposed on these calibration vectors for comparison. Each calibration vector displays peaks around 4300, 4400, and 4650 cm^{-1} all of which represent lactate absorptions. The magnitude of overlap

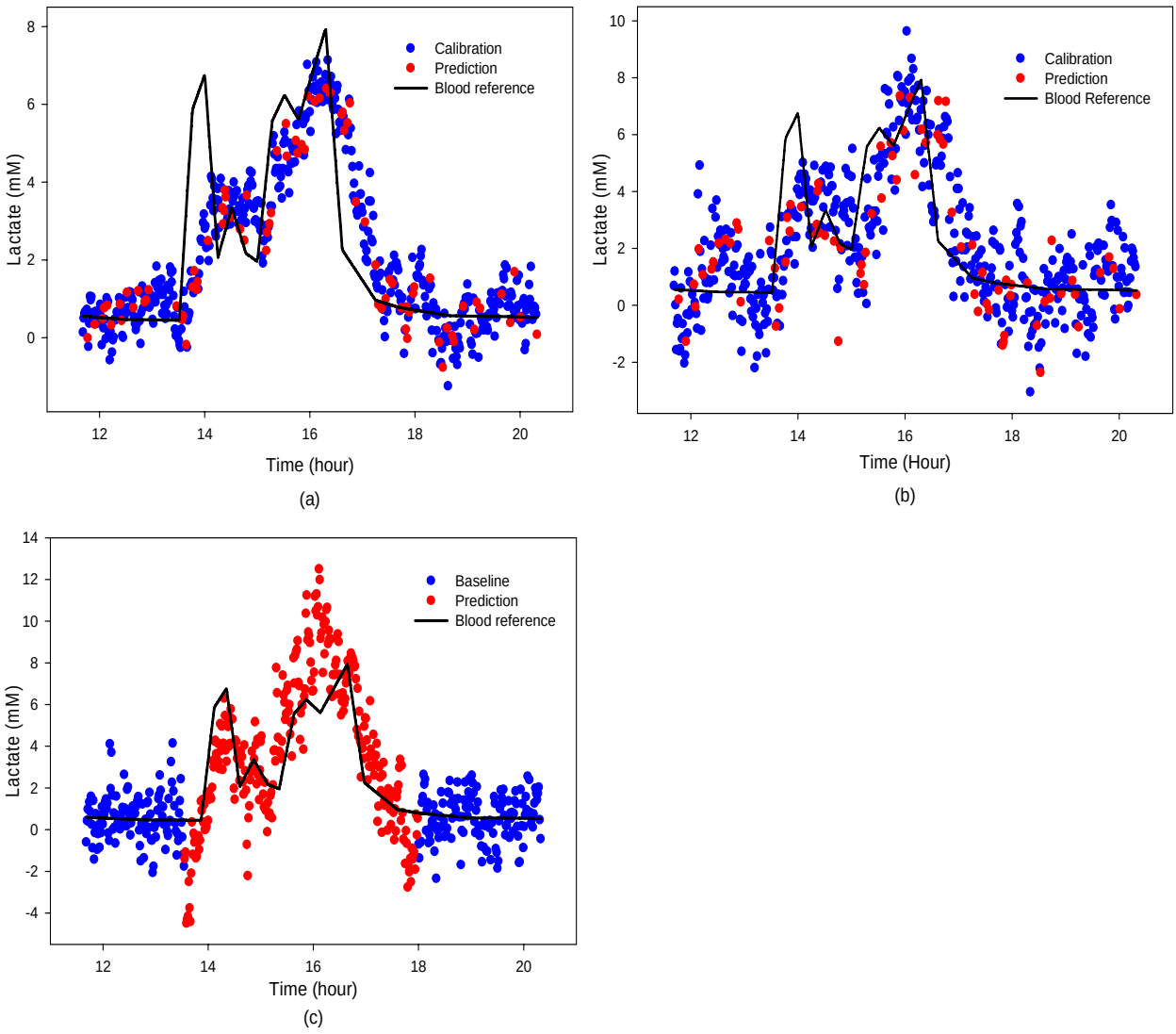

Figure V-4. Lactate (a) PLS, (b) HLA, and (c) NAS calibration and prediction results of animal models with lactate transients.

Table V-1. Summary of calibration and prediction results from lactate PLS, HLA, and NAS models.

	PLS	HLA	NAS
Spectral range (cm^{-1})	4810-4200		
Total number of spectra	553		
Spectra in calibration/baseline	470	470	268
Spectra in prediction	83	83	285
Latent variables	10	10	12
SEC (mM)	1.0	1.5	1.1
SEP (mM)	1.1	1.5	2.2

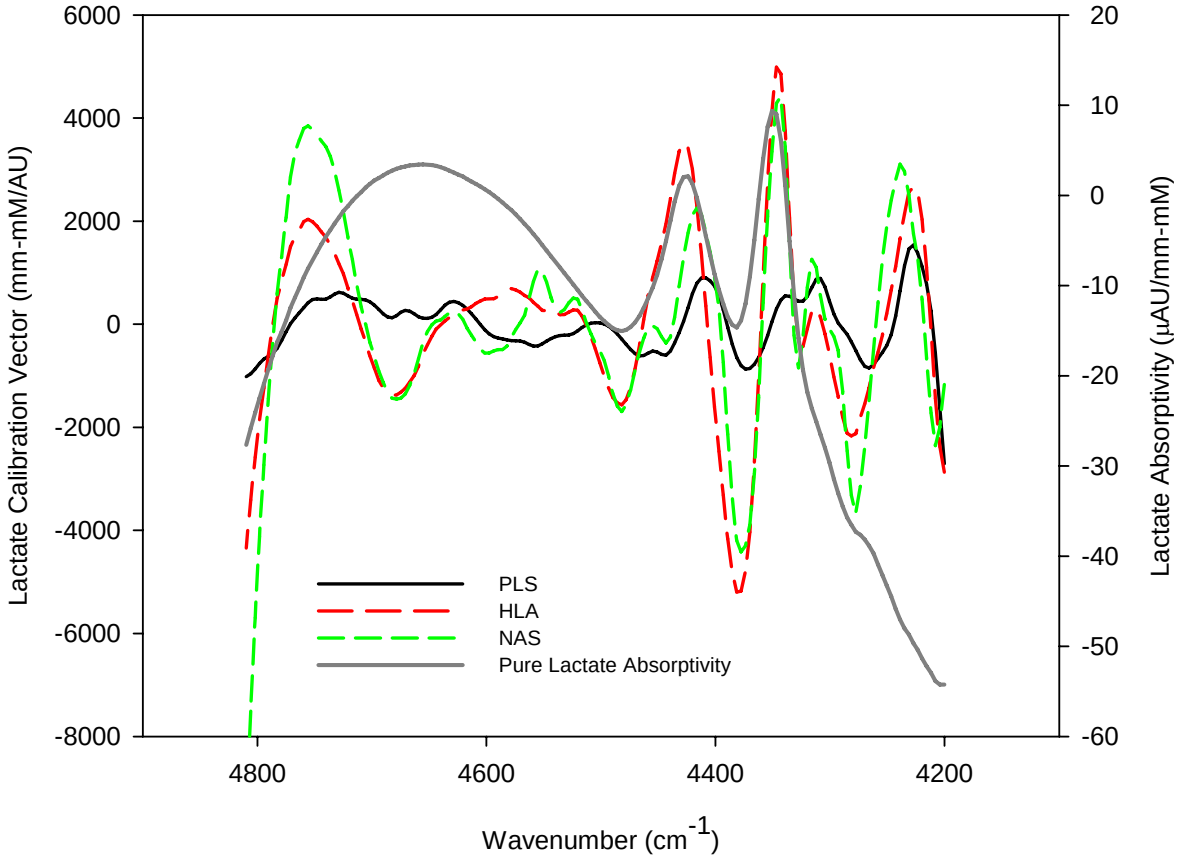

Figure V-5. Comparison of lactate calibration vectors (left axis) from PLS, HLA and NAS methods and pure lactate absorptivity spectrum (right axis).

between HLA and NAS vectors is greater than the overlap with the PLS vector. Since both NAS and HLA vectors are from the orthogonal part of pure lactate absorbance, both of them show the same selectivity for lactate. PLS vector has more subtle peaks and the major lactate absorption peaks are red shifted. Because PLS is a correlation based algorithm, results potentially suffer from matrix effects, which means the complexity of the matrix has a significant impact on the final results. In this lactate experiment, even though the SEC and SEP values from the PLS model are comparable to those from the HLA and NAS models, it does not mean that the PLS model can predict lactate concentrations with an equivalent selectivity. The shifted peaks in the PLS calibration vector could be affected by the fluctuation of other species, such as glucose for example.

All of the PLS, NAS, and HLA lactate models have equivalent calibration and prediction performances. Only the NAS and HLA calibration vectors demonstrate selectivity for lactate, while the PLS calibration vector has certain peak shifts due to matrix effects. It is questionable if the PLS model can selectively predict lactate. The results obtained above are preliminary and it is too early to conclude any NIR applications for *in vivo* lactate sensing. More experimental data are needed to expand this study.

For urea, blood urea levels varied from 5 to 60 mM. The blood urea level was maintained constant at ~5.5 mM for the first 1.8 hours. Then it was elevated to ~57 mM in the next 3.6 hours, and this level was maintained for another 2.8 hours. Unfortunately, the blood urea concentration was not able to decrease any further. Thus, only one baseline period, before the urea transient, was obtained. During the 8.2 hours of the urea clamp, 523 spectra were collected.

With only one baseline period, the NAS was not applicable in this study. The original purpose of the NAS method is to cover as much variance as possible during the entire experiment. Only one baseline period before the urea transient is insufficient to include enough variance. Therefore, only PLS and HLA calibration models were tested.

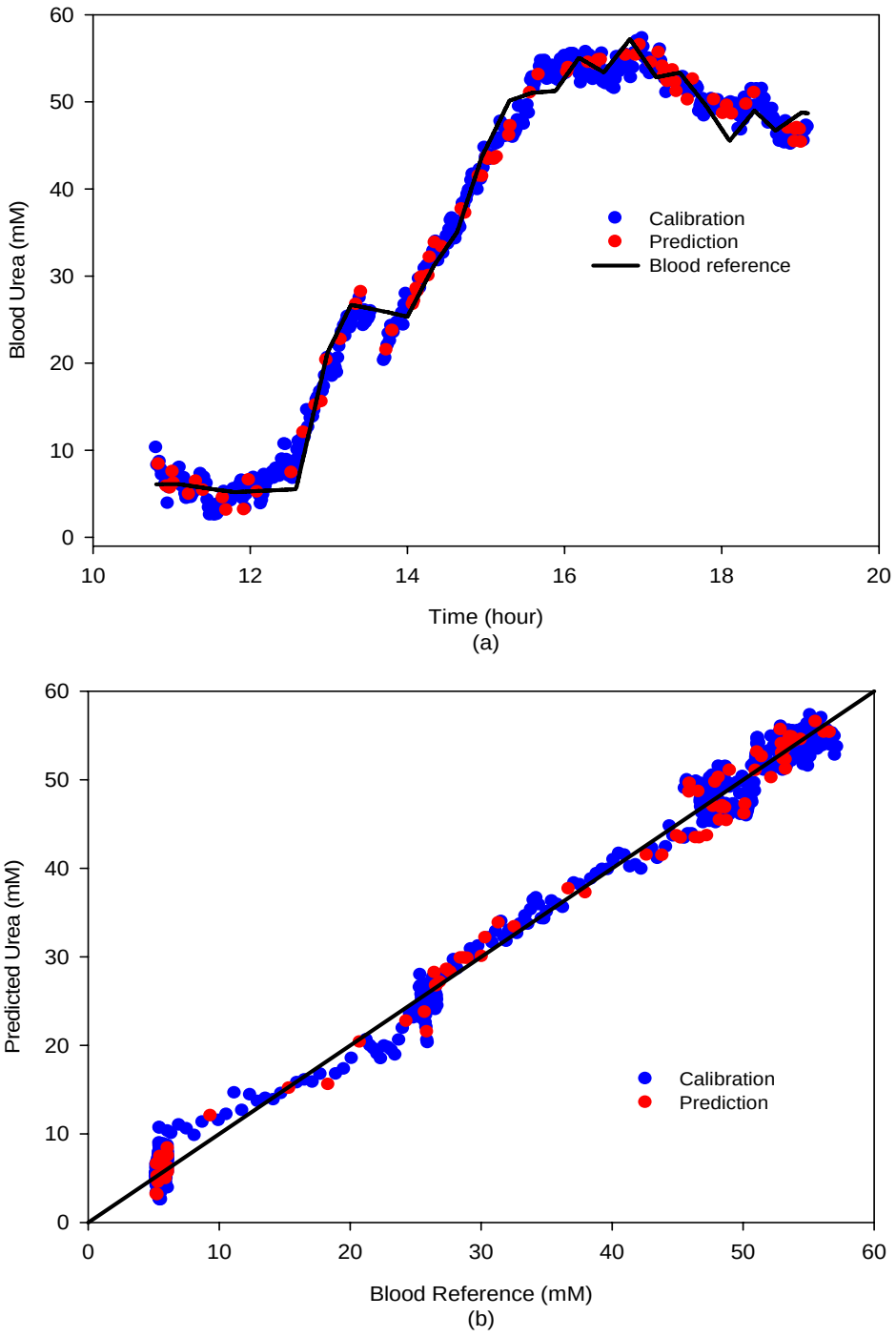

Figure V-6. PLS calibration and prediction results of the urea animal model with 7 latent variables.

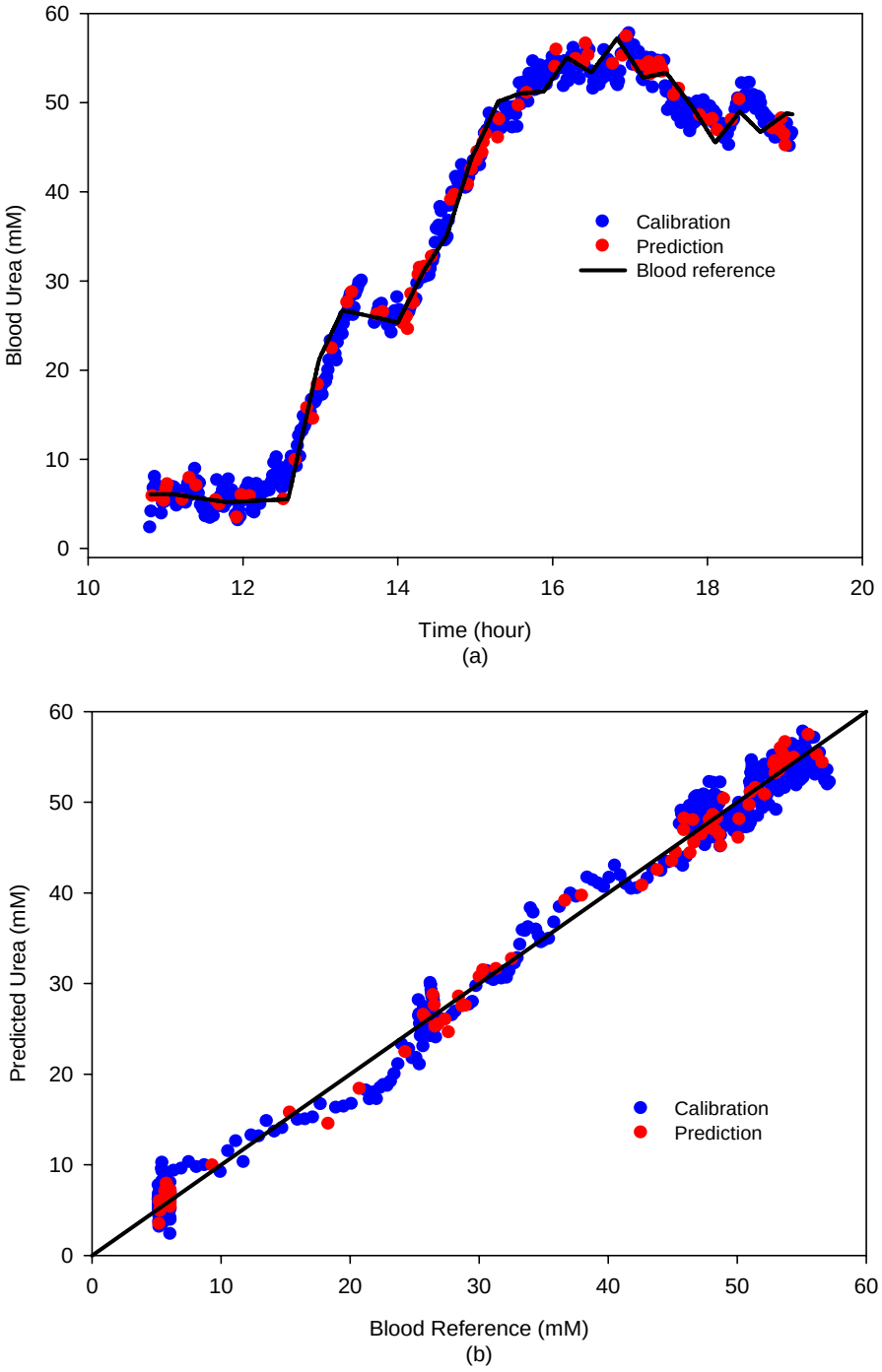

Figure V-7. HLA calibration and prediction results of the urea animal model with 7 latent variables.

Table V-2 PLS and HLA calibration and prediction results of urea animal model.

	PLS	HLA
Spectral range (cm^{-1})	4900-4200	
Total number of spectra	523	
Spectra in calibration	445	
Spectra in prediction	78	
Latent variables	7	10
SEC (mM)	1.9	1.9
SEP (mM)	1.7	1.5

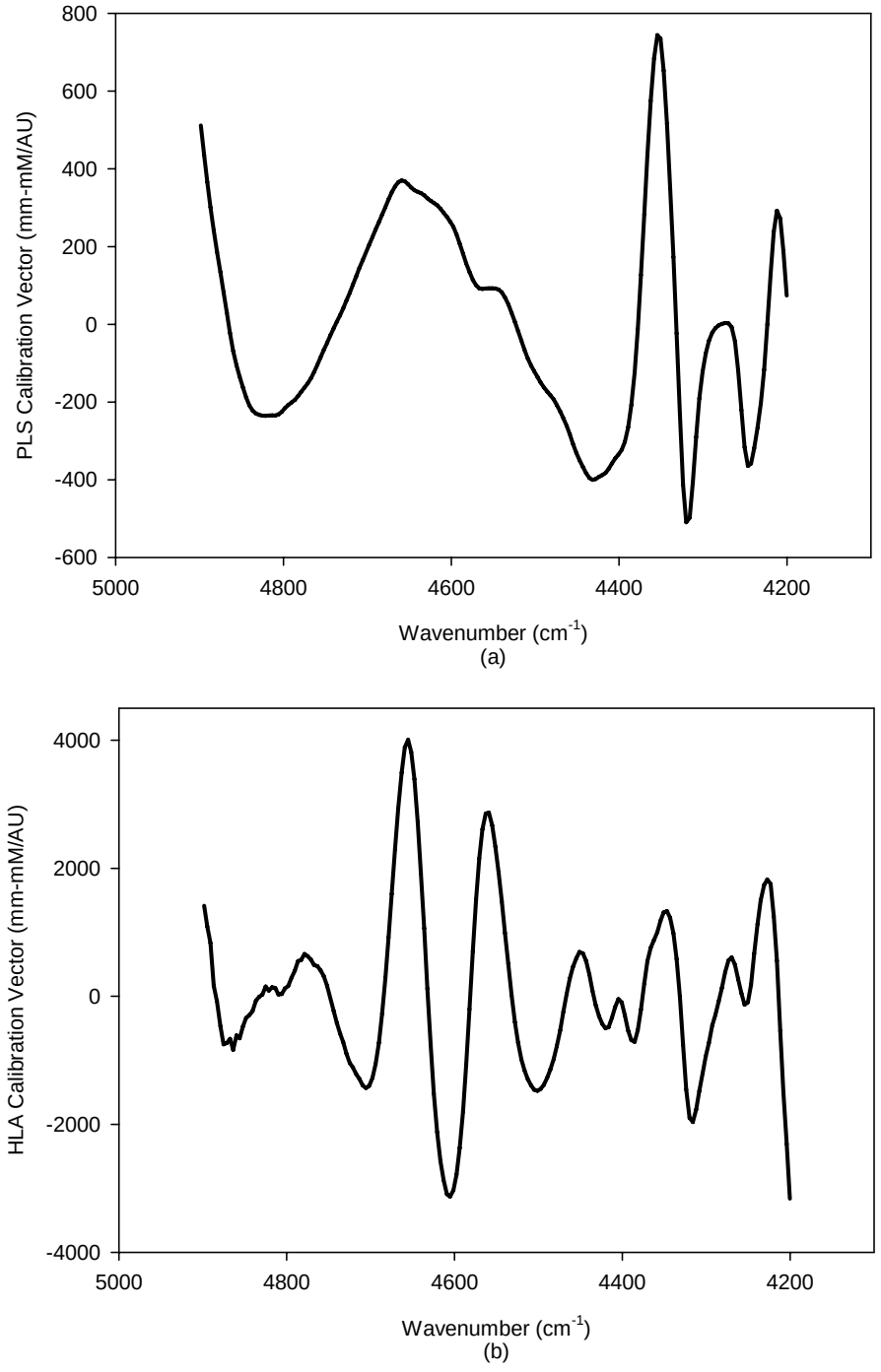

Figure V-8. Calibration vectors from (a) PLS and (b) HLA methods.

The 523 collected spectra were randomly split into 445 spectra in the calibration data set and 78 spectra used for prediction. The same calibration and prediction data sets were used for both the PLS and HLA models. Spectral range is from 4900 to 4200 cm^{-1} and the procedures to calculate the PLS and HLA calibration vectors are exactly the same as those used for lactate and glucose models discussed above.

The calibration and prediction results of the PLS and HLA calibration models are shown in Figures V-6 and 7, respectively. The straight line in Figures V-6 (b) and 7 (b) indicate the ideal correlation between predicted and reference values. For both calibration methods, the predicted values from both calibration and prediction data sets follow the blood references with excellent correlations between the predicted and blood reference values. The corresponding SEC and SEP values are summarized in Table V-2. With 7 latent variables, the PLS model can predict urea concentrations with an SEC of 1.9 mM and SEP of 1.7 mM. For the HLA model, 10 factors were used and the results demonstrate an SEC of 1.9 mM and an SEP of 1.5 mM. The calibration vectors for these two methods are shown in Figure V-8. The shapes of these two vectors look quite different. However, both of these two vectors have strong peaks at 4650 and 4550 cm^{-1} which are the combination of the symmetric (~3350 cm^{-1}) and asymmetric (3450 cm^{-1}) N-H stretching modes coupled with the N-H bending vibration (~1640-1600 cm^{-1}) in urea molecules. From this comparison, we can conclude that both PLS and HLA models show certain selectivity for urea, although differences in the overall shapes of these calibration vector is concerning.

Conclusions

Two biomolecules, lactate and urea, have been studied in this chapter because of their importance and significance in clinical chemistry. Two animal models with noninvasive skin NIR spectra were established. Different calibration methods including PLS, HLA, and NAS were applied. For lactate, too much fluctuation in the predicted

lactate concentrations was observed, which indicates a lack of precision. Both HLA and NAS calibration models demonstrate selectivity for lactate, while the PLS model may be affected by other interferences since this calibration vector failed to show features that overlap with lactate absorbance, as well as HLA and NAS calibration vectors. For urea, the NAS algorithm was not applicable because only one baseline period could be collected. The PLS and HLA models present good urea predictions. Although the calibration vectors of these two methods are quite different, both of them have strong peaks which overlap with known urea absorption bands. The results suggest that these two calibration models are selective for urea, but their differences are concerning.

Since only one animal model was established for each study, the information presented here must be considered preliminary. It is too early to make any significant conclusions based only two experiments. Clearly, more experiments are needed in the following respects: first, repeated procedures or more lactate and urea transients with proper concentration ranges; and second, incorporate more advanced instrumentation to reduce the instrumental sources of variations.

CHAPTER VI

FUTURE WORK

Research results presented in the previous chapters focus on applying Near infrared (NIR) spectroscopy on living tissue for noninvasive monitoring of biomolecules. Efforts were made from the following aspects: instrumentation, animal and human model establishment, and chemometric models. First, an instrument with suitably high *S/N* over the combination NIR spectrum is coupled with a user-friendly-friendly interface. The high power density external light source, interferometer, and low noise detector were used to achieve the high optical throughput and sufficient *S/N* levels for *in vivo* sensing of the targeted biomolecules. Second, animal models with varying concentrations of target analytes: glucose, lactate, and urea were achieved by cannulation surgery and peristaltic pump control system. Preliminary human baseline models with a population of 47 people are also described. Third, chemometric methods, including partial least squares (PLS), net analyte signal (NAS), and hybrid liNear analysis (HLA), were applied with the resulting measurement selectivity evaluated. To further validate these calibration models, attempts to use external validation data sets were made both physically and mathematically. All of these achievements advance the state-of the-art for noninvasive clinical monitoring. Advances are needed, however, before a viable clinical monitor will be available based on NIR technology. Several key areas for further development are discussed below.

Near-Infrared (NIR) Spectral Comparison of Animal Models with and without Anesthesia

Noninvasive NIR spectroscopy has been applied on anesthetized animal models in our previous work. Multivariate calibration models including PLS, NAS, and HLA demonstrate good glucose prediction ability. However, for the ultimate goal of noninvasive glucose sensing, the NIR spectra must be collected with human subjects who

are fully awake or asleep. Therefore, one concern is related to the effect of the anesthetic agent on the collected NIR spectra. Theoretically, 50 mg/kg pentobarbital would not have a significant spectroscopical impact. However, the secondary effects such as changes in blood pressure or tissue perfusion must be considered. Thus, one multiple day animal experiment was conducted to compare the skin spectra with and without the anesthetic agent.

In this study, NIR spectra were collected noninvasively on one animal over multiple days under conscious and anesthetized conditions. In the conscious study, the NIR spectra were collected on a fully awake animal without any medicine treatment. Normal level of anesthesia was maintained during the spectral collection with the anesthetized animal. Finally 7 days of conscious spectral data and 5 days of anesthetized spectral data were obtained. Spectral comparison between these two groups was made by principal component analysis (PCA). The comparison of principal component (PC) scores demonstrates major overlap between the noninvasive NIR spectra from these two study groups. PCA results demonstrate no significant difference between skin spectra collected from conscious and anesthetized animals, which means that the anesthesia has insignificant impact on the noninvasive NIR spectra and results from anesthetized animals can be extrapolated to non-anesthetized animals

Experimental Section

An adult male Sprague-Dawley rat (retired breeders, weighting ~ 400 g) was used as the animal in this experiment. Skin fold on the back of neck was selected as the measurement site as noted before.[76, 77, 94] *In vivo* NIR skin spectra were collected on the same instrument used in animal experiments described in Chapter IIs and III.

For the conscious measurements, the rat was restrained in a plastic cone (Braintree Scientific ING., Braintree, MA) during the spectral collection. The rat had been trained to stay calm while constrained in this manner. The same conscious

measurements were repeated for 7 days. Because the rat was awake in the restraint, it escaped the interface occasionally. The skin fold was reclamped afterwards and the data collection can . The total data collection time for each day varied from 30 minutes to 2 hours depending on the status of the rat. After the first stage of the 7-day conscious data collection completed, anesthetized measurements were conducted on the same animal and instrument. The spectral collection started right after the rat was anesthetized by pentobarbital (Ovation Pharmaceuticals, Deerfield, IL) at the dosage of 50 mg/kg. This dosage could maintain anesthesia for approximately 2 hours which was the spectral collection time used. The same anesthetized study was repeated for 5 days. At least 2 days interval was kept between two adjacent anesthetized experiments to provide the rat enough recovery time between treatments. One month after the last day of anesthetized experiment, two more days of conscious measurements were collected to finalize the experiment. During this process, the body weight was measured and recorded on each day.

Results and Discussion

In all 4865 spectra were collected during the entire study (2882 from the conscious condition and 1983 from the anesthetized condition). Each of skin absorbance spectrum was referenced to the average of 1 mm air spectra collected before and after the skin study to calculate the skin absorbance spectra. Spectra were further truncated to the region from 4900 to 4200 cm^{-1}, which is favorable for glucose sensing. Principal component analysis (PCA) was done under MATLAB® R2007a with a maximum of 12 latent variables.

Spectral loadings are shown in Figure VI-1. The first several loadings represent the most dominant strong absorbers in the skin tissue, such as water, fat, and proteins. Loadings with more latent variables are difficult to correlate with specific physiological components. As more latent variables are used, the loading spectral shapes show more

features. However, with up to 12 factors, no significant noise features are evident in the loading spectra. This indicates that it is safe to use up to 12 latent variables for modeling. PC scores were plotted with 2 adjacent PCs in Figures VI-2, 3, 4, 5, and 6. Each color indicates one day in the experiment. The first two plots in Figures VI-2 (a) and (b) show the most significant separation, which means spectra in each day is unique. Even spectra from the same day study fall into several clusters when the interface was repositioned on that day. These variances are mainly associated with changes of skin components from day to day at sensing spot, and difference in reclamping conditions, such as pressure and thickness. With these types of variances, it is meaningless to compare spectra from only two or three days. With fourteen days spectra for comparison, some distributions can be tracked. First, even though spectral from different days form different clusters, the clusters of the five days of anesthetized condition fall into the region of all the other conscious condition. This finding suggests the spectra from anesthetized studies are not significantly different from those in conscious studies. This result indicates that the anesthesia agent has neither direct nor secondary impacts on the *in vivo* skin spectra. As more latent variables are inspected, the magnitude of overlapping is higher, which indicates the differences in the skin components and interface conditions make more contribution in the first several factors while higher factors are less dependent on these parameters.

Figure VI-7 shows the residual RMS noise values measured after removing each latent variable in this PCA analysis. At 10 latent variables, the residual RMS noise is over 100 μAU, which is significantly higher than that of each single day study. This find indicates that the variances from different days and different interface applications contribute significantly to the day-to-day spectral variances.

Conclusions

From this multiple-day animal study, spectra from anesthetized and conscious

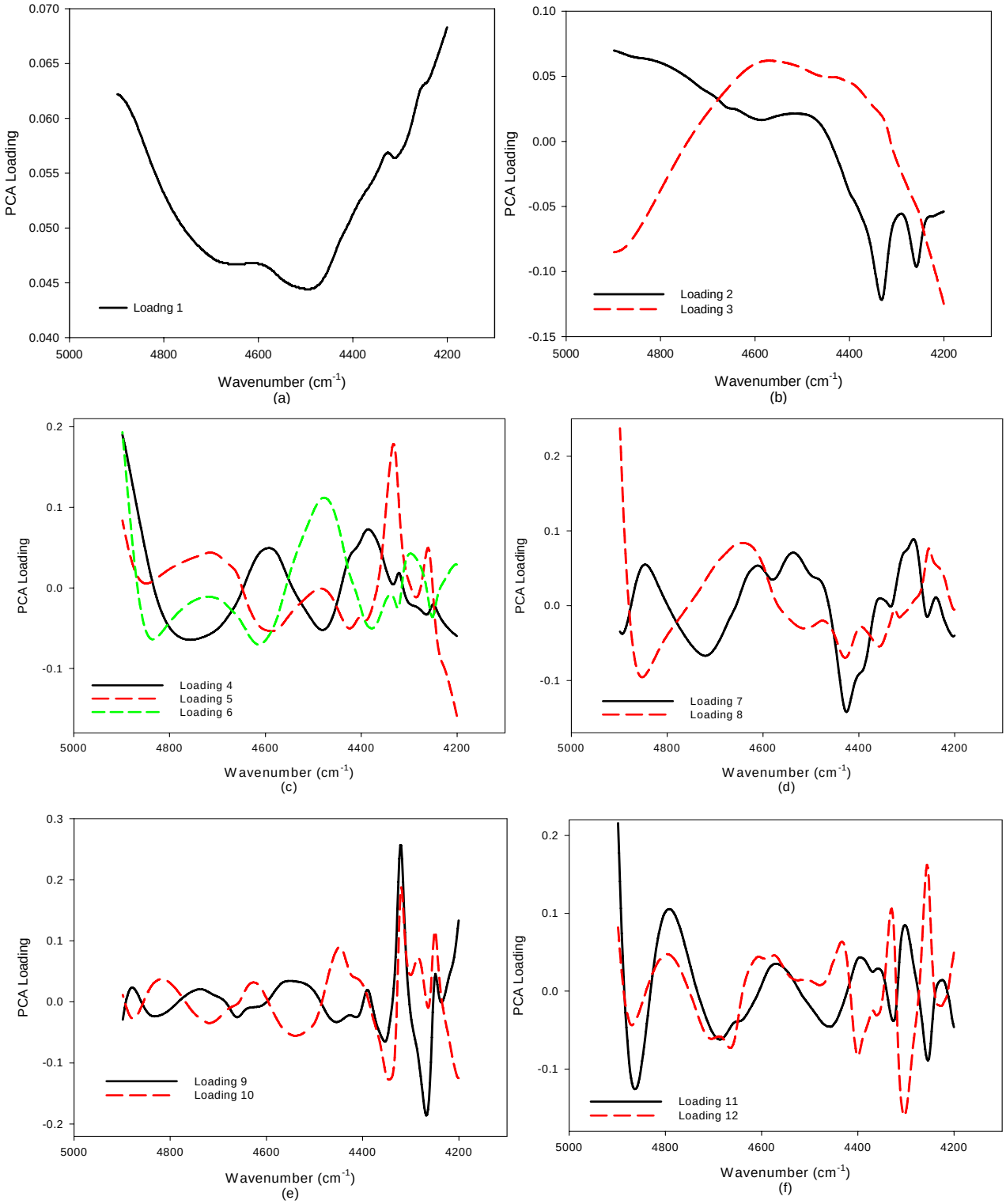

Figure VI-1. PCA loadings of all the NIR skin spectra from 14 day studies with 1 to 12 latent variables

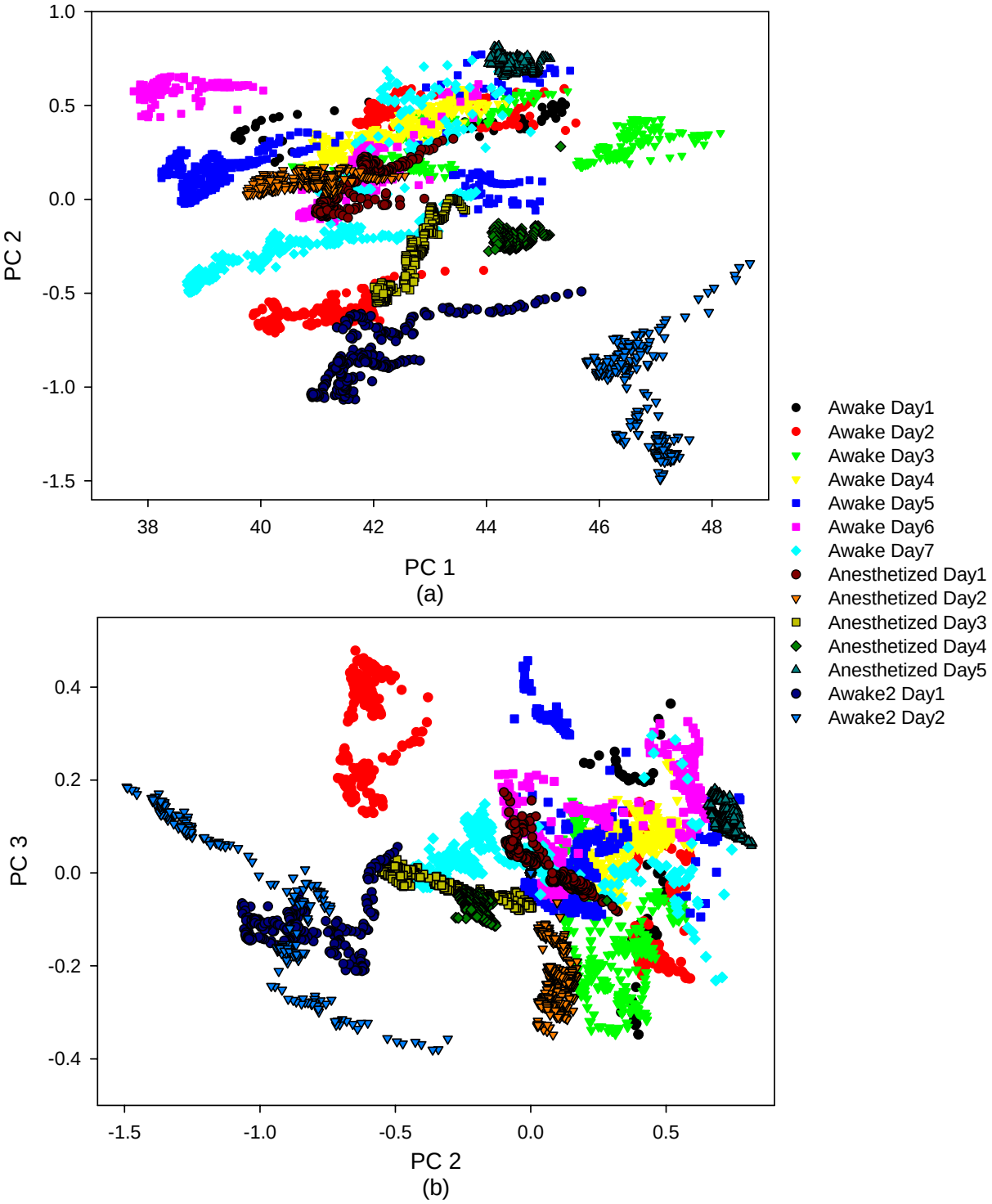

Figure VI-2. Principal component plots showing (a) PC 1 vs. PC 2 and (b) PC 2 vs. PC 3.

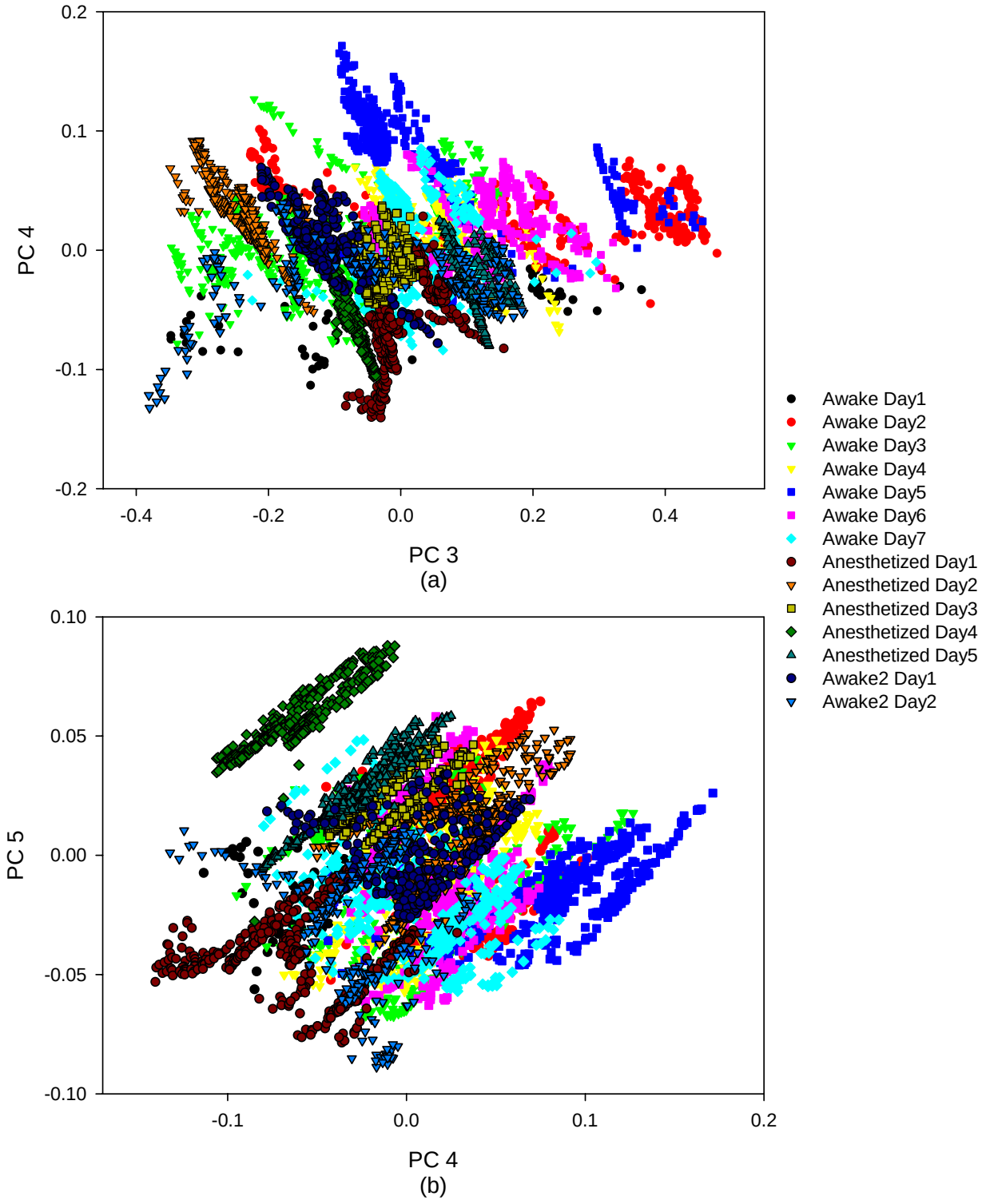

Figure VI-3. Principal component plots showing (a) PC 3 vs. PC 4 and (b) PC 4 vs. PC 5.

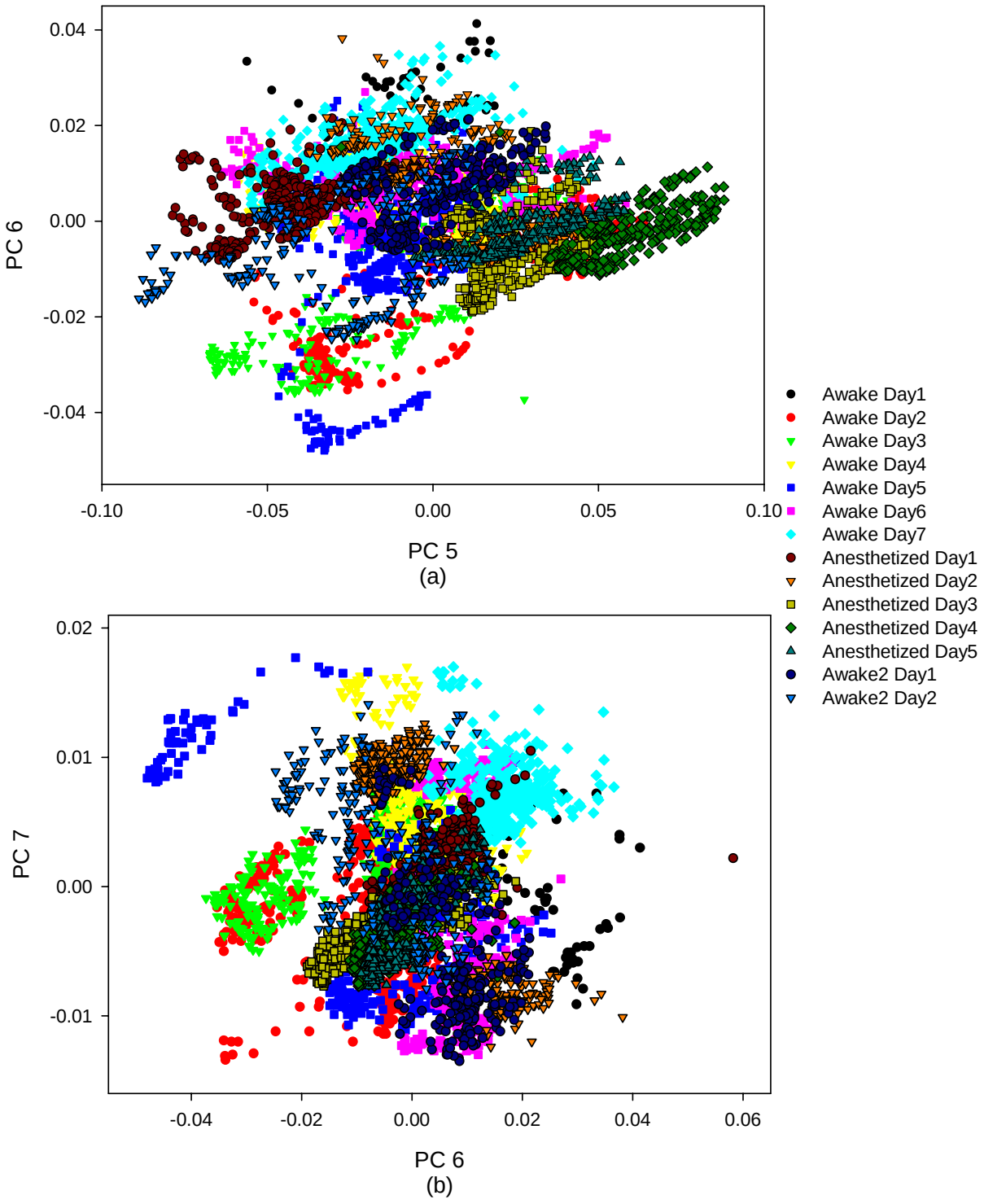

Figure VI-4. Principal component plots showing (a) PC 5 vs. PC 6 and (b) PC 6 vs. PC 7.

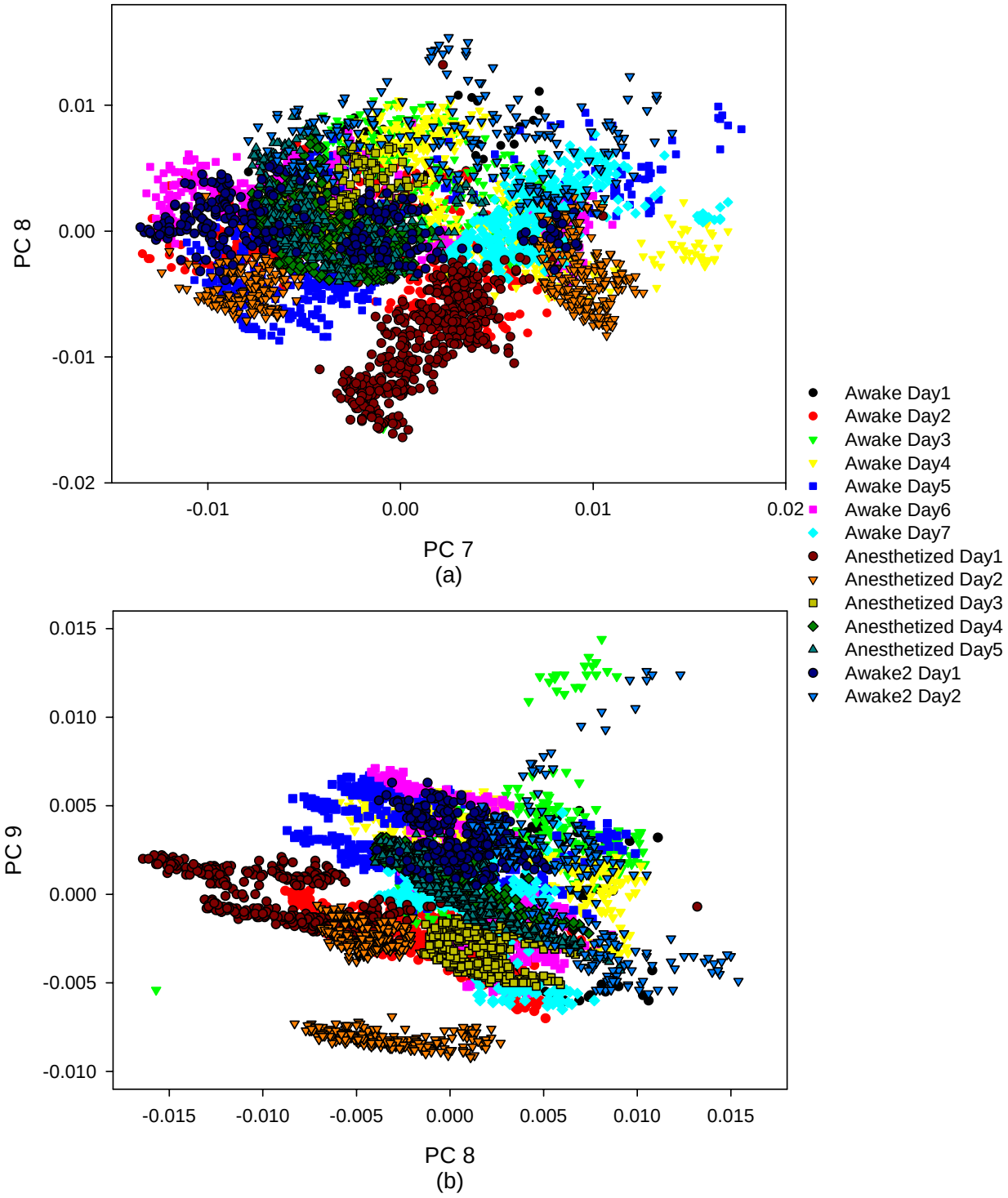

Figure VI-5. Principal component plots showing (a) PC 7 vs. PC 8 and (b) PC 8 vs. PC 9.

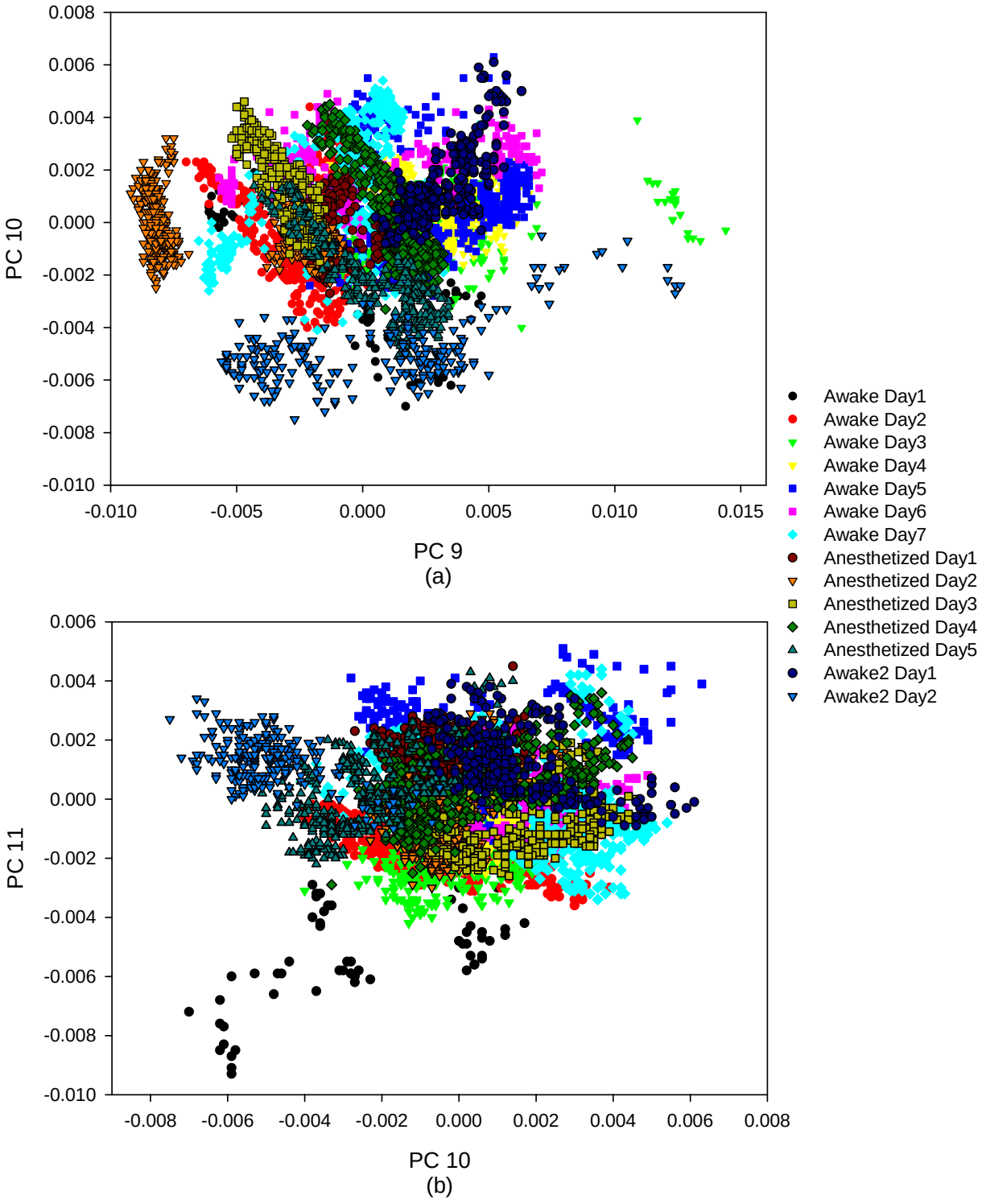

Figure VI-6 Principal component plots showing (a) PC 9 vs. PC 10 and (b) PC 10 vs. PC 11.

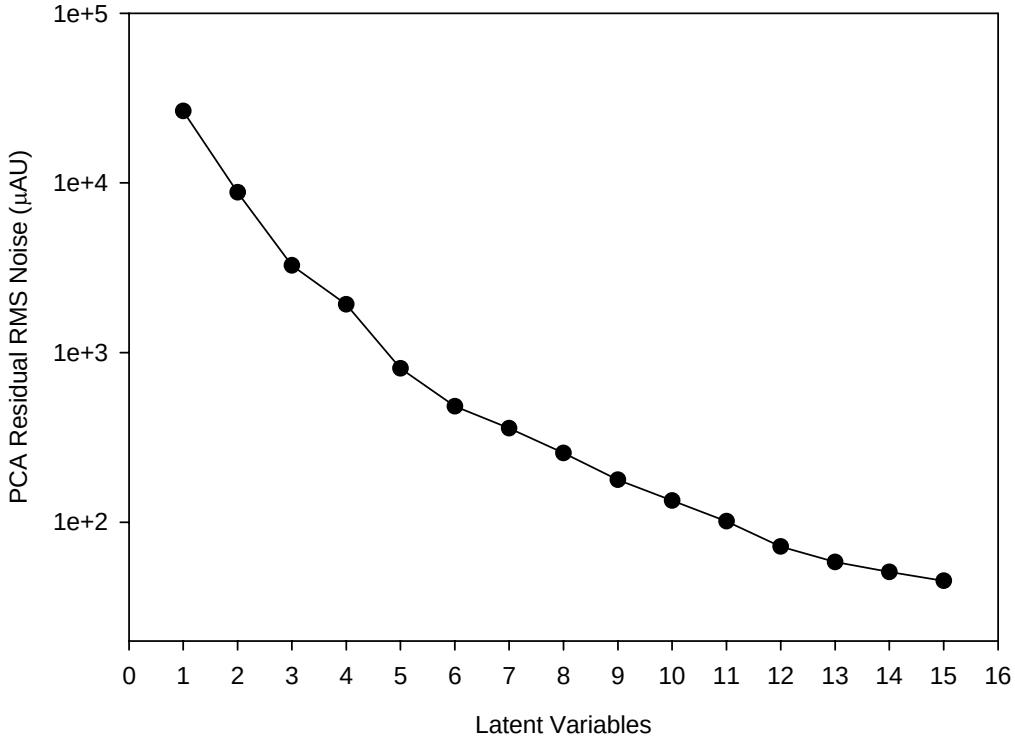

Figure VI-7. PCA residual RMS noise at each latent variable.

skin conditions were compared by PCA analysis. No significant noise features were found up to 12 latent variables, which indicates that a chemometric model with up to 12 latent variables has minimal chance of overfitting. PC score clusters overlap across providing significant evidence that the anesthesia agent causes no significant influence in the noninvasive skin spectra. Therefore, further animal studies from anesthetized and conscious studies can be combined for multivariate models.

New Surgical Procedure for Multiple Days Study

Animal models from multiple-day data collection periods are desired for more robust calibration models and the ability to access external validation. More glucose transients from multiple-day experiments would provide more variances due to the skin components and interface repositioning, thereby enhancing calibration models. In addition, the established models can be evaluated by external validations across different days. Here, a new surgical procedure is proposed for this purpose, and the preliminary surgery was tried on several animals.

In this survivable surgery, the animal was anesthetized with 50 mg/kg pentobarbital. Similar to the surgical procedure outlined in Chapter II, two catheters (Strategic Applications, Incorporated, Libertyville, IL) were inserted into femoral artery and vein, respectively. The rest of the tubing was placed underneath skin. The other end of each catheter came out the skin on the rat's back. Each exiting catheter tip was connected with one vascular access port (VAP) (Strategic Applications, Incorporated, Libertyville, IL). Then the two ports were sutured on the muscle subcutaneously and wounds on the back and leg areas were sutured. Within two weeks, the rat was recovered. Frequent arterial blood sampling and venous infusion can be done through these two ports.

With this new survivable surgery, new animal models with ports and catheters implanted will be beneficial for the collection of larger data sets with more flexibility

provided for the collection of calibration and validation spectral data. Hopefully, calibration models from multiple-day spectral data will capture more analyte-specific variances to make improve robustness and reliability.

Development of Instrumentation

Although both human and animal skin tissue show similar features in the NIR combination spectrum (5000-4000 cm^{-1}), the magnitude of absorbance and scattering are different for human and rat skin. The current instrumentation has sufficient *S/N* for animal experiment. For human subject experiment, a broader distribution of skin thickness and components suggest that the current *S/N* is not adequate. Therefore, improvements are needed to develop a stable spectrometer and a noninvaisve skin interface to enhance the optical throughput and increase S/N. Such improvements can be accomplished by: 1). increasing the radiant power of the light source to enhance the powers in the combination spectral region; 2). enhance the interface coupling to reduce light loss due to refractive index mismatch; 3).use a more sensitive extended InGaAs detector with a larger surface area to increase S/N of the detection optics.

Understanding the Skin Matrix

It is a great challenge to explore each individual component in the skin matrix. So far, only a few of the major components have been considered. However, many additional components can be spectroscopical contributions. A deeper understanding of the NIR spectral features and how these components behave will help to establish a more robust and selective calibration model for glucose, lactate, and urea.

Robust and Selective Calibration Models

With the development of chemometrics, new algorithms can be applied with better understanding between noninvasive spectra and target analyte information. Meanwhile, new approaches can be introduced to evaluate the robustness and selectivity

of the established models. In addition, more sophisticated algorithms will help isolate the target analyte information more efficiently to improve the prediction ability.

Noninvasive spectroscopical sensing has been developed for decades. With the achievements in this dissertation and contributions from other scientists, more and more people will benefit from the efforts we have made.

REFERENCES

(1) "National Diabetes Statistics" National Institutes of Health (NIH) http://diabetes.niddk.nih.gov/DM/PUBS/statistics/ **2007**

(2) http://www.onetouchgold.com/diabetesbasics/longtermcomplications.

(3) Braithwaite, S. S. "Defining the benefits of euglycemia in the hospitalized patient" *Journal of Hospital Medicine* **2007**, *2*, 5-12.

(4) The Diabetes Control and Complications Trial Research Group."Effect of Intensive Diabetes Treatment on The Development and Progression of Long-Term Complications in Adolescents with Insulin-Dependent Diabetes-Mellitus - Diabetes Control and Complications Trial" *Journal of Pediatrics*, **1994**; Vol. 125, pp 177-188.

(5) Subramanian, S. L.; Hirsch, I. B. "The utility and recent advances in self-monitoring of blood glucose in type 1 diabetes" *Diabetes Technology & Therapeutics* **2008**, *10*, S43-S50.

(6) Henning, T. P.; Cunningham, D. D. In *Commercial biosensors: application to clinical, bioprocess, and environmental samples*; G, R., Ed.; John Wiley & Sons: New York, **1998**, pp 3-46.

(7) Bai, C.; Graham, T. L.; Arnold, M. A. "Assessing and advancing technology for the noninvasive measurement of clinical glucose" *Analytical Letters* **2008**, *41*, 2773-2793.

(8) Garg, S. K. "The Future of continuous glucose monitoring" *Diabetes Technology & Therapeutics* **2009**, *11*, S1-S3.

(9) Skyler, J. S. "Continuous glucose monitoring: An Overview of its development" *Diabetes Technology & Therapeutics* **2009**, *11*, S5-S10.

(10) Cengiz, E.; Tamborlane, W. V. "A tale of two compartments: interstitial versus blood glucose monitoring" *Diabetes Technology & Therapeutics* **2009**, *11*, S11-S16.

(11) Tura, A.; Maran, A.; Pacini, G. "Non-invasive glucose monitoring: Assessment of technologies and devices according to quantitative criteria" *Diabetes Research And Clinical Practice* **2007**, *77*, 16-40.

(12) Clarke, W. L.; Cox, D.; Gonderfrederick, L. A.; Carter, W.; Pohl, S. L. "Evaluating clinical accuracy of systems for self-monitoring of blood-glucose" *Diabetes Care* **1987**, *10*, 622-628.

(13) Johnson, R. N.; Baker, J. R. "Error detection and measurement in glucose monitors" *Clinica Chimica Acta* **2001**, *307*, 61-67.

(14) Arnold, M. A.; Small, G. W. "Noninvasive glucose sensing" *Analytical Chemistry* **2005**, *77*, 5429-5439.

(15) Khalil, O. S. "Spectroscopic and clinical aspects of noninvasive glucose measurements" *Clinical Chemistry* **1999**, *45*, 165-177.

(16) Khalil, O. S. "Non-invasive glucose measurements at the dawn of the new millennium: An update." *Diabetes Technology & Therapeutics* **2004**, *6*, 660-697.

(17) Sapozhnikova, V. V.; Prough, D.; Kuranov, R. V.; Cicenaite, I.; Esenaliev, R. O. "Influence of osmolytes on in vivo glucose monitoring using optical coherence tomography" *Experimental Biology And Medicine* **2006**, *231*, 1323-1332.

(18) Kuranov, R. V.; Sapozhnikova, V. V.; Prough, D. S.; Cicenaite, I.; Esenaliev, R. O. "*In vivo* study of glucose-induced changes in skin properties assessed with optical coherence tomography" *Physics In Medicine And Biology* **2006**, *51*, 3885-3900.

(19) Larin, K. V.; Motamedi, M.; Ashitkov, T. V.; Esenaliev, R. O. "Specificity of noninvasive blood glucose sensing using optical coherence tomography technique: a pilot study" *Physics In Medicine And Biology* **2003**, *48*, 1371-1390.

(20) Esenaliev, R. O.; Larin, K. V.; Larina, I. V.; Motamedi, M. "Noninvasive monitoring of glucose concentration with optical coherence tomography" *Optics Letters* **2001**, *26*, 992-994.

(21) Yeh, S. J.; Hanna, C. F.; Khalil, O. S. "Monitoring blood glucose changes in cutaneous tissue by temperature-modulated localized reflectance measurements" *Clinical Chemistry* **2003**, *49*, 924-934.

(22) Mitragotri, S.; Coleman, M.; Kost, J.; Langer, R. "Analysis of ultrasonically extracted interstitial fluid as a predictor of blood glucose levels" *Journal of Applied Physiology* **2000**, *89*, 961-966.

(23) Ermolina, I.; Polevaya, Y.; Feldman, Y. "Analysis of dielectric spectra of eukaryotic cells by computer modeling" *European Biophysics Journal With Biophysics Letters* **2000**, *29*, 141-145.

(24) Lambert, J. L.; Pelletier, C. C.; Borchert, M. "Glucose determination in human aqueous humor with Raman spectroscopy" *Journal of Biomedical Optics* **2005**, *10*.

(25) Lin, S. Y.; Li, M. J.; Cheng, W. T. "FT-IR and Raman vibrational microspectroscopies used for spectral biodiagnosis of human tissues" *Spectroscopy-An International Journal* **2007**, *21*, 1-30.

(26) Pelletier, C. C.; Lambert, J. L.; Borchert, M. "Determination of glucose in human aqueous humor using Raman spectroscopy and designed-solution calibration" *Applied Spectroscopy* **2005**, *59*, 1024-1031.

(27) Ren, M.; Arnold, M. A. "Comparison of multivariate calibration models for glucose, urea, and lactate from Near-infrared and Raman spectra" *Analytical and Bioanalytical Chemistry* **2007**, *387*, 879-888.

(28) Stuart, D. A.; Yuen, J. M.; Lyandres, N. S. O.; Yonzon, C. R.; Glucksberg, M. R.; Walsh, J. T.; Van Duyne, R. P. "*In vivo* glucose measurement by surface-enhanced Raman spectroscopy" *Analytical Chemistry* **2006**, *78*, 7211-7215.

(29) Chen, J.; Arnold, M. A.; Small, G. W. "Comparison of combination and first overtone spectral regions for Near-infrared calibration models for glucose and other biomolecules in aqueous solutions" *Analytical Chemistry* **2004**, *76*, 5405-5413.

(30) Hull, E. L.; Ediger, M. N.; Unione, A. H. T.; Deemer, E. K.; Stroman, M. L.; Baynes, J. W. "Noninvasive, optical detection of diabetes: model studies with porcine skin" *Optics Express* **2004**, *12*, 4496-4510.

(31) Schleicher, E. D.; Wagner, E.; Nerlich, A. G. "Increased accumulation of the glycoxidation product N-epsilon(carboxymethyl)lysine in human tissues in diabetes and aging" *Journal of Clinical Investigation* **1997**, *99*, 457-468.

(32) Maynard, J. D.; Nguyen, C. M.; Rohrscheib, M.; Ediger, M. N.; Way, J. F. "Noninvasive type 2 diabetes screening - Superior or sensitivity to fasting plasma glucose and A1C" *Diabetes Care* **2007**, *30*, 1120-1124.

(33) Baca, J. T.; Finegold, D. N.; Asher, S. A. "Tear glucose analysis for the noninvasive detection and monitoring of diabetes mellitus" *Ocular Surface* **2007**, *5*, 280-293.

(34) Ben-Moshe, M.; Alexeev, V. L.; Asher, S. A. "Fast responsive crystalline colloidal array photonic crystal glucose sensors" *Analytical Chemistry* **2006**, *78*, 5149-5157.

(35) Alexeev, V. L.; Das, S.; Finegold, D. N.; Asher, S. A. "Photonic crystal glucose-sensing material for noninvasive monitoring of glucose in tear fluid" *Clinical Chemistry* **2004**, *50*, 2353-2360.

(36) March, W.; Lazzaro, D.; Rastogi, S. "Fluorescent measurement in the non-invasive contact lens glucose sensor" *Diabetes Technology & Therapeutics* **2006**, *8*, 312-317.

(37) Pickup, J. C.; Hussain, F.; Evans, N. D.; Rolinski, O. J.; Birch, D. J. S. "Fluorescence-based glucose sensors" *Biosensors & Bioelectronics* **2005**, *20*, 2555-2565.

(38) Badugu, R.; Lakowicz, J. R.; Geddes, C. D. "A glucose-sensing contact lens: from bench top to patient" *Current Opinion In Biotechnology* **2005**, *16*, 100-107.

(39) Badugu, R.; Lakowicz, J. R.; Geddes, C. D. "Ophthalmic glucose monitoring using disposable contact lenses - A review" *Journal of Fluorescence* **2004**, *14*, 617-633.

(40) Baca, J. T.; Taormina, C. R.; Feingold, E.; Finegold, D. N.; Grabowski, J. J.; Asher, S. A. "Mass spectral determination of fasting tear glucose concentrations in nondiabetic volunteers" *Clinical Chemistry* **2007**, *53*, 1370-1372.

(41) McNichols, R. J.; Cote, G. L. "Optical glucose sensing in biological fluids: an overview" *Journal of Biomedical Optics* **2000**, *5*, 5-16.

(42) Burns, D. A.; Ciurczak, E. W., Eds. *Handbook of Near-Infrared Analysis*, Second ed.; Marcel Dekker, Inc. New York, Basel, **2001**.

(43) Kemsley, E. K.; Tapp, H. S.; Binns, R.; Mackin, R. O.; Peyton, A. J. "Feasibility study of NIR diffuse optical tomography on agricultural produce" *Postharvest Biology And Technology* **2008**, *48*, 223-230.

(44) Williams, P.; Norris, K., Eds. *Near-Infrared Technology in the Agricultural and Food Industries*; American Association of Cereal Chemists Inc. St. Paul, MN, **1987**.

(45) Pallav, P.; Diamond, G. G.; Hutchins, D. A.; Green, R. J.; Gan, T. H. "A Near-infrared (NIR) technique for imaging food materials" *Journal of Food Science* **2009**, *74*, E23-E33.

(46) Kaffka, K. "How the NIR technology came to and spread in Europe for quality assessment and control in the food industry" *Acta Alimentaria* **2008**, *37*, 141-145.

(47) Buning-Pfaue, H.; Hartmann, R.; Harder, J.; Kehraus, S.; Urban, C. "NIR-spectrometric analysis of food. Methodical development and achievable performance values" *Fresenius Journal of Analytical Chemistry* **1998**, *360*, 832-835.

(48) Hoyer, H. "NIR on-line analysis in the food industry" *Process Control and Quality* **1997**, *9*, 143-152.

(49) Johnsen, E. "How to use on-line NIR in the feed and food industries" *Process Control and Quality* **1997**, *9*, 205-206.

(50) McClure, W. F.; Hamid, A. "Rapid NIR measurement of the chemical-composition of foods snd food-products.1. hardware" *American Laboratory* **1980**, *12*, 57-&.

(51) Syunyaev, R. Z.; Balabin, R. M.; Akhatov, I. S.; Safieva, J. O. "Adsorption of petroleum asphaltenes onto reservoir rock sands studied by Near-infrared (NIR) spectroscopy" *Energy & Fuels* **2009**, *23*, 1230-1236.

(52) Balabin, R. A.; Syunyaev, R. Z. "Petroleum resins adsorption onto quartz sand: Near infrared (NIR) spectroscopy study" *Journal of Colloid and Interface Science* **2008**, *318*, 167-174.

(53) Falla, F. S.; Larini, C.; Le Roux, G. A. C.; Quina, F. H.; Moro, L. F. L.; Nascimento, C. A. "Characterization of crude petroleum by NIR" *Journal of Petroleum Science and Engineering* **2006**, *51*, 127-137.

(54) Sando, G.; Dubois, J. ""Seeing" the chemicals in pharmaceutical tablets with NIR chemical imaging" *Chimica Oggi-Chemistry Today* **2010**, *28*, 40-42.

(55) Xiang, D.; Berry, J.; Buntz, S.; Gargiulo, P.; Cheney, J.; Joshi, Y.; Wabuyele, B.; Wu, H. Q.; Hamed, M.; Hussain, A. S.; Khan, M. A. "Robust calibration design in the Pharmaceutical Quantitative Measurements with Near-Infrared (NIR) spectroscopy: Avoiding the chemometric pitfalls" *Journal of Pharmaceutical Sciences* **2009**, *98*, 1155-1166.

(56) Blanco, M.; Cruz, J.; Bautista, M. "Development of a univariate calibration model for pharmaceutical analysis based on NIR spectra" *Analytical and Bioanalytical Chemistry* **2008**, *392*, 1367-1372.

(57) Blanco, M.; Bautista, M.; Alcala, M. "API determination by NIR Spectroscopy across pharmaceutical production process" *Aaps Pharmscitech* **2008**, *9*, 1130-1135.

(58) Amigo, J. M.; Cruz, J.; Bautista, M.; Maspoch, S.; Coello, J.; Blanco, M. "Study of pharmaceutical samples by NIR chemical-image and multivariate analysis" *Trac-Trends in Analytical Chemistry* **2008**, *27*, 696-713.

(59) Michelson, A. A. "Studies in optics" *University of Chicago Press* **1927**.

(60) Hendra, P. J. "How does FTIR work" *The Internet Journal of Vabrational Spectroscopy* **2001**, *5*, 2.

(61) Griffiths, P. R.; Haseth, J. A. D., Eds. *Fourier Transform Infrared Spectrometry*, 2nd ed.; John Wiley and Sons Inc: New York, **2007**.

(62) Jolliffe, I. T. *Principal Component Analysis*, 2nd ed. ed.; Springer, NY, **2002**.

(63) Shlens, J. "A Tutorial on Principal Component Analysis. " http://www.snl.salk.edu/~shlens/pca.pdf.

(64) Abdi, H.; Williams, L. J. "Principal Component Analysis" *Wiley Interdisciplinary Reviews: Computational Statistics* **2010**, *in press*.

(65) Esbensen, K. *Multivariate Analysis - in practice*, 3rd ed.; CAMO, 1998.

(66) Wall, M. E.; Rechtsteiner, A.; Rocha, L. M. In *A Practical Approach to Microarray Data Analysis*; Berrar, D. P., Dubitzky, W., Granzow, M., Eds.; Kluwer: Norwell, MA, **2003**, pp 91-109.

(67) Wold, H. In *Multivariate Analysis*; Krishnaiah, P. R., Ed.; Academic Press, NY, **1966**, pp 391-420.

(68) Wold, H. In *Quantitative Sociology: International perspectives on mathematical and statistical model building*; al., H. M. B. e., Ed. Academic Press, NY, **1975**, pp 307-357.

(69) Wold, S., Sjöström, M., Eriksson, L. " PLS-regression: a basic tool of chemometrics." *Chemometrics and Intelligent Laboratory Systems* **2001**, *58*, 109-130.

(70) Abdi, H. "Partial least squares regression and projection on latent structure regression (PLS-Regression)" *Wiley Interdisciplinary Reviews: Computational Statistics* **2010**, *2*, 97-106.

(71) Rosipal, R.; Kramer, N. In *Subspace, Latent Structure and Feature Selection Techniques*; al., S. e., Ed.; Springer-Verlag Berlin Heidelberg, **2006**, pp 34-51.

(72) Small, G. W. "Chemometrics and Near-infrared spectroscopy: Avoiding the pitfalls" *Trac-Trends in Analytical Chemistry* **2006**, *25*, 1057-1066.

(73) Amerov, A. K.; Chen, J.; Arnold, M. A. "Molar absorptivities of glucose and other biological molecules in aqueous solutions over the first overtone and combination regions of the Near-infrared spectrum" *Applied Spectroscopy* **2004**, *58*, 1195-1204.

(74) Amerov, A. K.; Chen, J.; Small, G. W.; Arnold, M. A. "Scattering and absorption effects in the determination of glucose in whole blood by Near-infrared spectroscopy" *Analytical Chemistry* **2005**, *77*, 4587-4594.

(75) Liu, L. Z.; Arnold, M. A. "Selectivity for glucose, glucose-6-phosphate, and pyruvate in ternary mixtures from the multivariate analysis of Near-infrared spectra" *Analytical And Bioanalytical Chemistry* **2009**, *393*, 669-677.

(76) Olesberg, J. T.; Liu, L.; Van Zee, V.; Arnold, M. A. "*In vivo* Near-infrared spectroscopy of rat skin tissue with varying blood glucose levels" *Proceedings of SPIE-The International Society for Optical Engineering* **2004**, *5325 (Optical Diagnostics and Sensing IV)*, 11-20.

(77) Olesberg, J. T.; Liu, L. Z.; Van Zee, V.; Arnold, M. A. "*In vivo* Near-infrared spectroscopy of rat skin tissue with varying blood glucose levels" *Analytical Chemistry* **2006**, *78*, 215-223.

(78) Alleso, M.; Velaga, S.; Alhalaweh, A.; Cornett, C.; Rasmussen, M. A.; van den Berg, F.; de Diego, H. L.; Rantanen, J. "Near-infrared spectroscopy for cocrystal screening. A comparative study with Raman spectroscopy" *Analytical Chemistry* **2008**, *80*, 7755-7764.

(79) Arnold, M. A.; Small, G. W.; Xiang, D.; Qui, J.; Murhammer, D. W. "Pure component selectivity analysis of multivariate calibration models from Near-infrared spectra" *Analytical Chemistry* **2004**, *76*, 2583-2590.

(80) Cho, D. S.; Olesberg, J. T.; Flanigan, M. J.; Arnold, M. A. "On-line Near-infrared spectrometer to monitor urea removal in real time during hemodialysis" *Applied Spectroscopy* **2008**, *62*, 866-872.

(81) Lee, Y.; Chung, H.; Arnold, M. A. "Improving the robustness of a partial least squares (PLS) model based on pure component selectivity analysis and range optimization: Case study for the analysis of an etching solution containing hydrogen peroxide" *Analytica Chimica Acta* **2006**, *572*, 93-101.

(82) Sulub, Y.; Small, G. W. "Simulated Radiance Profiles for Automating the Interpretation of Airborne Passive Multi-Spectral Infrared Images" *Applied Spectroscopy* **2008**, *62*, 1049-1059.

(83) Lorber, A. "Error propagation and figures of merit for quantification by solving matrix equations" *Analytical Chemistry* **1986**, *58*, 1167-1172.

(84) Lorber, A.; Faber, K.; Kowalski, B. R. "Net analyte signal calculation in multivariate calibration" *Analytical Chemistry* **1997**, *69*, 1620-1626.

(85) http://www.iupac.org/goldbook/S05606.pdf.

(86) Currie, L. A. "Detection: International update, and some emerging di-lemmas involving calibration, the blank, and multiple detection decisions" *Chemometrics and Intelligent Laboratory Systems* **1997**, *37*, 151-181.

(87) Berger, A. J.; Koo, T. W.; Itzkan, I.; Feld, M. S. "An enhanced algorithm for liNear multivariate calibration" *Analytical Chemistry* **1998**, *70*, 623-627.

(88) Shih, W. C.; Bechtel, K. L.; Feld, M. S. "Constrained regularization: Hybrid method for multivariate calibration" *Analytical Chemistry* **2007**, *79*, 234-239.

(89) McMurdy, J. W.; Berger, A. J. "Raman spectroscopy-based creatinine measurement in urine samples from a multipatient population" *Applied Spectroscopy* **2003**, *57*, 522-525.

(90) Espinosa-Mansilla, A.; Valenzuela, M. I. A.; de la Pena, A. M.; Salinas, F.; Canada, F. C. "Comparative study of partial least squares and a modification of hybrid liNear analysis calibration in the simultaneous spectrophotometric determination of rifampicin, pyrazinamide and isoniazid" *Analytica Chimica Acta* **2001**, *427*, 129-136.

(91) Goicoechea, H. C.; Olivieri, A. C. "Wavelength selection by net analyte signals calculated with multivariate factor-based hybrid liNear analysis (HLA). A theoretical and experimental comparison with partial least-squares (PLS)" *Analyst* **1999**, *124*, 725-731.

(92) Anonymous, Diabetes mellitus, World Health Organization, http://www.who.int/diabetes.

(93) Weast, R. C. *Handbook of Chemistry and Physis*; Chemical Rubber Company: Cleveland, OH, 1975.

(94) Arnold, M. A.; Liu, L.; Olesberg, J. T. "Selectivity assessment of noninvasive glucose measurements based on analysis of multivariate calibration vectors" *J Diabetes Science and Technology* **2007**, *1*, 454-462.

(95) http://diabetes.niddk.nih.gov/dm/pubs/type1and2/what.htm.

(96) Liu, L. "Identification of a selective glucose spectra signature for noninvasive Near infrared measurements with multivariate calibration approaches" PhD, University of Iowa, Iowa City, **2005**.

(97) Alexeeva, N. V.; Arnold, M. A. "Near-infrared microspectroscopic analysis of rat skin tissue heterogeneity in relation to noninvasive glucose sensing" *J Diabetes Science and Technology* **2009**, *3*, 219-232.

(98) Burmeister, J. J.; Arnold, M. A. "Evaluation of measurement sites for noninvasive blood glucose sensing with Near-infrared transmission spectroscopy" *Clinical Chemistry* **1999**, *45*, 1621-1627.

(99) Xiang, D. "Advances in Near-infrared glucose monitoring using pure component selectivity analysis for model characterization and a novel digital micromirror array spectrometer" PhD, University of Iowa, Iowa City, **2006**.

(100) http://www.fho-emden.de/~hoffmann/cielab03022003.pdf.

(101) Ingle, J. D.; Crouch, S. R. *Spectrochemical Analysis*, 1st ed.; Prentice Hall Inc: New Jersey, **1988.**

(102) Skoog, D. A.; Holler, F. J.; Nieman, T. A. *Principles of Instrumental Analysis*, 5th ed.; Saunders College Publishing: Philadelphia, **1998**.

(103) Philp, A.; Macdonald, A. L.; Watt, P. W. "Lactate - a signal coordinating cell and systemic function" *Journal of Experimental Biology* **2005**, *208*, 4561-4575.

(104) Klonoff, D. C. "Technology for portable measurement of blood lactate" *Diabetes Technology & Therapeutics* **2003**, *5*, 929-931.

(105) Luft, F. C. "Lactic acidosis update for critical care clinicians" *Journal of The American Society of Nephrology* **2001**, *12*, S15-S19.

(106) Eddy, C. V.; Arnold, M. A. "Near-infrared spectroscopy for measuring urea in hemodialysis fluids" *Clinical Chemistry* **2001**, *47*, 1279-1286.

(107) Olesberg, J. T.; Arnold, M. A.; Flanigan, M. J. "Online measurement of urea concentration in spent dialysate during hemodialysis" *Clinical Chemistry* **2004**, *50*, 175-181.

(108) Jensen, P. S.; Bak, J.; Andersson-Engels, S. "Influence of temperature on water and aqueous glucose absorption spectra in the Near- and mid-infrared regions at physiologically relevant temperatures" *Applied Spectroscopy* **2003**, *57*, 28-36.

(109) Shao, X. G.; Kang, J.; Cai, W. S. "Quantitative determination by temperature dependent Near-infrared spectra" *Talanta* **2010**, *82*, 1017-1021.